博 士 学 位 論 文

論文題目　Numerical Methods for Simulating Multiphysics Thermal-Fluid Flows of Supercritical Hydrocarbon

提　出　者　　東北大学大学院情報科学研究科

情報基礎科学専攻

学籍番号　C0ID1003

氏名　八柳秀門

TOHOKU UNIVERSITY
Graduate School of Information Sciences

Numerical Methods for Simulating Multiphysics Thermal-Fluid Flows of Supercritical Hydrocarbon (超臨界炭化水素におけるマルチフィジックス熱流動の数値解法)

A dissertation submitted for the degree of Doctor of Philosophy (Information Sciences)
Department of Computer and Mathematical Sciences

by

Shuto YATSUYANAGI

January 10, 2023

Numerical Methods for Simulating Multiphysics Thermal-Fluid Flows of Supercritical Hydrocarbon

Shuto YATSUYANAGI

Abstract

A supercritical fluid is a fluid in a state exceeding the critical pressure and critical temperature of a substance. At higher pressures than the critical pressure, the surface tension and latent heat approach zero, and the thermodynamic and transport properties drastically and continuously change crossing the pseudocritical line. In the present study, the unique transition state is called the transcritical condition. It is sometimes called the pseudo-boiling owing to its similarities with the boiling phenomenon at subcritical pressure. It is experimentally known that turbulent heat transfer characteristics and frictional stress characteristics vary significantly in the transcritical region. Hence, an understanding of the pseudo-boiling phenomenon in the transcritical region is crucial for industrial applications that utilize the supercritical fluid. Industrial applications of supercritical fluids actively utilize or inevitably encounter the pseudo-boiling phenomenon. In addition, chemical reactions such as nanoparticle formation and pyrolysis sometimes occur in supercritical fluid devices. Therefore, the internal flow of supercritical fluid devices may become a multiphysics flow in which multiple physical phenomena coexist and interfere with each other. Understanding the multiphysics flow that governs the characteristics of supercritical fluid devices is the key to further innovation.

Of among the industrial applications of supercritical fluids, a regenerative cooling system using hydrocarbon fuel as the working fluid has attracted the attention of many researchers in the context of the development of a hypersonic reusable launch vehicle. In the regenerative cooling system, the hydrocarbon fuel is fed into the cooling channel around the combustion chamber to cool the engine system with the heat exchange. Hydrocarbon fuels such as kerosene fuel have desirable characteristics for use as aviation fuel and rocket propellant, such as their high density, which allows for smaller fuel tanks, and ease of handling. However, there exist many unsolved aspects of multiphysics flows of hydrocarbons in the regenerative cooling system, and these are barriers to understanding the cooling characteristics. Another challenge is to develop robust numerical methods to simulate these unsolved hydrocarbon flows. The objective of this work is to develop a robust numerical method for supercritical multicomponent flows of hydrocarbons and to clarify the multiphysics flows of hydrocarbons that govern the characteristics of regenerative cooling systems.

The robust numerical method for simulating multicomponent and supercritical hydrocarbon flows is established. The spurious oscillations associated with the multicomponent and supercritical flows when using a fully conservative scheme are investigated in detail. The present study analytically clarifies the mechanism responsible for the generation of spurious oscillations in preconditioning systems. In a one-dimensional Euler system, I derived the temporal variation of the unknown variables in the case of a single fluid interface for different temperatures, and also at the material interface for a uniform fluid temperature. The temporal variation in the preconditioned system indicated that the spatial variations of the mass fraction and temperature caused spurious oscillations. Based on the analytical results, the double flux model (DFM) is extended to the preconditioning

method to eliminate the spurious pressure oscillations. Furthermore, the conservation errors due to the use of a quasi-conservative form are quantitatively evaluated. The proposed numerical methods are applied to a series of test cases to examine the performance of DFM and to demonstrate its suitability in simulations for multicomponent supercritical flows of hydrocarbons.

To investigate the effects of pyrolysis reaction on supercritical hydrocarbon flows, the present study conducts numerical simulations for supercritical *n*-octane flows with the pyrolysis reaction in a heated circular pipe. To clarify the effect of density change associated with the pyrolysis reaction, the k–ω SST+Mτ turbulence model is incorporated into the numerical method based on the preconditioning method. The pyrolysis reaction model is developed based on a series of zero-dimensional pyrolysis reaction calculations. The reaction equation is expressed as a one-step reaction, and the reaction rate constant is expressed by using the Alenius equation. The pyrolysis reaction model is validated compared to the experimental data of the mole fraction of decomposed components. Supercritical *n*-octane flows in a horizontal heated circular pipe with pyrolysis are conducted, and numerical results are compared with the experimental data about the outlet temperature and the conversion rate to validate the present numerical methods. The effect of density fluctuations on turbulent thermal diffusivity is discussed. Simulated results suggest that the consideration of the density fluctuations effect and the corresponding production of turbulent kinetic energy are key issues for reproducing the thermal fluid flows of supercritical hydrocarbons with pyrolysis. In addition, the capabilities and limitations of simple thermophysical property models for the mixture are evaluated through a comparison of results obtained using three mixture property models.

The mechanism of flow instability and the hydrodynamic characteristic curve, which is deeply related to the dynamic behavior of flow instability, are investigated for supercritical hydrocarbon flows. First, new numerical methods that can conduct the transient simulation for the flow instabilities under the transcritical and pyrolysis conditions are developed to clarify the mechanism of flow instability. The numerical methods are validated by referring to available numerical and experimental data on pressure drop and mass flow rate in a heated circular tube. First, steady-state simulations are conducted to obtain the hydrodynamic characteristic curve for *n*-dodecane flows. The effects of DFM and PSM on the hydrodynamic characteristic curves are investigated. Then, transient simulations are conducted for the flow instability of *n*-dodecane flows in a horizontal heated circular tube. The effects of pyrolysis reactions and pressure on the flow instability are evaluated for *n*-dodecane flows in a horizontal heated circular tube. Next, the hydrodynamic characteristic curves of a horizontal heated circular tube at supercritical pressure are investigated by using the large eddy simulation (LES) code. The numerical methods are validated by referring to available direct numerical simulation data of the turbulent channel flows and also the friction factor correlation of the adiabatic circular tube. Hydrodynamic characteristic curves are obtained under different three supercritical pressure conditions. To clarify the generation mechanisms of pressure-drop behind the formation of the hydrodynamic characteristic curves, the present LES analyzes the flow properties, such as the thermodynamic properties and local Nusselt number, and turbulence statistics in the heated circular tube.

Contents

Chapter 1

Introduction

1.1 Backgrounds and motivations

A supercritical fluid is a fluid in a state exceeding the critical pressure and critical temperature of a substance. Figure 1.1 shows the phase diagram for the pressure and temperature. The pseudocritical temperature, which exhibits a drastic change in thermophysical properties, depends on the pressure condition. The line connecting the pseudocritical temperature is called the pseudocritical line; this is indicated by the red line in Fig. 1.1. Figure 1.2 shows the temperature dependency of density, isobaric specific heat, viscosity, and thermal conductivity for *n*-dodecane at a supercritical pressure of 2 MPa and 5 MPa. The thermodynamic properties calculated by the perfect-gas relations and the transport properties calculated by Sutherland's law are also plotted in Fig. 1.2. When crossing the pseudocritical line, the fluid characteristic changes from a liquid-like high-density fluid to a gas-like low-density fluid. The isobaric specific heat peaks at the pseudocritical line. At higher pressures than the critical pressure, the surface tension and latent heat approach zero, and the thermodynamic and transport properties continuously change crossing the pseudocritical line. However, the changes occur abruptly over a narrow temperature range. In the present study, the unique transition state is called the transcritical condition. It is sometimes called the pseudo-boiling owing to its similarities with the boiling phenomenon at subcritical pressure. It is experimentally known that turbulent heat transfer characteristics [1] and frictional stress characteristics [2] vary significantly in the transcritical region. Hence, an understanding of the pseudo-boiling phenomenon in the transcritical region is crucial for industrial applications that utilize the supercritical fluid.

Supercritical fluids have been used in chemical processes such as nanoparticle formation [3], chromatography [4], and thin-film deposition for microelectronics [5], as well as working fluids in advanced power generation cycles [6] and spacecraft thermal protection systems [7]. Further expansion of the use of supercritical fluids is expected not only in terms of their efficiency but also in terms of their environmental friendliness and sustainability [8]. Industrial applications of supercritical fluids actively utilize or inevitably encounter unique thermophysical property changes in the transcritical state and chemical reactions. In addition, chemical reactions such as nanoparticle formation and pyrolysis sometimes occur in supercritical fluid devices. Therefore, the internal flow of supercritical fluid devices sometimes becomes a multiphysics flow in which multiple physical phenomena coexist and interfere. Understanding the multiphysics flow that governs the characteristics of supercritical fluid devices is the key to further innovation.

Experiments on supercritical fluids are difficult because they are generally under high-temperature and high-pressure conditions. The use of computational fluid dynamics (CFD), which enables fluid analysis

modeling on a computer, is expected to better explain multiphysics supercritical flows. However, there exist multiphysics flows that are difficult to simulate with conventional CFD tools, and a better understanding of their flow mechanisms is not an easy task. Further innovation and the expanded use of supercritical fluid devices require multiphysics CFD tools that can accurately simulate complex multiphysics flow at supercritical pressures.

Of among the industrial applications of supercritical fluids, a regenerative cooling system using hydrocarbon fuel as the working fluid has attracted the attention of many researchers in the context of the development of a hypersonic reusable launch vehicle. The regenerative cooling system is a highly efficient thermal protection technology for aerospace vehicles that use fuel or oxidizer as a coolant. The Japan Aerospace Exploration Agency (JAXA) has researched and developed a reusable launch vehicle called the Two-Stage-To-Orbit (TSTO) system [9]. Figure 1.3 shows an illustration of the booster stage in the TSTO system. The JAXA has considered applying the regenerative cooling system using hydrocarbon fuel to the launch vehicle. The hydrocarbon fuel is fed into the cooling channel around the combustion chamber to cool the engine system with the heat exchange. After that cooling process, it will be injected into the combustion chamber. In general, the pressure in the cooling channel is above the supercritical pressure of the hydrocarbon fuel to prevent heat transfer deterioration associated with boiling phenomena at subcritical pressure.

Hydrocarbon fuels such as kerosene fuel have desirable characteristics for use as aviation fuel and rocket propellant, such as their high density, which allows for smaller fuel tanks, and ease of handling. However, there exist many unsolved aspects of hydrocarbon flow at supercritical pressure in the regenerative cooling system, and these are barriers to understanding the cooling characteristics. Another challenge is to develop robust numerical methods to simulate these unresolved hydrocarbon flows. The present study focused on three issues: the development of a robust numerical method for supercritical hydrocarbon flow, the clarification of supercritical hydrocarbon flow with endothermic pyrolysis reaction, and the clarification of flow instabilities on supercritical hydrocarbon.

First, it is necessary to develop a robust numerical method for supercritical hydrocarbon flow. It is known that so-called spurious oscillations [10] occur when solving flows with thermophysical property changes using a fully conservative scheme. Spurious oscillations generate unphysical flow that, in the worst case, leads to the divergence of simulation. In the analysis of the regenerative cooling system, the occurrence of spurious oscillations is inevitable owing to the dramatic changes in thermophysical properties caused by pseudo-boiling and pyrolysis reactions of the hydrocarbon fuel. To accurately understand the multiphysics flow in a regenerative cooling system, the development of numerical methods that can prevent these spurious oscillations and that can stably simulate supercritical multicomponent flows is urgently needed.

The problem with respect to the presence of spurious oscillations in fully conservative schemes was first reported by Abgrall [10]. He reported spurious pressure oscillations occurring in multicomponent flows and proposed a quasi-conservative scheme for solving the mass fraction transport equation in a non-conservative form to prevent this problem. This idea was extended to higher-order accurate finite-volume [11] and finite-difference [12] schemes. In addition, various other numerical methods have been proposed, such as solving the pressure evolution equation instead of the total energy conservation equation [13] and introducing an additional evolution equation to maintain pressure equilibrium [14]. The double-flux model (DFM) [15] is a

quasi-conservative method developed by Abgrall and Karni for multicomponent nonreactive flows assuming thermally perfect gas. DFM has been extended to reactive flows [16] and transcritical flows [17]. These previous studies on DFM have been conducted under the assumption of ordinary compressible flow and for sufficiently high velocity forced convection. In contrast, low Mach number flows with density variations are also an important topic for practical applications such as chemical reactors and heat exchangers. Usually, the Navier–Stokes equations with low Mach number approximation [18, 19] or the preconditioning method [20-23] are considered the numerical methods of choice for such flows. The low Mach number approximation removes from the fundamental equations the effect of sound waves on the solution, whereas the preconditioning method can take into account the effect of sound waves. Versatile approaches to compressible and incompressible fluids, such as the preconditioning method, are important for a variety of industrial applications. Housman et al. [24] reported that the preconditioning methods also have spurious oscillation problems. Their proposed numerical method is based on a fully conservative preconditioned Euler system, but they attempted to prevent spurious oscillations by employing a hybrid scheme that switches to a non-conservative preconditioned Euler system near the material interface. Although they reported the effectiveness of their method in multidimensional problems, the mechanism of spurious oscillations in the preconditioned system was not investigated at all, and the conservation error resulting from the use of the non-conservative form was not evaluated.

The second issue is the clarification of supercritical hydrocarbon flow with endothermic pyrolysis reaction. Some polymer hydrocarbons contained in hydrocarbon fuels undergo endothermic pyrolysis reactions [25] at high temperatures above about 700 K, and they are called endothermic hydrocarbon fuels (EHFs). Although the effective utilization of endothermic reactions is expected to improve the cooling performance, the effect of pyrolysis reaction on hydrocarbon flows at supercritical pressure has never been sufficiently understood, and this is a barrier to the quantitative prediction of cooling performance. To enable the development of a highly efficient regenerative cooling system, a multiphysics CFD tool capable of reproducing the flow of supercritical hydrocarbons with pyrolysis reactions is needed.

The use of EHFs in regenerative cooling systems has been investigated since the 1960s. Nixon et al. [26] demonstrated that the selective dehydrogenation of methylcyclohexane using a Pt/Al_2O_3 catalyst could yield a total heat sink of 1300 Btu/lb at pressures up to 900 psi with maximum conversions of about 60%. Since then, various experimental studies have been conducted, including the application of cheaper catalysts to paraffinic fuels [27] and the evaluation of the endothermic properties of existing jet fuels [28]. Recently, many numerical and experimental studies for endothermic pyrolysis reaction of hydrocarbon fuels have been conducted. Ward et al. [29] developed a one-step global reaction model called the proportional product distribution (PPD) model for the mild cracking of *n*-decane and *n*-dodecane. The PPD model has been employed in many numerical studies [30-35] owing to its practical accuracy and simplicity. Zhu et al. [36] proposed a one-step global reaction model for *n*-decane containing 18 decomposition components at supercritical pressure. The model was valid for conversions less than 13%. The numerical studies that were carried out were based on the simplified pyrolytic reaction mechanisms, such as the PPD model [29] or the model proposed by Zhu et al. [36], ignored many important secondary chemical reactions, and the applicability of these numerical models was limited to the mild cracking conditions. For such a situation, Jiang et al. [37]

constructed a detailed reaction model for the aviation kerosene RP-3 considering 18 chemical species and 24 elementary reactions with C5–C11 alkene and cycloalkane lamps. Xu and Meng [38] employed the detailed reaction model proposed by Jiang et al. [37] and numerically studied the turbulent convective heat transfer of RP-3 in a circular cooling tube at a supercritical pressure of 5 MPa. More advanced numerical simulations targeting the carbon deposition [39-42], steam reforming [43, 44], and secondary flow in a curved channel [45] have recently been conducted as well. Despite these many studies, the interference mechanism between the pyrolysis reactions and the flow is still not fully understood. In particular, the effects of large density fluctuations associated with pyrolysis reactions on turbulent transport have not been discussed at all. Recent direct numerical simulations for transcritical turbulent boundary layers [46] have revealed that large density fluctuations associated with pseudo-boiling generate non-negligible turbulent kinetic energy in the case of ideal-gas flows with small density fluctuations, the density fluctuation effect is generally negligible. Because supercritical hydrocarbon flows with pyrolysis reactions can exhibit density fluctuations that are comparable to those of pseudo-boiling, it is expected that supercritical hydrocarbon flow analysis takes into account the density fluctuation effect of turbulence. However, the conventional Reynolds-averaged Navier–Stokes (RANS) models, such as the k–ε, k–ω, and k–ω SST model, neglect density fluctuation effects on turbulent kinetic energy generation and cannot account for them in the flow simulation. In this situation, Kawai and Oikawa [47] recently developed a new RANS model, the k–ω SST+M_τ model, which takes into account turbulent kinetic energy generation due to density fluctuations.

The third issue is the flow instabilities on supercritical hydrocarbon. The drastic flow rate fluctuation of hydrocarbon fuels in the transcritical region was observed in a heated circular tube [48]. This is called "flow instability" and can cause heat transfer deterioration and mechanical vibration, endangering the operation of the system. Understanding the flow instability mechanism using multiphysics CFD can aid in developing a reliable regenerative cooling system.

The flow instability in a heated tube is classified as static instability and dynamic instability: they indicate flow excursion or flow oscillation. The work on flow instability was started by Ledinegg [49], who demonstrated that the pressure drop in a heated channel is expressed as a cubic curve with respect to the flow rate. This relationship is well-known as the multi-valued hydrodynamic characteristic curve. The negative slope region in the hydrodynamic characteristic curve has been recognized as a necessary condition of flow excursion, which is one of the static instabilities. This flow excursion studied by Ledinegg is often called the Ledinegg instability. Starting with Ledinegg's study, and as the background of the design and operation of industrial systems utilizing two-phase flow, such as boiling water reactors, intensive research has been conducted from the 1960s to the present, and numerous amounts of experimental and numerical data have been obtained [50-52]. In recent years, with the increased industrial use of supercritical fluids, the phenomenon of flow fluctuation at supercritical pressure as well as subcritical pressure has attracted attention. Several numerical [53-72] and experimental [73-82] studies have been conducted on flow instability under supercritical pressure conditions. However, research into the flow instability of supercritical fluids is still in its infancy, and no consensus has been attained on the mechanism of flow instability, or even pertaining to its existence [74]. Nevertheless, Yang et al. [74-76] reported experimental data indicating the universal existence of flow instability of hydrocarbons at supercritical pressure, and detailed discussions on the mechanism of occurrence

are expected. In addition, although there are also some studies on the flow instability phenomenon in the pyrolysis region [69, 72, 77], the phenomenon has not been well understood owing to a lack of knowledge in both experiments and numerical simulations.

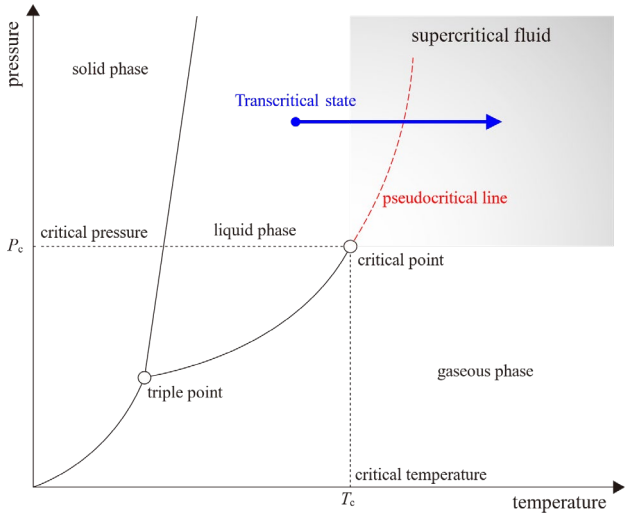

Figure 1.1. Phase diagram for pressure and temperature with pseudocritical line.

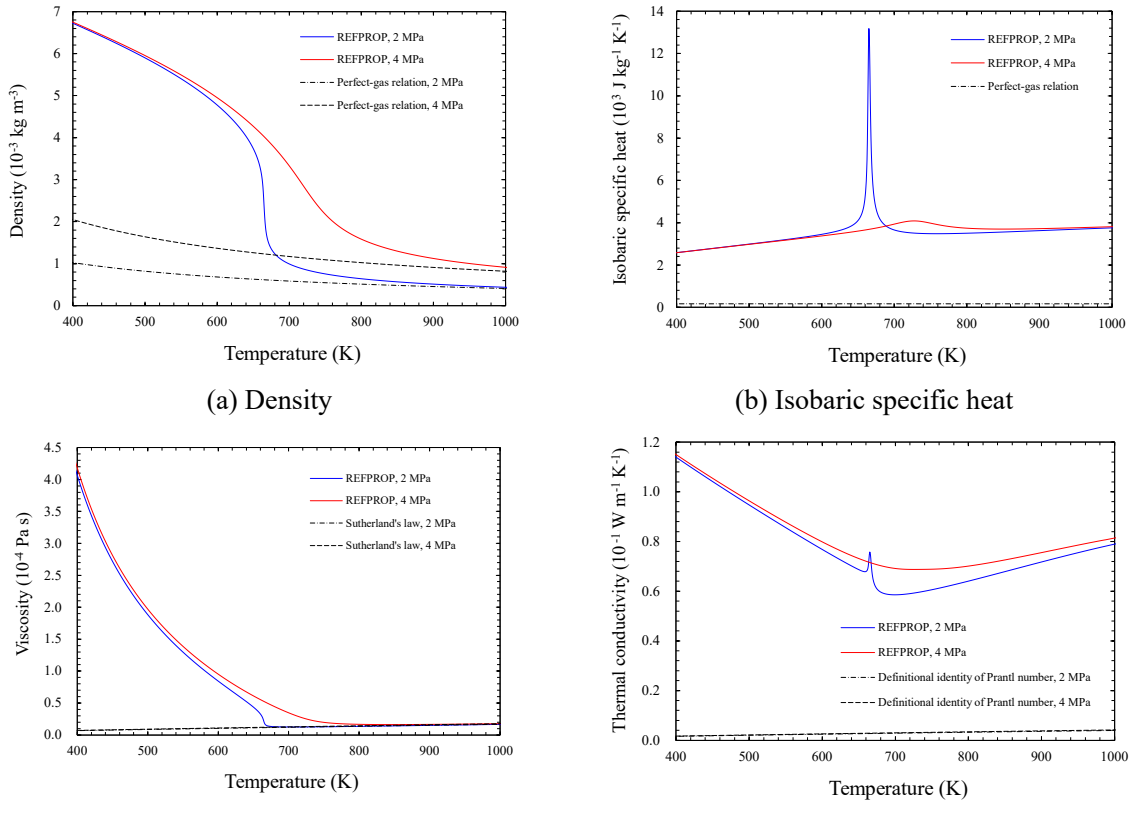

(a) Density

(b) Isobaric specific heat

(c) Viscosity

(d) Thermal conductivity

Figure 1.2. Thermophysical and transport properties for *n*-dodecane using REFPROP (NIST Standard Reference Database, Version 10.0), the perfect-gas relations, and Sutherland's law ($\mu = \mu_{1100\mathrm{K}}\,(1100+S)/(T+S)(T/1100)^{3/2}$ where $S = 600, \kappa = \mu c_p/Pr$, and $Pr = 0.72$) at $p = 2$ MPa and $p = 4$ MPa.

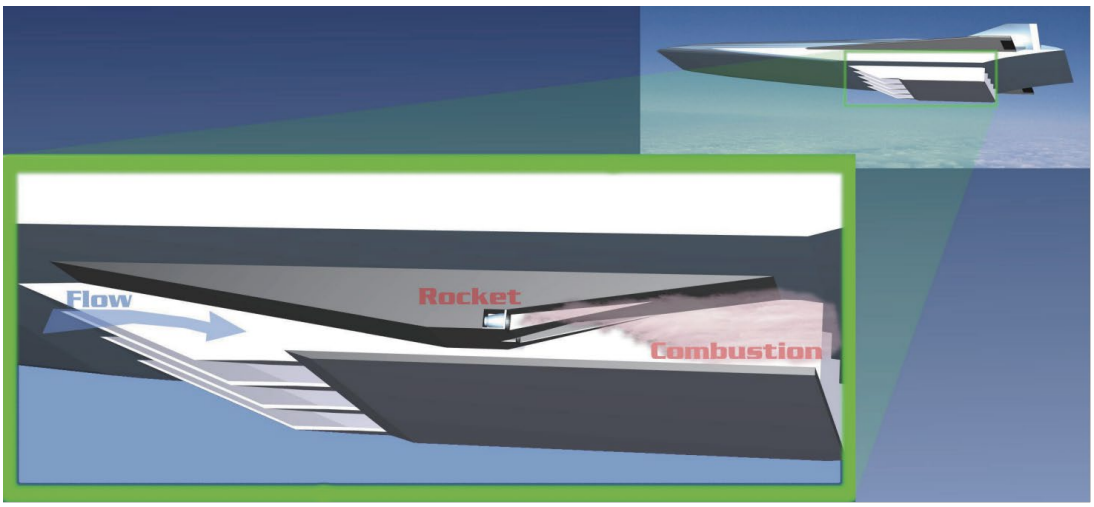

Figure 1.3. Illustration of booster stage in TSTO system [9].

1.2 Objectives

The objective of this work is to develop a robust numerical method for supercritical multicomponent flows of hydrocarbons and to clarify the multiphysics flows of supercritical hydrocarbons that govern the characteristics of regenerative cooling systems. To achieve the objective, this study specifically addresses the following three issues.

- Although the problem of spurious oscillations in the preconditioning method has been known for some time, the generation mechanism of such oscillations has not been investigated at all. This study analytically clarifies the mechanism responsible for the generation of spurious oscillations for preconditioning systems for which there is limited knowledge in the previous study. Based on the analytical results, a new DFM procedure for the preconditioning system was developed to establish a numerical method for preventing spurious oscillations in the preconditioning system.

- The existing studies on supercritical hydrocarbon flow with endothermic pyrolysis reactions did not consider the density fluctuation effects of turbulence. In this study, the k–ω SST+M_τ model is introduced into the preconditioned compressible Navier–Stokes equations, and numerical simulations are conducted for supercritical hydrocarbon flows in a horizontal heated circular tube to clarify the effect of density fluctuation associated with pyrolysis reactions on supercritical hydrocarbon flows.

- The flow oscillation phenomenon in a heated tube is one of the most important issues to consider when developing a reliable regenerative cooling system; however, the mechanism has not yet been understood owing to the lack of experimental data and the difficulty associated with performing robust simulations for the supercritical fluid flow. First, a new robust numerical method is developed that can conduct the transient simulation for the flow instabilities under the transcritical

and pyrolysis conditions. Transient simulations of flow instability in a heated circular tube are conducted using the developed numerical method to evaluate effects of the pyrolysis reaction and pressure on the flow instability. Next, the present study conducts numerical simulations for *n*-dodecane flows in a horizontal heated circular tube by using a robust three-dimensional large eddy simulation (LES) code toward the clarification of the generation mechanism of the hydrodynamic characteristic curve at supercritical pressure.

1.3 Outline of the thesis

The contents of this thesis are outlined as follows: The robust numerical method for simulating the multicomponent supercritical flows is established in Chapter 2, and numerical methods for this study are also provided. The spurious oscillations associated with the multicomponent and supercritical flows when a fully conservative scheme is employed are investigated in detail. The DFM is extended to the preconditioning method to eliminate the spurious pressure oscillations. The conservation error of mass, momentum, and total energy are evaluated. The proposed numerical methods are applied to a series of test cases to examine the performance of DFM and to demonstrate its suitability in simulations for multicomponent supercritical flows.

In Chapter 3, the modeling method for the pyrolysis reaction of hydrocarbons is established. Using Cantera software and the JetSurf model, a series of zero-dimensional pyrolysis reaction calculations of *n*-dodecane are conducted to define the reaction equation and reaction rate constants. Then, the pyrolysis reaction model is introduced to the numerical method based on the preconditioning method. Assuming an axisymmetric flow, the supercritical *n*-dodecane flows with the pyrolysis reaction in a heated circular pipe are simulated. The numerical results are compared with the experimental data about the outlet temperature and the conversion rate to validate the pyrolysis reaction model. In addition, the results of the *n*-dodecane flow are compared to those of the *n*-octane flow and the differences between both flows are discussed.

In Chapter 4, the effects of pyrolysis reaction on supercritical *n*-octane flows in a horizontal heated circular tube are elucidated. To clarify the effects of density fluctuations on the supercritical flow, the k–ω SST+Mτ turbulence model is introduced to the numerical method based on the preconditioning method. The detailed zero-dimensional reaction calculation estimated the endothermic energy and reaction rate. The thermophysical properties of the pure fluid are calculated by the polynomial equations defined in the Reference Fluid Thermodynamic and Transport Properties Database (REFPROP), and the mixture properties are modeled on the basis of the mass fraction. The numerical method was validated through comparisons with experimental data on the temperature and conversion rate. The capabilities and limitations of simple thermophysical property models for the mixture are evaluated by using the three mixture property models. The effect of density fluctuations on turbulent thermal diffusivity is discussed by employing the k–ω SST+M$_\tau$ turbulence model.

In Chapter 5, the mechanism of flow instability and the hydrodynamic characteristic curve, which is deeply related to the dynamic behavior of flow instability, are investigated. First, new numerical methods that can simulate the flow instabilities under the transcritical and pyrolysis conditions are developed to investigate the dynamic behavior of flow instability. The numerical methods are validated by referring to

available numerical and experimental data on pressure drop and mass flow rate in a heated circular tube. First, steady-state simulations are conducted to obtain the hydrodynamic characteristic curve for *n*-dodecane flows. The effects of DFM and PSM on the hydrodynamic characteristic curves are investigated. Then, transient simulations are conducted for the flow instability of *n*-dodecane flows in a horizontal heated circular tube. The effects of pyrolysis reactions and pressure on the flow instability are evaluated for *n*-dodecane flows in a horizontal heated circular tube. Next, the hydrodynamic characteristic curves of a horizontal heated circular tube at supercritical pressure are investigated by using the LES code. The numerical methods are validated by referring to available direct numerical simulation (DNS) data of the turbulent channel flows and also the friction factor correlation of the adiabatic circular tube. After the validation, the simulations for n-dodecane flows in a horizontal heated circular tube are conducted, and the pressure drop with respect to the mass flow rate, i.e., the hydrodynamic characteristic curves, are calculated for three different pressure conditions. To clarify the generation mechanisms of pressure-drop behind the formation of the hydrodynamic characteristic curves, the present LES analyzes the flow properties, such as the thermodynamic properties and local Nusselt number, and turbulence statistics in the heated circular tube.

In Chapter 6, the conclusions of this thesis are presented, and an outlook for future research is discussed.

References

1. D. Huang, Z. Wu, B. Sunden, W. Li, “A brief review on convection heat transfer of fluids at supercritical pressures in tubes and the recent progress,” Applied Energy, 162, (2016), 494-505.
2. X. Fang, Y. Xu, X. Su, R. Shi, “Pressure drop and friction factor correlations of supercritical flow,” Nuclear Engineering and Design, 242, (2012), 323-330.
3. T. Adschiri, Y. Hakuta, K. Sue, K. Arai, “Hydrothermal synthesis of metal oxide nanoparticles at supercritical conditions,” Journal of Nanoparticle Research, 3, (2001), 227–235.
4. M. Saito, “History of supercritical fluid chromatography: Instrumental development,” Journal of Bioscience and Bioengineering, 115, (2013), 590–599.
5. Y. Jianzhong, Z. Xianzhen, X. Qinqin, Z. Chuanjie, W. Aiqin, “Supercritical fluids deposition techniques for the formation of nanocomposites,” Progress in Chemistry, 21, (2009) 606–614.
6. V. Dostal, “A supercritical carbon dioxide cycle for next generation nuclear reactors,” In: Nuclear Engineering, Massachusetts Institute of Technology, (2004).
7. Y. Zhu, W. Peng, R. Xu, P. Jiang, “Review on active thermal protection and its heat transfer for airbreathing hypersonic vehicles,” Chinese Journal of Aeronautics, 31, (2018), 1929-1953.
8. Z. Knez, E. Markocic, M. Leitgeb, M. Primozic, M. Knez Hrncic, M. Skerget, “Industrial applications of supercritical fluids: A review,” Energy, 77, (2014), 235–243.
9. S. Tomioka, T. Hiraiwa, T. Saito, K. Kato, M. Kodera, K. Tani, “System analysis of a hydrocarbon-fueled RBCC engine applied to a TSTO launch vehicle,” Transactions of the Japan Society for Aeronautical and Space Sciences, Aerospace Technology Japan, 12 (29) (2014) 91–99.
10. R. Abgrall, “How to prevent pressure oscillations in multicomponent flow calculations: a quasi conservative approach,” Journal of Computational Physics, 125, (1996), 150–160.
11. E. Johnsen and T. Colonius, “Implementation of WENO schemes in compressible multicomponent flow problems,” Journal of Computational Physics, 219, (2006), 715–732.
12. T. Nonomura, S. Morizawa, H. Terashima, S. Obayashi, K. Fujii, “Numerical (error) issues on compressible multicomponent flows using a high-order differencing scheme: weighted compact nonlinear scheme,” Journal of Computational Physics, 231, (2012), 3181–3210.
13. H. Terashima and M. Koshi, “Approach for simulating gas-liquid-like flows under supercritical pressures using a high-order central differencing scheme,” Journal of Computational Physics, 231, (2012), 6907–6923.
14. C. Pantano, R. Saurel, T. Schmitt, “An oscillation free shock-capturing method for compressible van der Waals supercritical fluid flows,” Journal of Computational Physics, 335, (2017), 780–811.
15. R. Abgrall and S. Karni, “Computations of compressible multifluids,” Journal of Computational Physics, 169, (2001), 594–623.
16. G. Billet and R. Abgrall, “An adaptive shock-capturing algorithm for solving unsteady reactive flows,” Computers & Fluids, 32(10), (2003), 1473–1495.
17. P.C. Ma, Y. Lv, M. Ihme, “An entropy-stable hybrid scheme for simulations of transcritical real-fluid flows,” Journal of Computational Physics, 340, (2017), 330–357.

18. J.H. Bae, J.Y. Yoo, H. Choi, “Direct numerical simulation of turbulent supercritical flows with heat transfer,” Physics of Fluids, 17, (2005), 105104.
19. H. Nemati, A. Patel, B.J. Boersma, R. Pecnik, “Mean statistics of a heated turbulent pipe flow at supercritical pressure,” International Journal of Heat and Mass Transfer, 83, (2015), 741–752.
20. E. Turkel, “Preconditioning methods for solving the incompressible and low speed compressible equations,” Journal of Computational Physics, 72, (1987), 277–298.
21. Y.H. Choi, C.L. Merkle, “The application of preconditioning in viscous flows,” Journal of Computational Physics, 105, (1993), 207–223.
22. J.M. Weiss, W.A. Smith, “Preconditioning applied to variable and constant density flows,” AIAA Journal, 33, (1995), 2050–2056.
23. S. Yamamoto, “Preconditioning method for condensate fluid and solid coupling problems in general curvilinear coordinates,” Journal of Computational Physics, 207, (2005), 240–260.
24. J.A. Housman, C.C. Kiris, M.M. Hafez, “Time-derivative preconditioning methods for multicomponent flows. Part I: Riemann problems,” Journal of Applied Mechanics, 76, (2009), 021210.
25. H. Huang, L.J. Spadaccini, D.R. Sobel, “Fuel-cooled thermal management for advanced aeroengines,” Journal of Engineering for Gas Turbines and Power, 126, (2004), 284-293.
26. A.C. Nixon, G.H. Ackermars, L.E. Faith, R.D. Hawthorn, H.T. Henderson, A.W. Ritchie, L.B. Ryland, “Vaporization and endothermic fuels for advanced engine applications. Part 1. Studies of Thermal and Catalytic Reactions, Thermal Stabilities, and Combustion Properties of Hydrocarbon Fuels,” U.S. Air Force Technical Report AFAPL-TR-67-114, (1967).
27. D.R. Sobel and L. J. Spadaccini, ‘‘Hydrocarbon fuel cooling technologies for advanced propulsion,’’ Journal of Engineering for Gas Turbines and Power, 119, (1997), 344–351.
28. H. Huang, D.R. Sobel L.J. Spadaccini, “Endothermic heat-sink of hydrocarbon fuels for scramjet cooling,” 38th AIAA/ASME/SAE/ASEE joint propulsion conference & exhibit, AIAA-2002-3871, (2002).
29. T.A. Ward, J.S. Ervin, R.C. Striebich, S. Zabarnick, “Simulations of flowing mildly cracked normal alkanes incorporating proportional product distributions,” Journal of Propulsion and Power, 20 (3), (2004), 394–402.
30. B. Ruan, H. Meng, V. Yang, “Simplification of pyrolytic reaction mechanism and turbulent heat transfer of n-decane at supercritical pressures,” International Journal of Heat and Mass Transfer, 69, (2014), 455–463.
31. W. Bao, S. Zhang, J. Qin, W. Zhou, K. Xie, “Numerical analysis of flowing cracked hydrocarbon fuel inside cooling channels in view of thermal management,” Energy, 67, (2014), 149-161.
32. Y. Feng, J. Qin, S. Zhang, W. Bao, Y. Cao, H. Huang, Modeling and analysis of heat and mass transfers of supercritical hydrocarbon fuel with pyrolysis in minichannel, International Journal of Heat and Mass Transfer, 91, (2015), 520–531.
33. Y. Feng, Y. Jiang, X. Li, S. Zhang, J. Qin, Y. Cao, H. Huang, Numerical study on the influences of heat and mass transfers on the pyrolysis of hydrocarbon fuel in minichannel, Applied Thermal Engineering, 119, (2017), 650–658.

34. Y. Feng, S. Liu, J. Qin, Y. Cao, Y. Jiang, S. Zhang, Numerical study on the influence of turbulence on the pyrolysis of hydrocarbon fuel in mini-channel, International Journal of Heat and Mass Transfer, 119, (2018), 768–776.
35. Y. Feng, J. Qin, S. Liu, S. Zhang, Xin Li, Y. Cao, H. Huang, A simplification of pyrolytic reaction model of hydrocarbon fuel and its application in simulation of heated channel flow, International Journal of Thermal Sciences, 130, (2018), 10–18.
36. Y.H. Zhu, B. Liu, P.X. Jiang, Experimental and numerical investigations on n-decane thermal cracking at supercritical pressures in a vertical tube, Energy Fuels 28 (1) (2014) 466–474.
37. R.P. Jiang, G.Z. Liu, X.W. Zhang, "Thermal cracking of hydrocarbon aviation fuels in regenerative cooling microchannels," Energy Fuels, 27 (5), (2013), 2563–2577.
38. K. Xu and H. Meng, "Modeling and simulation of supercritical-pressure turbulent heat transfer of aviation kerosene with detailed pyrolytic chemical reactions," Energy & Fuels, 29, (2015), 4137–4149.
39. K. Xu and H. Meng, "Numerical study of fluid flows and heat transfer of aviation kerosene with consideration of fuel pyrolysis and surface coking at supercritical pressures," International Journal of Heat and Mass Transfer, 95, (2016), 806–814.
40. Z. Tao, X. Hu, J. Zhu, Z. Cheng, "Numerical Study of Flow and Heat Transfer of n-Decane with Pyrolysis and Pyrolytic Coking under Supercritical Pressures," Energy Fuels, 31, (2017), 8698−8707.
41. K. Xu, X. Sun, H. Meng, "Conjugate heat transfer, endothermic fuel pyrolysis and surface coking of aviation kerosene in ribbed tube at supercritical pressure," International Journal of Thermal Sciences, 132, (2018), 209−218.
42. X. Sun, K. Xu, H. Meng, "Supercritical-Pressure Heat Transfer, Pyrolytic Reactions, and Surface Coking of n-Decane in Helical Tubes," Energy Fuels, 32, (2018), 12298−12307.
43. S. Liu, Y. Feng, Y. Chu, K. Gong, Y. Cao, "Numerical study of catalytic steam reforming of aviation kerosene at supercritical pressures," Fuel, 212, (2018), 375–386.
44. S. Liu, Y. Feng, Y. Cao, K. Gong, W. Zhou, W. Bao, "Numerical simulation of supercritical catalytic steam reforming of aviation kerosene coupling with coking and heat transfer in mini-channel," International Journal of Thermal Sciences, 137, (2019), 199−214.
45. T. Jing, G. He, W. Li, D. Zhang, F. Qin, R. Li, "Flow and thermal analyses of supercritical hydrocarbon fuel in curved regenerative cooling channel around cavity in rocket based combined cycle engine," Applied Thermal Engineering, 145, (2018), 423–434.
46. S. Kawai, "Heated transcritical and unheated non-transcritical turbulent boundary layers at supercritical pressures," Journal of Fluid Mechanics, 865, (2019), 563-601.
47. S. Kawai, Y. Oikawa, "Turbulence modeling for turbulent boundary layers at supercritical pressure: a model for turbulent mass flux," Flow, Turbulence and Combustion, 104, (2020), 625–641.
48. B. Hitch and M. Karpuk, "Experimental investigation of heat transfer and flow instabilities in supercritical fuels," AIAA Paper 97-3043, (1997).
49. M. Ledinegg, "Instability flow during natural forced circulation," Warme, 61, (1938), 891–898.
50. J.A. Boure, A.E. Bergles, L.S. Tong, "Review of two-phase flow instability," Nuclear Engineering and Design, 25, (1973), 165–192.

51. S. Kakac, B. Bon, “A review of two-phase flow dynamic instabilities in tube boiling systems,” International Journal of Heat and Mass Transfer, 51, (2008), 399–433.
52. L.C. Ruspini, C.P. Marcel, A. Clausse, “Two-phase flow instabilities: a review,” International Journal of Heat and Mass Transfer, 71, (2014), 521–548.
53. W. Ambrosini, “On the analogies in the dynamic behaviour of heated channels with boiling and supercritical fluids,” Nuclear Engineering and Design, 237, (2007), 1164–1174.
54. W. Ambrosini and M. Sharabi, “Dimensionless parameters in stability analysis of heated channels with fluids at supercritical pressures,” Nuclear Engineering and Design, 238, (2008), 1917–1929.
55. W. Ambrosini, “Discussion on the stability of heated channels with different fluids at supercritical pressures,” Nuclear Engineering and Design, 239, (2009), 2952–2963.
56. E. Ampomah-Amoako, W. Ambrosini, “Developing a CFD methodology for the analysis of flow stability in heated channels with fluids at supercritical pressures,” Annals of Nuclear Energy, 54, (2013), 251–262.
57. M. Sharabi, W. Ambrosini, S. He, “Prediction of unstable behaviour in a heated channel with water at supercritical pressure by CFD models,” Annals of Nuclear Energy, 35, (2008), 767–782.
58. M. Sharabi, W. Ambrosini, S. He, Pei-Xue Jiang, Chen-Ru Zhao, “Transient three-dimensional stability analysis of supercritical water reactor rod bundle subchannels by a computational fluid dynamics code,” Journal of Engineering for Gas Turbines and Power, 131, (2009), 022903.
59. G. Dutta, C. Zhang, J. Jiang, “Analysis of flow induced density wave oscillations in the CANDU supercritical water reactor,” Nuclear Engineering and Design, 286, (2015), 150–162.
60. R. Upadhyay, G. Dutta, “Identification of safe and stable zone of operation in supercritical water reactor,” Nuclear Engineering and Design, 328, (2018), 209–227.
61. S.K. Rai, P. Kumar, V. Panwar, “Mathematical and numerical investigation of Ledinegg flow excursion and dynamic instability of natural circulation loop at supercritical condition,” Annals of Nuclear Energy, 155, (2021), 108129.
62. S.K. Rai, P. Kumar, V. Panwar, “Numerical analysis of influence of geometry and operating parameters on Ledinegg and dynamic instability on supercritical water natural circulation loop,” Nuclear Engineering and Design, 369, (2020), 110830.
63. V. Garg, G. Dutta, “Numerical study of external inertia and compressible volume on nuclear coupled density wave oscillations in a supercritical pressure channel,” Nuclear Engineering and Design, 363, (2020), 110607.
64. V. Garg, G. Dutta, “Understanding of thermal-hydraulic instabilities and the mutual interactions at supercritical pressure,” International Journal of Heat and Mass Transfer, 152, (2020), 119491.
65. F. Liu, J. Lv, B. Zhang, Z. Yang, “Nonlinear stability analysis of Ledinegg instability under constant external driving force,” Chemical Engineering Science, 206, (2019), 432–445.
66. E. Ebrahimnia, V. Chatoorgoon, S.J. Ormiston, “Numerical stability analyses of upward flow of supercritical water in a vertical pipe,” International Journal of Heat and Mass Transfer, 97, (2016), 828–841.

67. B.T. Swapnalee, P.K. Vijayan, M. Sharma, D.S. Pilkhwal, “Steady state flow and static instability of supercritical natural circulation loops,” Nuclear Engineering and Design, 245, (2012), 99–112.
68. J. Yu, S. Che, R. Li, B. Qi, “Analysis of Ledinegg flow instability in natural circulation at supercritical pressure,” Progress in Nuclear Energy, 53, (2011), 775–779.
69. W. Zhou, B. Yu, J. Qin, D. Yu, “Mechanism and influencing factors analysis of flowing instability of supercritical endothermic hydrocarbon fuel within a small-scale channel,” Applied Thermal Engineering, 71, (2014), 34–42.
70. Z. Zhang, C. Zhao, X. Yang, P. Jiang, J. Tu, S. Jiang, “Numerical study of the heat transfer and flow stability of water at supercritical pressures in a vertical tube,” Nuclear Engineering and Design, 325, (2017), 1–11.
71. Z. Zhang, C. Zhao, X. Yang, P. Jiang, S. Jiang, J. Tu, “Influences of tube wall on the heat transfer and flow instability of various supercritical pressure fluids in a vertical tube,” Applied Thermal Engineering, 147, (2019), 242–250.
72. Y. Jin, K. Wu, Y. Lu, X. Fan, “A one-dimensional transient calculation method for flow instability of supercritical hydrocarbon in cooling channels,” AIAA Propulsion and Energy Forum, (2021).
73. Z. Yang, Q. Bi, Z. Liu, Y. Guo, J. Yan, “Heat transfer to supercritical pressure hydrocarbons flowing in a horizontal short tube,” Experimental Thermal and Fluid Science, 61, (2015), 144–152.
74. Z. Yang, Y. Shan, B. Zhang, Y. Liu, “Hydrodynamic characteristics of cyclohexane in a horizontal mini-tube at trans- and supercritical pressures,” Applied Thermal Engineering, 129, (2018), 62–69.
75. Z. Yang and Y. Shan, “Experimental study on the onset of flow instability in small horizontal tubes at supercritical pressures,” Applied Thermal Engineering, 135, (2018), 504–511.
76. Z. Yang, T. Li, X. Zhao, T. Gao, B. Zhang, “Hydrodynamic and heat transfer characteristics of binary hydrocarbons at trans- and supercritical pressures,” Experimental Thermal and Fluid Science, 116, (2020), 110128.
77. Y. Guo, Q. Bi, Z. Liu, Z. Yang, L. Jiang, “Experimental investigation on thermal-hydraulic characteristics of endothermic hydrocarbon fuel in 1 mm and 2 mm diameter minichannels,” Applied Thermal Engineering, 122, (2017), 420–428.
78. T. Xiong, X. Yan, Z. Xiao, Y. Li, Y. Huang, J. Yu, “Experimental study on flow instability in parallel channels with supercritical water,” Annals of Nuclear Energy, 48, (2012), 60–67.
79. H. Wang, J. Zhou, Y. Pan, N. Wang, “Experimental investigation on the onset of thermo-acoustic instability of supercritical hydrocarbon fuel flowing in a small-scale channel,” Acta Astronautica, 117, (2015), 296–304.
80. G. Liu, Y. Huang, J. Wang, F. Lv, L.K. Leung, “Experiments on the basic behavior of supercritical CO2 natural circulation,” Nuclear Engineering and Design, 300, (2016), 376–383.
81. J. Yan, Y. Zhu, R. Zhao, S. Yan, P. Jiang, “Experimental investigation of the flow and heat transfer instabilities in n-decane at supercritical pressures in a vertical tube,” International Journal of Heat and Mass Transfer, 120, (2018), 987–996.
82. H. Pan, Q. Bi, W. Tan, P. Yang, F. Feng, “Dynamic flow instabilities of hydrocarbon fuel in a horizontal heating tube,” Acta Astronautica, 185, (2021), 89–101.`

Chapter 2

Robust numerical method for multi-component supercritical flows

2.1 Introduction

Multicomponent fluid flows in a supercritical state are used in various fields for thermal and chemical processes. The supercritical antisolvent technique is a method to fabricate nanoparticles in the mixing process of a liquid solvent and supercritical CO_2 [1]. In a regenerative cooling system for next-generation hypersonic aircrafts [2], a liquid hydrocarbon transits to the supercritical state for the heat reduction of the engine system. In addition, pyrolysis reactions occur above 800 K in the cooling channel, which generates lower alkanes and alkenes, resulting in multicomponent hydrocarbon flows. The decomposed components have a much lower density compared to the fed hydrocarbon. While the multicomponent flows in these processes are in a low Mach-number condition, such as natural and mixed convection, the density changes drastically with the transition to the supercritical state, resulting in generation of the lower alkane and alkene. The mass and thermal flow interact with the transition and chemical reactions. Hereafter, a robust and accurate numerical method for simulating multicomponent fluid flow in natural convection and mixed convection under a low Mach number condition is key to developing a highly efficient and reliable system.

A fully conservative scheme is the first choice to simulate multicomponent fluid flows even under low Mach number conditions. However, a fully conservative scheme has problems, specifically, the so-called spurious oscillations, when solving the flows with variable thermodynamic properties such as multicomponent flow and transcritical flows crossing the pseudo-boiling line. The spurious oscillations have a negative impact on the robustness and accuracy of numerical simulations. The work on spurious oscillations was initiated by Abgrall [3]. He reported the spurious pressure oscillation that occurred on multicomponent nonreactive flows and proposed a quasi-conservative method, which solves the nonconservative form of the mass fraction equation to avoid numerical oscillation problems. This idea was extended to a higher-order finite volume and difference scheme [4,5]. The method proposed by Terashima and Koshi [6] solves the pressure evolution equation instead of the total energy conservation equation. Consistent numerical diffusion terms were added for the velocity equilibrium and to avoid mass fraction and temperature oscillations at the fluid interfaces. Pantano et al. [7] developed an Euler system for flows with shock waves and transcritical contact. They proposed an additional evolution equation to maintain the mechanical equilibrium in nonuniform velocity fields and demonstrated numerical simulations under the conditions of nonuniform velocities, such as shock waves. Abgrall and Karni [8] proposed a double-flux model (DFM) with a single-

fluid flavor algorithm for a calorically perfect gas. The DFM does not require any additional equations for the original governing equations. The DFM was extended to reactive flows by Billet and Abgrall [9], and more recently, to transcritical flows by Ma et al. [10]. These studies were developed and investigated for forced convections at sufficiently high velocities assuming ordinary compressible flows. On the other hand, low Mach number conditions with density changes are also a crucial topic for practical applications, such as in chemical reactors and heat exchangers. The removing acoustic approach is a method to simulate low Mach number flows without the acoustic effects, in which the Navier–Stokes equations with the low-Mach-number approximation are employed [11,12]. In this approach, the effects of acoustic waves on the solution are removed from the fundamental equation. The pressure is decomposed into a thermodynamic part and a hydrodynamic part, and thermophysical property variations caused by hydrodynamic pressure fluctuations are neglected. Versatile approaches for the compressible and incompressible fluid flows are important for simulating the fluid flows in various industrial applications. The preconditioning method has been proposed [13–15] for very low Mach-number flows with compressible Navier–Stokes equations. Yamamoto [16] simulated the natural convection of condensate fluid flows using a precondition-ing method. Housman et al. [17] reported that the preconditioning method also had a spurious oscillation problem, and they employed a hybrid scheme that solves the preconditioned Euler system of nonconservative form near the material interface to avoid spurious oscillations. The mechanism of spurious oscillations in the preconditioning method has not been sufficiently investigated, and the conservation errors due to the use of a non-conservative scheme have not been evaluated.

In this study, the DFM is applied to the preconditioning method using the original and simplified preconditioning matrix, based on the mechanism of spurious oscillations. One- and two-dimensional simulations were performed using the proposed method. First, the mechanism of spurious oscillations is demonstrated in a one-dimensional preconditioned system, and the DFM is applied to the preconditioning method while discussing the conservation error. Additionally, I investigated the one-dimensional flow problem with the DFM technique using a simplified preconditioning matrix, because the simplification may cause spurious oscillations at the material interface. The two-dimensional advection of methane in an *n*-dodecane atmosphere at supercritical pressure was simulated to investigate the multi-dimensional capability and robustness of the proposed method for a binary fluid flow condition. The natural convection of *n*-dodecane in the square cavity was simulated, which demonstrates the validity of the proposed method for a transcritical condition in a very low Mach-number flow. Finally, as a practical application for reactive flows under transcritical conditions, the proposed method is applied to *n*-dodecane flows with a pyrolysis reaction in a heated circular tube. The outlet conversion rates of the reacted *n*-dodecane were compared with the experimental data.

Nomenclature

c	speed of sound
E	total internal energy per unit volume
g	gravitational acceleration
g_{ij}	metrics $\nabla\xi_i \cdot \nabla\xi_j$ $(i, j = 1, 2)$
h	enthalpy per unit mass
h_p	partial derivative of enthalpy with respect to pressure
h_T	partial derivative of enthalpy with respect to temperature
h_{Y_n}	partial derivative of enthalpy with respect to mass fraction of nth component
J	Jacobian of transformation
k	turbulent kinetic energy
p	pressure
R	gas constant
T	temperature
t	time
U_i	contravariant velocities ($i = 1, 2$)
u_i	velocities ($i = 1, 2$)
x_i	Cartesian coordinates ($i = 1, 2$)
Y_n	mass fraction of the nth component

Greek symbol

θ	preconditioning parameter
κ	thermal conductivity
κ_t	turbulent thermal conductivity
μ	molecular viscosity
μ_t	eddy viscosity
ξ_i	general curvilinear coordinates ($i = 1, 2$)
ρ	density
ρ_s	standard density
ρ_p	partial derivative of density with respect to pressure
ρ_T	partial derivative of density with respect to temperature
ρ_{Y_n}	partial derivative of density with respect to mass fraction of nth component
τ	pseudo time
τ_{ij}	viscous stress tensors ($i, j = 1, 2$)
ω	specific turbulent dissipation rate

2.2 Numerical methods

2.2.1 Fundamental equations for multicomponent low Mach-number flows

The fundamental equations consist of the conservation equations of mass, momentum, total energy, and the mass fraction of the 1st, …, $(n-1)$th component, coupled with the transport equations for turbulent kinetic energy and a specific turbulent dissipation rate. Here, n represents the number of components. The set of equations is expressed in the system equation of the two-dimensional general curvilinear coordinates. Additionally, the preconditioning matrix [16] is adopted for the system and can be written in vector form as follows:

$$\frac{\partial \boldsymbol{Q}}{\partial t}+\boldsymbol{\Gamma}\frac{\partial \widehat{\boldsymbol{Q}}}{\partial \tau}+\frac{\partial \boldsymbol{F}_i}{\partial \xi_i}+\frac{\partial \boldsymbol{F}_{vi}}{\partial \xi_i}+\boldsymbol{S}=0 \quad (i=1,2), \tag{2.1}$$

where

$$\boldsymbol{\Gamma}=\begin{bmatrix}
\theta & 0 & 0 & \rho_T & 0 & 0 & \rho_{Y_1} & \cdots & \rho_{Y_{n-1}} \\
\theta u_1 & \rho & 0 & \rho_T u_1 & 0 & 0 & \rho_{Y_1} u_1 & \cdots & \rho_{Y_{n-1}} u_1 \\
\theta u_2 & 0 & \rho & \rho_T u_2 & 0 & 0 & \rho_{Y_1} u_2 & \cdots & \rho_{Y_{n-1}} u_2 \\
\theta H-(1-\rho h_p) & \rho u_1 & \rho u_2 & \rho_T H+\rho h_T & 0 & 0 & \rho_{Y_1} H+\rho h_{Y_1} & \cdots & \rho_{Y_{n-1}} H+\rho h_{Y_{n-1}} \\
\theta k & 0 & 0 & \rho_T k & \rho & 0 & \rho_{Y_1} k & \cdots & \rho_{Y_{n-1}} k \\
\theta \omega & 0 & 0 & \rho_T \omega & 0 & \rho & \rho_{Y_1} \omega & \cdots & \rho_{Y_{n-1}} \omega \\
\theta Y_1 & 0 & 0 & \rho_T Y_1 & 0 & 0 & \rho_{Y_1} Y_1+\rho & \cdots & \rho_{Y_{n-1}} Y_1 \\
\vdots & \vdots & \vdots & \vdots & \vdots & \vdots & \vdots & \ddots & \vdots \\
\theta Y_{n-1} & 0 & 0 & \rho_T Y_{n-1} & 0 & 0 & \rho_{Y_1} Y_{n-1} & \cdots & \rho_{Y_{n-1}} Y_{n-1}+\rho
\end{bmatrix},$$

$$\boldsymbol{Q}=J\begin{bmatrix}\rho\\ \rho u_1\\ \rho u_2\\ E\\ \rho k\\ \rho\omega\\ \rho Y_1\\ \vdots\\ \rho Y_{n-1}\end{bmatrix},\ \widehat{\boldsymbol{Q}}=J\begin{bmatrix}p\\ u_1\\ u_2\\ T\\ k\\ \omega\\ Y_1\\ \vdots\\ Y_{n-1}\end{bmatrix},\ \boldsymbol{F}_i=J\begin{bmatrix}\rho U_i\\ \rho u_1 U_i+\dfrac{\partial \xi_i}{\partial x_1}p\\ \rho u_2 U_i+\dfrac{\partial \xi_i}{\partial x_2}p\\ (E+p)U_i\\ \rho k U_i\\ \rho\omega U_i\\ \rho Y_1 U_i\\ \vdots\\ \rho Y_{n-1}U_i\end{bmatrix},$$

$$\boldsymbol{F}_{\boldsymbol{v}i} = -J\frac{\partial \xi_i}{\partial x_j}\begin{bmatrix} 0 \\ \tau_{j1} \\ \tau_{j2} \\ \tau_{jk}u_k + (\kappa+\kappa_t)\dfrac{\partial T}{\partial x_j} \\ \sigma_{kj} \\ \sigma_{\omega j} \\ 0 \\ \vdots \\ 0 \end{bmatrix}, \boldsymbol{S} = -J\begin{bmatrix} 0 \\ 0 \\ (\rho_s-\rho)g \\ (\rho_s-\rho)gu_2 \\ s_k \\ s_\omega \\ s_{Y_1} \\ \vdots \\ s_{Y_{n-1}} \end{bmatrix}.$$

$\boldsymbol{\Gamma}$ is the preconditioning matrix. As $\tau \to \infty$, the pseudo-time term in Eq. (2.1) converges to zero and the equation becomes the conservative system. $H = (E+p)/\rho = h + u_i^2/2$. $\widehat{\boldsymbol{Q}}$, $\boldsymbol{F}_i$, $\boldsymbol{F}_{\boldsymbol{v}i}$, and $\boldsymbol{S}$ are the vectors of the unknown variables, inviscid flux, viscous flux, and source term, respectively. The dissipation and source terms of the turbulence model, σ_{kj}, $\sigma_{\omega j}$, s_k, and s_ω are as defined by Menter [18] and Kawai [19]. s_{Y_n} is the mass generation rate for the nth component. The preconditioning parameter θ is defined as follows:

$$\theta = \frac{1}{U_r^2} - \frac{\rho_T(1-\rho h_p)}{\rho h_T}, \tag{2.2}$$

where U_r is a switching parameter. In this study, I employed

$$U_r = \min[c, \max(u, 3u_\infty)]. \tag{2.3}$$

The local velocity is defined as $u = \sqrt{u_i u_i}$, and u_∞ is a reference velocity defined by the inlet or the maximum velocity.

The second-order explicit Runge–Kutta scheme was used for time integration. The numerical flux was evaluated using the preconditioned flux-vector splitting scheme derived by Yamamoto [16]. The unknown variables were interpolated using the second-order MUSCL scheme.

2.2.2 Spatial difference method

The Godunov type scheme is employed in this study. The solution of governing equations is assumed to be constant in the computation cell, and the temporal variation in the cell is computed by the numerical flux in/out across the cell. The key to the Godunov-type scheme is how to evaluate the numerical flux at the cell interface. An approximate Riemann solver is widely used as an evaluation method of the numerical flux. In this study, the preconditioning flux-vector splitting (FVS) scheme proposed by Yamamoto [16] is employed to evaluate the numerical flux.

The numerical flux defined at a cell interface can be written by the FVS form as follow:

$$\tilde{\boldsymbol{F}}_i = \tilde{\boldsymbol{F}}_i^{+} + \tilde{\boldsymbol{F}}_i^{-} = \boldsymbol{A}_i^{+}\boldsymbol{Q}^{\mathrm{L}} + \boldsymbol{A}_i^{-}\boldsymbol{Q}^{\mathrm{R}}. \tag{2.4}$$

Here, Euler's homogeneity relation $\boldsymbol{F} = \boldsymbol{A}\boldsymbol{Q}$ is applied. The superscripts $\pm$ indicate the sign of characteristic speeds. The subscript i $(i = 1, 2)$ represents each coordinate. $\boldsymbol{A}_i$ are the Jacobian matrix of the conserved form. $\boldsymbol{Q}^{\mathrm{L}}$ and $\boldsymbol{Q}^{\mathrm{R}}$ are the unknown vectors extrapolated at the left and right sides of the interface, respectively.

To be compatible with the preconditioned system, Eq. (2.4) is recast in terms of primitive variables $\widehat{\boldsymbol{Q}}$ using preconditioned eigenvalues. $\boldsymbol{A}_i\boldsymbol{Q}$ in Eq. (2.4) is rewritten as follows:

$$\boldsymbol{A}_i\boldsymbol{Q} = \boldsymbol{\Gamma}\,\boldsymbol{\Gamma}^{-1}\frac{\partial \boldsymbol{F}_i}{\partial \boldsymbol{Q}}\boldsymbol{Q} = \boldsymbol{\Gamma}\left(\boldsymbol{\Gamma}^{-1}\frac{\partial \boldsymbol{F}_i}{\partial \widehat{\boldsymbol{Q}}}\right)\widehat{\boldsymbol{Q}} = \boldsymbol{\Gamma}\,\hat{\boldsymbol{A}}_i\widehat{\boldsymbol{Q}}, \tag{2.5}$$

$\hat{\boldsymbol{A}}_i$ are the preconditioned Jacobian matrix of the conservative form and written in detailed as follow:

$$\begin{aligned}
\hat{\boldsymbol{A}}_i &= \boldsymbol{\Gamma}^{-1}\frac{\partial \boldsymbol{F}_i}{\partial \widehat{\boldsymbol{Q}}} \\
&= \begin{bmatrix}
\dfrac{[\rho h_T \rho_p + \rho_T(1-\rho h_p)]U_i}{\rho h_T\theta + \rho_T(1-\rho h_p)} & \dfrac{\xi_{i,1}\rho^2 h_T}{\rho h_T\theta + \rho_T(1-\rho h_p)} & \dfrac{\xi_{i,2}\rho^2 h_T}{\rho h_T\theta + \rho_T(1-\rho h_p)} & 0 \\
\dfrac{\xi_{i,1}}{\rho} & U_i & 0 & 0 \\
\dfrac{\xi_{i,2}}{\rho} & 0 & U_i & 0 \\
\dfrac{(\rho_p-\theta)(1-\rho h_p)U_i}{\rho h_T\theta + \rho_T(1-\rho h_p)} & \dfrac{\xi_{i,1}(1-\rho h_p)U_i}{\rho h_T\theta + \rho_T(1-\rho h_p)} & \dfrac{\xi_{i,2}(1-\rho h_p)U_i}{\rho h_T\theta + \rho_T(1-\rho h_p)} & U_i \\
0 & 0 & 0 & 0 \\
0 & 0 & 0 & 0 \\
0 & 0 & 0 & 0 \\
\vdots & \vdots & \vdots & \vdots \\
0 & 0 & 0 & 0
\end{bmatrix} \\
&\quad \begin{bmatrix}
0 & 0 & 0 & \cdots & 0 \\
0 & 0 & 0 & \cdots & 0 \\
0 & 0 & 0 & \cdots & 0 \\
0 & 0 & 0 & \cdots & 0 \\
U_i & 0 & 0 & \cdots & 0 \\
0 & U_i & 0 & \cdots & 0 \\
0 & 0 & U_i & \cdots & 0 \\
\vdots & \vdots & \vdots & \ddots & \vdots \\
0 & 0 & 0 & \cdots & U_i
\end{bmatrix},
\end{aligned} \tag{2.6}$$

where

$$
\boldsymbol{\Gamma}^{-1} = \begin{bmatrix}
\frac{h_T(\rho + \sum_{m=1}^{n-1} \rho_{Y_m} Y_m) - \rho_T(u_i^2 - H + \sum_{m=1}^{n-1} h_{Y_m} Y_m)}{\rho h_T \theta + \rho_T(1 - \rho h_p)} \\
-\frac{u_1}{\rho} \\
-\frac{u_2}{\rho} \\
\frac{1 - h_p(\rho + \sum_{m=1}^{n-1} \rho_{Y_m} Y_m) + \theta(u_i^2 - H + \sum_{m=1}^{n-1} h_{Y_m} Y_m) + \sum_{m=1}^{n-1} \rho_{Y_m} Y_m / \rho}{\rho h_T \theta + \rho_T(1 - \rho h_p)} \\
-\frac{k}{\rho} \\
-\frac{\omega}{\rho} \\
-\frac{Y_1}{\rho} \\
\vdots \\
-\frac{Y_{n-1}}{\rho}
\end{bmatrix}
$$

$$
\begin{bmatrix}
\frac{u_1 \rho_T}{\rho h_T \theta + \rho_T(1 - \rho h_p)} & \frac{u_2 \rho_T}{\rho h_T \theta + \rho_T(1 - \rho h_p)} & \frac{-\rho_T}{\rho h_T \theta + \rho_T(1 - \rho h_p)} & 0 & 0 \\
-\frac{u_1}{\rho} & 0 & 0 & 0 & 0 \\
0 & -\frac{u_2}{\rho} & 0 & 0 & 0 \\
\frac{-u_1 \theta}{\rho h_T \theta + \rho_T(1 - \rho h_p)} & \frac{-u_2 \theta}{\rho h_T \theta + \rho_T(1 - \rho h_p)} & \frac{\theta}{\rho h_T \theta + \rho_T(1 - \rho h_p)} & 0 & 0 \\
0 & 0 & 0 & \frac{1}{\rho} & 0 \\
0 & 0 & 0 & 0 & \frac{1}{\rho} \\
0 & 0 & 0 & 0 & 0 \\
\vdots & \vdots & \vdots & \vdots & \vdots \\
0 & 0 & 0 & 0 & 0
\end{bmatrix}
\tag{2.7}
$$

$$
\begin{bmatrix}
\frac{\rho_T h_{Y_1} - \rho_{Y_1} h_T}{\rho h_T \theta + \rho_T(1 - \rho h_p)} & \cdots & \frac{\rho_T h_{Y_{n-1}} - \rho_{Y_{n-1}} h_T}{\rho h_T \theta + \rho_T(1 - \rho h_p)} \\
0 & \cdots & 0 \\
0 & \cdots & 0 \\
\frac{\rho_{Y_1} h_p - \theta h_{Y_1} - \rho_{Y_1} / \rho}{\rho h_T \theta + \rho_T(1 - \rho h_p)} & \cdots & \frac{\rho_{Y_{n-1}} h_p - \theta h_{Y_{n-1}} - \rho_{Y_{n-1}} / \rho}{\rho h_T \theta + \rho_T(1 - \rho h_p)} \\
0 & \cdots & 0 \\
\frac{1}{\rho} & \cdots & 0 \\
\vdots & \ddots & \vdots \\
0 & \cdots & \frac{1}{\rho}
\end{bmatrix},
$$

and

$$\frac{\partial \boldsymbol{F}_i}{\partial \widehat{\boldsymbol{Q}}} = \begin{bmatrix} \rho_p U_i & \xi_{i,1}\rho & \xi_{i,2}\rho & \rho_T U_i & 0 \\ \rho_p u_1 U_i + \xi_{i,1} & \xi_{i,1}\rho u_1 + \rho U_i & \xi_{i,2}\rho u_1 & \rho_T u_1 U_i & 0 \\ \rho_p u_2 U_i + \xi_{i,2} & \xi_{i,1}\rho u_2 & \xi_{i,2}\rho u_2 + \rho U_i & \rho_T u_2 U_i & 0 \\ \rho_p h U_i + \rho h_p U_i & \rho u_1 U_i + \xi_{i,1}\rho h & \rho u_2 U_i + \xi_{i,2}\rho h & \rho_T h U_i + \rho h_T U_i & 0 \\ \rho_p k U_i & \xi_{i,1}\rho k & \xi_{i,2}\rho k & \rho_T k U_i & \rho U_i \\ \rho_p \omega U_i & \xi_{i,1}\rho\omega & \xi_{i,2}\rho\omega & \rho_T \omega U_i & 0 \\ \rho_p Y_1 U_i & \xi_{i,1}\rho Y_1 & \xi_{i,2}\rho Y_1 & \rho_T Y_1 U_i & 0 \\ \vdots & \vdots & \vdots & \vdots & \vdots \\ \rho_p Y_{n-1} U_i & \xi_{i,1}\rho Y_{n-1} & \xi_{i,2}\rho Y_{n-1} & \rho_T Y_{n-1} U_i & 0 \end{bmatrix},$$

$$\begin{bmatrix} 0 & \rho_{Y_1} U_i & \cdots & \rho_{Y_{n-1}} U_i \\ 0 & \rho_{Y_1} u_1 U_i & \cdots & \rho_{Y_{n-1}} u_1 U_i \\ 0 & \rho_{Y_1} u_2 U_i & \cdots & \rho_{Y_{n-1}} u_2 U_i \\ 0 & \rho_{Y_1} H U_i + \rho h_{Y_1} U_i & \cdots & \rho_{Y_{n-1}} H U_i + \rho h_{Y_{n-1}} U_i \\ 0 & \rho_{Y_1} k U_i & \cdots & \rho_{Y_{n-1}} k U_i \\ \rho U_i & \rho_{Y_1} \omega U_i & \cdots & \rho_{Y_{n-1}} \omega U_i \\ 0 & \rho_{Y_1} Y_1 U_i + \rho U_i & \cdots & \rho_{Y_{n-1}} Y_1 U_i \\ \vdots & \vdots & \ddots & \vdots \\ 0 & \rho_{Y_1} Y_1 U_i & \cdots & \rho_{Y_{n-1}} Y_{n-1} U_i + \rho U_i \end{bmatrix}. \tag{2.8}$$

The eigenvalues of preconditioned Jacobian matrix $\hat{\boldsymbol{A}}_i$ are derived from the characteristic equation as follow:

$$\left|\hat{\boldsymbol{A}}_i - \hat{\lambda}_i \boldsymbol{I}\right| = 0, \tag{2.9}$$

where $\hat{\lambda}_i$ and $\boldsymbol{I}$ are eigenvalues of the preconditioned Jacobian matrix and unit matrix. The eigenvalues are the solutions of the algebraic equation for $\hat{\lambda}_i$, and are obtained as follows:

$$\hat{\lambda}_{i1} = U_i, \tag{2.10a}$$

$$\hat{\lambda}_{i3} = \frac{(1+\alpha)U_i}{2} + \hat{c}_i\sqrt{g_{ii}}, \tag{2.10b}$$

$$\hat{\lambda}_{i4} = \frac{(1+\alpha)U_i}{2} - \hat{c}_i\sqrt{g_{ii}}. \tag{2.10c}$$

$\hat{c}_i$ are the numerical speed of sound and are defined as follow:

$$\hat{c}_i = \frac{1}{2}\sqrt{U_i^2(1+\alpha)^2/g_{ii} + 4U_r^2}, \tag{2.11}$$

where

$$\alpha = U_r^2\left(\rho_p + \frac{\rho_T(1-\rho h_p)}{\rho h_T}\right). \tag{2.12}$$

If U_r equals the physical speed of sound, α is reduced to unity and characteristic speeds and physical speed of sound for compressible flows is equal to the original value.. The diagonal matrix of eigenvalues is defined as follow:

$$\boldsymbol{\Lambda}_1 = \begin{bmatrix} \hat{\lambda}_{11} & 0 & 0 & 0 & 0 & 0 & 0 & \cdots & 0 \\ 0 & \hat{\lambda}_{13} & 0 & 0 & 0 & 0 & 0 & \cdots & 0 \\ 0 & 0 & \hat{\lambda}_{11} & 0 & 0 & 0 & 0 & \cdots & 0 \\ 0 & 0 & 0 & \hat{\lambda}_{14} & 0 & 0 & 0 & \cdots & 0 \\ 0 & 0 & 0 & 0 & \hat{\lambda}_{11} & 0 & 0 & \cdots & 0 \\ 0 & 0 & 0 & 0 & 0 & \hat{\lambda}_{11} & 0 & \cdots & 0 \\ 0 & 0 & 0 & 0 & 0 & 0 & \hat{\lambda}_{11} & \cdots & 0 \\ \vdots & \vdots & \vdots & \vdots & \vdots & \vdots & \vdots & \ddots & \vdots \\ 0 & 0 & 0 & 0 & 0 & 0 & 0 & \cdots & \hat{\lambda}_{11} \end{bmatrix}, \tag{2.13a}$$

$$\boldsymbol{\Lambda}_2 = \begin{bmatrix} \hat{\lambda}_{21} & 0 & 0 & 0 & 0 & 0 & 0 & \cdots & 0 \\ 0 & \hat{\lambda}_{21} & 0 & 0 & 0 & 0 & 0 & \cdots & 0 \\ 0 & 0 & \hat{\lambda}_{23} & 0 & 0 & 0 & 0 & \cdots & 0 \\ 0 & 0 & 0 & \hat{\lambda}_{24} & 0 & 0 & 0 & \cdots & 0 \\ 0 & 0 & 0 & 0 & \hat{\lambda}_{21} & 0 & 0 & \cdots & 0 \\ 0 & 0 & 0 & 0 & 0 & \hat{\lambda}_{21} & 0 & \cdots & 0 \\ 0 & 0 & 0 & 0 & 0 & 0 & \hat{\lambda}_{21} & \cdots & 0 \\ \vdots & \vdots & \vdots & \vdots & \vdots & \vdots & \vdots & \ddots & \vdots \\ 0 & 0 & 0 & 0 & 0 & 0 & 0 & \cdots & \hat{\lambda}_{21} \end{bmatrix}. \tag{2.13b}$$

The left eigenvector is orthogonal to all vectors composing the matrix $\left|\hat{\boldsymbol{A}}_i - \hat{\lambda}_i \boldsymbol{I}\right|$. Therefore,

$$\boldsymbol{L}_i\left|\hat{\boldsymbol{A}}_i - \hat{\lambda}_i \boldsymbol{I}\right| = 0. \tag{2.14}$$

Left eigenvectors are determined to satisfy Eq. (2.14).

$$\boldsymbol{L}_1 = \begin{bmatrix} 1 & 0 & 0 & -\dfrac{\rho h_T}{1-\rho h_p} & 0 & 0 & 0 & \cdots & 0 \\ 1 & \xi_{1,1} l_1^+ & \xi_{1,2} l_1^+ & 0 & 0 & 0 & 0 & \cdots & 0 \\ 0 & \xi_{1,2} & -\xi_{1,1} & 0 & 0 & 0 & 0 & \cdots & 0 \\ 1 & \xi_{1,1} l_1^- & \xi_{1,2} l_1^- & 0 & 0 & 0 & 0 & \cdots & 0 \\ 0 & 0 & 0 & 0 & 1 & 0 & 0 & \cdots & 0 \\ 0 & 0 & 0 & 0 & 0 & 1 & 0 & \cdots & 0 \\ 0 & 0 & 0 & 0 & 0 & 0 & 1 & \cdots & 0 \\ \vdots & \vdots & \vdots & \vdots & \vdots & \vdots & \vdots & \ddots & \vdots \\ 0 & 0 & 0 & 0 & 0 & 0 & 0 & \cdots & 1 \end{bmatrix}, \tag{2.15a}$$

$$\boldsymbol{L}_2 = \begin{bmatrix} 1 & 0 & 0 & -\dfrac{\rho h_T}{1-\rho h_p} & 0 & 0 & 0 & \cdots & 0 \\ 0 & -\xi_{2,2} & \xi_{2,1} & 0 & 0 & 0 & 0 & \cdots & 0 \\ 1 & \xi_{2,1} l_2^+ & -\xi_{2,2} l_2^+ & 0 & 0 & 0 & 0 & \cdots & 0 \\ 1 & \xi_{2,1} l_2^- & \xi_{2,2} l_2^- & 0 & 0 & 0 & 0 & \cdots & 0 \\ 0 & 0 & 0 & 0 & 1 & 0 & 0 & \cdots & 0 \\ 0 & 0 & 0 & 0 & 0 & 1 & 0 & \cdots & 0 \\ 0 & 0 & 0 & 0 & 0 & 0 & 1 & \cdots & 0 \\ \vdots & \vdots & \vdots & \vdots & \vdots & \vdots & \vdots & \ddots & \vdots \\ 0 & 0 & 0 & 0 & 0 & 0 & 0 & \cdots & 1 \end{bmatrix}. \tag{2.15b}$$

The right eigenvector is the inversed matrix of $\boldsymbol{L}_i$.

$$\boldsymbol{R}_1 = \boldsymbol{L}_1^{-1} = \begin{bmatrix} 0 & -\dfrac{l_1^-}{l_1^+ - l_1^-} & 0 \\ 0 & \dfrac{\xi_{1,1}}{(\xi_{1,1}^2+\xi_{1,2}^2) l_1^+ - (\xi_{1,1}^2+\xi_{1,2}^2) l_1^-} & \dfrac{\xi_{1,2}}{\xi_{1,1}^2+\xi_{1,2}^2} \\ 0 & \dfrac{\xi_{1,2}}{(\xi_{1,1}^2+\xi_{1,2}^2) l_1^+ - (\xi_{1,1}^2+\xi_{1,2}^2) l_1^-} & -\dfrac{\xi_{1,1}}{\xi_{1,1}^2+\xi_{1,2}^2} \\ -\dfrac{1-\rho h_p}{\rho h_T} & -\dfrac{(1-\rho h_p) l_1^-}{\rho h_T (l_1^+ - l_1^-)} & 0 \\ 0 & 0 & 0 \\ 0 & 0 & 0 \\ 0 & 0 & 0 \\ \vdots & \vdots & \vdots \\ 0 & 0 & 0 \end{bmatrix} \tag{2.16a}$$

$$
\begin{bmatrix}
\dfrac{l_1^+}{l_1^+ - l_1^-} & 0 & 0 & 0 & \cdots & 0 \\
-\dfrac{\xi_{1,1}}{(\xi_{1,1}^2+\xi_{1,2}^2)l_1^+ - (\xi_{1,1}^2+\xi_{1,2}^2)l_1^-} & 0 & 0 & 0 & \cdots & 0 \\
-\dfrac{\xi_{1,2}}{(\xi_{1,1}^2+\xi_{1,2}^2)l_1^+ - (\xi_{1,1}^2+\xi_{1,2}^2)l_1^-} & 0 & 0 & 0 & \cdots & 0 \\
\dfrac{(1-\rho h_p)l_1^+}{\rho h_T(l_1^+ - l_1^-)} & 0 & 0 & 0 & \cdots & 0 \\
0 & 1 & 0 & 0 & \cdots & 0 \\
0 & 0 & 1 & 0 & \cdots & 0 \\
0 & 0 & 0 & 1 & \cdots & 0 \\
\vdots & \vdots & \vdots & \vdots & \ddots & \vdots \\
0 & 0 & 0 & 0 & \cdots & 1
\end{bmatrix},
$$

$$
\boldsymbol{R}_2 = \boldsymbol{L}_2^{-1} = \begin{bmatrix}
0 & 0 & -\dfrac{l_2^-}{l_2^+ - l_2^-} \\
0 & \dfrac{\xi_{2,2}}{\xi_{2,1}^2+\xi_{2,2}^2} & \dfrac{\xi_{2,1}}{(\xi_{2,1}^2+\xi_{2,2}^2)l_2^+ - (\xi_{2,1}^2+\xi_{2,2}^2)l_2^-} \\
0 & -\dfrac{\xi_{2,1}}{\xi_{2,1}^2+\xi_{2,2}^2} & \dfrac{\xi_{2,2}}{(\xi_{2,1}^2+\xi_{2,2}^2)l_2^+ - (\xi_{2,1}^2+\xi_{2,2}^2)l_2^-} \\
-\dfrac{1-\rho h_p}{\rho h_T} & 0 & -\dfrac{(1-\rho h_p)l_2^-}{\rho h_T(l_2^+ - l_2^-)} \\
0 & 0 & 0 \\
0 & 0 & 0 \\
0 & 0 & 0 \\
\vdots & \vdots & \vdots \\
0 & 0 & 0
\end{bmatrix}
$$

$$
\begin{bmatrix}
\dfrac{l_2^+}{l_2^+ - l_2^-} & 0 & 0 & 0 & \cdots & 0 \\
-\dfrac{\xi_{2,1}}{(\xi_{2,1}^2+\xi_{2,2}^2)l_2^+ - (\xi_{2,1}^2+\xi_{2,2}^2)l_2^-} & 0 & 0 & 0 & \cdots & 0 \\
-\dfrac{\xi_{2,2}}{(\xi_{2,1}^2+\xi_{2,2}^2)l_2^+ - (\xi_{2,1}^2+\xi_{2,2}^2)l_2^-} & 0 & 0 & 0 & \cdots & 0 \\
\dfrac{(1-\rho h_p)l_2^+}{\rho h_T(l_2^+ - l_2^-)} & 0 & 0 & 0 & \cdots & 0 \\
0 & 1 & 0 & 0 & \cdots & 0 \\
0 & 0 & 1 & 0 & \cdots & 0 \\
0 & 0 & 0 & 1 & \cdots & 0 \\
\vdots & \vdots & \vdots & \vdots & \ddots & \vdots \\
0 & 0 & 0 & 0 & \cdots & 1
\end{bmatrix}, \tag{2.16b}
$$

where $l^{\pm}$ is given by

$$
l^{\pm} = \frac{\rho U_r^2}{U_i\,(\alpha-1)/2 \pm \hat{c}_i\sqrt{g_{ii}}}. \tag{2.17}
$$

Eventually, the preconditioned Jacobian matrix $\hat{\boldsymbol{A}}_i$ is diagonalized by using the diagonal matrix $\boldsymbol{\Lambda}_i$ and eigenvectors $\boldsymbol{L}_i$ and $\boldsymbol{R}_i$ as follow:

$$\hat{\boldsymbol{A}}_i = \boldsymbol{R}_i \boldsymbol{\Lambda}_i \boldsymbol{L}_i. \tag{2.18}$$

From the above discussion, $\boldsymbol{\Gamma}\hat{\boldsymbol{A}}_i^{\pm}\boldsymbol{Q}^{\mathrm{M}}\ (\mathrm{M}=\mathrm{L},\mathrm{R})$ is expressed as a sub-vector form by

$$\boldsymbol{\Gamma}\widehat{\boldsymbol{A}}_i^{\pm}\boldsymbol{Q}^{\mathrm{M}} = \boldsymbol{\Gamma}\boldsymbol{R}_i\boldsymbol{\Lambda}_i\boldsymbol{L}_i\widehat{\boldsymbol{Q}}^{\boldsymbol{M}} = \hat{\lambda}_{i1}^{\pm}\boldsymbol{\Gamma}\widehat{\boldsymbol{Q}}^{\boldsymbol{M}} + \frac{\hat{\lambda}_{ia}^{\pm}}{\hat{c}_i\sqrt{g_{ii}}}\boldsymbol{Q}_{ia} + \frac{\hat{\lambda}_{ib}^{\pm}}{\hat{c}_i^2}\boldsymbol{Q}_{ib}. \tag{2.19}$$

The Eq. (2.19) is the preconditioned FVS form derived by Yamamoto [16]. $\boldsymbol{Q}_{ia}$ and $\boldsymbol{Q}_{ib}$ are the sub-vectors defined as follows:

$$\boldsymbol{Q}_{ia} = \hat{q}_1^M\boldsymbol{Q}_{ic} + \rho\hat{U}_i\boldsymbol{Q}_d, \tag{2.20a}$$

$$\boldsymbol{Q}_{ib} = \frac{\rho\hat{U}_i\hat{c}_i^2}{g_{ii}}\boldsymbol{Q}_{ic} + \frac{\hat{q}_1^M\hat{c}_i^2}{\hat{U}_r^2}\boldsymbol{Q}_d, \tag{2.20b}$$

where $\hat{q}_j^M$ and $\hat{U}_i[=(\partial\xi_i/\partial x_j)\hat{q}_j^M\ (j=1,2)]$ are the jth element of $\widehat{\boldsymbol{Q}}$ and the contravariant velocities extrapolated from left and right directions. $\boldsymbol{Q}_{ic}$ and $\boldsymbol{Q}_d$ are the sub-vectors given as follows:

$$\boldsymbol{Q}_{ic} = [0 \quad \partial\xi_i/\partial x_1 \quad \partial\xi_i/\partial x_2 \quad U_i \quad 0 \quad 0 \quad 0 \quad \cdots \quad 0], \tag{2.21a}$$

$$\boldsymbol{Q}_d = [1 \quad u_1 \quad u_2 \quad H \quad k \quad \omega \quad Y_1 \quad \cdots \quad Y_n]. \tag{2.21b}$$

The preconditioned FVS form can be modified to the preconditioned flux-difference splitting form. The upwind-type numerical flux in the preconditioned system is defined at a cell interface as follow:

$$\tilde{\boldsymbol{F}}_{j+1/2} = \frac{1}{2}\left[\boldsymbol{F}_i\left(\widehat{\boldsymbol{Q}}^{\mathrm{L}}\right) + \boldsymbol{F}_i\left(\widehat{\boldsymbol{Q}}^{\mathrm{R}}\right) - \boldsymbol{\Gamma}\left|\hat{\boldsymbol{A}}_i\right|\Delta\widehat{\boldsymbol{Q}}\right], \tag{2.22}$$

where $\Delta\widehat{\boldsymbol{Q}} = \widehat{\boldsymbol{Q}}^{\mathrm{R}} - \widehat{\boldsymbol{Q}}^{\mathrm{L}}$. Here, the dissipation term of upwind-type numerical flux is written using the preconditioned flux-vector splitting form of Eq. (2.19) as follow:

$$\boldsymbol{\Gamma}\left|\widehat{\boldsymbol{A}}_i\right|\widehat{\boldsymbol{Q}}^{\boldsymbol{M}} = \left|\hat{\lambda}_{i1}\right|\boldsymbol{\Gamma}\widehat{\boldsymbol{Q}}^{\boldsymbol{M}} + \frac{\left|\hat{\lambda}_{ia}\right|}{\hat{c}_i\sqrt{g_{ii}}}\boldsymbol{Q}_{ia} + \frac{\left|\hat{\lambda}_{ib}\right|}{\hat{c}_i^2}\boldsymbol{Q}_{ib}. \tag{2.23}$$

2.2.3 Time integration with dual time-stepping method

The dual time-stepping technique by Weiss and Smith [15] with the explicit Runge–Kutta scheme is employed. The physical time-derivative in Eq. (2.1) is discretized using a second-order backward difference as follow:

$$\boldsymbol{M}\ \delta\widehat{\boldsymbol{Q}} = -\alpha_l \delta\tau \left[\frac{3\boldsymbol{Q}^l - 4\boldsymbol{Q}^n + \boldsymbol{Q}^{n-1}}{2\delta t} + \frac{\partial \boldsymbol{F}_i^l}{\partial \xi_i} + \frac{\partial \boldsymbol{F}_{vi}^l}{\partial \xi_i} + \boldsymbol{S}^l \right]. \tag{2.24}$$

Here, the superscripts n and l represent the physical time step and stage counter of Runge–Kutta scheme, respectively. $\delta(\cdot) = (\cdot)^{l+1} - (\cdot)^l$ indicates the temporal variation of the lth stage of the Runge–Kutta scheme. δt and $\delta\tau$ are the physical and pseudo time step, respectively. α_l is the Runge–Kutta coefficients. The matrix $\boldsymbol{M}$ was introduced by Weiss and Smith [15] and defined by the preconditioning matrix $\boldsymbol{\Gamma}$ and Jacobian matrix $\boldsymbol{N}$ as

$$\boldsymbol{M} = \frac{3\delta\tau}{2\delta t}\boldsymbol{N} + \boldsymbol{\Gamma} = \left(\frac{3\delta\tau}{2\delta t} + 1\right) \times$$

$$\begin{bmatrix}
\theta' & 0 & 0 & \rho_T & 0 & 0 & \rho_{Y_1} & \cdots & \rho_{Y_{n-1}} \\
\theta' u_1 & \rho & 0 & \rho_T u_1 & 0 & 0 & \rho_{Y_1} u_1 & \cdots & \rho_{Y_{n-1}} u_1 \\
\theta' u_2 & 0 & \rho & \rho_T u_2 & 0 & 0 & \rho_{Y_1} u_2 & \cdots & \rho_{Y_{n-1}} u_2 \\
\theta' H - (1-\rho h_p) & \rho u_1 & \rho u_2 & \rho_T H + \rho h_T & 0 & 0 & \rho_{Y_1} H + \rho h_{Y_1} & \cdots & \rho_{Y_{n-1}} H + \rho h_{Y_{n-1}} \\
\theta' k & 0 & 0 & \rho_T k & \rho & 0 & \rho_{Y_1} k & \cdots & \rho_{Y_{n-1}} k \\
\theta' \omega & 0 & 0 & \rho_T \omega & 0 & \rho & \rho_{Y_1} \omega & \cdots & \rho_{Y_{n-1}} \omega \\
\theta' Y_1 & 0 & 0 & \rho_T Y_1 & 0 & 0 & \rho_{Y_1} Y_1 + \rho & \cdots & \rho_{Y_{n-1}} Y_1 \\
\vdots & \vdots & \vdots & \vdots & \vdots & \vdots & \vdots & \ddots & \vdots \\
\theta' Y_{n-1} & 0 & 0 & \rho_T Y_{n-1} & 0 & 0 & \rho_{Y_1} Y_{n-1} & \cdots & \rho_{Y_{n-1}} Y_{n-1} + \rho
\end{bmatrix}, \tag{2.25}$$

where

$$\boldsymbol{N} = \frac{\partial \boldsymbol{Q}}{\partial \widehat{\boldsymbol{Q}}}, \tag{2.26a}$$

$$\theta' = \frac{\frac{3\delta\tau}{2\delta t}\rho_p + \theta}{\frac{3\delta\tau}{2\delta t} + 1}. \tag{2.26b}$$

The density of the multicomponent flow depends not only on the pressure and temperature but also on the mass fraction of each component. $\boldsymbol{M}$ can be simplified by omitting the partial derivatives with respect to the mass fractions [20, 21] as

$$\boldsymbol{M}_{\mathrm{s}} = \left(\frac{3\delta\tau}{2\delta t}+1\right)\begin{bmatrix} \theta' & 0 & 0 & \rho_T & 0 & 0 & 0 & \cdots & 0 \\ \theta' u_1 & \rho & 0 & \rho_T u_1 & 0 & 0 & 0 & \cdots & 0 \\ \theta' u_2 & 0 & \rho & \rho_T u_2 & 0 & 0 & 0 & \cdots & 0 \\ \theta' H - (1-\rho h_p) & \rho u_1 & \rho u_2 & \rho_T H + \rho h_T & 0 & 0 & 0 & \cdots & 0 \\ \theta' k & 0 & 0 & \rho_T k & \rho & 0 & 0 & \cdots & 0 \\ \theta' \omega & 0 & 0 & \rho_T \omega & 0 & \rho & 0 & \cdots & 0 \\ \theta' Y_1 & 0 & 0 & \rho_T Y_1 & 0 & 0 & \rho & \cdots & 0 \\ \vdots & \vdots & \vdots & \vdots & \vdots & \vdots & \vdots & \ddots & \vdots \\ \theta' Y_{n-1} & 0 & 0 & \rho_T Y_{n-1} & 0 & 0 & 0 & \cdots & \rho \end{bmatrix}. \tag{2.27}$$

Note that this simplification changes the system of equations so that they become physically incorrect system of equations. This simplification facilitates implementing a flow solver for multicomponent fluid flows when dealing with a larger number of species. The error by $\boldsymbol{M}_{\mathrm{s}}$ is discussed in following section by one-dimensional simulation.

The dual time-stepping technique with the LU-SGS scheme is used in Chapter 5. The derivation in two dimension is shown here. Note that the extension to derivation in three dimensions is straightforward. The fundamental equations of Eq. (2.1) can be also written as follow:

$$\frac{\partial \boldsymbol{Q}}{\partial t} + \boldsymbol{\Gamma}\frac{\partial \widehat{\boldsymbol{Q}}}{\partial \tau} + \theta_L\left(\frac{\partial \boldsymbol{F}_i^{m+1}}{\partial \xi_i} + \frac{\partial \boldsymbol{F}_{vi}^{m+1}}{\partial \xi_i} + \boldsymbol{S}^{m+1}\right) = -(1-\theta_L)\left(\frac{\partial \boldsymbol{F}_i^{m}}{\partial \xi_i} + \frac{\partial \boldsymbol{F}_{vi}^{m}}{\partial \xi_i} + \boldsymbol{S}^{m}\right), \tag{2.28}$$

where m represents the pseudo time step. The subscript i $(i=1,2)$ represents each coordinate. For the explicit scheme $\theta_L = 0$ and for the implicit scheme $\theta_L = 1$ and. Discretizing the physical time-derivative by the second-order backward difference and the pseudo time-derivative by the first-order forward difference yields the following equation.

$$\begin{aligned} \frac{3\boldsymbol{Q}^{m+1} - 4\boldsymbol{Q}^{n} + \boldsymbol{Q}^{n-1}}{2\Delta t} + \boldsymbol{\Gamma}\frac{\widehat{\boldsymbol{Q}}^{m+1} - \widehat{\boldsymbol{Q}}^{m}}{\Delta\tau} + \theta_L\left(\frac{\partial \boldsymbol{F}_i^{m+1}}{\partial \xi_i} + \frac{\partial \boldsymbol{F}_{vi}^{m+1}}{\partial \xi_i} + \boldsymbol{S}^{m+1}\right) \\ = -(1-\theta_L)\left(\frac{\partial \boldsymbol{F}_i^{m}}{\partial \xi_i} + \frac{\partial \boldsymbol{F}_{vi}^{m}}{\partial \xi_i} + \boldsymbol{S}^{m}\right). \end{aligned} \tag{2.29}$$

The inviscid flux is linearized as follow:

$$\frac{\partial \boldsymbol{F}_i}{\partial \tau} = \frac{\partial \boldsymbol{F}_i}{\partial \widehat{\boldsymbol{Q}}}\frac{\partial \widehat{\boldsymbol{Q}}}{\partial \tau} = \hat{\boldsymbol{A}}_i\frac{\partial \widehat{\boldsymbol{Q}}}{\partial \tau}. \tag{2.30}$$

Therefore

$$\boldsymbol{F}_i^{m+1} = \boldsymbol{F}_i^m + \hat{\boldsymbol{A}}_i \Delta \widehat{\boldsymbol{Q}}, \tag{2.31}$$

where $\Delta \widehat{\boldsymbol{Q}} = \widehat{\boldsymbol{Q}}^{m+1} - \widehat{\boldsymbol{Q}}^m$. Substituting Eq. (2.31) into Eq. (2.29),

$$\begin{aligned} &\frac{3\boldsymbol{Q}^{m+1} - 4\boldsymbol{Q}^n + \boldsymbol{Q}^{n-1}}{2\Delta t} + \boldsymbol{\Gamma}\frac{\widehat{\boldsymbol{Q}}^{m+1} - \widehat{\boldsymbol{Q}}^m}{\Delta \tau} + \theta_L \left(\frac{\partial \boldsymbol{F}_i^m}{\partial \xi_i} + \frac{\partial \hat{A}_i}{\partial \xi_i} \Delta \widehat{\boldsymbol{Q}} + \frac{\partial \boldsymbol{F}_{vi}^{m+1}}{\partial \xi_i} + \boldsymbol{S}^{m+1} \right) \\ &\qquad = -(1-\theta_L)\left(\frac{\partial \boldsymbol{F}_i^m}{\partial \xi_i} + \frac{\partial \boldsymbol{F}_{vi}^m}{\partial \xi_i} + \boldsymbol{S}^m \right). \end{aligned} \tag{2.32}$$

Treating the inviscid flux vector implicitly and the viscous flux vector and source vector explicitly, and rearranging the equations, the following equation is obtained.

$$\left(\boldsymbol{M} + \Delta \tau \frac{\partial \hat{\boldsymbol{A}}_i}{\partial \xi_i} \right) \Delta \widehat{\boldsymbol{Q}} = -\Delta \tau \left[\frac{3\boldsymbol{Q}^m - 4\boldsymbol{Q}^n + \boldsymbol{Q}^{n-1}}{2\Delta t} + \frac{\partial \boldsymbol{F}_i^m}{\partial \xi_i} + \frac{\partial \boldsymbol{F}_{vi}^m}{\partial \xi_i} + \boldsymbol{S}^m \right]. \tag{2.33}$$

Note that the following relationship is used.

$$\boldsymbol{Q}^{m+1} = \boldsymbol{Q}^m + \Delta \boldsymbol{Q}. \tag{2.34}$$

Multiplying the LHS and RHS by $\boldsymbol{M}^{-1}$,

$$\begin{aligned} &\left[\boldsymbol{I} + \Delta \tau \boldsymbol{M}^{-1} \frac{\partial \hat{\boldsymbol{A}}_i}{\partial \xi_i} \right] \Delta \widehat{\boldsymbol{Q}} \\ &\qquad = -\Delta \tau \boldsymbol{M}^{-1} \left[\frac{3\boldsymbol{Q}^m - 4\boldsymbol{Q}^n + \boldsymbol{Q}^{n-1}}{2\Delta t} + \frac{\partial \boldsymbol{F}_i^m}{\partial \xi_i} + \frac{\partial \boldsymbol{F}_{vi}^m}{\partial \xi_i} + \boldsymbol{S}^m \right] = \mathbf{RHS}. \end{aligned} \tag{2.35}$$

The left-hand side is expressed by the upwind form as follow:

$$\left[\boldsymbol{I} + \Delta \tau \boldsymbol{M}^{-1} \left(\Delta_i^- \hat{\boldsymbol{A}}_i^+ + \Delta_i^+ \hat{\boldsymbol{A}}_i^- \right) \right] \Delta \widehat{\boldsymbol{Q}} = \mathbf{RHS}, \tag{2.36}$$

where $\Delta_i^{\pm}$ are the forward and backward difference operators. Evaluated by the first-order upwind difference scheme, the following equation is obtained.

$$
\begin{aligned}
&\left\{\boldsymbol{I}+\Delta\tau\left[\left(\boldsymbol{M}^{-1}\hat{A}_1^+\right)_{i,j}-\left(\boldsymbol{M}^{-1}\hat{A}_1^-\right)_{i,j}+\left(\boldsymbol{M}^{-1}\hat{A}_2^+\right)_{i,j}-\left(\boldsymbol{M}^{-1}\hat{A}_2^-\right)_{i,j}\right]\right\}\Delta\widehat{\boldsymbol{Q}}\\
&\qquad+\Delta\tau\left[-\left(\boldsymbol{M}^{-1}\hat{A}_1^+\Delta\widehat{\boldsymbol{Q}}\right)_{i-1,j}+\left(\boldsymbol{M}^{-1}\hat{A}_1^-\Delta\widehat{\boldsymbol{Q}}\right)_{i+1,j}\right.\\
&\qquad\left.-\left(\boldsymbol{M}^{-1}\hat{A}_2^+\Delta\widehat{\boldsymbol{Q}}\right)_{i,j-1}+\left(\boldsymbol{M}^{-1}\hat{A}_2^-\Delta\widehat{\boldsymbol{Q}}\right)_{i,j+1}\right]\\
&\qquad=\mathbf{RHS},
\end{aligned}
\tag{2.37}
$$

where the subscript (i,j) indicates the grid point where the time-derivative flux is defined. Here, introducing following definitions,

$$
\boldsymbol{L}=-\Delta\tau\left[\left(\boldsymbol{M}^{-1}\hat{\boldsymbol{A}}_1^+\right)_{i-1,j}+\left(\boldsymbol{M}^{-1}\hat{\boldsymbol{A}}_2^+\right)_{i,j-1}\right],
\tag{2.38a}
$$

$$
\boldsymbol{D}=\left\{\boldsymbol{I}+\Delta\tau\left[\left(\boldsymbol{M}^{-1}\hat{\boldsymbol{A}}_1^+\right)_{i,j}-\left(\boldsymbol{M}^{-1}\hat{\boldsymbol{A}}_1^-\right)_{i,j}+\left(\boldsymbol{M}^{-1}\hat{\boldsymbol{A}}_2^+\right)_{i,j}-\left(\boldsymbol{M}^{-1}\hat{\boldsymbol{A}}_2^-\right)_{i,j}\right]\right\},
\tag{2.38b}
$$

$$
\boldsymbol{U}=\Delta\tau\left[\left(\boldsymbol{M}^{-1}\hat{\boldsymbol{A}}_1^-\right)_{i+1,j}+\left(\boldsymbol{M}^{-1}\hat{\boldsymbol{A}}_2^-\right)_{i,j+1}\right].
\tag{2.38c}
$$

Eq. (2.37) is written using Eqs. (2.38a)-(2.38c) as follow:

$$
(\boldsymbol{L}+\boldsymbol{D}+\boldsymbol{U})\Delta\widehat{\boldsymbol{Q}}=\mathbf{RHS}.
\tag{2.39}
$$

Eq. (2.39) is LDU factorized as follow:

$$
(\boldsymbol{D}+\boldsymbol{L})\boldsymbol{D}^{-1}(\boldsymbol{D}+\boldsymbol{U})\Delta\widehat{\boldsymbol{Q}}=\mathbf{RHS}.
\tag{2.40}
$$

Defining $\Delta\widehat{\boldsymbol{Q}}^*$ as follow:

$$
\Delta\widehat{\boldsymbol{Q}}^*\equiv\boldsymbol{D}^{-1}(\boldsymbol{D}+\boldsymbol{U})\Delta\widehat{\boldsymbol{Q}}.
\tag{2.41}
$$

Therefore, Eq. (2.39) is solved in a following two-step:

$$
\Delta\widehat{\boldsymbol{Q}}^*=\boldsymbol{D}^{-1}\left(\mathbf{RHS}-\boldsymbol{L}\Delta\widehat{\boldsymbol{Q}}^*\right),
\tag{2.42a}
$$

$$
\Delta\widehat{\boldsymbol{Q}}=\Delta\widehat{\boldsymbol{Q}}^*-\boldsymbol{D}^{-1}\boldsymbol{U}\Delta\widehat{\boldsymbol{Q}}.
\tag{2.42b}
$$

$\boldsymbol{M}^{-1}\hat{\boldsymbol{A}}_i^{\pm}$ are defined as follows:

$$\boldsymbol{M}^{-1}\hat{\boldsymbol{A}}_i^{\pm} = \frac{1}{2}\left(\boldsymbol{M}^{-1}\hat{\boldsymbol{A}}_i \pm r_i \boldsymbol{I}\right), \tag{2.43}$$

where

$$r_i = \sigma \max\left[\hat{\lambda}\left(\boldsymbol{M}^{-1}\hat{\boldsymbol{A}}_i\right)\right]. \tag{2.44}$$

σ is a constant greater than unity. $\hat{\lambda}\left(\boldsymbol{M}^{-1}\hat{\boldsymbol{A}}_i\right)$ are the eigenvalues of $\boldsymbol{M}^{-1}\hat{\boldsymbol{A}}_i$. Substituting Eq. (2.43) into Eq. (2.38b),

$$\boldsymbol{D} = \{1 + \Delta\tau[r_1 + r_2]\}\boldsymbol{I}. \tag{2.45}$$

$\boldsymbol{D}$ is a scalar matrix. Therefore, $\boldsymbol{D}^{-1}$ is easily determined by calculating the inverse of the scalar matrix. Since the approximation of the Jacobian matrix destroys the linearization of the inviscid flux in Eq. (2.32), the conservation law is not satisfied strictly. However, the LHS value is almost zero when the solution converges, it may not be a critical problem for application. Finally, Eqs. (2.42a) and (2.42b) are calculated by the forward and the backward sweep on the hyper plane as follows:

$$\Delta\widehat{\boldsymbol{Q}}^{*}_{i,j,k} = \boldsymbol{D}^{-1}\left\{\mathbf{RHS} + \Delta\tau\left[\left(\boldsymbol{M}^{-1}\hat{\boldsymbol{A}}_1^{+}\Delta\widehat{\boldsymbol{Q}}^{*}\right)_{i-1,j} + \left(\boldsymbol{M}^{-1}\hat{\boldsymbol{A}}_2^{+}\Delta\widehat{\boldsymbol{Q}}^{*}\right)_{i,j-1}\right]\right\}, \tag{2.46a}$$

$$\Delta\widehat{\boldsymbol{Q}}_{i,j,k} = \Delta\widehat{\boldsymbol{Q}}^{*}_{i,j,k} - \boldsymbol{D}^{-1}\Delta\tau\left[\left(\boldsymbol{M}^{-1}\hat{\boldsymbol{A}}_1^{-}\Delta\widehat{\boldsymbol{Q}}\right)_{i+1,j} + \left(\boldsymbol{M}^{-1}\hat{\boldsymbol{A}}_2^{-}\Delta\widehat{\boldsymbol{Q}}\right)_{i,j+1}\right]. \tag{2.46b}$$

The time-derivative fluxes are evaluated by using preconditioned FVS scheme. However, $\widehat{\boldsymbol{Q}}^{\mathrm{M}}$ in Eq. (2.19) is replaced by $\Delta\widehat{\boldsymbol{Q}}$.

2.2.4 Thermophysical properties model for fluid mixture

I employ the Helmholtz free-energy equation of state (EoS) for the thermophysical properties defined in the Reference Fluid Thermodynamic and Transport Properties Database (REFPROP) [22], and Amagat's law is used to define the mixture properties [23]. The look-up tables are used to reduce the calculation costs owing to the complex calculation procedure of the Helmholtz free-energy EoS. In this method, the thermophysical properties in the pressure and temperature parameter space are calculated using REFPROP at a preset

constant interval to create look-up tables. Pre-prepared look-up tables are used to evaluate the quantities in the flow simulation. The data points of look-up tables in the pressure and temperature parameter space are set with a constant interval of $\Delta p = 0.002\ \mathrm{MPa}$ and $\Delta T = 0.2\ \mathrm{K}$ in all the problems, and the values are interpolated with linear interpolation. The Helmholtz free-energy A normalized by the gas constant and temperature, the so-called reduced Helmholtz free energy, is calculated as follows:

$$\alpha(\delta,\tau) = \frac{A}{RT} = \alpha^0(\delta,\tau) + \alpha^{\mathrm{r}}(\delta,\tau), \tag{2.47}$$

where $\delta = \rho/\rho_{\mathrm{c}}$ and $\tau = T_{\mathrm{c}}/T$. ρ_{c} and T_{c} are the density and temperature at the critical point, respectively. The reduced Helmholtz free energy generally consists of the reduced ideal-gas part α^0 and the reduced residual part α^{r}. The Helmholtz free-energy EoS for each component is defined in the REFPROP. Thermophysical properties, such as pressure, enthalpy, and isobaric heat capacity, can be obtained from the Helmholtz free-energy EoS.

The mixture was modeled such that each component had the same pressure and temperature under local thermodynamic equilibrium conditions. The mixture properties were given by Amagat's law of mixture. Each component occupies a partial volume, and the sum of the partial volumes yields the total volume of the mixture. Amagat's law leads to the definition of partial density for each individual component, that is, the molecular weight of each component divided by the partial volume of each component. The mixture density and enthalpy are defined as follows:

$$\frac{1}{\rho} = \sum_{i=1}^{n} \frac{Y_i}{\rho_i(p,T)}, \tag{2.48a}$$

$$h = \sum_{i=1}^{n} Y_i h_i(p,T). \tag{2.48b}$$

ρ_i and h_i indicate the density and enthalpy of each component, respectively. The partial derivatives of the density and enthalpy are defined as follows:

$$\rho_p = \rho^2 \sum_{i=1}^{n} \frac{Y_i}{\rho_i^2} \frac{\partial \rho_i}{\partial p}, \qquad \rho_T = \rho^2 \sum_{i=1}^{n} \frac{Y_i}{\rho_i^2} \frac{\partial \rho_i}{\partial T}, \qquad \rho_{Y_i} = \rho^2 \left(\frac{1}{\rho_n} - \frac{1}{\rho_i} \right), \tag{2.49a}$$

$$h_p = \sum_{i=1}^{n} Y_i \frac{\partial h_i}{\partial p}, \qquad h_T = \sum_{i=1}^{N} Y_i \frac{\partial h_i}{\partial T}, \qquad h_{Y_i} = h_i - h_n. \tag{2.49b}$$

The physical speed of sound for the mixture is specified by:

$$c = \sqrt{\frac{\rho h_T}{\rho_T(1-\rho h_p)+\rho h_T \rho_p}}, \tag{2.50}$$

where the density and partial derivatives on the right-hand side of Eq. (2.50) are calculated from the property and mass fraction of each component, as shown in Eqs. (2.48a), (2.49a), and (2.49b). The physical speed of sound is calculated in each physical and inner iteration.

Figure 2.1 shows the density and speed of sound for *n*-dodecane calculated using the Helmholtz free-energy EoS and Peng–Robinson (PR) EoS. The calculated results were compared with the available experimental data in the literature [24, 25]. The maximum density error of the PR EoS was 10.17%, whereas that of the Helmholtz free-energy EoS was only 0.02%. The numerical analysis of a regenerative cooling system that uses liquid hydrocarbon fuel requires consideration of liquid phase flows over a wide range of temperatures. Therefore, the Helmholtz free-energy EoS is a suitable choice for multicomponent hydrocarbon flows with the transition to the supercritical state.

The mixture viscosity and thermal conductivity were evaluated using Wilke's semi-empirical mixing law [26] as follows:

$$\mathcal{T} = \sum_{i=1}^{n} \frac{Y_i \mathcal{T}_i}{\sum_{j=1}^{n} Y_j \phi_{ij}}, \tag{2.51}$$

where $\mathcal{T}$ and $\mathcal{T}_i$ indicate the viscosity or thermal conductivity of the mixture and each component, respectively. $\phi_{ij} = (M_j/M_i)^{\frac{1}{2}}$ proposed by Herning and Zipperer [27] is used, where M is the molecular weight of each component. The viscosity and thermal conductivity of each component were calculated using the REFPROP.

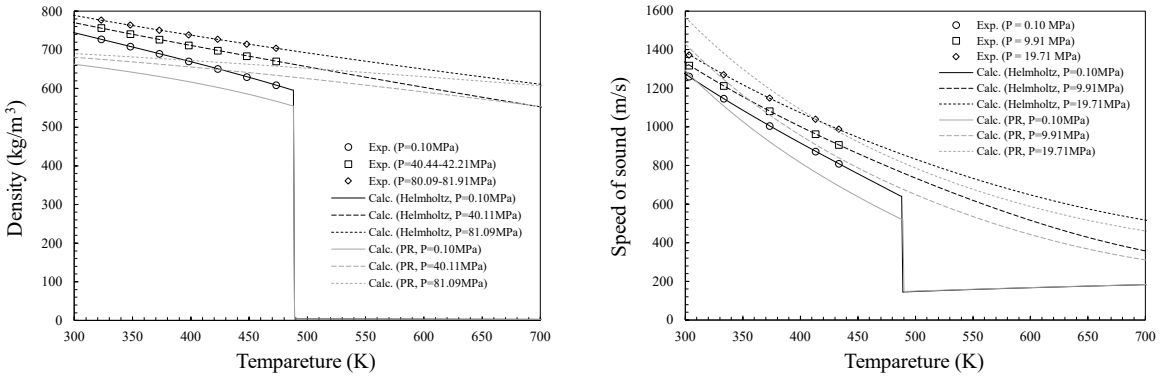

(a) Density (b) Speed of sound

Figure 2.1. Thermophysical properties of *n*-dodecane calculated using the Helmholtz free-energy EoS and PR EoS.

2.3 Spurious oscillations problem

2.3.1 Mechanism of spurious oscillations in the preconditioned system

Abgrall [3] revealed the mechanism of spurious oscillations of multicomponent flows in compressible Navier–Stokes equations. In this section, the mechanism of spurious oscillations in the preconditioned system is described using a one-dimensional Euler system by the analysis method employed by Abgrall [3, 8].

A one-dimensional Euler system applied to a binary mixture is solved in a uniform velocity and pressure field as the initial condition. The temporal variation of the inner iteration in dual time-stepping is expressed from Eq. (2.24) as follow:

$$\delta\widehat{\boldsymbol{Q}}_j = -\alpha_l \delta\tau \boldsymbol{M}^{-1}\left(\frac{3\boldsymbol{Q}_j^l - 4\boldsymbol{Q}_j^n + \boldsymbol{Q}_j^{n-1}}{2\delta t} + \frac{\partial \boldsymbol{F}_j^l}{\partial x}\right) = -\alpha_l \delta\tau(\boldsymbol{P}^{-1}\boldsymbol{\mathcal{R}}^1 + \boldsymbol{M}^{-1}\boldsymbol{\mathcal{R}}^2), \tag{2.52}$$

where

$$\boldsymbol{M} = \boldsymbol{N}\boldsymbol{P}, \tag{2.53a}$$

$$\boldsymbol{M}^{-1} = \boldsymbol{P}^{-1}\boldsymbol{N}^{-1}, \tag{2.53b}$$

$$\boldsymbol{\mathcal{R}}^1 = \frac{3\widehat{\boldsymbol{Q}}_j^l - 4\widehat{\boldsymbol{Q}}_j^n + \widehat{\boldsymbol{Q}}_j^{n-1}}{2\delta t}, \tag{2.53c}$$

$$\boldsymbol{\mathcal{R}}^2 = \frac{\partial \boldsymbol{F}_j^l}{\partial x}. \tag{2.53d}$$

$\boldsymbol{M}$ consists of the matrix $\boldsymbol{P}$ for the effect of preconditioning and the Jacobian matrix $\boldsymbol{N}$. The inverse matrices $\boldsymbol{M}^{-1}$ and $\boldsymbol{P}^{-1}$ are expressed as follows:

$$\boldsymbol{M}^{-1} = d \times \begin{bmatrix} \dfrac{h_T(\rho + \rho_{Y_1}Y_1) - \rho_T(u^2 - H + h_{Y_1}Y_1)}{\rho h_T\theta' + \rho_T(1-\rho h_p)} & \dfrac{u\rho_T}{\rho h_T\theta' + \rho_T(1-\rho h_p)} \\ -\dfrac{u}{\rho} & \dfrac{1}{\rho} \\ \dfrac{1 - h_p(\rho + \rho_{Y_1}Y_1) + \theta'(u^2 - H + h_{Y_1}Y_1) + \rho_{Y_1}Y_1/\rho}{\rho h_T\theta' + \rho_T(1-\rho h_p)} & \dfrac{-u\theta'}{\rho h_T\theta' + \rho_T(1-\rho h_p)} \\ -\dfrac{Y_1}{\rho} & 0 \end{bmatrix} \tag{2.54a}$$

$$\begin{bmatrix} \dfrac{-\rho_T}{\rho h_T\theta' + \rho_T(1-\rho h_p)} & \dfrac{\rho_T h_{Y_1} - \rho_{Y_1} h_T}{\rho h_T\theta' + \rho_T(1-\rho h_p)} \\ 0 & 0 \\ \dfrac{\theta'}{\rho h_T\theta' + \rho_T(1-\rho h_p)} & \dfrac{\rho_{Y_1} h_p - \theta' h_{Y_1} - \rho_{Y_1}/\rho}{\rho h_T\theta' + \rho_T(1-\rho h_p)} \\ 0 & \dfrac{1}{\rho} \end{bmatrix},$$

$$\boldsymbol{P}^{-1} = d \begin{bmatrix} \dfrac{\rho\rho_p h_T - \rho_T(\rho h_p - 1)}{\rho h_T\theta' + \rho_T(1-\rho h_p)} & 0 & 0 & 0 \\ 0 & 1 & 0 & 0 \\ \dfrac{\theta'(\rho h_p - 1) - \rho_p(\rho h_p - 1)}{\rho h_T\theta' + \rho_T(1-\rho h_p)} & 0 & 1 & 0 \\ 0 & 0 & 0 & 1 \end{bmatrix}, \tag{2.54b}$$

where

$$d = \frac{1}{\dfrac{3\delta\tau}{2\delta t} + 1}. \tag{2.55}$$

The subscript j represents the value at a grid point. In a uniform velocity and pressure field, $\boldsymbol{\mathcal{R}}^1 = (\mathcal{R}_1^1, \mathcal{R}_2^1, \mathcal{R}_3^1, \mathcal{R}_4^1)^{\mathrm{T}}$ are written as follows:

$$\mathcal{R}_1^1 = 0, \tag{2.56a}$$

$$\mathcal{R}_2^1 = 0, \tag{2.56b}$$

$$\mathcal{R}_3^1 = \frac{3T_j^l - 4T_j^n + T_j^{n-1}}{2\delta t}, \tag{2.56c}$$

$$\mathcal{R}_4^1 = \frac{3Y_{1,j}^l - 4Y_{1,j}^n + Y_{1,j}^{n-1}}{2\delta t}. \tag{2.56d}$$

$\boldsymbol{\mathcal{R}}^2 = (\mathcal{R}_1^2, \mathcal{R}_2^2, \mathcal{R}_3^2, \mathcal{R}_4^2)^{\mathrm{T}}$ are derived from the conservation equations of mass, momentum, total energy, and mass fraction in a one-dimensional Euler system using a first-order Godunov scheme with an upwind scheme, as follows:

$$\mathcal{R}_1^2 = \frac{1}{\Delta x} u_j^l \Delta\rho^l, \tag{2.57a}$$

$$\mathcal{R}_2^2 = \frac{1}{\Delta x}(u_j^l)^2 \Delta\rho^l, \tag{2.57b}$$

$$\mathcal{R}_3^2 = \frac{1}{\Delta x} u_j^l \left[\Delta(\rho h)^l + \frac{1}{2}(u_j^l)^2 \Delta\rho^l\right], \tag{2.57c}$$

$$\mathcal{R}_4^2 = \frac{1}{\Delta x} u_j^l \Delta(\rho Y_1)^l. \tag{2.57d}$$

where Δx is the grid spacing. In addition, $\Delta(\cdot)^l = (\cdot)_j^l - (\cdot)_{j-1}^l$ represents spatial variation. Substituting Eqs. (2.56a) – (2.56d) and Eqs. (2.57a) – (2.57d) into Eq. (2.52), the temporal variation in velocity is derived as follows:

$$\begin{aligned}
\delta u_j &= -\alpha_l \delta\tau[(\mathrm{P}_{21}^{-1} + \mathrm{P}_{22}^{-1} + \mathrm{P}_{23}^{-1} + \mathrm{P}_{24}^{-1})\boldsymbol{\mathcal{R}}^1 + (\mathrm{M}_{21}^{-1} + \mathrm{M}_{22}^{-1} + \mathrm{M}_{23}^{-1} + \mathrm{M}_{24}^{-1})\boldsymbol{\mathcal{R}}^2] \\
&= -\alpha_l d \frac{\delta\tau}{\Delta x}\left[-\frac{u_j^l}{\rho_j^l}\, u_j^l \Delta\rho^l + \frac{1}{\rho_j^l}(u_j^l)^2 \Delta\rho^l\right] \\
&= 0.
\end{aligned} \tag{2.58}$$

where $d = (3\delta\tau/2\delta t + 1)^{-1}$. P_{ij}^{-1} and M_{ij}^{-1} represents the (i,j) element of $\boldsymbol{P}^{-1}$ and $\boldsymbol{M}^{-1}$. Eq. (2.58) shows that spurious oscillations in velocity do not occur directly. However, once pressure oscillations occur at a certain time step, the velocity equilibrium cannot be maintained at the next. Similarly, the pressure and temperature temporal variations are expressed as follows:

$$\begin{aligned}
\delta p_j &= -\alpha_l \delta\tau[(\mathrm{P}_{11}^{-1} + \mathrm{P}_{12}^{-1} + \mathrm{P}_{13}^{-1} + \mathrm{P}_{14}^{-1})\boldsymbol{\mathcal{R}}^1 + (\mathrm{M}_{11}^{-1} + \mathrm{M}_{12}^{-1} + \mathrm{M}_{13}^{-1} + \mathrm{M}_{14}^{-1})\boldsymbol{\mathcal{R}}^2] \\
&= -\alpha_l d \frac{\delta\tau}{\Delta x}\frac{u_j^l}{X_j^l}[\rho_j^l h_{T,j}^l\, \Delta\rho^l - \rho_{T,j}^l(\rho_j^l \Delta h^l - \Delta\rho^l \Delta h^l) \\
&\qquad + (\rho_{T,j}^l h_{Y_1,j}^l - \rho_{Y_1,j}^l h_{T,j}^l)(\rho_j^l \Delta Y_1^l - \Delta\rho^l \Delta Y_1^l)],
\end{aligned} \tag{2.59a}$$

$$\begin{aligned}
\delta T_j &= -\alpha_l \delta\tau[(\mathrm{P}_{31}^{-1} + \mathrm{P}_{32}^{-1} + \mathrm{P}_{33}^{-1} + \mathrm{P}_{34}^{-1})\boldsymbol{\mathcal{R}}^1 + (\mathrm{M}_{31}^{-1} + \mathrm{M}_{32}^{-1} + \mathrm{M}_{33}^{-1} + \mathrm{M}_{34}^{-1})\boldsymbol{\mathcal{R}}^2] \\
&= -\alpha_l d\delta\tau \left\{\frac{3T_j^l - 4T_j^n + T_j^{n-1}}{2\delta t}\right. \\
&\qquad + \frac{1}{\Delta x}\frac{u_j^l}{X_j^l}\left[(1 - \rho_j^l h_{p,j}^l)\Delta\rho^l + \theta_j'^{,l}(\rho_j^l \Delta h^l - \Delta\rho^l \Delta h^l)\right. \\
&\qquad \left.\left. + (\rho_{Y_1,j}^l h_{p,j}^l - \theta_j'^{,l} h_{Y_1,j}^l - \rho_{Y_1,j}^l/\rho_j^l)(\rho_j^l \Delta Y_1^l - \Delta\rho^l \Delta Y_1^l)\right]\right\},
\end{aligned} \tag{2.59b}$$

where

$$X_j^l = \rho_j^l h_{T,j}^l \theta_j'^{,l} + \rho_{T,j}^l (1 - \rho_j^l h_{p,j}^l). \tag{2.60}$$

Assuming smooth parts of the flow, I used the following identity, which holds for the product of the variation.

$$\Delta(ab)_j = b_j \Delta(a)_j + a_j \Delta(b)_j - \Delta(a)_j \Delta(b)_j. \tag{2.61}$$

Here, the pressure must be uniform at time n, because the initial condition assumes a uniform velocity and pressure field. Therefore, the spatial variation of the density and enthalpy can be expressed $\Delta\rho(\Delta T, \Delta Y_1)$ and $\Delta h(\Delta T, \Delta Y_1)$, respectively. In the following, I analyze the spurious oscillations separately for the two situations, that is, the single fluid interface for different temperatures $(\Delta T \neq 0, \Delta Y_1 = 0)$ and the material interface for uniform fluid temperature $(\Delta T = 0, \Delta Y_1 \neq 0)$.

In the case of the single fluid interface for different temperatures $(\Delta T \neq 0, \Delta Y_1 = 0)$, substituting the spatial variation of $\Delta Y_1 = 0$ into Eq. (2.59a), I obtain the following:

$$\delta p_j = -\alpha_l d \frac{\delta\tau}{\Delta x} \frac{u_j^l}{X_j^l} [\rho_j^l h_{T,j}^l \, \Delta\rho^l - \rho_{T,j}^l (\rho_j^l \Delta h^l - \Delta\rho^l \Delta h^l)]. \tag{2.62}$$

In this situation, the spatial variations in density and enthalpy are expressed as $\Delta\rho(\Delta T)$ and $\Delta h(\Delta T)$, therefore it is inevitable to avoid spurious oscillations unless the temperature is uniform at a certain control volume $[j - 1/2\,, j + 1/2]$. In short, Eq. (2.62) suggests that spurious oscillations may occur even in a single fluid when solving the flows with thermodynamic property changes, such as transcritical flows.

Next, the pressure and temperature equilibria are derived at the material interface for uniform temperature conditions $(\Delta T = 0, \Delta Y_1 \neq 0)$. I can obtain the following relations by spatially differentiating Eqs. (2.48a) and (2.48b).

$$\Delta\rho^l = \frac{(\rho_j^l)^2 \left(\dfrac{1}{\rho_{2,j}^l} - \dfrac{1}{\rho_{1,j}^l} \right) \Delta Y_1^l}{1 + \rho_j^l \left(\dfrac{1}{\rho_{2,j}^l} - \dfrac{1}{\rho_{1,j}^l} \right) \Delta Y_1^l} = \frac{\rho_j^l \rho_{Y_1,j}^l \Delta Y_1^l}{\rho_j^l + \rho_{Y_1,j}^l \Delta Y_1^l}, \tag{2.63a}$$

$$\Delta h^l = (h_{1,j}^l - h_{2,j}^l) \Delta Y_1^l = h_{Y_1,j}^l \Delta Y_1^l. \tag{2.63b}$$

To derive Eq. (2.63a), I used the following identity for the quotient of the variation:

$$\Delta\left(\frac{a}{b}\right)_i = \frac{b_i\Delta(a)_i - a_i\Delta(b)_i}{b_i^2 - b_i\Delta(a)_i}. \tag{2.64}$$

The temporal variations in pressure and temperature are expressed by Eqs. (2.59a), (2.59b), (2.63a), and (2.63b) as

$$\delta p_j = \delta T_j = 0. \tag{2.65}$$

Thus, the pressure and temperature equilibria are satisfied at the material interface $(\Delta T = 0, \Delta Y_1 \neq 0)$, where the pressure, velocity, and temperature are uniform. This result is consistent with the analysis of Jenny et al. [28] for a perfect gas mixture.

The simplified matrices $\boldsymbol{M}_{\mathrm{s}}^{-1}$ and $\boldsymbol{P}_{\mathrm{s}}^{-1}$ for $\widehat{\boldsymbol{Q}} = (p, u, T, Y_1)^{\mathrm{T}}$ systems are written as follows:

$$\begin{aligned}
&\boldsymbol{M}_{\mathrm{s}}^{-1} \\
&= d\begin{bmatrix}
\dfrac{\rho h_T + \rho_T(H-u^2)}{\rho h_T\theta' + \rho_T(1-\rho h_p)} & \dfrac{u\rho_T}{\rho h_T\theta' + \rho_T(1-\rho h_p)} & \dfrac{-\rho_T}{\rho h_T\theta' + \rho_T(1-\rho h_p)} & 0 \\
-\dfrac{u}{\rho} & \dfrac{1}{\rho} & 0 & 0 \\
\dfrac{(1-\rho h_p) - \theta'(H-u^2)}{\rho h_T\theta' + \rho_T(1-\rho h_p)} & \dfrac{-u\theta'}{\rho h_T\theta' + \rho_T(1-\rho h_p)} & \dfrac{\theta'}{\rho h_T\theta' + \rho_T(1-\rho h_p)} & 0 \\
-\dfrac{Y_1}{\rho} & 0 & 0 & \dfrac{1}{\rho}
\end{bmatrix},
\end{aligned} \tag{2.66a}$$

$$\boldsymbol{P}_{\mathrm{s}}^{-1} = \boldsymbol{P}^{-1}. \tag{2.66b}$$

In this case, Eq. (2.59a) and (2.59b) can be transformed as follows:

$$\begin{aligned}
\delta p_j &= -\alpha_l\delta\tau\big[(\mathrm{P}_{\mathrm{s},11}^{-1} + \mathrm{P}_{\mathrm{s},12}^{-1} + \mathrm{P}_{\mathrm{s},13}^{-1} + \mathrm{P}_{\mathrm{s},14}^{-1})\boldsymbol{\mathcal{R}}^1 \\
&\qquad + (\mathrm{M}_{\mathrm{s},11}^{-1} + \mathrm{M}_{\mathrm{s},12}^{-1} + \mathrm{M}_{\mathrm{s},13}^{-1} + \mathrm{M}_{\mathrm{s},14}^{-1})\boldsymbol{\mathcal{R}}^2\big] \\
&= -\alpha_l d\frac{\delta\tau}{\Delta x}\frac{u_j^l}{X_j^l}[\rho_j^l h_{T,j}^l\,\Delta\rho^l - \rho_{T,j}^l(\rho_j^l\Delta h^l - \Delta\rho^l\Delta h^l)],
\end{aligned} \tag{2.67a}$$

$$\begin{aligned}
\delta T_j &= -\alpha_l\delta\tau\big[(\mathrm{P}_{\mathrm{s},31}^{-1} + \mathrm{P}_{\mathrm{s},32}^{-1} + \mathrm{P}_{\mathrm{s},33}^{-1} + \mathrm{P}_{\mathrm{s},34}^{-1})\boldsymbol{\mathcal{R}}^1 \\
&\qquad + (\mathrm{M}_{\mathrm{s},31}^{-1} + \mathrm{M}_{\mathrm{s},32}^{-1} + \mathrm{M}_{\mathrm{s},33}^{-1} + \mathrm{M}_{\mathrm{s},34}^{-1})\boldsymbol{\mathcal{R}}^2\big] \\
&= -\alpha_l d\frac{\delta\tau}{\Delta x}\frac{u_j^l}{X_j^l}[(1-\rho_j^l h_{p,j}^l)\Delta\rho^l + \theta'^{,l}(\rho_j^l\Delta h^l - \Delta\rho^l\Delta h^l)].
\end{aligned} \tag{2.67b}$$

The spatial variations in density and enthalpy are expressed as $\Delta\rho(\Delta Y_1)$ and $\Delta h(\Delta Y_1)$, therefore spurious oscillations are inevitable, unless the mass fraction is uniform at a certain control volume $[j-1/2\,,j+1/2]$.

The above discussion clearly shows that residual $\boldsymbol{\mathcal{R}}^2$ causes numerical oscillations, whereas the residual $\boldsymbol{\mathcal{R}}^1$ related to dual time stepping does not. In the next section, the DFM for the preconditioning method is developed to avoid numerical oscillations induced by the residual $\boldsymbol{\mathcal{R}}^2$.

2.3.2 Double-flux model for preconditioned system

I developed the DFM for the preconditioning method based on the above discussion, and the original DFM [8]. To avoid spurious oscillations of pressure, two different numerical fluxes $\tilde{\boldsymbol{F}}^{\mathrm{L}}_{j+1/2}$ and $\tilde{\boldsymbol{F}}^{\mathrm{R}}_{j+1/2}$ are defined at the interface between the control volume j and $j+1$ as follows:

$$\tilde{\boldsymbol{F}}^{\mathrm{R}}_{j+1/2} = \tilde{\boldsymbol{F}}_{j+1/2}\left(\widehat{\boldsymbol{Q}}^{\mathrm{L}}_{j+1/2}, \widehat{\boldsymbol{Q}}^{\mathrm{R}}_{j+1/2}; \varphi_{j+1}\right), \tag{2.68a}$$

$$\tilde{\boldsymbol{F}}^{\mathrm{L}}_{j+1/2} = \tilde{\boldsymbol{F}}_{j+1/2}\left(\widehat{\boldsymbol{Q}}^{\mathrm{L}}_{j+1/2}, \widehat{\boldsymbol{Q}}^{\mathrm{R}}_{j+1/2}; \varphi_{j}\right). \tag{2.68b}$$

$\tilde{\boldsymbol{F}}^{\mathrm{L}}_{j+1/2}$ and $\tilde{\boldsymbol{F}}^{\mathrm{R}}_{j+1/2}$ were used as the numerical fluxes at the interface of each grid instead of Eq. (2.22). Here, when the matrix $\boldsymbol{M}$, the temporal variations at the interface for different temperatures (Eq. (2.62)) are kept equal to zero assuming the uniform temperature by

$$\varphi = T. \tag{2.69}$$

The simplified matrix $\boldsymbol{M}_{\mathrm{s}}$ is attractive for practical use because the matrix $\boldsymbol{M}$ for a multi-component system becomes complex, increasing the number of components. On the other hand, when using $\boldsymbol{M}_{\mathrm{s}}$, spurious oscillations are generated at the material interface, as shown in Section 2.3.1. Thus, the following option for the definition of φ can be considered:

$$\varphi = T \text{ and } Y_1. \tag{2.70}$$

The temporal variations (Eqs. (2.67a) and (2.67b)) were kept equal to zero using Eqs. (2.70), and the pressure and temperature equilibria are satisfied at the material interface $(\Delta T = 0, \Delta Y_1 \neq 0)$ despite using the simplified preconditioning matrix $\boldsymbol{M}_{\mathrm{s}}$. The definitions of the numerical flux, such as those in Eqs. (2.68a) and (2.68b), are equal in that φ is considered uniform at a certain control volume $[j-1/2\,, j+1/2]$. As discussed in Section 2.3.1, Eqs. (2.70) enable the avoidance of spurious oscillations for the numerical method with the simplified preconditioning matrix. Finally, the residuals $\boldsymbol{\mathcal{R}}^2$ are obtained as follows:

$$\boldsymbol{\mathcal{R}}^2 = \frac{\partial \boldsymbol{F}^l_j}{\partial x} = \frac{\left[\tilde{\boldsymbol{F}}^{\mathrm{L}}_{j+1/2}\left(\widehat{\boldsymbol{Q}}^{\mathrm{L}}_{j+1/2}, \widehat{\boldsymbol{Q}}^{\mathrm{R}}_{j+1/2}; \varphi_j\right) - \tilde{\boldsymbol{F}}^{\mathrm{R}}_{j-1/2}\left(\widehat{\boldsymbol{Q}}^{\mathrm{L}}_{j-1/2}, \widehat{\boldsymbol{Q}}^{\mathrm{R}}_{j-1/2}; \varphi_j\right)\right]^l}{\Delta x}. \tag{2.71}$$

The thermophysical properties and conservative variables are updated to the next time step from the unknown variables. When adopting the DFM, a unique numerical flux cannot be defined at the cell interface.

Thus, conservative errors are inevitably generated, and this is a so-called quasi-conservative method. In this study, the total density is a function of pressure, temperature, and mass fraction, and is updated using the EoS. Hence, the conservation errors were generated not only in the total energy but also in the mass and momentum. In this section, I employ a first-order upwind scheme and explicit time integration for the simple discussion about the spurious oscillations. The errors induced by these properties also occur in general numerical scheme. In the following section, the conservation errors for the mass, momentum, and total energy are quantified using DFM.

2.4 Numerical results

2.4.1 One-dimensional advection problems

One-dimensional advection problems were simulated to demonstrate the numerical oscillations with and without DFM in fluids with different temperatures and binary fluids. The fundamental equations solved in this subsection are the Euler system. The pressure was set to 3.0 MPa, which is above the critical pressure of *n*-dodecane. The advection velocity is 1.0 m/s. The Mach number based on the initial velocity is 6.2×10^{-3} at 800 K. The total computational grid number was 100, and the grid spacing was uniform. The computational domain is $x \in [0,1]$ m with periodic boundary conditions. The Courant–Friedrichs–Lewy (CFL) number in the physical time step was set to 1.0. The CFL numbers for the pseudo-time step were set to 0.5 in these and following simulations, the local time stepping was employed, and $\delta\tau/\delta t$ in this section was less than unity. The numerical results are compared with the exact solutions, and the conservation errors due to the DFM procedure were quantified.

The advection of *n*-dodecane with an interface of different temperatures was simulated with and without DFM in the preconditioned numerical method. The initial conditions were set by providing sharp jumps in temperature, as follows:

$$T = \begin{cases} T_{\max} = 800 \text{ K}, & 0.25 \text{ m} < x < 0.75 \text{ m} \\ T_{\min} = 400 \text{ K}, & \text{otherwise} \end{cases}. \tag{2.72}$$

Because the temperature conditions are set to cross the pseudo-boiling line, large thermophysical property changes such as density and enthalpy jumps exist in the computational domain.

Figure 2.2 shows the profiles of the pressure variation from an initial value, velocity, temperature, and density at $t = 0.05$ s. In this test case, the inner iteration of dual time-stepping is set to 50 to decrease the temperature residual by 10 orders of magnitude. As shown in Section 2.3.1, the spatial variation in density causes spurious oscillations. Therefore, the pressure equilibrium could not be maintained in the simulation without the DFM. The numerical result with DFM enables the simulation of *n*-dodecane at different temperatures without spurious oscillations, despite the large thermophysical property jumps, and the results are consistent with the exact solutions.

As an example of multicomponent flow, the advection of the interface between *n*-dodecane and propylene at a uniform temperature is simulated. The initial conditions are given by sharp jumps in the mass fraction as follows:

$$Y_1 = \begin{cases} Y_{1,\max} = 1, & 0.25 \text{ m} < x < 0.75 \text{ m} \\ Y_{1,\min} = 0, & \text{otherwise} \end{cases}. \tag{2.73}$$

Y_1 is the mass fraction of *n*-dodecane. The temperature is set to a uniform value at 900 K. Figure 2.3 displays the profiles of the pressure variation from an initial value, velocity, temperature, and density at $t = 0.05$ s for the numerical results of the original preconditioned numerical method without DFM, the simplified preconditioned numerical method without and with DFM. The original preconditioned numerical method reproduces consistent results even without DFM treatment for the binary fluid problem. The simplified preconditioning matrix is another choice for the binary fluid problem in terms of ease of implementation. The numerical results obtained using the simplified preconditioned numerical method indicate that the DFM treatment of the binary fluid is essential to avoid spurious oscillations. The effects of acoustics are not important in these and following numerical simulations. Further discussion and careful treatment are needed if the simplified matrix is used for general flow problems.

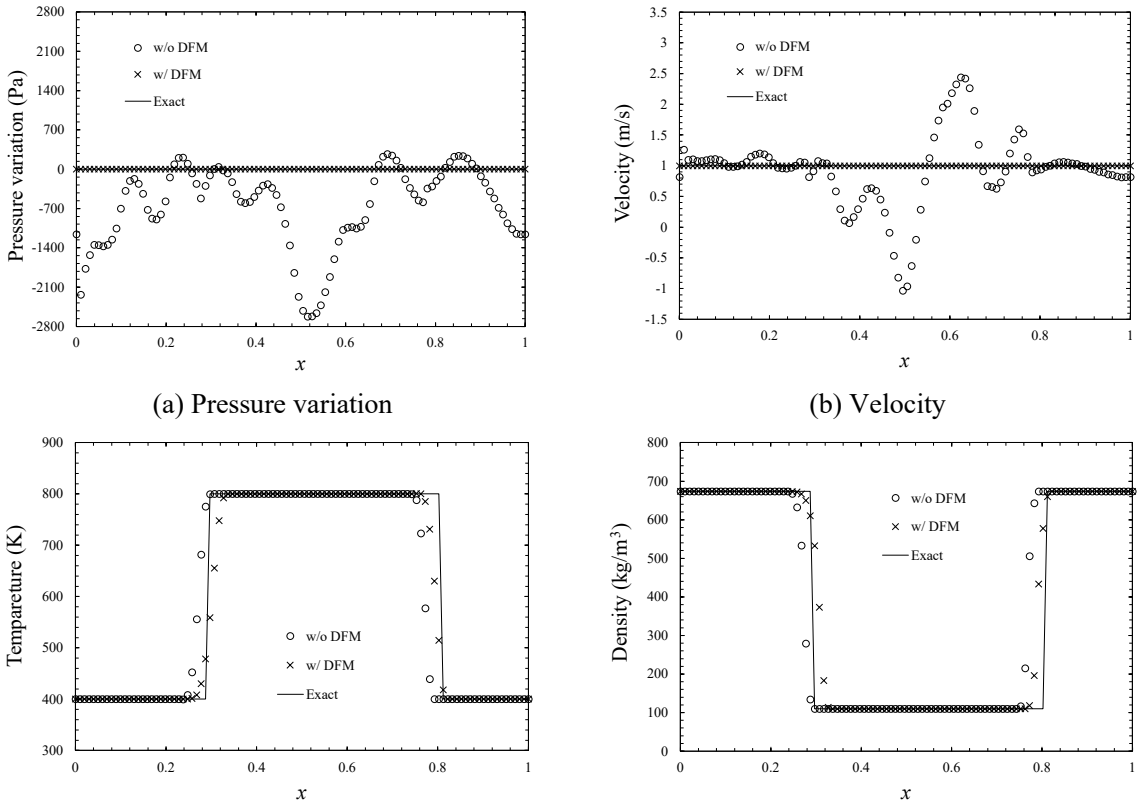

(a) Pressure variation (b) Velocity

(c) Temperature (d) Density

Figure 2.2. Profiles of a one-dimensional advection of *n*-dodecane interface at $t = 5.0 \times 10^{-2}$ s.

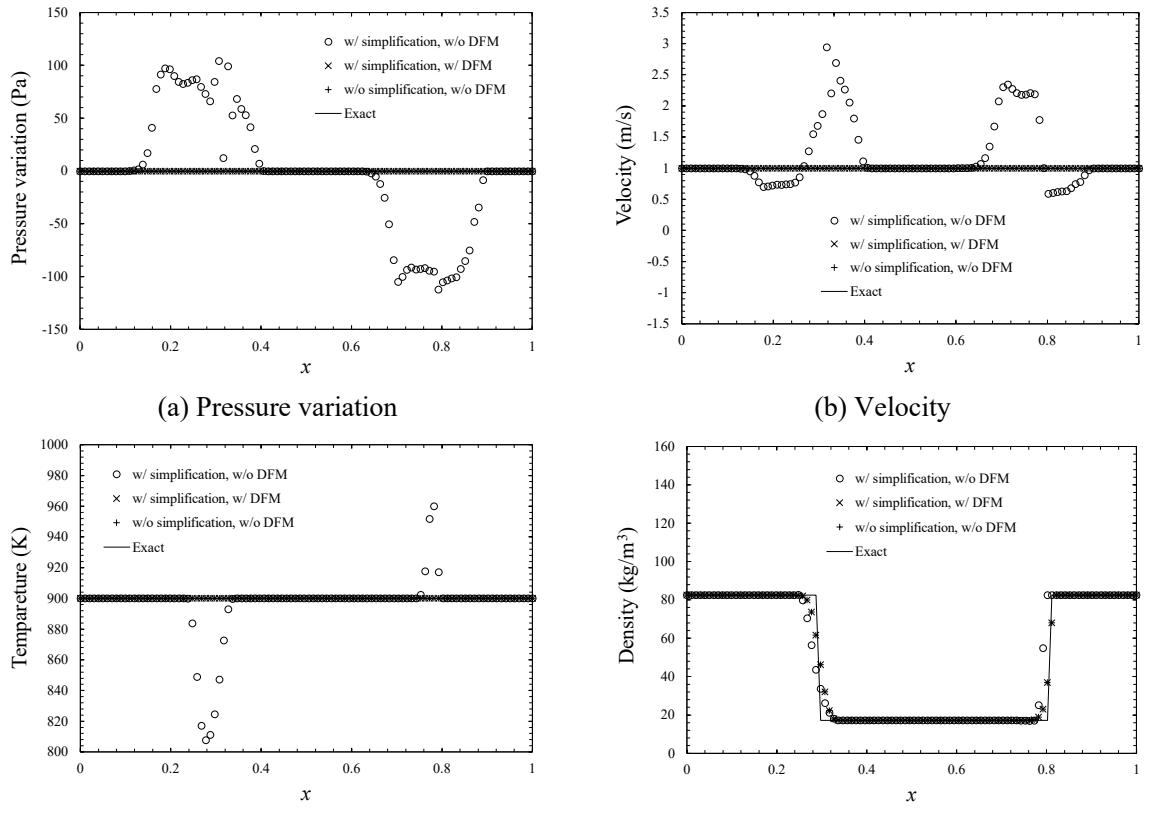

(a) Pressure variation (b) Velocity

(c) Temperature (d) Density

Figure 2.3. Profiles of a one-dimensional advection of material interface of *n*-dodecane and propylene at $t = 5.0 \times 10^{-2}$ s.

Figure 2.4 demonstrates the convergence history during inner iterations of dual time-stepping at physical $t = 5.0 \times 10^{-2}$ s. When using the original matrix $\boldsymbol{M}$, the residual dropped to ten orders of magnitude within 50 inner iterations. The errors caused by the simplified matrix $\boldsymbol{M}_{\mathrm{s}}$ as Eqs. (2.67a) and (2.67b) not only induced numerical oscillations but also caused the convergence in the inner iteration to deteriorate. The DFM improves convergence to the same order as that obtained using the original matrix $\boldsymbol{M}$.

The conservation errors using DFM were evaluated to confirm the reliability of the proposed method. A conservation-error analysis was conducted for the mass, momentum, and total energy for a one-dimensional advection. The conservation errors at time step *n* are defined as follow:

$$\varepsilon^n = \left| \frac{\sum_{j=1}^{j_{\max}} (W^n - W^0)}{\sum_{j=1}^{j_{\max}} W^0} \right|. \tag{2.74}$$

Here, W^0 is the conservative variables $[\rho, \rho u, E]^{\mathrm{T}}$ at the initial condition.

Figure 2.5 shows the conservation errors on a one-dimensional advection of the *n*-dodecane interface and material interface of *n*-dodecane and propylene. For advection of the *n*-dodecane interface, Figure 2.5(a) shows that the conservation error gradually increases with physical time, reaching 2.1% for total energy error and 2.3% for mass and momentum error at $t = 0.1$ s. In the case of material interface advection, the trend

of increasing conservation errors is the same as those in *n*-dodecane interface; however, the errors for all conserved quantities are smaller than those in the *n*-dodecane interface advection problem because of the smaller spatial variations in density and enthalpy that cause the errors. While the conservation error due to the DFM should be discussed with the numerical results in each computational condition, Abgrall and Karni [8] showed that the DFM reproduced reasonable results even for flows with strong shock waves. In this study, I simulated the natural and mixed convection of binary and multicomponent fluid flows near the critical point. The conservation errors come out to be the same as in this section.

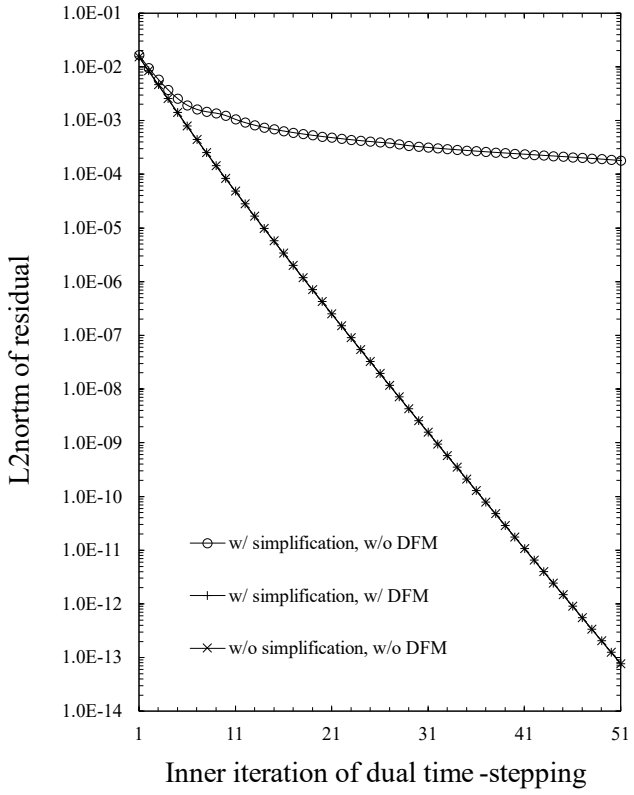

Figure 2.4. Comparison of convergence history during inner iterations of dual time-stepping at physical $t = 5.0 \times 10^{-2}$ s.

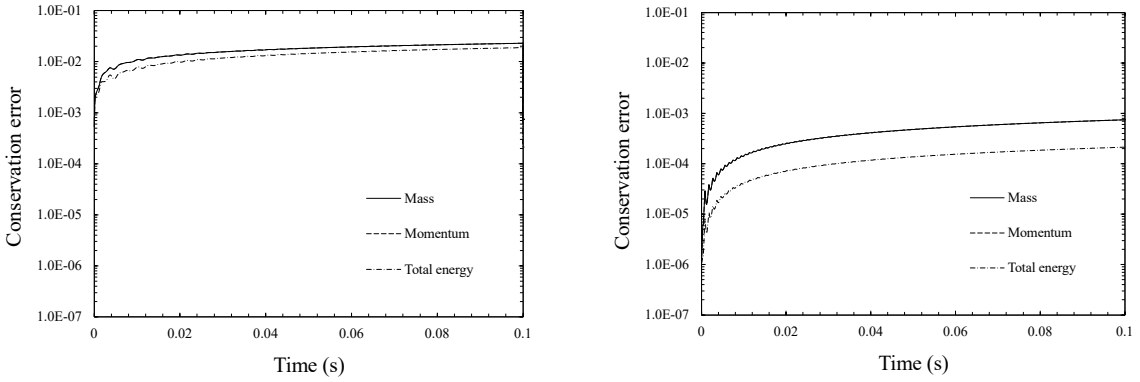

(a) *n*-dodecane interface

(b) material interface between *n*-dodecane and propylene

Figure 2.5. Conservation errors for a one-dimensional advection.

The influence of conservation errors because of the DFM on the spatial accuracy is evaluated. For a computational grid with N_1 and N_2 cells in one direction with errors E_1 and E_2 respectively, the spatial accuracy $\mathcal{O}(\Delta x^n)$ can be written as follows:

$$\mathcal{O}(\Delta x^n) = \ln\left(\frac{E_2}{E_1}\right) \ln\left(\frac{N_1}{N_2}\right). \tag{2.75}$$

Where the temperature error (L2 norm) is expressed by the difference from the exact solutions as follows:

$$\text{Error} = \frac{1}{N^2}\sqrt{\sum_{j=1}^{jmax}(T_j - T_{e,j})^2}. \tag{2.76}$$

Where N indicates the total grid number. Table 2.1 and Figure 2.6 shows the temperature error (L2 norm) with respect to the computational grid number on the one-dimensional advection of the *n*-dodecane interface. When the number of computational grids is small, the spatial accuracy is degraded because of the conservation error by DFM and is smaller than the theoretical accuracy of 2. As the grid number increases, the conservation error by DFM decreases [10], and the spatial accuracy converges to the theoretical accuracy.

Table 2.1. Error (L2 norm) with respect to the computational grid number

Computational grid number	Error (L2 norm)	$\mathcal{O}(\Delta x^n)$
50	1.65E-02	
100	4.82E-03	1.80
200	1.37E-03	1.82
400	3.81E-04	1.86
800	1.00E-04	1.93

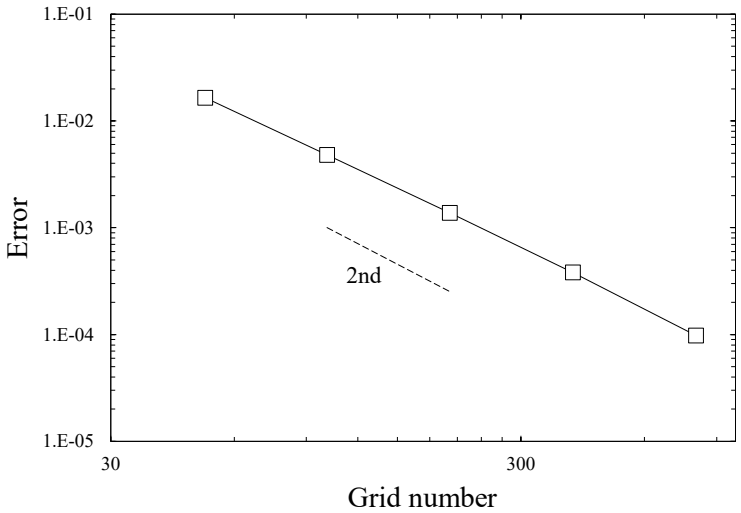

Figure 2.6. Temperature error (L2 norm) with respect to the computational grid number on the one-dimensional advection of the *n*-dodecane interface.

2.4.2 Two-dimensional advection of methane in the *n*-dodecane atmosphere

An advection problem of binary hydrocarbons is carried out to examine the behavior of the present method for multicomponent flow, extending to a two-dimensional Euler problem. I consider a system that uses the original matrix $\boldsymbol{M}$ without simplification. A schematic of this simulation is shown in Figure 2.7. The temperatures of methane and *n*-dodecane are 900 K and 400 K, respectively, and a temperature jump exists at the material interface. The pressure is set to 6.0 MPa, which is above the critical pressure of *n*-dodecane and methane. The Mach number based on the initial velocity is 5.2×10^{-3} in *n*-dodecane. This situation is similar to the hydrocarbon flow in the regenerative cooling channel. The grid has 100×100 points in the *x*- and *y*-directions. The gravitational force in the source term was ignored in this section. The CFL number in the physical time step was set to 1.0 and $\delta\tau/\delta t$ was less than unity. The inner iteration of dual time-stepping was set to 50 to decrease the residual by 10 orders of magnitude. Comparisons were made between the results without DFM and those with DFM.

Figure 2.8 shows the results for the pressure, velocity in the *x*-direction, and temperature at $t = 10^{-4}$ s without the DFM. In this configuration, the initial uniform pressure and velocity should be maintained. However, the results indicate that spurious oscillations cannot be avoided at the material interface where the temperature is non-uniform. As shown in Figures 8(a) and 8(b), the pressure and velocity equilibria cannot be maintained near the interface. Note that, although not shown here, spurious oscillations do not occur at the material interface if the temperature is uniform, as already shown in Section 2.3.1.

Figure 2.9 shows the results of the DFM for the same test case, as shown in Fig. 2.8. In contrast to the results in Fig. 2.8, the pressure and velocity equilibria were maintained at the interface. Despite the material interface and temperature jump, the present method demonstrates the robustness and multidimensional capability of the binary fluid flow problem.

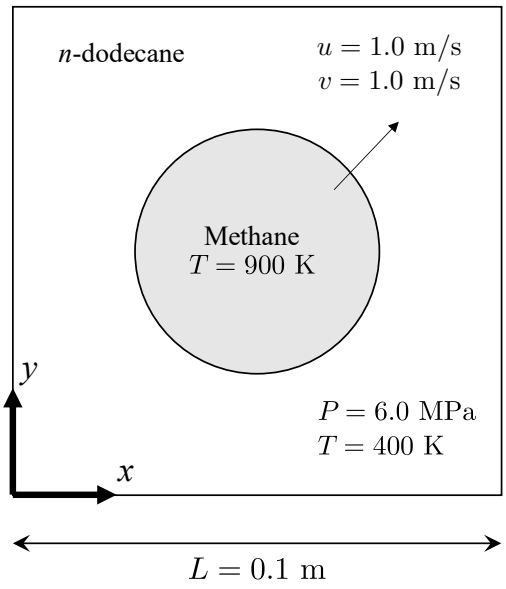

Figure 2.7. Schematic of two-dimensional advection problem.

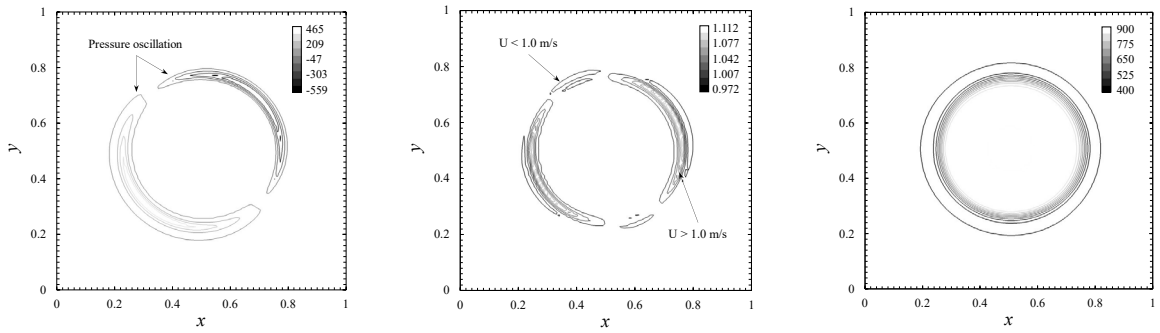

(a) Pressure variation (Pa) (b) Velocity (m/s) (c) Temperature (K)

Figure 2.8. Two-dimensional advection at $t = 10^{-4}$ s without the DFM.

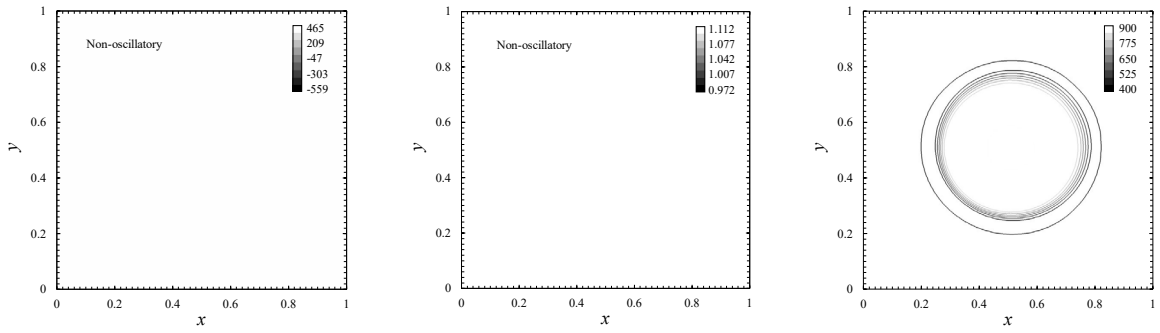

(a) Pressure variation (Pa) (b) Velocity (m/s) (c) Temperature (K)

Figure 2.9. Two-dimensional advection at $t = 10^{-4}$ s with the DFM.

2.4.3 Natural convection of *n*-dodecane in a square cavity

A natural convection problem under transcritical conditions was simulated to show the further capability of the present method at very low Mach number conditions. Figure 2.10 shows a schematic of the two-dimensional natural convection in a square cavity. Nonslip and isothermal conditions were imposed for the right and left sides of the cavity. The temperatures of the right and left sides were 445 K and 885 K, respectively, which were below and above the critical temperature. The nonslip and adiabatic wall conditions were imposed on the top and bottom of the cavity. The initial fluid temperature was 445 K, and the initial fluid pressure was set to 2.1 MPa. The initial density is set to the standard density. The source term in Eq. (2.1) was treated explicitly in the natural convection flow problem and the following pyrolytic reaction flow problem. I simulated the natural convection of *n*-dodecane for Rayleigh numbers of 10^4, 10^5, and 10^6, which is a low Mach number condition of less than 1.0×10^{-4}. The grids used here are 41×41(coarse), 201×201(medium), and 301×301(fine). The fluid was *n*-dodecane in the entire computational domain, and the pyrolysis of *n*-dodecane was ignored in these cases. In these cases, the physical time step was set to 10^{-5} at all grid points to compare the flow field at the same physical time, and $\delta\tau/\delta t$ was less than unity.

Figure 2.11 displays the convergence history for the natural convection of supercritical *n*-dodecane using a 41×41 grid system. The residuals decrease by four orders of magnitude within 15 iterations in all conditions, even under low Mach number conditions.

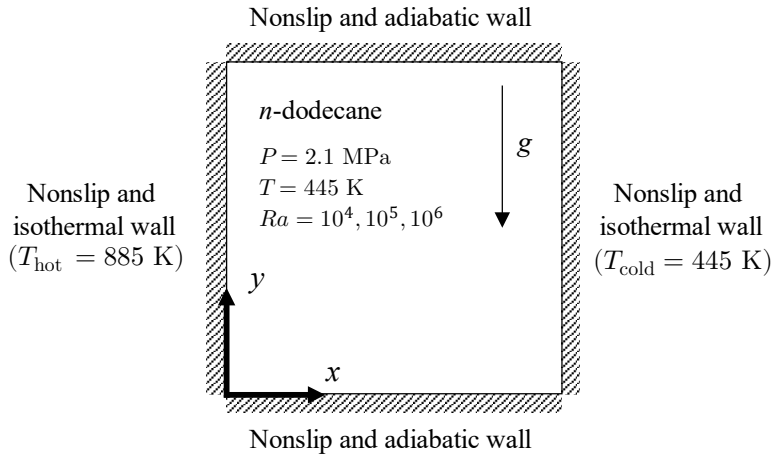

Figure 2.10. Schematic of two-dimensional natural convection of *n*-dodecane under a transcritical condition.

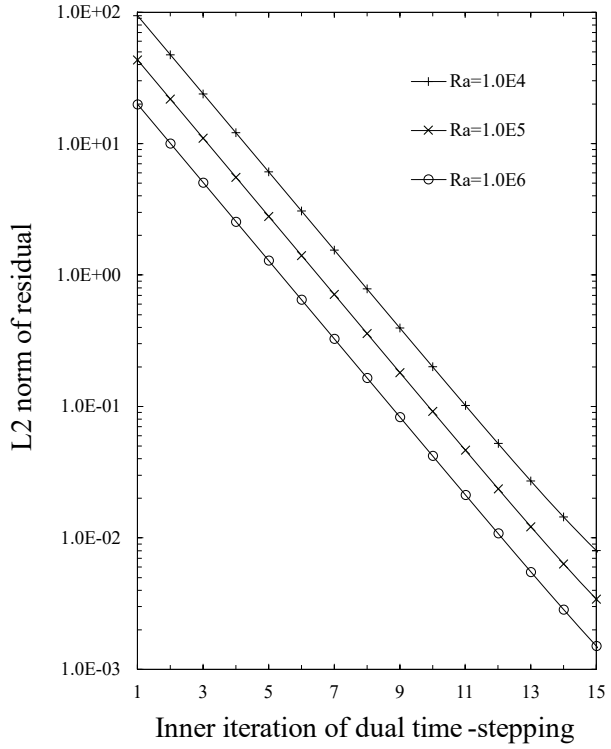

Figure 2.11. Convergence history of the DTS inner iterations at three Rayleigh number.

Figure 2.12 shows the contours of temperature, density, and pressure for the results with and without DFM at $t = 0.05$ s. The fluid temperature increased due to heat conduction at the left side of the cavity, whereas the fluid density decreased because of thermal expansion. The heated fluid forms a thermal plume by the buoyancy effect on the left side of the cavity, whose density is 12 times smaller than that in the initial fluid. The spatial variation of the density in the cavity was quite large because of the temperature condition crossing the pseudo-boiling line. The results with the DFM exhibit a reasonable pressure distribution. In contrast, the result without the DFM exhibits a large pressure oscillation. The pressure oscillation occurs at the transcritical interface only in the result without the DFM owing to the large spatial variation of the density.

The pressure oscillation affects the formation of the thermal plume, which results in a difference in the temperature and velocity distributions.

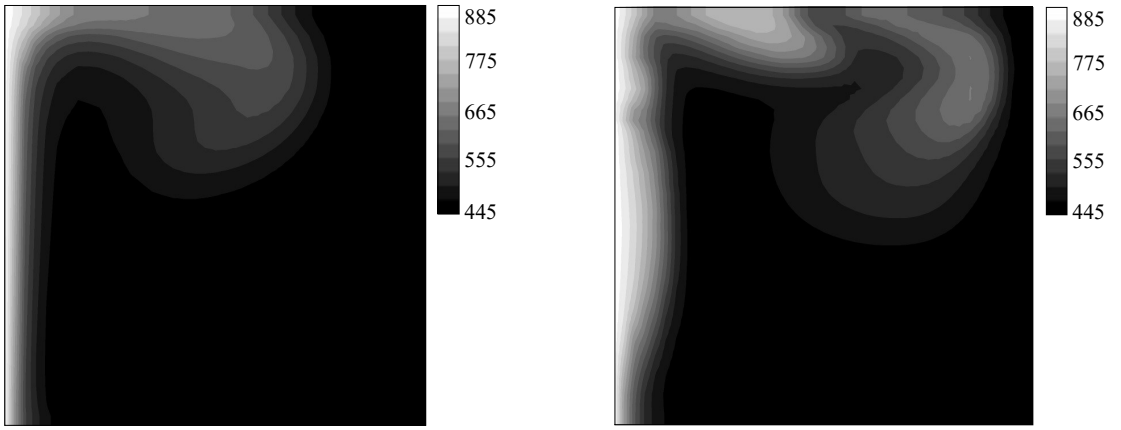

with DFM without DFM

(a) Temperature (K)

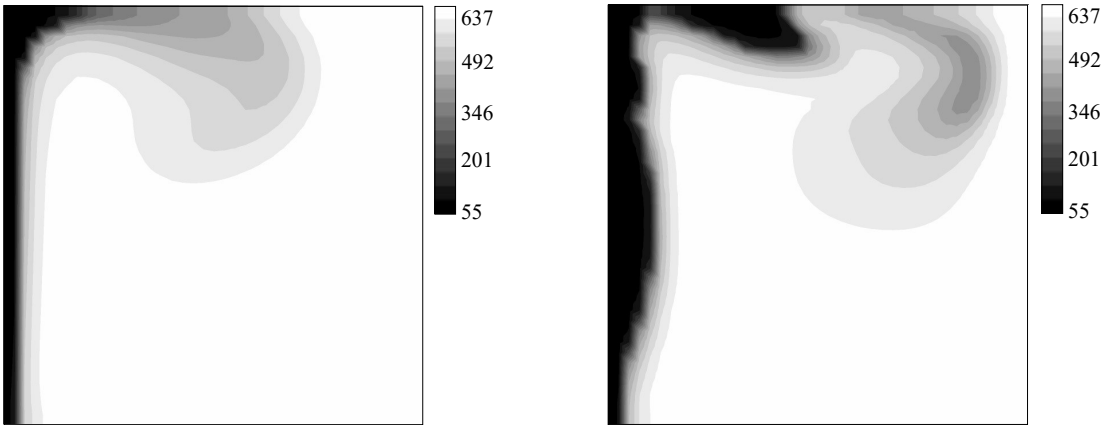

with DFM without DFM

(b) Density (kg/m^3)

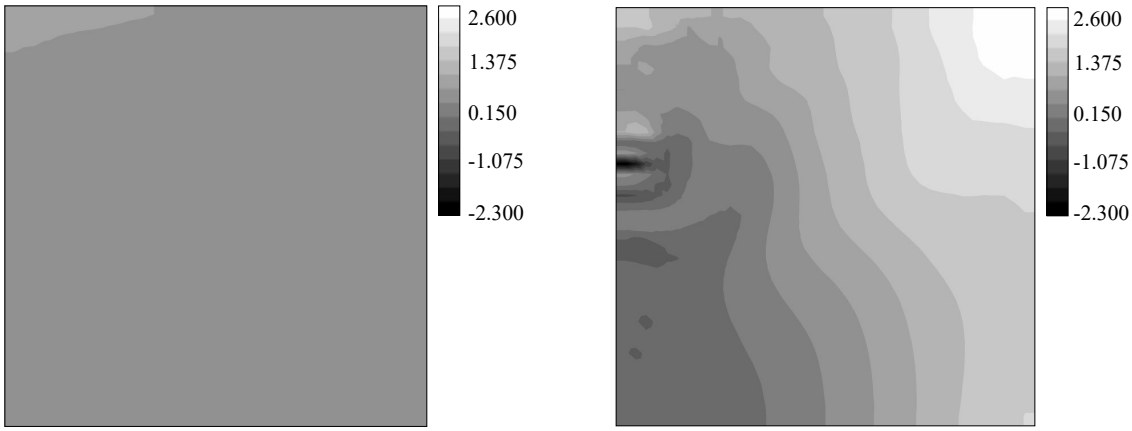

with DFM without DFM

(c) Pressure variation (Pa)

Figure 2.12. Numerical results of *n*-dodecane natural convection using 41×41 grid at $Ra = 10^6$ and $t = 0.05$ s.

Figure 2.13 shows the velocity profiles in the *x*-direction for each grid system at $x = 0.1$. For the DFM results, a smooth profile is obtained in all grid systems. Although the velocity profiles without DFM using fine and medium grids are similar to the results with DFM, the profile without DFM using a coarse grid is clearly different from the other results. The oscillated velocity profile is related to the pressure distribution without the DFM in Figure 2.12(c). Despite the absence of DFM, the results using fine and medium grids showed similar velocity profiles to those with DFM, because the finer grid enabled the capture of the spatial gradient of density, which induced numerical oscillations.

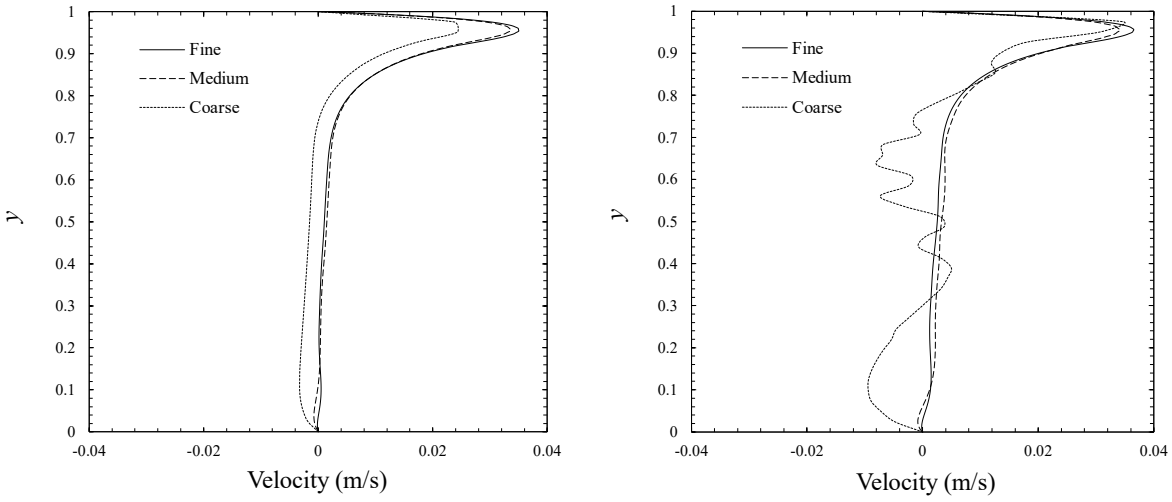

with DFM　　without DFM

Figure 2.13. Velocity profiles in the *x*-direction for each grid system at $x = 0.1$, $Ra = 10^6$, and $t = 0.05$ s.

2.4.4 *N*-dodecane flows with pyrolysis reaction in a heated circular pipe

N-dodecane flows with a pyrolysis reaction under transcritical conditions are simulated in a heated circular pipe as a practical flow problem for multicomponent fluid flows and transcritical flows. A simplified preconditioning matrix $\boldsymbol{M}_{\mathrm{s}}$ was used in all cases of this section because the implementation for multi-component flows was easier than the original preconditioning matrix. Figure 2.14 shows a schematic of a heated circular pipe flow, assuming a two-dimensional axisymmetric flow. The computational grid consisted of 201×71, which had a heating section of 220 mm and two adiabatic sections of 101 mm and 185 mm. The pipe radius is 1.975 mm. The inlet mass flow rate, inlet temperature, and outlet pressure are 60 g/min, 623 K, and 2.0 MPa, respectively. Isothermal conditions at 1023 K were imposed in the heating section, which was above the critical temperature. Mach number based on the inlet flow is 7.3×10^{-4}. The gravitational force in the source term was ignored in this section. *N*-dodecane decomposes by pyrolysis above 800 K, resulting in a multicomponent flow in the heating channel by the decomposed components. The axisymmetric and endothermic energy terms were added to the fundamental equation in Eq. (2.1). The physical time step was set to 10^{-5}. In this section, whereas $\delta\tau$ is slightly higher than δt near the axis, the results obtained by the dual-time stepping coincided with the converged results without the dual-time stepping. Therefore, $\delta\tau/\delta t >$

1 does not affect the converged solutions. The inner iteration of dual time-stepping was set to 10 to decrease the residual by 3 orders of magnitude. The production rate and endothermic energy were estimated using a zero-dimensional pyrolysis reaction modeling method, which considers 16 decomposed components (H_2, CH_4, C_2H_4, C_2H_6, C_3H_6, C_3H_8, 1-C_4H_8, *n*-C_4H_{10}, 1-C_5H_{10}, *n*-C_5H_{12}, *n*-C_6H_{14}, *n*-C_7H_{16}, *n*-C_8H_{18}, *n*-C_9H_{20}, *n*-$C_{10}H_{22}$, and *n*-$C_{11}H_{24}$). The zero-dimensional pyrolysis reaction modeling methodis presented in detail in Chapter 3. Table 2.2 shows the critical density, temperature, and pressure of the decomposed components calculated using REFPROP.

Figure 2.15 shows the contours of temperature, density, and mass fraction of unreacted *n*-dodecane with and without DFM in the heating section and the subsequent adiabatic section, scaling to 1/10 in the axial direction. The temperature was increased by the heated wall, and the thermal boundary developed along the flow channel. The mass fraction of unreacted *n*-dodecane decreased in the high-temperature region due to the pyrolysis reaction. The density changes rapidly near the heated wall because of the transition to the supercritical state and the decomposed lower hydrocarbon. The fluid temperature in the boundary layer was locally below the inlet temperature in the numerical results without the DFM. As discussed in Section 2.3.1, pressure and temperature oscillations at the material interface are inevitable when using a simplified preconditioning matrix. The temperature distribution affected the pyrolysis reaction and the mass fraction distribution. Therefore, spurious oscillation is a critical issue for actual flow problems in pyrolysis and transcritical flows. On the other hand, when applying the DFM, converged results without any spurious oscillations were obtained. DFM is effective in avoiding catastrophic situations caused by numerical errors, even when using a simplified preconditioning matrix.

The outlet conversion rates of *n*-dodecane simulated by the present method were compared with the experimental data measured in the experimental apparatus developed by Kurihara [29] under different wall temperature conditions. Table 2.3 lists the computational and experimental conditions used. The inlet fluid temperature was slightly higher than that in the previous case. The radius and length of the heating pipe have the same configuration, as shown in Fig. 2.14. The outlet conversion rate at a position 54 mm behind the heating section was compared with the experimental data. Three grid systems were used as a grid convergence study in fine (201×101), medium (201×71), and coarse (201×41). The grid convergence for the axial direction was checked in Chapter 3. The errors in the outlet temperature between 201 and 501 for the axial direction were less than 0.5%.

Figure 2.16 shows a comparison of the conversion rates between the simulation results and the experimental data. The error bars in the experimental data are defined as values within three standard deviations of the five experiments. Although the results of the coarse grid underestimate the experimental data for all wall temperature conditions, the results for the medium and fine grids are within the error bar. A comparison with experimental data demonstrates that the present method can reproduce the pyrolysis reaction of *n*-dodecane in a heated circular pipe. The proposed method enables stable simulation of hydrocarbon flows with pyrolysis, which has a drastic change in density near the heated wall.

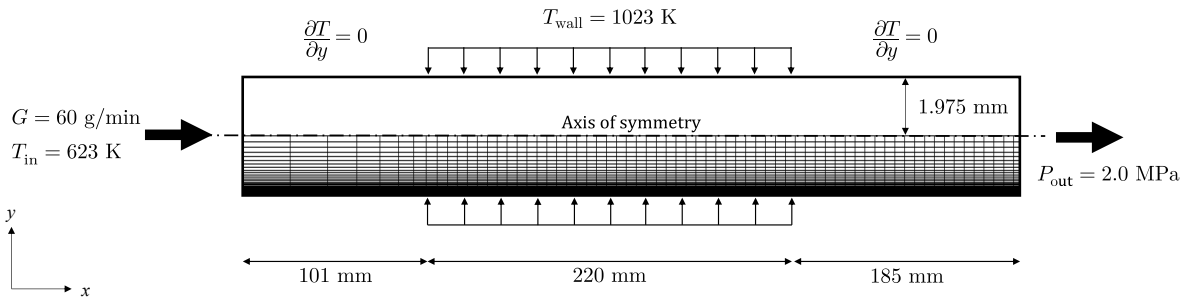

Figure 2.14. Schematic of *n*-dodecane flow in a circular pipe under a transcritical condition.

Table 2.2. Critical properties of *n*-dodecane and its decomposed components

Components	Chemical formula	p_c (MPa)	T_c (K)	ρ_c (kg/m^3)
Hydrogen	H_2	1.30	33.15	31.26
Methane	CH_4	4.60	190.6	162.7
Ethylene	C_2H_4	5.04	282.4	214.2
Ethane	C_2H_6	4.87	305.3	206.2
Propylene	C_3H_6	4.56	364.2	229.6
Propane	C_3H_8	4.25	369.9	220.5
1-butene	C_4H_8	4.01	419.3	237.9
N-butane	C_4H_{10}	3.80	425.1	228.0
1-pentene	C_5H_{10}	3.60	465.7	242.0
N-pentane	C_5H_{12}	3.37	469.7	231.6
N-hexane	C_6H_{14}	3.04	507.8	233.2
N-heptane	C_7H_{16}	2.74	540.2	233.5
N-octane	C_8H_{18}	2.48	568.7	232.0
N-nonane	C_9H_{20}	2.28	594.6	232.1
N-decane	$C_{10}H_{22}$	2.10	617.7	233.3
N-undecane	$C_{11}H_{24}$	1.99	638.8	236.8
N-dodecane	$C_{12}H_{26}$	1.82	658.1	226.5

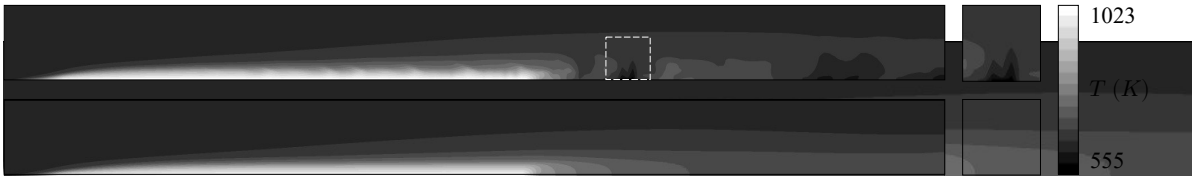

(a) Temperature (K), up: without DFM, down: with DFM.

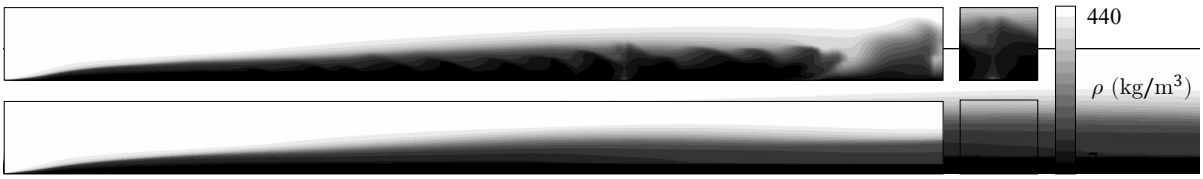

(b) Density (kg/m^3), up: without DFM, down: with DFM.

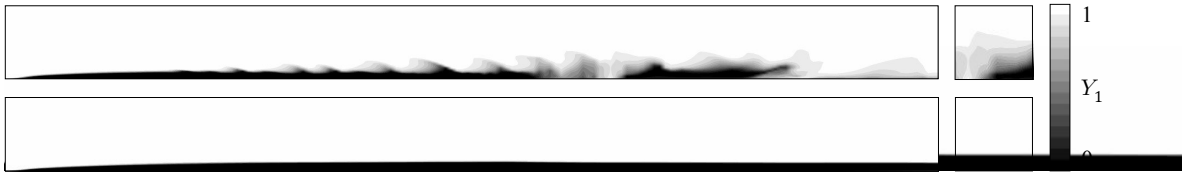

(c) Mass fraction of unreacted *n*-dodecane, up: without DFM, down: with DFM.

Figure 2.15. Numerical results of the *n*-dodecane flows with pyrolysis under a transcritical condition.

Table 2.3. Computational and experimental conditions for *n*-dodecane flows with pyrolysis reaction

Pressure (MPa)	Mass flow rate (g/min)	Inlet temperature (K)	Wall temperature (K)
6.0	50	695.10	823.15
		690.70	848.15
		695.62	873.15
		696.02	923.15
		699.14	973.15
		696.34	998.15

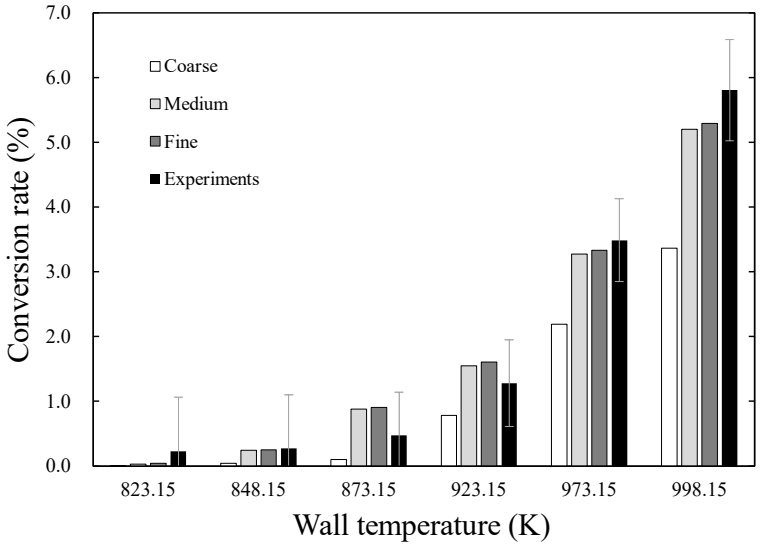

Figure 2.16. Numerical results of conversion rates with experimental data.

2.5 Conclusions

A double-flux model coupled with the preconditioning method was developed to simulate multicomponent fluid flows in transcritical conditions. The original preconditioning matrix and simplified preconditioning matrix were used for low Mach-number flows, such as natural and mixed convective flows, where the simplified preconditioning matrix omitted the partial derivatives with respect to mass fractions. The thermophysical properties were calculated using the Helmholtz free-energy EoS defined in REFPROP. Amagat's mixture law and Wilke's mixing law were used to determine the thermophysical properties of the mixture. First, in a one-dimensional Euler system, I derived the temporal variation of the unknown variables in the case of a single fluid interface for different temperatures, and also at the material interface for a uniform fluid temperature. The temporal variation in the preconditioned system indicated that the uniform mass fraction and temperature in the double-flux approach improved the pressure and temperature equilibrium if the simplified preconditioning matrix was used, while the original preconditioning matrix was satisfied by the uniform temperature assumption. One- and two-dimensional advection problems with and without the double flux treatment were simulated to demonstrate the numerical oscillations for the flows at different temperatures or binary fluids. The present method enabled the simulation of the binary fluid flow and the fluid flow with a large temperature difference without spurious oscillations, although the double flux treatment affected the conservation of not only the total energy but also the mass and momentum, owing to the preconditioning matrix. The numerical simulation of natural convective flows in a square cavity demonstrated the capability of a very low Mach-number flow problem with a large temperature difference crossing the pseudo-boiling line under supercritical pressure conditions. Finally, as a practical problem, *n*-dodecane flows with the pyrolysis reaction in a heated circular tube were simulated assuming axisymmetric conditions. Pyrolysis occurred near the heating wall, and the density changed rapidly because of the transition to the supercritical state and the decomposed lower hydrocarbon in the thermal boundary. The numerical results without any spurious oscillations were obtained using the proposed method. A comparison with

experimental data showed that the present method could reproduce the pyrolysis reaction of *n*-dodecane in a heated circular pipe. These results indicate that the double-flux model with the preconditioning method is a useful approach to reproduce the temperature and velocity profiles without spurious oscillations because they have a crucial effect on the pyrolysis reaction in thermal hydrocarbon flows.

References

1. J. Sierra-Pallares, D. L. Marchisio, M. T. Parra-Santos, J. García-Serna, F. Castro, M. J. Cocero, “A computational fluid dynamics study of supercritical antisolvent precipitation: Mixing effects on particle size,” AIChE journal, 58(2), (2012), 385–398.
2. S. Tomioka, T. Hiraiwa, T. Saito, K. Kato, M. Kodera, K. Tani, “System analysis of a hydrocarbon-fueled RBCC engine applied to a TSTO launch vehicle,” Transaction of Japan Society for Aeronautical and Space Sciences, 12 (29), (2014), 91–99.
3. R. Abgrall, “How to prevent pressure oscillations in multicomponent flow calculations: A quasi conservative approach,” Journal of Computational Physics, 125, (1996), 150-160.
4. E. Johnsen, T. Colonius, “Implementation of WENO schemes in compressible multicomponent flow problems,” Journal of Computational Physics, 219, (2006), 715-732.
5. T. Nonomura, S. Morizawa, H. Terashima, S. Obayashi, K. Fujii, “Numerical (error) issues on compressible multicomponent flows using a high-order differencing scheme: weighted compact nonlinear scheme,” Journal of Computational Physics, 231, (2012), 3181–210.
6. H. Terashima, M. Koshi, “Approach for simulating gas-liquid-like flows under supercritical pressures using a high-order central differencing scheme,” Journal of Computational Physics, 231, (2012), 6907–6923.
7. C. Pantano, R. Saurel, T. Schmitt, “An oscillation free shock-capturing method for compressible van der Waals supercritical fluid flows,” Journal of Computational Physics, 335, (2017), 780–811.
8. R. Abgrall, S. Karni, “Computations of compressible multifluids,” Journal of Computational Physics, 169, (2001), 594–623.
9. G. Billet, R. Abgrall, “An adaptive shock-capturing algorithm for solving unsteady reactive flows,” Computers & Fluids, 32 (10), (2003), 1473–1495.
10. P. C. Ma, Y. Lv, M. Ihme, “An entropy-stable hybrid scheme for simulations of transcritical real-fluid flows,” Journal of Computational Physics, 340, (2017), 330–357.
11. J.H. Bae, J.Y. Yoo, H. Choi, “Direct numerical simulation of turbulent supercritical flows with heat transfer,” Physics of Fluids, 17, (2005), 105104.
12. H. Nemati, A. Patel, B.J. Boersma, R. Pecnik, “Mean statistics of a heatedturbulent pipe flow at supercritical pressure,” International Journal of Heat and Mass Transfer, 83, (2015), 741–752.
13. E. Turkel, “Preconditioning methods for solving the incompressible and low speed compressible equations,” Journal of Computational Physics, 72, (1987), 277–298.
14. Y.-H. Choi, C.L. Merkle, “The application of preconditioning in viscous flows,” Journal of Computational Physics, 105, (1993), 207–223.
15. J.M. Weiss, W.A. Smith, “Preconditioning applied to variable and constant density flows,” AIAA Journal, 33, (1995), 2050–2056.
16. S. Yamamoto, “Preconditioning method for condensate fluid and solid coupling problems in general curvilinear coordinates,” Journal of Computational Physics, 207, (2005), 240–260.

17. J. A. Housman, C. C. Kiris, M. M. Hafez, “Time-derivative preconditioning methods for multicomponent flows. Part I: Riemann problems,” Journal of Applied Mechanics, 76, (2009), 021210.
18. F.R. Menter, “Two-equation eddy-viscosity turbulence models for engineering applications,” AIAA Journal, 32(8), (1994), 598–1605.
19. S. Kawai, Y. Oikawa, “Turbulence modeling for turbulent boundary layers at supercritical pressure: a model for turbulent mass flux,” Flow, Turbulence and Combustion, 104, (2020), 625–641.
20. S. Venkateswaran, M. Deshpande, C.L. Merkle, “The application of preconditioning to reacting flow computations,” Proceedings of the 12th AIAA Computational Fluid Dynamics Conference, (1995), AIAA Paper 95-1673.
21. H. Meng and V. Yang, “A unified treatment of general fluid thermodynamics and its application to a preconditioning scheme,” Journal of Computational Physics, 189, (2003), 277–304.
22. E.W. Lemmon, I.H. Bell, M.L. Huber, M.O. McLinden, “NIST standard reference database 23: Reference fluid thermodynamic and transport properties-REFPROP,” Version 10.0, National Institute of Standards and Technology, (2018).
23. D. Li, S. Venkateswaran, J. W. Lindau, C. L. Merkle, “A unified computational formulation for multi-component and multi-phase flows,” Proceedings of the 43rd AIAA Aerospace Sciences Meeting and Exhibit, (2005), AIAA-2005-1391.
24. D. R. Caudwell, J. P. M. Trusler, V. Vesovic, W. A. Wakeham, “The viscosity and density of *n*-dodecane and *n*-octadecane at pressures up to 200 MPa and temperatures up to 473 K,” International Journal of Thermophysics 25 (5), (2004), 1339–1352.
25. T. S. Khasanshin, A. P. Shchemelev, “Sound velocity in liquid *n*-alkanes,” High Temperature, 39, (2001), 60–67.
26. C. R. Wilke, “A viscosity equation for gas mixtures,” Journal of Chemical Physics, 18, (1950), 517–519.
27. F. Herning, and L. Zipperer, “Beitrag zur Berechnung der Zähigkeit Technischer Gasgemische aus den Zähigkeitswerten der Einzelbestandteile,” Gas- und Wasserfach, 79 (1936).
28. P. Jenny, B. Müller, H. Thomann, “Correction of conservative Euler solvers for gas mixtures,” Journal of Computational Physics, 132, (1997), 91–107.
29. K. Kurihara, T. Miyaura, Y. Daimon, S. Tomioka, “Study on chemical heat sink of *n*-dodecane under supercritical condition,” Proceedings of 32nd ISTS & NSAT, (2019), 2019–i-13.

Chapter 3
Pyrolysis reaction modeling and flow simulation of supercritical hydrocarbon

3.1 Introduction

Reusable launch vehicles have been proposed by the Japan Aerospace Exploration Agency, and the use of the rocket-based combined-cycle engine incorporating a conventional rocket engine into the scramjet duct is planned for this purpose [1]. The regenerative cooling system using hydrocarbon fuels is a crucial technology for preventing thermal damage to engine systems. Since hydrocarbon fuel can be stored at room temperature and has a higher density than has liquid-hydrogen fuel, the tank volume can be small, and it is easy to handle. Although hydrocarbon fuel has the preferred features for fuel in aerospace aircraft, it has the disadvantage of small heat absorption due to a low specific heat capacity. Therefore, the use of an additional heat sink brought about by the endothermic pyrolysis reaction to improve the cooling capacity is being considered. To design a reliable and efficient regenerative cooling system, it is necessary to establish a numerical method to understand the pyrolysis characteristics and hydrocarbon flows in the cooling channel.

Ward et al. [2] developed the proportional-product-distribution model of pyrolysis reaction and simulated it for *n*-decane and *n*-dodecane in a circular pipe under supercritical-pressure conditions. Jiang et al. [3] developed a pyrolysis reaction model based on their experiments using tubes of various lengths. The reaction model included 18 chemical species and 24 elementary reactions. Zhu et al. [4] performed pyrolysis experiments on *n*-decane under supercritical-pressure conditions and developed a global reaction model including 18 components using experimental data with a conversion rate of less than 13%. To date, detailed reaction models considering many secondary reactions or decomposed components have been proposed, and they have been consistent with experimental data; however, in practice, evaluation of the accuracy and limitations of the simple pyrolysis reaction model is still crucial. In previous research [5], I developed an *n*-octane pyrolysis reaction model that does not require any preliminary experiments, which is based on zero-dimensional-reaction simulations by Cantera [6] and the KUCRS [7] model. Aviation*n*-jet fuels such as kerosene consist of a mixture of several hydrocarbons, and the main components include not only straight-chain hydrocarbons such as *n*-octane and *n*-

dodecaned but also cyclic hydrocarbons. These hydrocarbons respectively occur under different pyrolysis reactions, and the thermophysical properties are not the same. Although the pyrolysis reactions and thermophysical properties are expected to have a significant effect upon the flows in the cooling channel, the difference in the flow among these hydrocarbons has not been fully clarified.

In this study, I extend previous pyrolysis reaction model [5] for *n*-octane to *n*-dodecane. I perform zero-dimensional reaction simulations of *n*-dodecane using Cantera [6] and the JetSurf model proposed by Wang et al. [8] and define the reaction equation, reaction rate constant, and endothermic energy. The pyrolysis reaction model incorporates numerical method [9] based on the preconditioning method for solving the compressible Navier–Stokes equations using the Reference Fluid Thermodynamic and Transport Properties Database (REFPROP) [10]. I simulate the supercritical *n*-dodecane flows in a heated circular pipe with pyrolysis, assuming an axisymmetric flow. The numerical results are compared with those of experiment to validate the present numerical methods. The simulated results were compared with those for *n*-octane to clarify the effects of different thermophysical properties upon the flows.

Nomenclature

C_p	isobaric specific heat
e	total internal energy per unit volume
H_0	endothermic energy per unit mass by pyrolysis
J	Jacobian of transformation
k	turbulent kinetic energy
p	pressure
r	radius of a circular channel
s_{Y_n}	production term of the *n*th component by pyrolysis
T	temperature
T_{w}	wall temperature in the heating section
T_{in}	inlet temperature in the test section
t	time
U_i	contravariant velocities ($i = 1, 2$)
u_i	velocities ($i = 1, 2$)
x_i	Cartesian coordinates ($i = 1, 2$)
Y_0	mass fraction of unreacted hydrocarbon
Y_n	mass fraction of the *n*th decomposed component

Greek symbol

δ_{ij}	Kronecker delta ($i, j = 1, 2$)
θ	preconditioning parameter
κ	thermal conductivity
κ_t	eddy thermal conductivity
μ	molecular viscosity
μ_t	eddy viscosity
ξ_i	general curvilinear coordinates ($i = 1, 2$)
ρ	density
τ_{ij}	viscous stress tensors ($i, j = 1, 2$)
ω	specific turbulent dissipation rate

3.2 Numerical method

3.2.1 Fundamental equations

The fundamental equations are the two-dimensional axisymmetric Navier–Stokes equations coupled with the conservation equations of turbulent kinetic energy (TKE), specific turbulent dissipation rate, and species. For the RANS turbulence model, I employ the k-ω SST+M$_\tau$ model proposed by Kawai and Oikawa [11]. The preconditioning method [12] is applied to the set of fundamental equations and can be written in the following vector form:

$$\boldsymbol{\Gamma}\frac{\partial \widehat{\boldsymbol{Q}}}{\partial t}+\frac{\partial \boldsymbol{F}_i}{\partial \xi_i}+\frac{\partial \boldsymbol{F}_{vi}}{\partial \xi_i}+\boldsymbol{S}+\boldsymbol{H}=0 \quad (i=1,2), \tag{3.1}$$

where

$$\boldsymbol{\Gamma}=\begin{bmatrix} \theta & 0 & 0 & \rho_T & 0 & 0 & 0 & \cdots & 0 \\ \theta u_1 & \rho & 0 & \rho_T u_1 & 0 & 0 & 0 & \cdots & 0 \\ \theta u_2 & 0 & \rho & \rho_T u_2 & 0 & 0 & 0 & \cdots & 0 \\ \theta h-1+\rho h_p & \rho u_1 & \rho u_2 & \rho_T h+\rho h_T & 0 & 0 & 0 & \cdots & 0 \\ \theta k & 0 & 0 & \rho_T k & \rho & 0 & 0 & \cdots & 0 \\ \theta \omega & 0 & 0 & \rho_T \omega & 0 & \rho & 0 & \cdots & 0 \\ \theta Y_0 & 0 & 0 & \rho_T Y_0 & 0 & 0 & \rho & 0 & 0 \\ \vdots & \vdots & \vdots & \vdots & \vdots & \vdots & 0 & \ddots & 0 \\ \theta Y_n & 0 & 0 & \rho_T Y_n & 0 & 0 & 0 & 0 & \rho \end{bmatrix}, \widehat{\boldsymbol{Q}}=J\begin{bmatrix} p \\ u_1 \\ u_2 \\ T \\ k \\ \omega \\ Y_0 \\ \vdots \\ Y_n \end{bmatrix},$$

$$\boldsymbol{F}_i=J\begin{bmatrix} \rho U_i \\ \rho u_1 U_i+\dfrac{\partial \xi_i}{\partial x_1}p \\ \rho u_2 U_i+\dfrac{\partial \xi_i}{\partial x_2}p \\ (e+p)U_i \\ \rho k U_i \\ \rho \omega U_i \\ \rho Y_0 U_i \\ \vdots \\ \rho Y_n U_i \end{bmatrix}, \boldsymbol{F}_{\boldsymbol{v}i}=J\frac{\partial \xi_i}{\partial x_j}\begin{bmatrix} 0 \\ \tau_{j1} \\ \tau_{j1} \\ \tau_{jk}u_k+(\kappa+\kappa_t)\dfrac{\partial T}{\partial x_j} \\ \sigma_{kj} \\ \sigma_{\omega j} \\ 0 \\ \vdots \\ 0 \end{bmatrix}, \boldsymbol{S}=-J\begin{bmatrix} 0 \\ 0 \\ 0 \\ H_{Y_0} \\ s_k \\ s_\omega \\ s_{Y_0} \\ \vdots \\ s_{Y_n} \end{bmatrix},$$

$$\boldsymbol{H}=-\frac{J}{r}\begin{bmatrix} \rho u_2 \\ \rho u_1 u_2 \\ \rho (u_2)^2 \\ (e+p)u_2-(\kappa+\kappa_t)\dfrac{\partial T}{\partial x_2} \\ \rho k u_2 \\ \rho \omega u_2 \\ \rho Y_0 u_2 \\ \vdots \\ \rho Y_n u_2 \end{bmatrix}.$$

$\boldsymbol{\Gamma}$ is a preconditioning matrix, and θ is the preconditioning parameter defined by Weiss and Smith [12]. $\widehat{\boldsymbol{Q}}$, $\boldsymbol{F}_i$, $\boldsymbol{F}_{\boldsymbol{v}i}$, $\boldsymbol{S}$, and $\boldsymbol{H}$ are the vectors of unknown primitive variables, inviscid flux, viscous flux, the source term, and the axisymmetric term, respectively. σ_{kj}, $\sigma_{\omega j}$, s_ω, and s_k are defined by Kawai and Oikawa [11]. The preconditioned flux-vector-splitting method and the preconditioning LU-SGS scheme proposed by Yamamoto [13] are employed as numerical methods in the present work.

3.2.2 Pyrolysis reaction model of hydrocarbons

I performed the zero-dimensional (0-D) isothermal-isobaric reaction considering 62 elementary reactions and 348 chemical species at 6.0 MPa using JetSurf [8] and Cantera [6]. The pyrolysis reaction of *n*-dodecane for 0.9 s was simulated at 800, 820, 900, 950, and 1000 K, respectively. Figure 3.1 shows the simulated molar fractions for the decomposed components comparing with the experimental data [14]. The white bars indicate the 0-D simulation results at the temperature of 1000 K, the conversion rate of 9.8%, and the pressure of 6.0 MPa. The black bars indicate the experimental data for the flows in a heated circular pipe at the wall temperature of 1013 K, the conversion rate of 9.8%, and the pressure of 6.0 MPa, details of which are given in reference [14]. Since all error bars expressed by the standard deviation for the five experimental data are within 0.5%, these are omitted in the Fig. 3.1. In the experiment, the sum of the molar fractions of CH_4, C_2H_4, C_2H_6, C_3H_6, and C_3H_8 exceeded 60% of the total; thus, these substances greatly influence the reaction heat and the mixture's thermophysical properties. The molar fractions of these major components were consistent with the experimental results; however, the incorporation of all elementary reactions and species considered in the 0-D reaction simulation into the flow simulation is unrealistic because of the large computational cost. Therefore, the pyrolysis reaction of *n*-dodecane in the flow simulation can be simplified into a one-step reaction as follows:

$$\begin{aligned}\mathrm{C_{12}H_{26}} \rightarrow\ & 0.003\mathrm{H_2} + 0.105\mathrm{CH_4} + 0.156\mathrm{C_2H_4} + 0.106\mathrm{C_2H_6} + 0.121\mathrm{C_3H_6} + 0.068\mathrm{C_3H_8} \\ & + 0.103\mathrm{C_4H_8} + 0.024\mathrm{C_4H_{10}} + 0.084\mathrm{C_5H_{10}} + 0.011\mathrm{C_5H_{12}} + 0.075\mathrm{C_6H_{14}} \\ & + 0.046\mathrm{C_7H_{16}} + 0.035\mathrm{C_8H_{18}} + 0.028\mathrm{C_9H_{20}} + 0.025\mathrm{C_{10}H_{22}} + 0.010\mathrm{C_{11}H_{24}}.\end{aligned} \tag{3.2}$$

The molar fractions of decomposed components are obtained by the arithmetic average value of the 0-D simulation results under each temperature condition. Note that the alkenes above C_5 are not considered for simplicity, and these molar fractions are added to those of alkanes with the same carbon number. The reaction rate of *n*-dodecane can be expressed as

$$\frac{d[\mathrm{C_{12}H_{26}}]}{dt} = -k_c[\mathrm{C_{12}H_{26}}], \tag{3.3}$$

where k_c is a reaction rate constant. Using the Alenius equation, k_c is mathematically expressed as follow:

$$k_c = A \exp\left(-\frac{E_a}{RT}\right). \tag{3.4}$$

A is the frequency factor, and E_a is the activation energy. Figure 3.2 shows the Arrhenius plots of *n*-dodecane pyrolysis reaction. The intercept and slope of this plot give the value of $A = 2.47 \times 10^{15}\ \mathrm{s}^{-1}$ and $E_a = 259.39\ \mathrm{kJ/mol}$. These values are close to the available reference values as shown in Table 3.1.

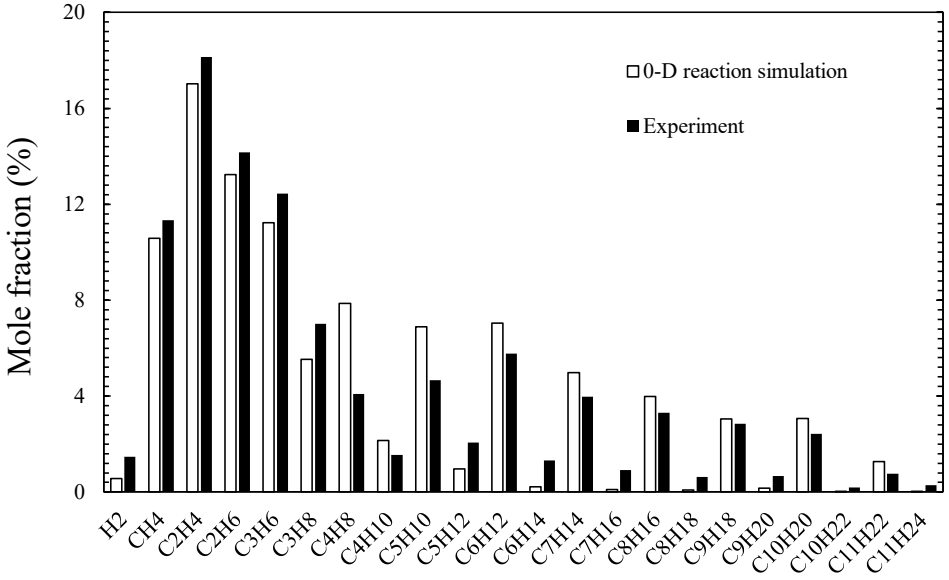

Figure 3.1. Simulated mole fraction of decomposed components with experimental data.

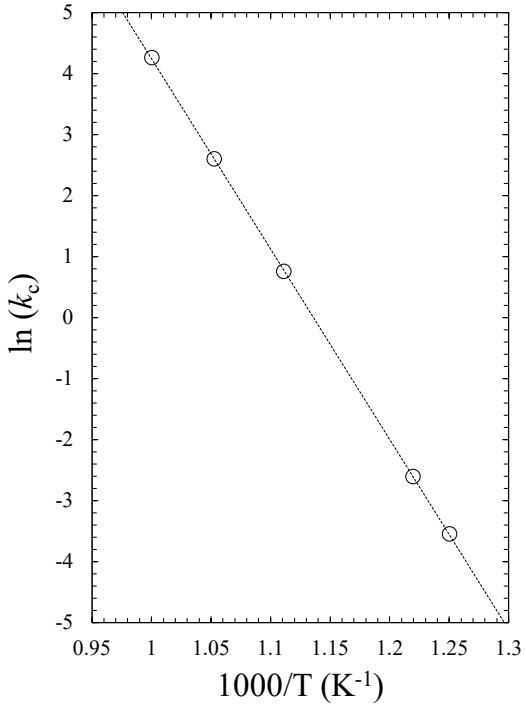

Figure 3.2. Arrhenius plot of *n*-dodecane pyrolysis reaction calculated by Cantera.

Table 3.1. Arrhenius equation parameters used in the CFD simulations

Parent fuel	Present 0-D model, $P = 6.0$ MPa and $T = 800$–1000 K		Ward et al. [2], $P = 3.45$ MPa and $T = 773$–873 K		Zhou and Crynes [15], $P = 9.2$ MPa and $T = 523$–713 K	
	E_a, kJ/mol	A, s^{-1}	E_a, kJ/mol	A, s^{-1}	E_a, kJ/mol	A, s^{-1}
N-dodecane	259.39	2.47×10^{15}	271.96	1.0×10^{16}	271.96	3.7×10^{16}

3.2.3 Thermophysical properties model for fluid mixture

The fed hydrocarbons, such as *n*-dodecane and *n*-octane, are decomposed into hydrocarbons with a smaller molecular weight above about 800 K by the pyrolysis reaction. Each component has unique thermophysical properties. In this study, I employ the Helmholtz-type equation of state defined in REFPROP to calculate each component's properties. The mixture's properties are defined by Amagat's mixture law, and the details are shown by Li et al. [16]. The mixture density, internal energy, enthalpy, and entropy are given as follows:

$$\varphi(p,T) = \sum_{i=1}^{N} Y_i \varphi_i(p,T). \tag{3.5}$$

Here, φ_i indicates the density, internal energy, enthalpy, or entropy for each component. The partial derivatives, ρ_p, ρ_T, h_p, and h_T are defined as follows:

$$\rho_p = \rho^2 \sum_{i=1}^{N} \frac{Y_i}{\rho_i^2} \frac{\partial \rho_i}{\partial p}, \tag{3.6a}$$

$$\rho_T = \rho^2 \sum_{i=1}^{N} \frac{Y_i}{\rho_i^2} \frac{\partial \rho_i}{\partial T}, \tag{3.6b}$$

$$h_p = \sum_{i=1}^{N} Y_i \frac{\partial h_i}{\partial p}, \tag{3.6c}$$

$$h_T = \sum_{i=1}^{N} Y_i \frac{\partial h_i}{\partial T}. \tag{3.6d}$$

Figure 3.3 compares the densities among pure *n*-dodecane, pure *n*-octane, completely decomposed *n*-dodecane, and completely decomposed *n*-octane at 6.0 MPa. The maximum difference for the pure fed hydrocarbons is 200 kg/m^3 near 700 K; with increasing temperature, this difference becomes small. The decomposed components' mixture densities are much smaller than the density of the pure fed hydrocarbons, reaching less than 30 kg/m^3 from 800 to 1000 K. The species and proportion of decomposed components are

similar between *n*-dodecane and *n*-octane; therefore, the difference of density between completely decomposed *n*-dodecane and *n*-octane is less than 2.0 kg/m^3 at 900 K.

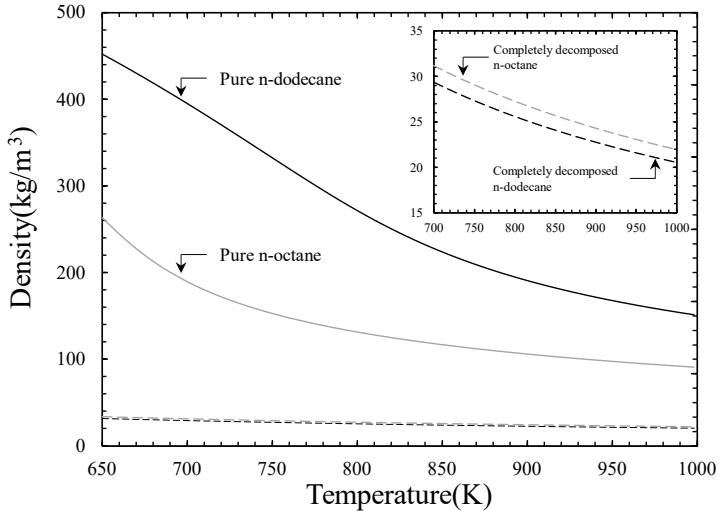

Figure 3.3. Comparison of the densities among pure *n*-dodecane, pure *n*-octane, completely decomposed *n*-dodecane, and completely decomposed *n*-octane at 6.0 MPa.

3.3 Numerical results and discussion

3.3.1 Supercritical *n*-dodecane flows in a heated circular pipe

Figure 3.4 shows a schematic of the test section used to measure the supercritical *n*-dodecane flows. The test section consists of an adiabatic section of 101 mm, a heating section of 220 mm, and another adiabatic section of 56 mm. The flow path is a stainless-steel pipe with an inner diameter of 3.95 mm. A heater is connected around the pipe in the heating section. The outer-wall temperature of the pipe in the heating section is measured with a thermocouple and controlled to a constant value to realize an isothermal-wall condition. The *n*-dodecane is heated to the temperature at which pyrolysis reaction starts in the test section. A preheater is connected upstream of the test section to achieve a constant inlet temperature. The inlet and outlet temperatures are measured with the thermocouple at the joints. The details of the experimental setup including a test section were shown in the past study by Kurihara et al. [14].

Figure 3.5 presents a schematic of the numerical simulation and computational grids. These grids have 201 × 71 grid points. Like the experimental apparatus, the computational domain consists of three sections: an inlet adiabatic section of 101 mm, a heating section of 220 mm, and an outlet adiabatic section of 56 mm. The hydrocarbon flows were assumed to be axisymmetric. Table 3.2 shows Computational conditions for n-dodecane flows in a circular tube. The inlet hydrocarbon temperatures are set to the experimental data measured at T_{up}. The wall temperature in the heating section is kept at a constant temperature.

Figures 3.6 show the temperature and density contours at $T_w = 873.15$ K, which scaled down to 1/10 in the axial direction. In the figures, the flow direction is from left to right. The fluid temperature gradually increases toward the outlet, and the thermal boundary layer develops gradually. The temperature distribution

is almost uniform at the outlet cross section. The density decreases in the thermal boundary layer owing to thermal expansion. The inlet density is 396 kg/m^3, whereas the density near the heated wall is about 200 kg/m^3.

Figures 3.7 show the temperature and density contours at $T_w = 973.15$ K. The temperature near the heated wall exceeds that at $T_w = 873.15$ K. The temperature's nonuniformity remains at the outlet cross section. The density in the flow channel is smaller than that at $T_w = 873.15$ K because of the stronger heating and thermal expansion. Additionally, since *n*-dodecane decomposed into hydrocarbons which have a smaller density than *n*-dodecane above 800 K, the density near the heated wall is about 1/20 of fed *n*-dodecane because of the decomposed components.

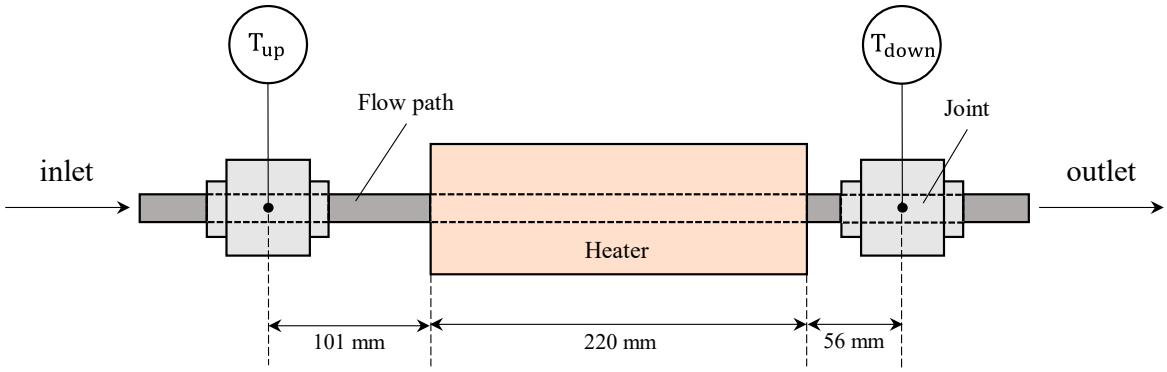

Figure 3.4. Schematic of the test section.

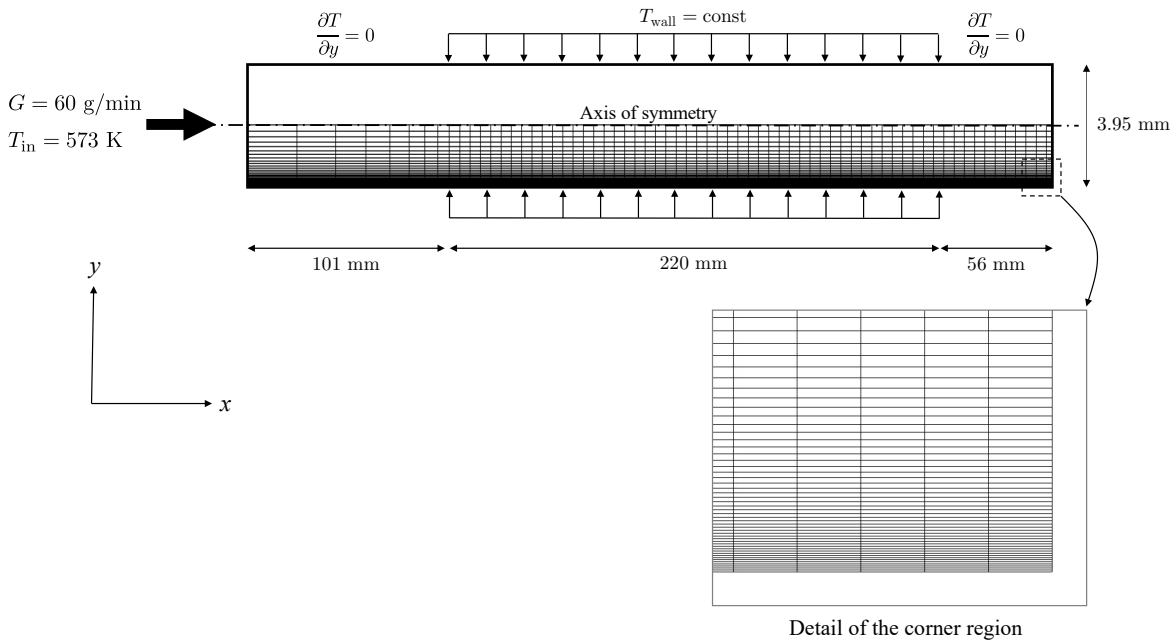

Figure 3.5. Schematic and computational grids for numerical simulations of circular pipe flows.

Table 3.2. Computational conditions for *n*-dodecane flows in a circular tube

Pressure (MPa)	Mass flow rate (g/min)	T_{in} (K)	T_{wall} (K)
6.0	50	693.36	748.15
		691.56	773.15
		695.10	823.15
		690.70	848.15
		695.62	873.15
		696.02	923.15
		699.14	973.15
		696.34	998.15

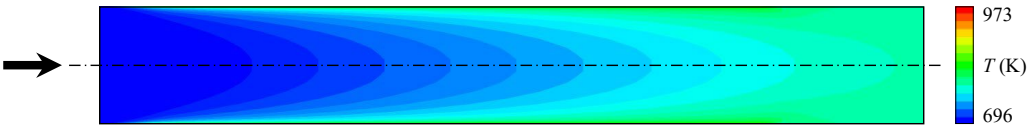

(a) Temperature

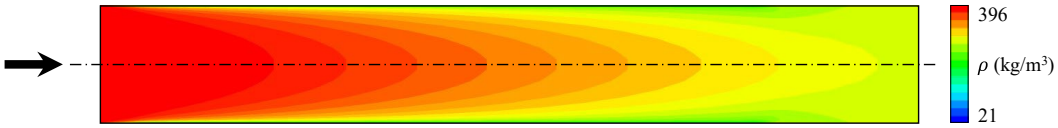

(b) Density

Figure 3.6. Contours of temperature and density at $T_w = 873.15$ K.

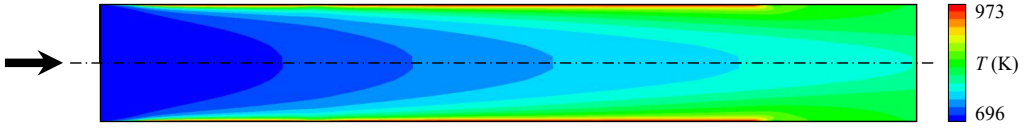

(a) Temperature

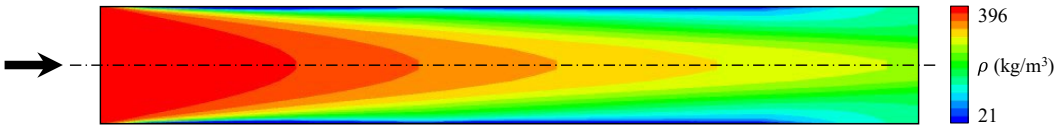

(b) Density

Figure 3.7. Contours of temperature and density at $T_w = 973.15$ K.

Figure 3.8 shows the outlet temperatures under each wall temperature condition. The black squares and white circles indicate experimental and simulation results, respectively. The outlet temperatures were

consistent with the experimental results, and the maximum error was 3.2%. Both the experimental and simulation results, the outlet temperature increase with the wall temperature condition, although the rate of increase tends to decrease at $T_w = 873.15$ K or higher.

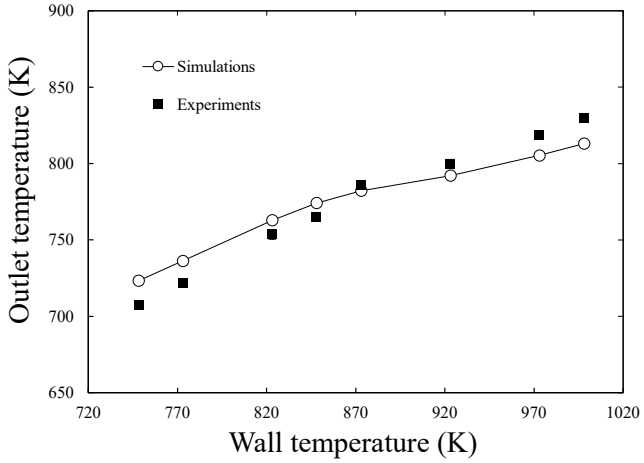

Figure 3.8. Outlet temperature under each wall temperature condition.

Figure 3.9 shows the outlet conversion rate under each wall temperature condition. The black bars and white bars indicate experimental and simulation results, respectively. All simulation results were within the error bars of experimental data and show the good agreement with the experiments. Both the experimental and simulation results, the outlet conversion rate increase with the wall temperature condition as well as the outlet temperature.

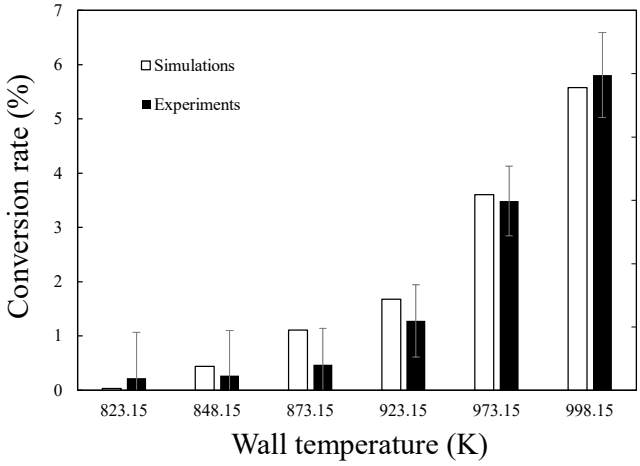

Figure 3.9. Conversion rate under each wall temperature condition.

Figures 3.10 show the radial distribution of dimensionless temperature, thermal diffusivity by turbulence ($\kappa_t/\rho C_p$), and TKE at the midpoint of the heating section ($x_1/r = 110$), respectively, at wall temperatures of 773.15, 873.15, and 973.15 K. In Fig. 3.10(a), the temperature is normalized by the wall temperature. The higher the wall temperature, the greater the difference between it and the main flow temperature. The thermal diffusivity by turbulence for the case with $T_w = 973.15$ K is smaller than that of the other cases over the

whole cross-sectional region and close to zero at $x_2/r < 0.03$, as shown in Fig. 3.10(b). Although the thermal diffusivities by turbulence under $T_w = 973.15$ K at $x_2/r < 0.2$ are almost the same between the simulation results for 773.15 and 873.15 K, the result for 773.15 K is greater than that for 873.15 K at $x_2/r > 0.2$. The results show that the higher the wall temperature, the lower the thermal diffusivity by turbulence, and hence, the lower the dimensionless temperature of the main flow (Fig. 3.10(a)). Fig. 3.10(c) shows the TKE at the cross section ($x_1/r = 110$). The TKE becomes large near the wall because the radial gradient of the axial velocity is large. The peak values of $T_w = 773.15$ K and 873.15 K are almost the same, but the TKE of $T_w = 873.15$ K is smaller than that of 773.15 K for $x_2/r > 0.12$. A high TKE influences the thermal diffusivities by turbulence at $T_w = 773.15$ K and 873.15 K in Fig. 3.10(b), and the difference in the thermal diffusivity with turbulence tends to become great as the distance from the wall increases. In the TKE for $T_w = 973.15$ K, the peak value is smaller compared to $T_w = 773.15$ K and 873.15 K. Thus, the thermal diffusivity by turbulence of 973.15 K is also smaller than those in $T_w = 773.15$ K and 873.15 K (Fig. 3.10 (b)). Those TKE distributions show that the higher the wall temperature, the smaller the TKE.

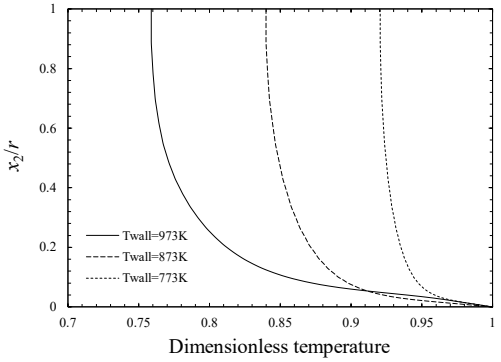

(a) Dimensionless temperature distribution

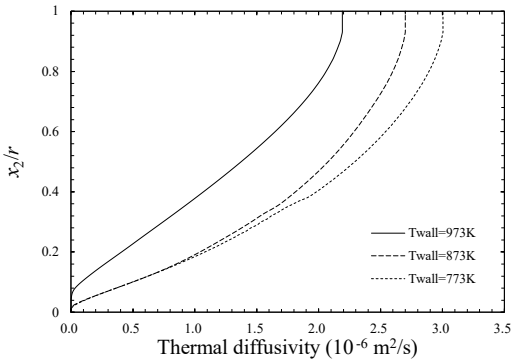

(b) Turbulent thermal diffusivity distribution

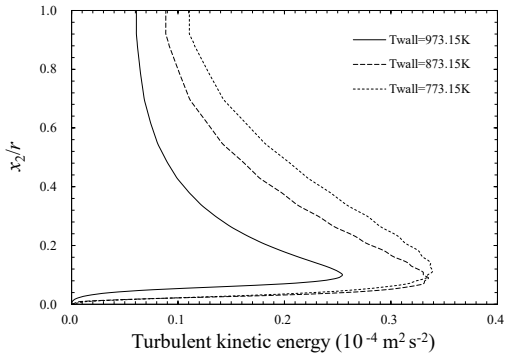

(c) TKE distribution

Figure 3.10. Distributions of the dimensionless temperature, turbulent thermal diffusivity, and turbulent kinetic energy (TKE) at the cross section ($x_1/r = 110$) under wall temperature conditions of 773.15, 873.15, and 973.15 K.

This trend can be explained by a series of processes: as the temperature increases, the density decreases owing to thermal expansion, resulting in a decrease in TKE production. In particular, for a wall temperature

of 973.15 K, the density decreases significantly because of the effects of the decomposed components in addition to thermal expansion (Fig. 3.7(b)); therefore, the TKE rapidly decreases at $x_2/r < 0.08$ compared to other results.

To summarize the above discussion, the radial heat transfer in a flow channel deteriorates with increasing wall temperature because of the decrease in thermal diffusivity by turbulence as a result of low density. This effect becomes more pronounced when pyrolysis reaction occurs because the density significantly decreases because of the effect of decomposed components with a smaller density. Hence, the rate of increase in outlet temperature with the wall temperature condition decreases under high-temperature conditions above 873.15 K; these results suggest that consideration of density change due to the effects of thermal expansion and decomposed components is crucial for reproducing the temperature distribution in the flow channel.

3.3.2 Comparison of supercritical *n*-dodecane flow and *n*-octane flow

Here, I present a comparison of supercritical *n*-dodecane flow and *n*-octane flow at a mass flow rate of 50 g/min and a pressure of 6.0 MPa. Note that the validation of the *n*-octane pyrolysis reaction model used in this section is shown in Chapter 4.

Figures 3.11 compare the contours of temperature, density, and mass fraction of unreacted fed hydrocarbon, respectively, at a wall temperature of 998.15 K. The upper half shows the results for *n*-octane, and the lower half shows those for *n*-dodecane. The temperature of *n*-octane is almost uniform at the outlet cross section, as shown in Fig. 3.11(a), but that of *n*-dodecane remains nonuniform. Such a difference in the temperature distribution is caused by that in the thermal diffusivity. As Fig. 3.3 illustrates, there is a density difference between *n*-dodecane and *n*-octane; therefore, the contour is significantly different, and the density of *n*-octane is smaller than that of *n*-dodecane. The average density of *n*-dodecane at the outlet is 196 kg/m^3,

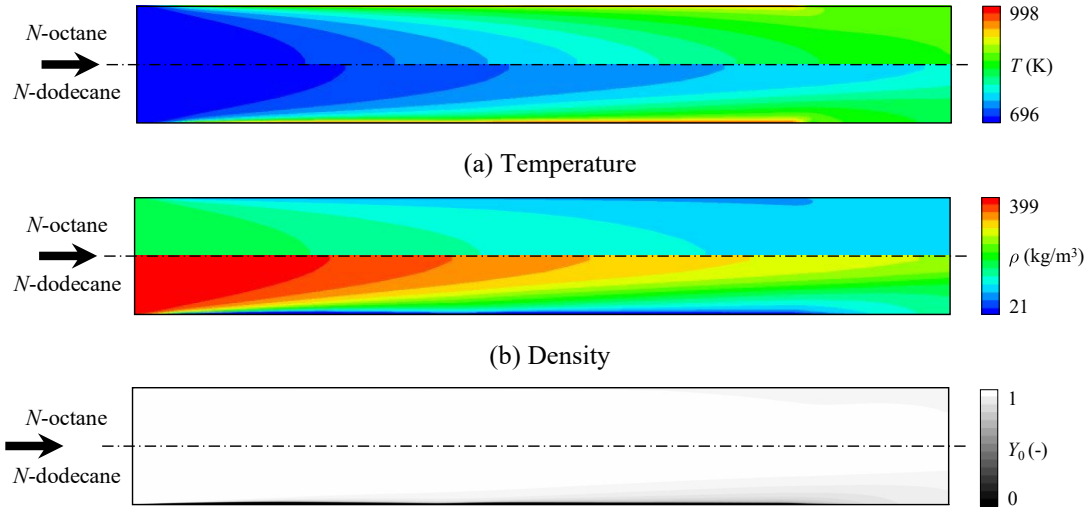

(a) Temperature

(b) Density

(c) Mass fraction of unreacted fed hydrocarbon

Figure 3.11. Comparison of the simulation results of *n*-dodecane flow and *n*-octane flow at $T_w = 998.15$ K.

whereas that of *n*-octane is 103 kg/m^3. Nevertheless, the species and proportions of the decomposed components are similar between *n*-dodecane and *n*-octane; therefore, the densities of *n*-dodecane and *n*-octane are almost the same near the heated wall where pyrolysis occurs. Comparing the mass fractions of unreacted *n*-dodecane and *n*-octane, *n*-dodecane is found to decompose more than *n*-octane. The average velocities of *n*-dodecane and *n*-octane were 0.27 and 0.52 m/s at the midpoint of the heating section, respectively, because of the density difference shown in Fig. 3.11(b). Therefore, the residence time of *n*-dodecane in the flow channel is longer than that of *n*-octane.

Figures 3.12 show the radial distributions of temperature, thermal diffusivity, and mass fraction of unreacted fed hydrocarbon, respectively, for *n*-dodecane flow and *n*-octane flow in the outlet heating section ($x_1/r = 160$) at $T_w = 998.15$ K. Fig. 3.12(a) shows the temperature distribution at the cross section ($x_1/r = 160$); although the wall temperature conditions are the same in both flows, there is a difference of about 80 K at the center of the circular pipe, and the temperature of *n*-octane is higher. On the other hand, the temperature of the *n*-dodecane flow is always higher than that of *n*-octane flow for the fluid temperature above 900 K ($x_2/r < 0.09$), where the reaction rate constant increases significantly. Fig. 3.12(b) shows the total thermal diffusivity, expressed as the summation of the thermal diffusivity by molecular dynamics and by turbulence ($(\kappa + \kappa_t)/\rho C_p$). In both flows, the thermal diffusivity becomes large because of the effect of decomposed components near the heated wall. These components, such as C_2H_4 and C_2H_6, have high thermal diffusivities owing to their molecular dynamics. In particular, the *n*-dodecane flow has a high conversion rate,

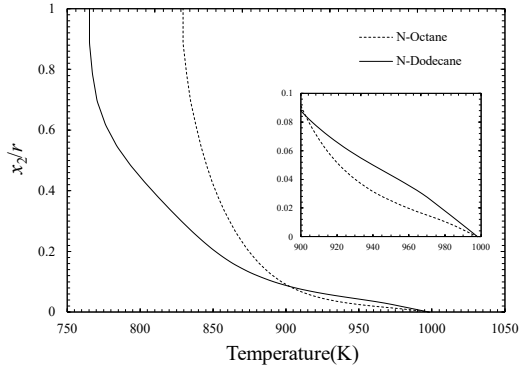

(a) Temperature distribution

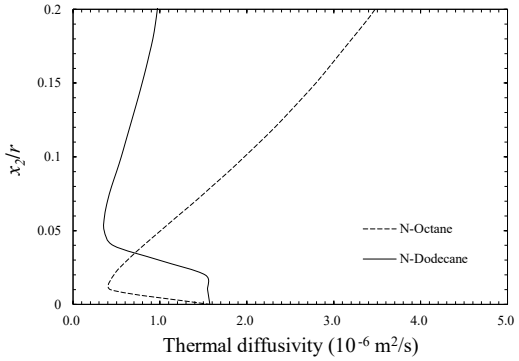

(b) Thermal diffusivity distribution near the heated wall ($x_2/r < 0.2$)

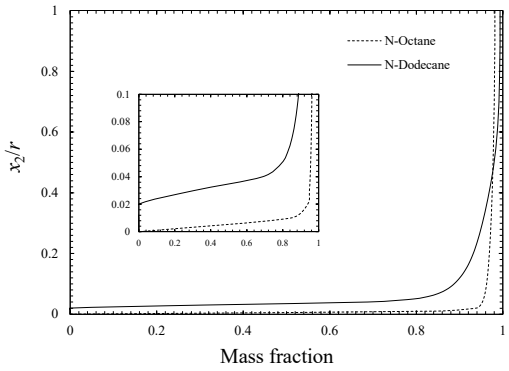

(c) Mass fraction distribution of unreacted fed hydrocarbons

Figure 3.12. Comparison of the radial distributions for *n*-dodecane flow and *n*-octane flow at the cross section ($x_1/r = 160$) at $T_w = 998.15$ K.

such that the area with high thermal diffusivity near the wall is wider than that of *n*-octane. Therefore, the temperature of *n*-dodecane flow is always higher than that of *n*-octane flow at $x_2/r < 0.09$ (Fig. 3.12(a)). The thermal diffusivities of *n*-dodecane and *n*-octane have minimum values at $x_2/r = 0.05$ and $x_2/r = 0.01$, respectively. Then, as the distance from the wall increases, the thermal diffusivities increase because the component due to turbulence increases. The thermal diffusivity by turbulence of the *n*-octane flow is greater than that of the *n*-dodecane flow because the high axial velocity leads to a great TKE in the *n*-octane flow. Thus, as shown in Fig. 3.12(a), the main flow temperature of *n*-octane is higher than that of *n*-dodecane. Fig. 3.12(c) shows the mass fraction of unreacted *n*-dodecane and *n*-octane. In both flows, pyrolysis occurs mainly near the heated wall. The conversion rate of *n*-octane is 3.1% at the cross section of $x_1/r = 160$, whereas that of *n*-dodecane is 5.0% at the same cross section. The following three points can be presented as reasons for the conversion rate of *n*-dodecane to be greater than that of *n*-octane. First, the reaction rate constant of *n*-dodecane is larger than that of *n*-octane at high temperature conditions. Second, the temperature of *n*-dodecane flow is always higher than that of *n*-octane flow in the temperature area above 900 K ($x_2/r < 0.09$), where the reaction rate constant increases significantly, as shown in Fig. 3.12(a). Therefore, the pyrolysis reaction of *n*-dodecane can proceed more rapidly at $x_2/r < 0.09$. Finally, the residence time of *n*-dodecane in the heating section is longer than that of *n*-octane because of the slower axial velocity of *n*-dodecane.

As mentioned above, the conversion rate is closely related not only to the reaction rate constant but also to thermal flows in the heated pipe. In particular, the temperature distribution greatly influences the conversion rate. Therefore, accurate estimations of the thermophysical properties that determine thermal diffusivity ($(\kappa + \kappa_t)/\rho C_p$) are essential to reproduce the conversion rate accurately.

Figure 3.13 compares the outlet conversion rate for *n*-dodecane flows and *n*-octane flows at each wall temperature condition. In both flows, the higher the wall temperature, the larger the outlet conversion rate; and the conversion rates of *n*-dodecane flows are larger than those of *n*-octane flows under all wall temperature conditions. For example, the outlet conversion rate of *n*-dodecane flow is 5.58% at $T_w = 998.15$ K, whereas that of *n*-octane flow is 3.10%. This trend can be explained in the same way as in Fig. 3.12(c).

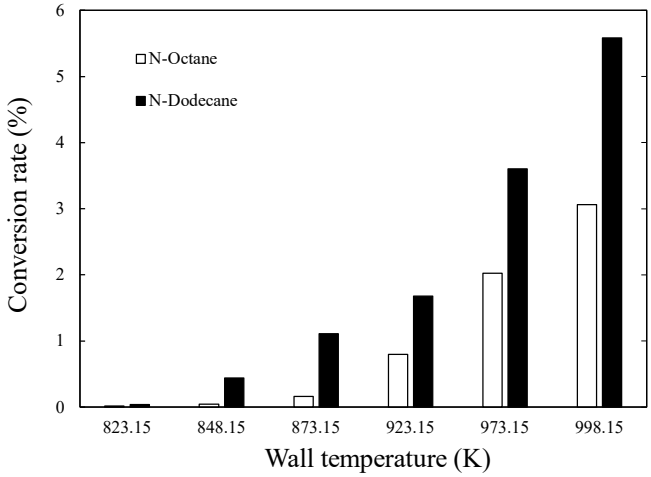

Figure 3.13. Comparison of the outlet conversion rate for *n*-dodecane and *n*-octane at each wall temperature condition.

The reasons for the large conversion rate of *n*-dodecane flows at a cross section of $x_1/r = 160$ were the large reaction rate constant, long residence time, and large high-temperature area. Since the total mass is conserved in the computational domain, this explanation can be applied not only to the conversion rate at $x_1/r = 160$ but also to the outlet conversion rate. Thus, the outlet conversion rate of *n*-dodecane flow is always greater than that of *n*-octane.

3.4 Conclusions

Supercritical *n*-dodecane ($C_{12}H_{26}$) flows in a heated circular pipe with pyrolysis were investigated using the present numerical method and pyrolysis reaction model. This model was developed on the basis of the results of 0-D simulation using JetSurf and Cantera. The thermophysical properties of pure *n*-dodecane and its decomposed components were calculated by the Helmholtz free-energy equation of state, as defined in REFPROP. First, the numerical results of the *n*-dodecane flow were compared with the experimental ones. The outlet temperatures were consistent with the experimental results. I found that the radial heat transfer in a flow channel deteriorates with increasing wall temperature because of the decrease in turbulent thermal diffusivity as a result of reduced density. Next, I compared *n*-dodecane flow and *n*-octane flow at $T_w = 998.15$ K. In the results for both *n*-dodecane and *n*-octane flows, pyrolysis mainly occurred in a high-temperature region near the heated wall. The difference in thermophysical properties affects the temperature distribution and residence time in the heated pipe, resulting in differences in the conversion rate. These results indicate that the accurate prediction of thermal flows and conversion rate in the pyrolysis process necessitate the consideration of not only the fed hydrocarbon but also the decomposed component in the thermophysical properties. The turbulent thermal diffusivity also affects the conversion rate because of differences in the thermal boundary.

References

1. S. Tomioka, T. Hiraiwa, T. Saito, K. Kato, M. Kodera, K. Tani, “System analysis of a hydrocarbon-fueled RBCC engine applied to a TSTO launch vehicle,” Transaction of Japan Society for Aeronautical and Space Sciences, 12–29, (2014), 91–99.
2. T.A. Ward, J.S. Ervin, R.C. Striebich, S. Zabarnick, “Simulations of flowing mildly-cracked normal alkanes incorporating proportional product distributions,” Journal of Propulsion and Power, 20–3, (2004), 394–402.
3. R.P. Jiang, G.Z. Liu, X.W. Zhang, “Thermal cracking of hydrocarbon aviation fuels in regenerative cooling microchannels,” Energy Fuels, 27–5, (2013), 2563–2577.
4. Y.H. Zhu, B. Liu, P.X. Jiang, “Experimental and numerical investigations on *n*-decane thermal cracking at supercritical pressures in a vertical tube,” Energy Fuels, 28 –1, (2014), 466–474.
5. T. Furusawa, N. Taki, S. Yatsuyanagi, S. Yamamoto, T. Miyaura, S. Tomioka, “Numerical simulation of supercritical octane flows in a heated circular tube with simple thermal cracking model,” ASME-JSME-KSME 2019 8th Joint Fluids Engineering Conference, (2019).
6. D.G. Goodwin, H.K. Moffat, R.L. Speth, “Cantera: An object-oriented software toolkit for chemical kinetics, thermodynamics and transport processes,” http://www.cantera.org.
7. A. Miyoshi, “Knowledge-basing utilities for complex reaction systems (KUCRS) software library,” http://akrmys.com/KUCRS/.
8. F.N. Egolfopoulos, H. Wang, R.K. Hanson, D.F. Davidson, C.T. Bowman, H. Pitsch, C.K. Law, N.P. Cernansky, D.L. Miller, W. Tsang, R.P. Lindstedt, A. Violi, “JetSurF–A jet surrogate fuel model (Version2.0),” https://web.stanford.edu/group/haiwanglab/JetSurF/JetSurF2.0/Index.html
9. S. Yamamoto, T. Furusawa, R. Matsuzawa, “Numerical simulation of supercritical carbon dioxide flows across critical point,” International Journal of Heat and Mass Transfer, 54–4, (2011), 774–782.
10. E.W. Lemmon, I.H. Bell, M.L. Huber, M.O. McLinden, “NIST standard reference database 23: Reference fluid thermodynamic and transport properties-REFPROP,” Version 10.0, National Institute of Standards and Technology, (2018).
11. S. Kawai, Y. Oikawa, “Turbulence modeling for turbulent boundary layers at supercritical pressure: a Model for turbulent mass flux,” Flow, Turbulence and Combustion, 104, (2020), 625–641.
12. J.M. Weiss, W.A. Smith, “Preconditioning applied to variable and constant density flows,” AIAA Journal, 33–11, (1995), 2050–2056.
13. S. Yamamoto, “Preconditioning method for condensate fluid and solid coupling problems in general curvilinear coordinates,” Journal of Computational Physics, 207–1, (2005), 240–260.
14. K. Kurihara, T. Miyaura, Y. Daimon, S. Tomioka, “Study on chemical heat sink of n-dodecane under supercritical condition,” Proceedings of 32nd ISTS & NSAT, (2019), 2019–i-13.
15. P. Zhou and B. Crynes, “Thermolytic reactions of dodecane,” Industrial and Engineering Chemistry Process Design and Development, 25, (1986), 508–514.
16. D. Li, S. Venkateswaran, J. W. Lindau, C. L. Merkle, “A unified computational formulation for multi-component and multi-phase flows,” 43rd AIAA Aerospace Sciences Meeting and Exhibit, (2005).

Chapter 4

Numerical study of multi-component effects by pyrolysis on supercritical hydrocarbon flows

4.1 Introduction

The two-stage-to-orbit reusable launch vehicle is a next-generation space transportation system concept proposed by the Japan Aerospace Exploration Agency [1]. It employs rocket-based combined-cycle engines in the first-stage vehicle, whereas the regenerative cooling system in the engines uses kerosene as a fuel and coolant. As a coolant, kerosene is fed into the cooling channel around the combustion chamber to cool the engine system by sensible heat before it is injected into the combustor. In general, the coolant in the cooling channels achieves a high pressure and ultimately reaches a supercritical state. Hydrocarbon fuels in the cooling channels decompose by pyrolysis reactions at temperatures above 800 K, while the additional effects of endothermic reactions increase the cooling capacity required for hypersonic flight. Thus, the accurate prediction of thermal fluid flows along with the interactions of the endothermic reaction and heat transfer in the channel flow is crucial to developing a reliable cooling system.

Pizzarelli et al. [2] investigated supercritical methane flows in a heated rectangular channel. Ward et al. [3] developed a proportional product distribution (PPD) model and numerically investigated the pyrolysis of supercritical decane and dodecane in a circular pipe. Ruan et al. [4] proposed a modified PPD model that can simplify pyrolysis as a set of 12 species reactions. Feng et al. incorporated a preconditioning method by assuming a slow flow into a numerical solution, analyzed the heat and mass transport of supercritical hydrocarbon fuel, clarified its interaction with turbulence [5–7], and further simplified the PPD model based on the corresponding state principle [8]. Jiang et al. [9] conducted pyrolysis experiments using tubes of varying lengths and constructed a reaction model of 18 chemical species and 24 elementary reactions with C5–C11 alkene and cycloalkane lamps. Applying the Soave–Redlich–Kwong equation of state (EOS), Xu et al. [10] proposed a mixture model for unreacted and reacted alkanes and simulated the pyrolysis with detailed models of chemical reactions. Zhu et al. [11] performed pyrolysis experiments on *n*-decane at a supercritical pressure and proposed a global model containing 18 decomposition components. On the basis of this model, they carried out flow analysis with three different turbulence models under the same conditions as the experiment.

Flow analysis of three-dimensional complex shapes, coking, steam reforming reactions, and other complex physical phenomena have recently been considered [12–18].

The decomposed fluid consists of many types of hydrocarbons, such as C_2H_6, C_3H_8, and C_4H_{10}. Decomposed components have a much lower density and isobaric specific heat compared with the fed fluid. For example, the density of *n*-octane (C_8H_{18}) and C_2H_6 are 99.2 kg/m^3 and 23.8 kg/m^3 at 6 MPa and 900 K, respectively. The capabilities and limitations of thermophysical property models for a mixture of decomposed components have not been discussed in detail. Pyrolysis occurs in the high-temperature region near heated walls, and the accurate reproduction of thermal boundary layers is crucial for predicting the effect of endothermic reactions. Furthermore, the eddy viscosity enhances the thermal diffusivity in high Reynolds number conditions. The density changes caused by pyrolysis may affect the turbulent boundary layer. However, existing numerical studies employ conventional Reynolds-averaged Navier–Stokes (RANS) simulation models, such as the *k*–ε, *k*–ω, and *k*-ω shear-stress transport (SST) models, which do not consider the effects of density change on the production of turbulent kinetic energy. In two-equation RANS simulation models, the turbulent kinetic energy is calculated by the production, convection, and dissipation terms. Recently, Kawai developed a new SST turbulence model [19, 20] called the $k-\omega$ SST $+ M_\tau$ model, which considers the production of turbulent kinetic energy caused by the density change. The $k-\omega$ SST $+ M_\tau$ model was developed on the basis of direct numerical simulation results and is expected to be applicable to the rapid changes in fluid density caused by the pyrolysis of hydrocarbons. Ward et al. [3] simulated *n*-decane flows with pyrolysis in the case where wall temperature conditions were 773 K – 873 K and the pyrolysis in the main flow region were discussed. I focus on the pyrolysis reaction of *n*-octane in the thermal boundary near the heated wall, especially when the wall temperature is above 873 K.

In this study, I simulated supercritical octane flows with a pyrolysis reaction and considered the multicomponent effects of density changes on thermophysical properties and turbulent kinetic energy production. The endothermic energy and reaction rate in the reaction model were estimated using a detailed chemical reaction. The thermophysical properties of the mixture fluid by pyrolysis were modeled on the basis of the mass fraction of decomposed components, whose properties were calculated by the polynomial equations defined in the Reference Fluid Thermodynamic and Transport Properties Database (REFPROP) [21]. The effects of thermophysical property changes caused by decomposed components were investigated by comparing the numerical results of each thermophysical property model. The turbulent thermal diffusivity in high-temperature hydrocarbon flows was also discussed using the $k-\omega$ SST $+ M_\tau$ model.

Nomenclature

C_p	isobaric specific heat
e	total internal energy per unit volume
H_0	endothermic energy of unit mass by pyrolysis
J	Jacobian of transformation
k	turbulent kinetic energy
p	pressure
r	radius of a circular channel
R	gas constant
s_{Y_n}	production term of the nth component by pyrolysis
T	temperature
T_{w}	wall temperature in the heating section
T_{in}	inlet temperature in the heating section
t	time
U_i	contravariant velocities ($i = 1, 2$)
u_i	velocities ($i = 1, 2$)
x_i	Cartesian coordinates ($i = 1, 2$)
Y_0	mass fraction of unreacted octane
Y_n	mass fraction of the nth component

Greek symbol

δ_{ij}	Kronecker's delta ($i, j = 1, 2$)
θ	preconditioning parameter
κ	thermal conductivity
κ_t	eddy thermal conductivity
μ	molecular viscosity
μ_t	eddy viscosity
ξ_i	general curvilinear coordinates ($i = 1, 2$)
ρ	density
τ_{ij}	viscous stress tensors ($i, j = 1, 2$)
ω	specific turbulent dissipation rate

4.2 Numerical method

4.2.1 Fundamental equations

The fundamental equations employed herein were based on two-dimensional axisymmetric Navier–Stokes equations coupled with conservation equations for turbulent kinetic energy and a specific turbulent dissipation rate. The conservation of mass of each decomposed hydrocarbon component was added to the fundamental equations. The set of equations was further modified by the preconditioning method by Yamamoto [22] in the form of general curvilinear coordinates expressed in vector form:

$$\boldsymbol{\Gamma}\frac{\partial\widehat{\boldsymbol{Q}}}{\partial t}+\frac{\partial\boldsymbol{F}_i}{\partial\xi_i}+\frac{\partial\boldsymbol{F}_{vi}}{\partial\xi_i}+\boldsymbol{S}+\boldsymbol{H}=0\quad(i=1,2), \tag{4.1}$$

where

$$\boldsymbol{\Gamma}=\begin{bmatrix}\theta & 0 & 0 & \rho_T & 0&0&0&\cdots&0\\ \theta u_1 & \rho & 0 & \rho_T u_1 & 0&0&0&\cdots&0\\ \theta u_2 & 0 & \rho & \rho_T u_2 & 0&0&0&\cdots&0\\ \theta h-1+\rho h_p & \rho u_1 & \rho u_2 & \rho_T h+\rho h_T & 0&0&0&\cdots&0\\ \theta k & 0 & 0 & \rho_T k & \rho&0&0&\cdots&0\\ \theta\omega & 0 & 0 & \rho_T\omega & 0&\rho&0&\cdots&0\\ \theta Y_0 & 0 & 0 & \rho_T Y_0 & 0&0&\rho&0&0\\ \vdots & \vdots & \vdots & \vdots & \vdots&\vdots&0&\ddots&0\\ \theta Y_n & 0 & 0 & \rho_T Y_n & 0&0&0&0&\rho\end{bmatrix},\ \widehat{\boldsymbol{Q}}=\begin{bmatrix}p\\u_1\\u_2\\T\\k\\\omega\\Y_0\\\vdots\\Y_n\end{bmatrix},$$

$$\boldsymbol{F}_i=\begin{bmatrix}\rho U_i\\ \rho u_1U_i+\dfrac{\partial\xi_i}{\partial x_1}p\\ \rho u_2U_i+\dfrac{\partial\xi_i}{\partial x_2}p\\ (e+p)U_i\\ \rho kU_i\\ \rho\omega U_i\\ \rho Y_0U_i\\ \vdots\\ \rho Y_nU_i\end{bmatrix},\ \boldsymbol{F}_{\boldsymbol{v}i}=J\frac{\partial\xi_i}{\partial x_j}\begin{bmatrix}0\\ \tau_{j1}\\ \tau_{j1}\\ \tau_{jk}u_k+(\kappa+\kappa_t)\dfrac{\partial T}{\partial x_j}\\ \sigma_{kj}\\ \sigma_{\omega j}\\ 0\\ \vdots\\ 0\end{bmatrix},\ \boldsymbol{S}=-J\begin{bmatrix}0\\0\\0\\H_{Y_0}\\s_k\\s_\omega\\s_{Y_0}\\\vdots\\s_{Y_n}\end{bmatrix},$$

$$\boldsymbol{H}=-\frac{J}{r}\begin{bmatrix}\rho u_2\\ \rho u_1u_2\\ \rho(u_2)^2\\ (e+p)u_2-(\kappa+\kappa_t)\dfrac{\partial T}{\partial x_2}\\ \rho ku_2\\ \rho\omega u_2\\ \rho Y_0u_2\\ \vdots\\ \rho Y_nu_2\end{bmatrix}.$$

Here, $\widehat{\boldsymbol{Q}}$, $\boldsymbol{F}_i$, $\boldsymbol{F}_{\boldsymbol{v}i}$, $\boldsymbol{S}$, and $\boldsymbol{H}$ are the vectors of unknown primitive variables, inviscid flux, viscous flux, source term, and axisymmetric term, respectively. $\boldsymbol{\Gamma}$ is a preconditioning matrix with the preconditioning parameter by Weiss et al. [23]. Y_n $(n = 0,1,2, \dots,)$ is a set of species mass fractions of unreacted-fed and decomposed hydrocarbons. σ_{kj}, $\sigma_{\omega j}$, s_ω, and s_k are as defined by Menter [24] and Kawai [19, 20]. s_{Y_n} is the mass generation rate of the nth component in the pyrolysis of a fed hydrocarbon. H_{Y_0} represents the endothermic energy generated by pyrolysis. The numerical methods used include a preconditioning flux vector splitting method and the lower-upper symmetric Gauss–Seidel preconditioning scheme proposed by Yamamoto [22].

4.2.2 Chemical reaction modeling of pyrolysis

Using the Knowledge-basing Utilities for Complex Reaction Systems (KUCRS), a modeling tool for the oxidation/combustion reaction of hydrocarbons [25], along with a numerical zeroth-dimensional (0-D) simulation, I developed a database of complex reaction systems for octane pyrolysis. The KUCRS platform provides the chemical reaction mechanisms, rate constants for elementary processes, and thermochemical data as a polynomial constant in NASA format. In the chemical reaction, the thermodynamic and transport data of substances, such as specific heat, enthalpy, and entropy, were obtained using the following polynomial equations:

$$\frac{C_{p_k}^{\ 0}}{R} = a_{1k} + a_{2k}T + a_{3k}T^2 + a_{4k}T^3 + a_{5k}T^4, \tag{4.2a}$$

$$\frac{H_k^0}{RT} = a_{1k} + \frac{a_{2k}}{2}T + \frac{a_{3k}}{3}T^2 + \frac{a_{4k}}{4}T^3 + \frac{a_{5k}}{5}T^4 + \frac{a_{6k}}{T}, \tag{4.2b}$$

$$\frac{S_k^0}{RT} = a_{1k}\ln T + a_{2k}T + \frac{a_{3k}}{2}T^2 + \frac{a_{4k}}{3}T^3 + \frac{a_{5k}}{5}T^5 + a_{7k}. \tag{4.2c}$$

where $C_{p_k}^{\ 0}$, H_k^0, and S_k^0 are the isobaric specific heat, enthalpy, and entropy of a substance in the chemical reaction, respectively. a_{1k}, a_{2k}, ..., a_{7k} are the coefficients defined in the KUCRS, with k representing each substance. Note that the coefficient sets were provided for low- and high-temperature conditions, with the latter exceeding 1000 K. In the octane pyrolysis, I established a total of 3689 formulas with 550 species. The chemical reaction equations were numerically simulated as a 0-D problem with Cantera [26], an open-source software for simulating chemical kinetics, thermodynamics, and transport processes.

Figure 4.1 shows the simulated mole fractions of the decomposed components along with the experimental data obtained by Kurihara et al. [27]. The black hatched bars indicate the numerical results of the 0-D simulation at 1000 K and 6.0 MPa. The components experimentally decomposed by pyrolysis were measured by the flows in a heated circular pipe at 1023 K, as shown in the experimental apparatus section. In the figure, the error bars in the experimental results indicate the values within three standard deviations for the five cases in the experimental measurements. The mole fractions of C_1–C_3 hydrocarbons, such as CH_4,

C_2H_4, C_2H_6, and C_3H_6, exceeded those of the other hydrocarbons in the 0-D simulation. The differences in mole fractions between the zero-dimensional simulation and the experimental results are 3.0% (H_2), 3.9% (CH_4), 4.3% (C_2H_6), and 4.7% (C_3H_8), respectively. Although the results of the pyrolytic model differed from the experimental data, the main aim of this study is to reveal the effects of thermophysical properties. The thermophysical properties interpolated by the mole fractions in the 0-D simulation have a less than 1% difference from those by the mole fractions in experiment. Thus, the thermophysical properties in this study can be used to discuss the effects of multicomponent thermophysical properties on the thermal flow.

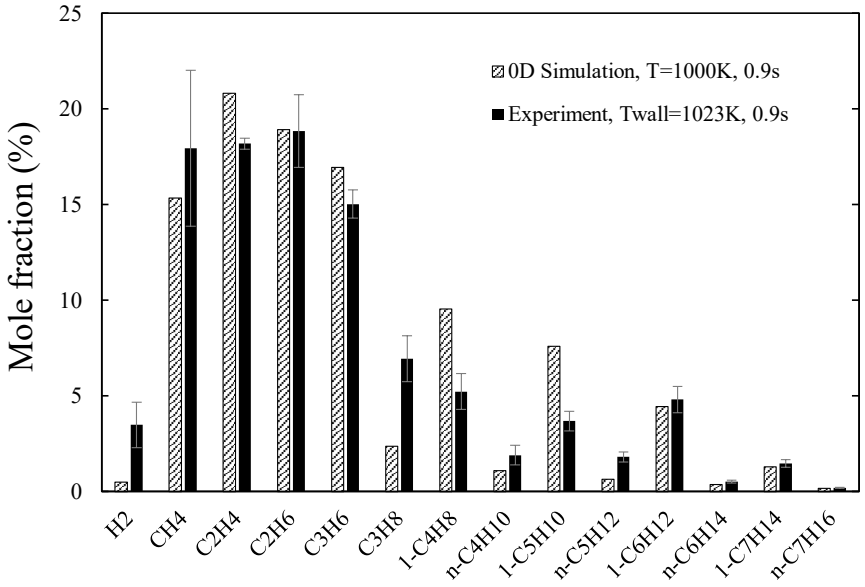

Figure 4.1. Simulated mole fraction of decomposed components with experimental data.

The reaction rate constant k_c in each temperature condition is shown in Figure 4.2; the lines represent the simulation results obtained with KUCRS and Cantera. I obtained a linear approximation of each temperature condition, and k_c linearly increased by < 1 s at each temperature. The value of k_c can be approximated using the least-squares method. Using the Alenius equation, k_c is mathematically expressed as

$$k_c = A \exp\left(\frac{-E}{RT}\right). \tag{4.3}$$

with the frequency factor $A = 1.1 \times 10^{13}\ \mathrm{s}^{-1}$ and activation energy $E = 236.7\ \mathrm{kJ/mol}$ for octane pyrolysis based on the simulation results (Fig. 4.2). This value of E is close to the value of $E = 236\ \mathrm{kJ/mol}$ determined by Kunzru [28] at $T = 923\text{–}998\ \mathrm{K}$. I employed $E = 236.7\ \mathrm{kJ/mol}$ for calculating k_c in the numerical simulation. The actual pyrolysis reaction includes thousands of chemical reactions. However, such detailed modeling requires significant computational time to deal with the thermal boundary in multidimensional fluid dynamics problems. A similar discussion was presented by Ward et al. [3], who developed a PPD model of *n*-decane for computational fluid dynamics (CFD) simulation. In the PPD

model, the mole fractions of the major decomposed components were averaged as a general reaction mechanism based on experimental data. Ruan et al. [4] and Feng et al. [5] simulated the thermal flows of *n*-decane with a PPD model. Here, I employed the same strategy as Ward et al. [3] using 0-D simulation. The decomposition of *n*-octane by pyrolysis in flow simulations can be calculated as

$$\frac{d[\mathrm{C_8H_{18}}]}{dt} = -k_c[\mathrm{C_8H_{18}}]. \tag{4.4}$$

The reaction rate constant k_c is defined by Eq. (4.3). Considering 12 components, the overall reaction is expressed as follows:

$$\begin{aligned}\mathrm{C_8H_{18}} \rightarrow\ & 0.004\mathrm{H_2} + 0.126\mathrm{CH_4} + 0.29\mathrm{C_2H_4} + 0.193\mathrm{C_2H_6} + 0.149\mathrm{C_3H_6} \\ & + 0.004\mathrm{C_3H_8} + 0.097\mathrm{C_4H_8} + 0.001\mathrm{C_4H_{10}} + 0.069\mathrm{C_5H_{12}} \\ & + 0.05\mathrm{C_6H_{14}} + 0.017\mathrm{C_7H_{16}}.\end{aligned} \tag{4.5}$$

The conservation of mass of the decomposed components was simulated based on the fundamental equations considering the mass generation. In general, pyrolysis is an endothermic reaction describing hydrocarbon decomposition. The endothermic energy by octane pyrolysis is illustrated in Figure 4.3, where the dots and line indicate the simulation results and approximation by the least-squares method, respectively. It can be observed that the endothermic energy linearly increased with the conversion rate under different temperature conditions. The endothermic energy of octane was determined as $H_0 = 17.8\ \mathrm{kJ/kg}$ from the activation energy $E_i = 236.7$ kJ/mol, which was then used to obtain the endothermic energy term in Eq. (4.1) as follows:

$$H_{Y_0} = \rho k Y_0 H_0. \tag{4.6}$$

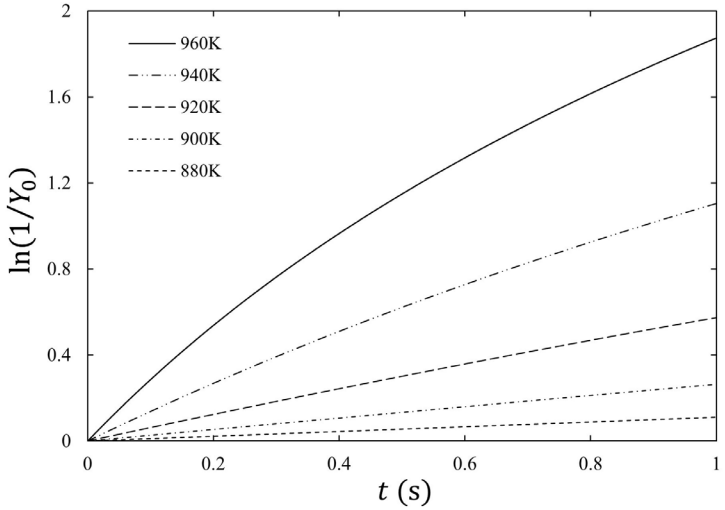

Figure 4.2. Simulated reaction rate of octane at a specified temperature condition.

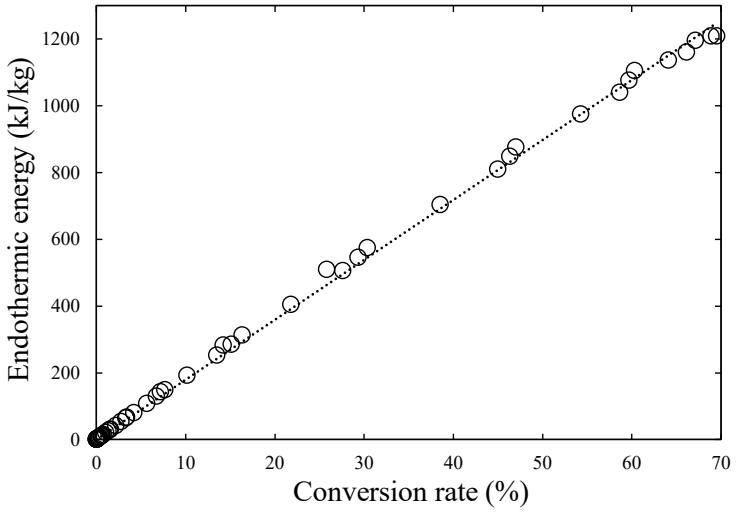

Figure 4.3. Endothermic energy of pyrolysis by simulation. The dots indicate the simulation results forming a linear approximation.

4.2.3 Thermophysical properties of multicomponent hydrocarbon flows

Hydrocarbons are decomposed by pyrolysis in an endothermic reaction under high-temperature conditions. The decomposed hydrocarbons range from C_1–C_7, each with different thermophysical properties. The density and thermal conductivity of C_2H_6, C_3H_8, and C_4H_{10} are 23.8 kg/m^3 and 0.136 W/mK, 35.1 kg/m^3 and 0.146 W/mK, and 46.3 kg/m^3 and 0.134 W/mK, respectively, at 6 MPa and 900 K. Accordingly, I developed three thermophysical property models as a mixture of multiple hydrocarbon components to simulate reacted supercritical octane flows. Table 4.1 lists the approximate mole fractions in each thermophysical property model using the results from KUCRS and Cantera. The 4-component model approximates the thermophysical properties of unreacted octane and three components (C_2H_4, C_3H_6, and C_4H_8) with carbon numbers 2–4. The 12-component model approximates the thermophysical properties of unreacted octane and 11 components (H_2, CH_4, C_2H_4, C_2H_6, C_3H_6, C_3H_8, C_4H_8, C_4H_{10}, C_5H_{12}, C_6H_{14}, and C_7H_{16}) in the flow simulations. For each component, the decomposed mole fraction is approximated as the sum of similar carbon numbers. The one-component model ignores the effects of the thermophysical properties of decomposed hydrocarbons. For all component models, the endothermic energy in Eq. (4.6) was used in the flow simulation. The one-component model means that only the effects of endothermic energy were considered. All thermophysical properties of each component were calculated using the polynomial equations defined in REFPROP. As shown in Table 4.1, the thermophysical properties of almost all decomposed components, taken from REFPROP, are defined for a limited temperature and pressure range, i.e., below 900 K and 100 MPa. Linear extrapolation was employed when the fluid temperature exceeded 900 K, although octane pyrolysis mainly occurred above 800 K. The difference between the 1-, 4-, and 12-component models is much larger than those of linear extrapolations. The thermophysical properties of unreacted octane were also calculated using REFPROP and were the same as that of the 1-component model in Figure 4.4. Subsequently, the thermophysical properties

of the decomposed hydrocarbons were averaged on the mass fraction of each component $(Y_0, Y_1, Y_2, Y_3, \ldots, Y_n)$ as

$$\varphi_m(p,T) = \sum Y_n \varphi_n(p,T). \tag{4.7}$$

where φ_m and φ_n are the thermophysical properties of the mixture and nth components, respectively. Figs. 4.4 show the density and viscosity of each component model at 6.0 MPa. The values from the mixing rule of the Helmholtz free energy equation (REFPROP) for the 12-component models are also shown in Fig. 4.4. The difference between Eq. (4.79) and the mixing rule of the Helmholtz free energy equation is 3.2% and 1.4% for the density and viscosity, respectively, at 950 K. The difference between Eq. (4.7) and the mixing rule by Helmholtz free energy equation is not negligible. However, the relative comparisons are essential to reveal the effects of the thermophysical properties in the component models and turbulence models. For each component model, the density changed significantly near the critical point. Although the viscosity at high temperatures was similar for all component models, the thermal conductivity varied in the high-temperature region.

Table 4.1. Approximate mole fraction of each component model in the *n*-octane pyrolytic reaction

Species	0-D simulation	Thermophysical property models		EOS in REFPROP ✓: Available ×: Not available
		12-component	4-component	
H_2	0.004	0.004	-	✓
CH_4	0.126	0.126	-	✓
C_2H_4	0.290	0.290	0.613	✓
C_2H_6	0.193	0.193	-	✓
C_3H_6	0.149	0.149	0.153	✓
C_3H_8	0.004	0.004	-	✓
C_4H_8	0.097	0.097	0.234	✓
C_4H_{10}	0.001	0.001	-	✓
C_5H_{10}	0.068	-	-	×
C_5H_{12}	0.001	0.069	-	✓
C_6H_{12}	0.045	-	-	×
C_6H_{14}	0.005	0.05	-	✓
C_7H_{14}	0.016	-	-	×
C_7H_{16}	0.001	0.017	-	✓

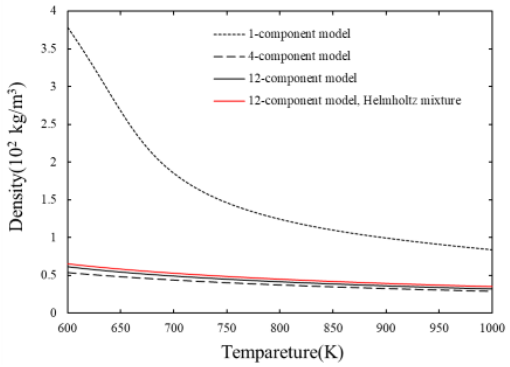

(a) Density

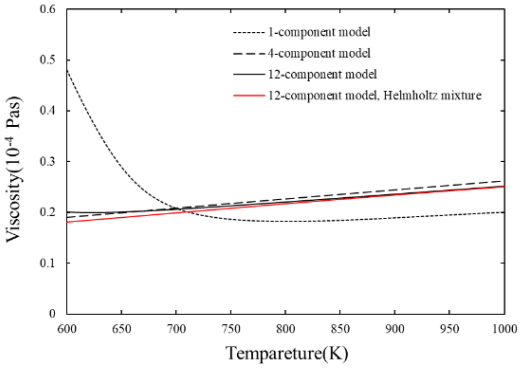

(b) Viscosity

Figure 4.4. Thermophysical properties for each component model determined from Eq. (4.7) and REFPROP at 6 MPa under 100% decomposition condition.

4.2.4 Turbulence model with the density change by pyrolysis

It is known that the density near the heated wall changes not only by thermal expansion but also by pyrolysis. Here, I employed Kawai's $k-\omega$ SST $+ M_\tau$ model, which considers the turbulent kinetic energy production caused by the fluid density change. The conservation of turbulent kinetic energy and the specific turbulent dissipation rate of $k-\omega$ SST $+ M_\tau$ as Cartesian coordinates can be defined by

$$\frac{D\rho k}{Dt} = \tau_{ij}\frac{\partial u_i}{\partial x_j} + M_\tau - \beta^*\rho\omega k + \frac{\partial}{\partial x_j}\left[\mu + \sigma_k\mu_t\frac{\partial k}{\partial x_j}\right], \tag{4.8}$$

and

$$\frac{D\rho\omega}{Dt} = \frac{\gamma}{\nu_t}\tau_{ij}\frac{\partial u_i}{\partial x_j} - \beta\rho\omega^2 + \frac{\partial}{\partial x_j}\left[\mu + \sigma_\omega\mu_t\frac{\partial\omega}{\partial x_j}\right] + 2(1-F_1)\rho\sigma_{\omega 2}\frac{1}{\omega}\frac{\partial k}{\partial x_j}\frac{\partial\omega}{\partial x_j}, \qquad (i,j=1,2) \tag{4.9}$$

with the parameters β^*, β, σ_k, and $\sigma_{\omega 2}$ defined by Menter [24]. M_τ is the mass flux contribution term by density change developed by Kawai [19, 20] expressed as

$$M_\tau = -\frac{\mu_t}{\rho^2 C_\rho}\left\{\frac{\partial\rho}{\partial x_1}\left(\frac{\partial\tau_{21}}{\partial x_1}+\frac{\partial\tau_{22}}{\partial x_2}\right) + \frac{\partial\rho}{\partial x_2}\left(\frac{\partial\tau_{11}}{\partial x_1}+\frac{\partial\tau_{12}}{\partial x_2}\right)\right\}, \tag{4.10}$$

where C_ρ is the model parameter. Here, I employed $C_\rho = 3\times10^{-3}$.

4.3 Numerical simulation of supercritical *n*-octane flows

4.3.1 Experimental apparatus

Figures 4.5(a) and (b) show the flow channel developed by Kurihara et al. [27] to measure the supercritical octane flows in pyrolysis reactions. Kurihara et al. [27] measured the outlet temperature and conversion rate of heated *n*-octane flows. Two series-coupled SUS304 circular pipes with a length of 110 mm and inner radius of 1.95 mm were heated by embedding five cartridge heaters. The heating apparatus was a cylindrical type made of oxygen-free copper. The wall temperature was maintained at the target value by controlling the current value of the heater. The wall temperature at the center of the heating section was used for temperature control. Note that the wall temperature was not completely uniform in the axial direction, although each of the five cartridge heaters was individually controlled. The inlet and outlet temperatures were measured at 773.15, 873.15, 923.15, 973.15, and 1023.15 K. As shown in Fig. 4.5(a), cross joints were installed upstream, midstream, and downstream of the two series-coupled circular pipes. K-type thermocouples were connected to measure the temperature of the fluid. The inlet mass flow rate and pressure were set to 25 g/min and 6.0 MPa, respectively.

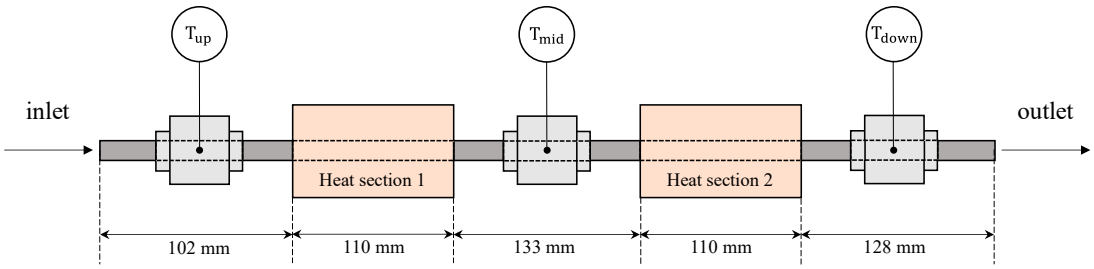

(a) A schematic diagram of the flow channel

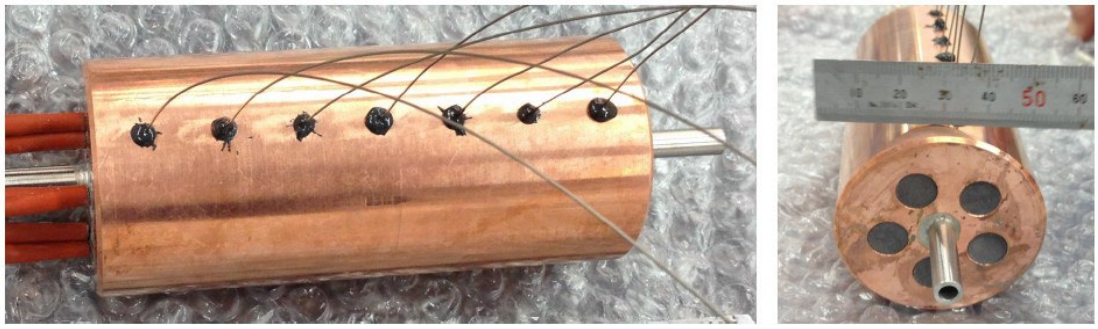

(b) Photographic images of the heating section

Figure 4.5. Flow channel in experimental measurements.

4.3.2 Setups of numerical simulations

The fundamental equations were solved using the numerical method shown in Section 4.2.1. The simulation of supercritical octane flows in the circular pipes was conducted separately for heating sections 1 and 2. The inlet profile in heating section 2 was given uniformly. Therefore, note that the inlet conditions in heating

section 2 did not take into account the non-uniformity because of the flow in heating section 1. The velocity and temperature fluctuations at the inlet could induce three-dimensional turbulent flows in the actual channel, which is a three-dimensional circular pipe with heating sections. The inlet fluctuations could also affect the outlet temperature, especially in high-temperature cases, because the gap between the five experiments was wider in these conditions. I simulated the thermal flows in a heated tube with an axisymmetric assumption, ignoring the three-dimensional effect to reduce the computation time with RANS simulations. The computational domain consisted of an adiabatic inlet section, a heating section, and an adiabatic outlet section measuring 102, 110, and 80 mm in length, respectively, with a pipe radius of 1.95 mm, as indicated in Section 4.3.1. Figure 4.6 shows a schematic of the numerical simulation in the shooter-scaled axial direction. The flow in the circular pipe was assumed to be axisymmetric. The computational grids had 201 × 501 grid points. The grid convergence was confirmed using four computational grids (201 × 71, 501 × 71, 201 × 301, and 201 × 501 in the axial and radial directions, respectively). The errors of the obtained outlet temperature between 201 × 301 and 201 × 501, and between 201 × 71 and 501 × 71, were less than 0.5%. Although the 201 × 301 grid could be used for the numerical simulation, the 201 × 501 grid was selected for improved reproduction of the temperature and velocity boundary layers. Another reason for selecting fine grids is to avoid the numerical oscillations induced by density changes due to the pyrolysis reaction. Abgrall [29] investigated the so-called spurious oscillations caused by the variations in thermodynamic properties, such as multicomponent flow. In this study, I employed the conventional in-house code and required many grid points to avoid numerical oscillation for multicomponent flows. In each computation condition, the minimum y^+ was less than 0.005, and the inlet turbulence intensity was 1.0%. The heated wall section in the circular pipe was maintained at a constant and uniform temperature. I set the outlet pressure to 6.0 MPa and the inlet pressure to the Neumann condition in all cases. As shown in the following section, the pressure variations in the heating section were less than 100 Pa. The buoyancy effect was negligible in the simulation because of the low Richardson number (< 0.4) in all cases. In particular, supercritical octane flows at $T_w = 773.15, 873.15, 923.15, 973.15, \text{and } 1023$ K were simulated using the thermophysical properties of the 1-, 4-, and 12-component models of decomposed hydrocarbons, respectively, taking into account the endothermic energy by pyrolysis. In each case, the inlet temperature of heating sections 1 and 2 was set according to the experimentally measured temperature. Table 4.2 lists the simulation conditions for each case. The inlet temperatures of each heating section were set based on the experimental data. The wall temperature in the heating section was maintained at a constant value. The Reynolds numbers ranged from 5000 to 7500 at the inlet point. The Reynolds numbers also slightly differed from each other owing to the density and viscosity difference caused by inlet temperature conditions.

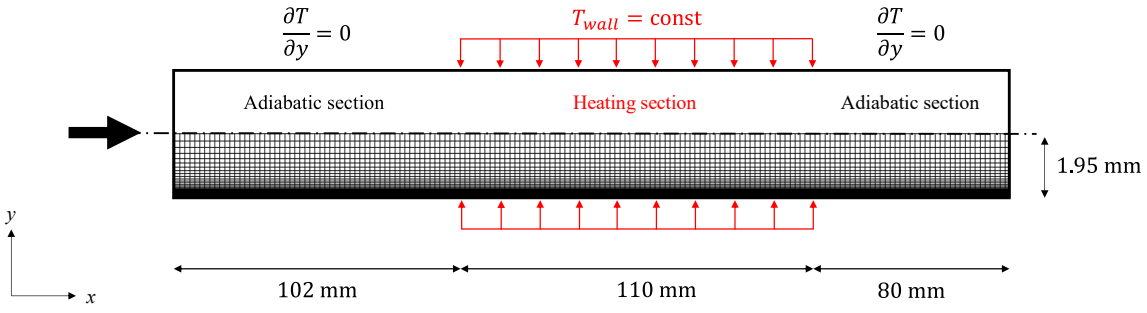

Figure 4.6. Schematic and computational grids for the numerical simulations of circular pipe flows.

Table 4.2. Computational conditions for supercritical octane flows

Mass flow rate (g/min)	Pressure (MPa)	T_{in} of heating section 1 (K)	Re_{in} of heating section 1	T_{in} of heating section 2 (K)	Re_{in} of heating section 2	T_{w} (K)
		661.31	5196	679.64	5920	773.15
		683.80	6061	736.58	7153	873.15
25	6.0	680.88	5963	756.30	7319	923.15
		682.96	6034	760.62	7343	973.15
		682.64	6023	780.02	7420	1023.15

4.3.3 Numerical results with multicomponent thermophysical properties

Figures 4.7 show the contours of the density, temperature, and mass fraction of unreacted octane, and the pressure at the cross-section of the 1-, 4-, and 12-component models, respectively, at $T_w = 1023.15$ K. Each figure was scaled to 1/10 in the axial direction for ease of viewing. The $k - \omega$ SST $+ M_\tau$ model was used as the turbulence model in these results. It can be seen that the fluid temperature increased gradually owing to heat transfer from the wall, in contrast to the density pattern due to thermal expansion. Octane decomposed into smaller hydrocarbon components at above 800 K by pyrolysis. The fluid temperature reached 800 K in a small region near the heated wall, which reduced the mass fraction of unreacted octane to 0. Accordingly, the densities of the 4- and 12-component models were much lower than those of the 1-component model in the high-temperature region, as the two former models considered the thermophysical properties of the mixture due to pyrolysis. The pressure variations in the channel were less than 100 Pa, and sufficiently small to estimate the reaction rate using the temperature, as shown in Eq. (4.3).

Figures 4.8 show the density and unreacted octane distribution of the 12-component model at $T_w = 923.15, 973.15, \text{and } 1023.15$ K, as well as those of the 4- and 1-component models at $T_w = 1023.15$ K. The ratios x_1/r and x_2/r represent the normalized distances from the circular pipe inlet and the circular pipe wall, respectively. Pyrolysis occurred mainly in the region with less than $x_2/r = 0.1$, whereas the mass fraction of the unreacted octane mass fraction (Y_0) decreased to 0 at the heated wall in high wall temperature conditions. The reaction region changed in accordance with the wall temperature and became narrower at lower wall temperatures. The density was lowest at the heating wall and rapidly changed with the reaction rate. Comparing the component models, the distribution of Y_0 was slightly different because of the difference in the thermal boundary layer in each case. Although Y_0 dropped to 0 at the heated wall in all models, the density of the 1-component model was much higher than that of the multicomponent models. It should be noted that the 4- and 12-component models considered not only the thermophysical properties of octane but also those of the smaller decomposed hydrocarbon components such as C_2H_4, C_3H_6, and C_4H_8.

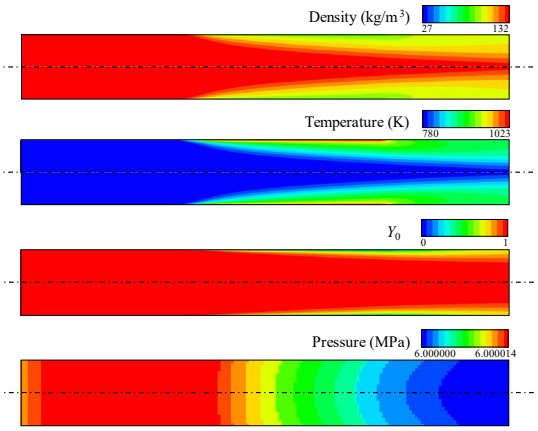

(a) 1-component model

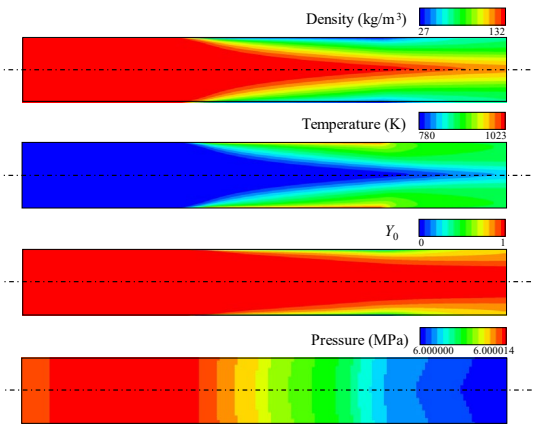

(b) 4-component model

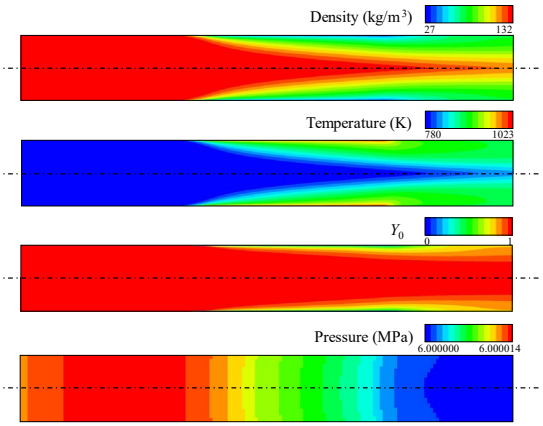

(c) 12-component model

Figure 4.7. Density, temperature, and mass fraction of unreacted octane (Y_0) of the 1-, 4-, and 12 component models at $T_w = 1023.15$ K.

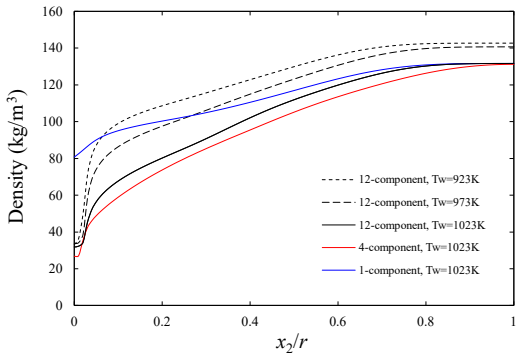

(a) Density

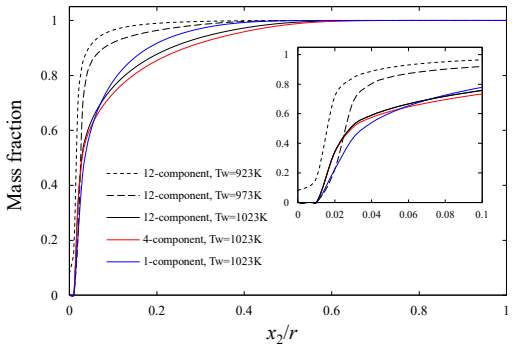

(b) Unreacted octane mass fraction (Y_0)

Figure 4.8. Cross-sectional density and unreacted octane mass fraction at $x_1/r = 95$.

On the other hand, the 1-component model assumed that the thermophysical properties of the reacted fluid were the same as those of pure octane. Because the density of the smaller hydrocarbons is much lower than that of the fed octane, the multicomponent thermophysical property models were able to reproduce the rapid change in density caused by pyrolysis. The thermophysical properties of the decomposed hydrocarbons were

calculated using the mole fraction (Table 4.1) of each thermophysical property model. C_4H_8 accounted for 23% of the decomposed components in the 4-component model, whereas the 12-component model contained 9.7% (C_4H_8), 0.1% (C_4H_{10}), 6.9% (C_5H_{12}), 5% (C_6H_{14}), and 1.7% (C_7H_{16}); hence, the density of the 4-component model was overestimated to be lower than that of the precise 12-component model.

4.3.4 Turbulent kinetic energy and temperature profile in the heating section

Figure 4.9 displays the contours of density, temperature, and mass fraction of unreacted octane at the cross-section of the $k-\omega$ SST+M_τ model compared with the results of the conventional $k-\omega$ SST turbulence model under the conditions of the 12-component model at $T_w = 1023.15$ K. It can be seen that the temperature of the $k-\omega$ SST+M_τ model after the heating section became almost uniform at the cross-section, while non-uniformity remained in the conventional $k-\omega$ SST model. The low-density region corresponding to the high-temperature region became wider, resulting in the low mass fraction of unreacted octane. In the $k-\omega$ SST+M_τ model, the M_τ term in Eq. (4.8) produced the turbulent kinetic energy caused by the density change. Such turbulent energy production near the heated wall affected the thermal boundary layer, leading to pyrolysis over a wide region.

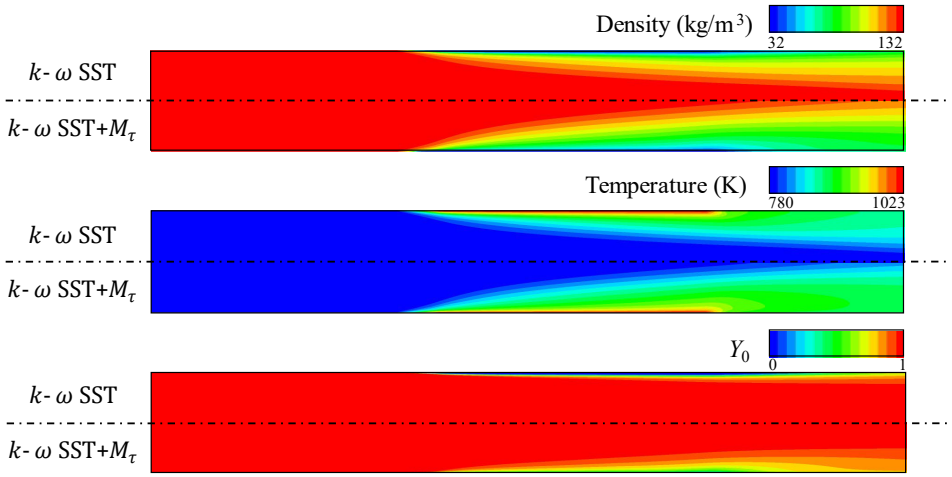

Figure 4.9. Density, temperature, and mass fraction of unreacted octane (Y_0) at $T_w = 1023.15$ K (upper half: conventional $k-\omega$ SST; lower half: $k-\omega$ SST+M_τ).

Figure 4.10 shows the axial velocity profiles of the $k-\omega$ SST+M_τ and conventional $k-\omega$ SST models with 12 components. The black dotted line represents the logarithmic velocity profile by $1/0.41\log(y^+)+5.2$. Note the similarity in the velocity profiles of each model regardless of the wall temperature conditions. Moreover, whereas the velocity of the $k-\omega$ SST+M_τ model followed a logarithmic profile near the wall, that of the conventional $k-\omega$ SST with the 12-component model was much higher than the results of the $k-\omega$ SST+M_τ model, mainly because of the lack of eddy viscosity caused by density change. Kawai et al. [19, 20] obtained similar results with the density fluctuations of the trans-critical flows of hydrogen.

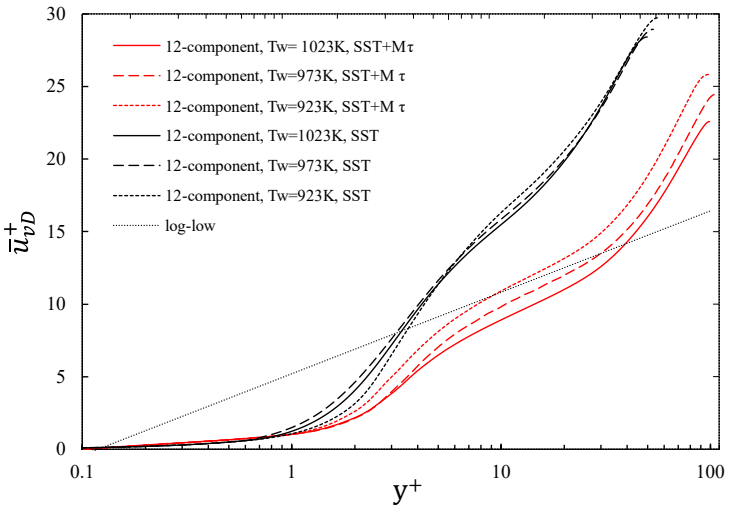

Figure 4.10. Velocity profiles near the heated wall at $T_w = 1023.15$ K and $x_1/r = 95$.

Figure 4.11 shows the cross-sectional eddy viscosity distribution in the heating section at $x_1/r = 50, 65, 80, \text{and } 95$, where $x_1/r = 50$ and $x_1/r = 95$ are the approximate inlet and outlet positions, respectively. The results of the $k-\omega$ SST+M_τ model (1-component model and 12-component model) and the conventional $k-\omega$ SST model (12-component model) are shown in Fig. 4.11. The maximum eddy viscosity at $x_1/r = 50$ was approximately 5.0 in all cases. In cases with the $k-\omega$ SST+M_τ model, the eddy viscosity increased gradually at $x_1/r = 65, 80, \text{and } 95$ in both component models, while the eddy viscosity decreased in the case with the conventional $k-\omega$ SST model. At $x_2/r < 0.1$, the eddy viscosity was suppressed, especially at $T_w = 1023.15$ K. Near the heated wall, the low eddy viscosity resulted in a thin high-temperature region (Fig. 4.7). The turbulent kinetic energy generated by M_τ caused a higher eddy viscosity relative to the $k-\omega$ SST model. The region in $x_2/r < 0.1$ also demonstrated a much higher eddy viscosity compared with that of the $k-\omega$ SST model. Accordingly, the eddy viscosity of the 12-component model reached a higher peak value than that of the 1-component model, mainly because of the rapid density change caused by the smaller hydrocarbons. Indeed, the effects of density change and the M_τ term on the hydrocarbon flow with pyrolysis reactions are significant to predict the eddy viscosity near the heating wall during pyrolysis. Essentially, I observed a significant difference in the eddy viscosity of the present and conventional models in the high-temperature condition.

Figure 4.12 shows the cross-sectional thermal diffusivity at $T_w = 1023.15$ K and $x_1/r = 95$. The solid lines indicate the thermal diffusivity by turbulence calculated by $\mu_t/\rho Pr_t$, where Pr_t is the turbulent Prandtl number. The dotted lines indicate the thermal diffusivity by molecular dynamics calculated by $\kappa/\rho C_p$. Decomposed hydrocarbons, such as CH_4 and C_2H_6, have high thermal diffusivity. The fluid decomposed by the 12-component model included smaller hydrocarbons generated by pyrolysis in the high-temperature region; thus, the thermal diffusivity near the wall in this model was four times higher than that in the 1-component model. The thermal diffusivity by molecular dynamics in the main flow region was the same for all component models because of the low decomposition rate of octane. The thermal diffusivity by turbulence relied on the eddy viscosity, with a peak similar to that shown in Fig. 4.11(b). In particular, the thermal diffusivity due to turbulence in the $k-\omega$ SST+M_τ model was larger than that in the conventional

model, especially when the 12-component model was applied. The high total thermal diffusivity by molecular dynamics and turbulence in the $k-\omega$ SST+M_τ model with the 12-component model promoted the expansion of a high-temperature region in the main flow region, whereas the thermal diffusivity in the conventional $k-\omega$ SST model was high only near the heated wall.

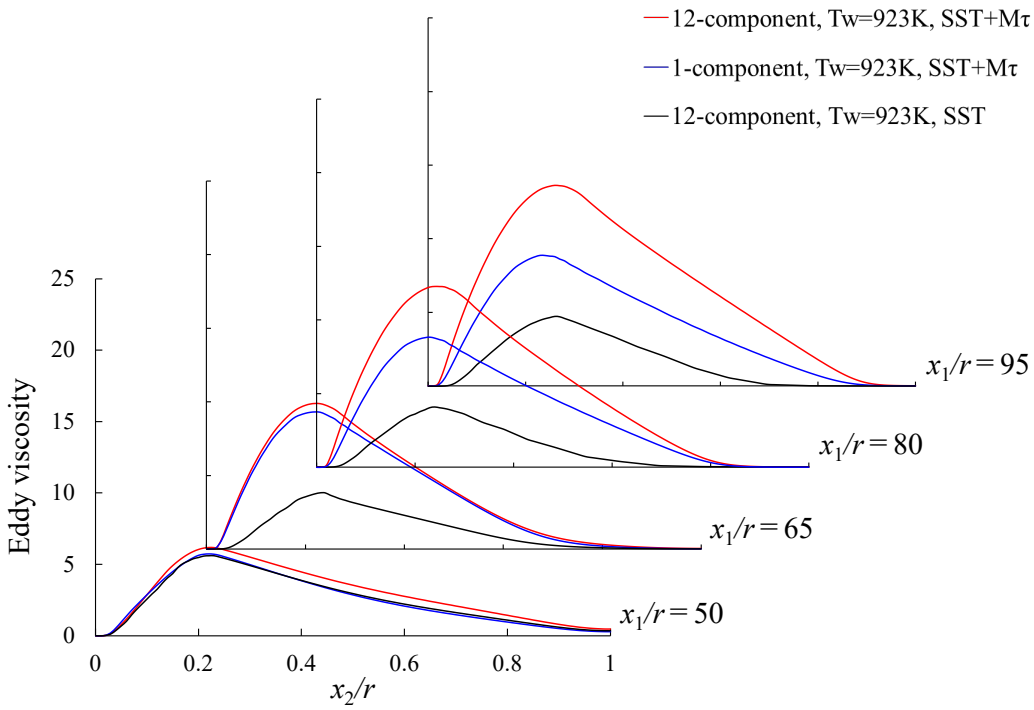

(a) $T_w = 923.15$ K

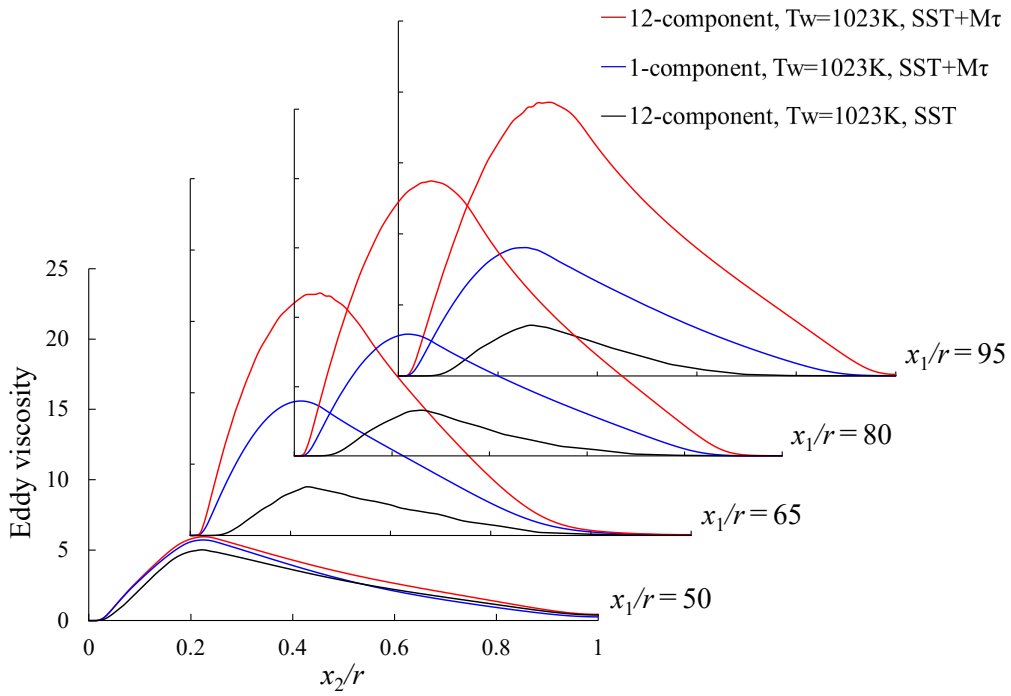

(b) $T_w = 1023.15$ K

Figure 4.11. Cross-sectional eddy viscosity distributions at $x_1/r = 50, 65, 80, \text{and } 95$.

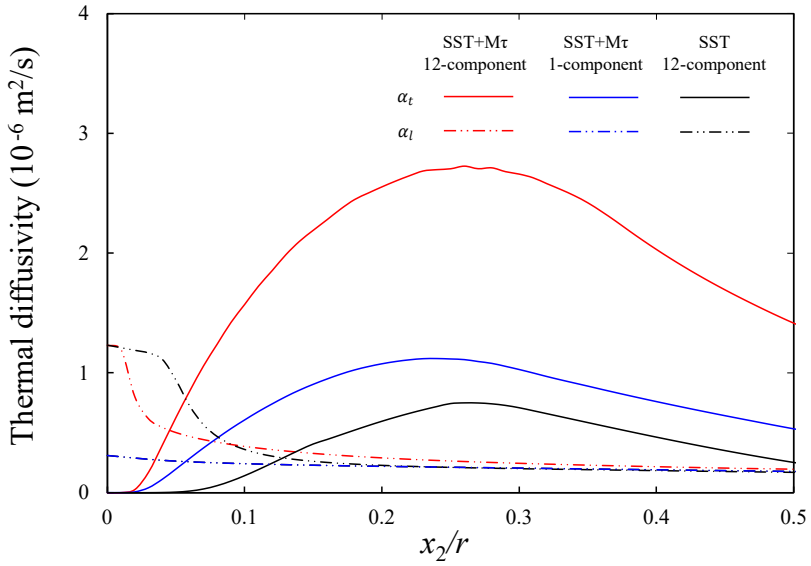

Figure 4.12. Cross-sectional thermal diffusivity at $x_1/r = 95$. The solid lines indicate the thermal diffusivity by eddy viscosity. The dotted lines indicated the thermal diffusivity by molecular dynamics.

Figure 4.13 shows the temperature distributions at $x_1/r = 95$. In the case of the 12-component model with the conventional $k-\omega$ SST model, the high-temperature region developed near the heated wall, even if the temperature in the main flow region was lower than that in the $k-\omega$ SST+M_τ model because of the low thermal diffusivity due to turbulence. This implies that only the fluid near the hot wall was heated, which allowed the fluid temperature of the $k-\omega$ SST model near the wall to rise beyond that of the $k-\omega$ SST+M_τ model. In the case of $k-\omega$ SST+M_τ with both component models, the high thermal diffusivity due to turbulence created a wider high-temperature region compared with that of the conventional

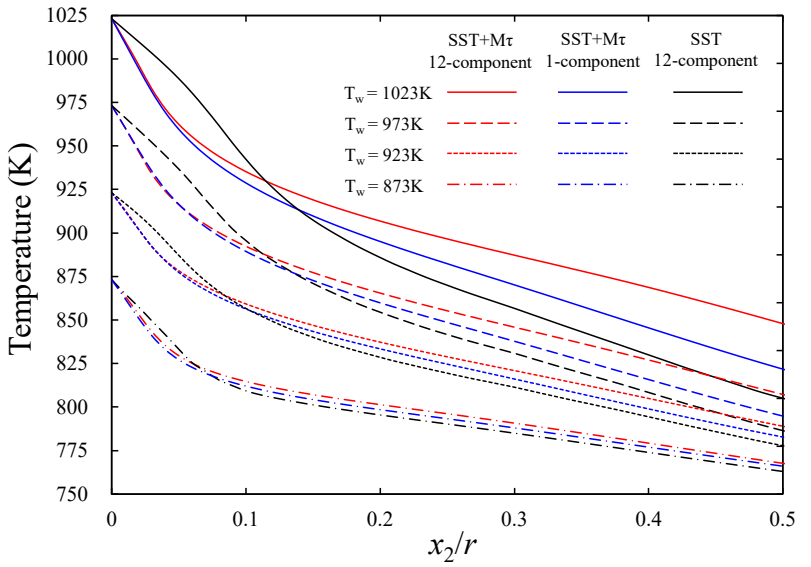

Figure 4.13. Cross-sectional temperature at $x_1/r = 95$ with multicomponent effect and production of turbulent kinetic energy.

$k-\omega$ SST model. The difference in temperature distribution between the two turbulence models was greater in higher wall temperature conditions. In the case where $T_w = 873$ K, the temperature distributions are almost the same for each component and turbulence model. The turbulent kinetic energy generation by the $k-\omega$ SST+M_τ model did not affect the temperature distribution for conditions below $T_w = 873.15$ K because of the low reaction rate and small temperature difference between the fluid and the heated wall. As octane is decomposed by pyrolysis at above 800 K, the high-temperature region above 800 K was much wider in the 12-component model with $k-\omega$ SST+M_τ in the case above $T_w = 923.15$ K, leading to the high conversion rate of pyrolysis.

Figure 4.14 shows the outlet temperatures of the heating pipe compared with the experimental data using each thermophysical property model. The error bars in the experimental data are defined as values within three standard deviations of the five experiments. For all thermophysical property models, the numerical results at wall temperatures below 950 K agreed with the experimental data, with a slight difference in values.

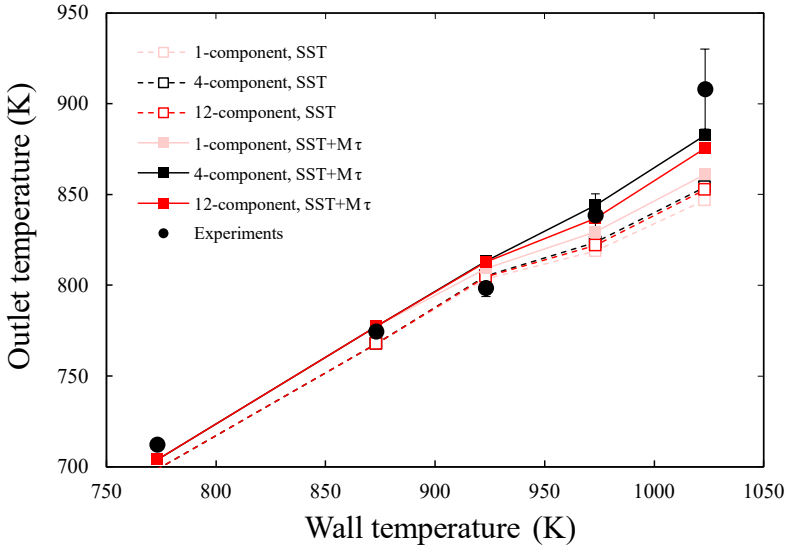

Figure 4.14. Outlet temperature with multicomponent effect and production of turbulent kinetic energy.

The numerical results of the $k-\omega$ SST model showed that the outlet temperatures in high wall temperature cases above 950 K were underestimated for all thermophysical property models, with a maximum difference of 50 K at $T_w = 1023.15$ K. The outlet temperatures of the 12- and 4-component models were slightly higher than those of the 1-component model. In the numerical simulations, the heating wall was maintained at a constant temperature according to the experimental conditions. The total heat in the section depends on the thermal boundary in each case. The thermal diffusivities in the 100% decomposition condition of the 1-, 4- 12- component models are $2.6 \times 10^{-7}\ m^2/s$, $6.7 \times 10^{-7}\ m^2/s$, and $6.3 \times 10^{-7}\ m^2/s$, respectively, at 950 K. The difference in total heat caused a slight difference in the outlet temperature of each component model. In all cases with the $k-\omega$ SST+M_τ model, the high turbulent thermal diffusivity due to the production of turbulent kinetic energy led to the higher outlet temperature compared with the conventional model. For instance, at $T_w = 973.15$ K and 1023.15 K, the outlet temperature with the production of turbulent kinetic energy was much higher than that with the conventional model. As shown in Fig. 4.12,

production of turbulent kinetic energy is responsible for the higher fluid temperature, owing to the high thermal diffusivity in the mainstream region. The effect of density change was much stronger at $T_w = 1023.15$ K. The 12- and 4-component models with the $k-\omega$ SST+M_τ model provided reasonable results with the experimental outlet temperature. At $T_w = 1023.15$ K, the outlet temperature of the 1-component model with $k-\omega$ SST+M_τ was slightly lower than that of the 12- and 4-component models. Because of the small number of components considered, the density of decomposed octane in the 4-component model was overestimated (Fig. 4.8(a)). The large density gradient in the 4-component model caused a slightly higher outlet temperature owing to the turbulent kinetic energy produced by the density change. Meanwhile, the 1-component model ignored the multicomponent effects on the thermophysical properties, which indicates that the turbulent kinetic energy generated by the multicomponent density change caused by pyrolysis is important for predicting the temperature distribution in uniform wall temperature cases.

The outlet conversion rate of each component model is shown in Figure 4.15. Because of the small amount of reaction at low fluid temperature, the decomposed hydrocarbons were not detected at $T_w = 773.15$ K and 823.15 K. In the case where $T_w = 873.15$ K, the maximum difference of the conversion rate between the case w/ and w/o M_τ term is less than 0.04% for each component model. These results indicate that the production of turbulent kinetic energy by the density fluctuation has no significant effect on the pyrolysis reaction below $T_w = 873.15$ K. In the case of a uniform fluid temperature flow where pyrolysis occurs mainly in the entire flow region, while it occurs near the thermal boundary in this study, the production of turbulent kinetic energy by the density fluctuation may have less impact on the conversion rate. The conversion rate increased linearly with the heated wall temperature in the experiments and reached 20% at $T_w = 1023.15$ K. The maximum conversion rate achieved in the numerical simulation with the conventional $k-\omega$ SST model was less than 5%. The conversion rates with the $k-\omega$ SST+M_τ model and 4- and 12-component models are compatible with the experimental results within a 2% difference for all wall temperatures. As shown in Fig. 4.13, the fluid temperature with the $k-\omega$ SST+M_τ model was higher than that with the conventional $k-\omega$ SST model because of the high thermal diffusivity caused by turbulence. In the results with the conventional $k-\omega$ SST model, the conversion rates at the outlet were not significantly different between the thermophysical property models, which considered the effects of the thermophysical properties of the decomposed components. In the 12-component model considering the thermophysical properties of several decomposed substances, the density decreased rapidly near the heated wall where pyrolysis occurred. As shown in Fig. 4.14, the outlet temperature in the 1-component model was lower than that in the other component models owing to the changes in thermophysical properties due to pyrolysis. This resulted in the slight underestimation of the conversion rate in the 1-component model because of the low fluid temperature at $T_w = 973.15$ K and 1023.15 K. At $T_w = 923.15$ K, the density change due to pyrolysis had a slight impact on the temperature distribution (Fig. 4.13), leading to the minimal difference in conversion rates between the 4- and 12-component models. On the basis of these numerical results, it can be concluded that the thermophysical properties were changed by the multicomponents, and the thermal diffusivities caused by turbulence flows are equally essential for the accurate prediction of supercritical hydrocarbon flows with pyrolysis. In this case, uniform wall temperature conditions were employed to reproduce the experimental conditions. The density difference between the fluid and heating

wall was much higher than in the case with a constant heat flux. The $k-\omega$ SST+M_τ model, which reproduced the production of turbulent kinetic energy by the density change, had a significant effect under uniform temperature conditions. However, the turbulence model effect should be thoroughly studied under constant heat flux conditions. There is still a difference with the experimental data in the case of $T_w = 1023.15$ K. Further physics or modeling is required to reproduce the flows with high wall temperature.

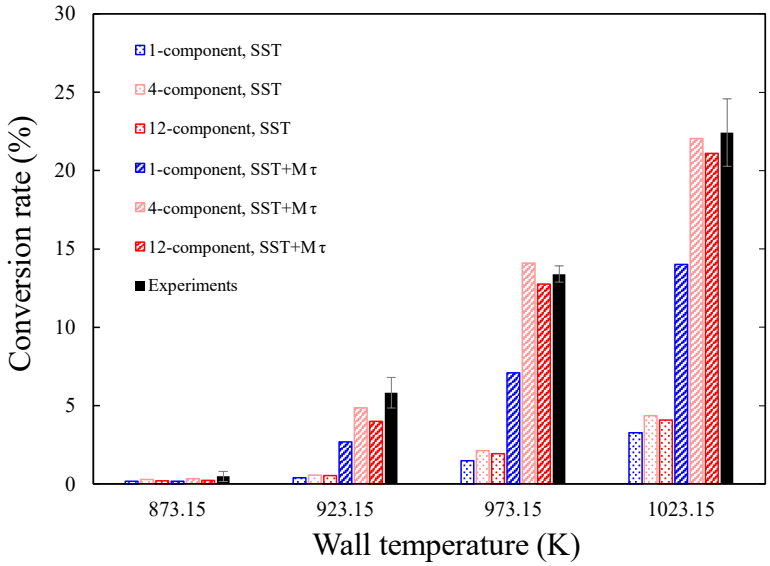

Figure 4.15. Outlet conversion rate with multicomponent effect and production of turbulent kinetic energy.

4.4 Conclusions

I conducted supercritical octane flow simulations with pyrolysis and considered the multicomponent effects of the changes in thermophysical properties. In the flow simulations, I determined the thermophysical properties of each component using the polynomial equations defined in REFPROP. I estimated the thermophysical properties of a mixture of decomposed components and a fed hydrocarbon by linear interpolation of the mass fraction of each component. In essence, the 4- and 12-component models considered the density change caused by hydrocarbons decomposed by pyrolysis, whereas the 1-component model assumed that the thermophysical properties were the same as those of pure *n*-octane. The reaction rate and endothermic energy were estimated based on the 0-D simulation of pyrolysis. The mole fraction of C_1–C_3 hydrocarbons exceeded that of the other hydrocarbons in the 0-D simulation. The maximum difference was 4.7% for the mole fraction of C_3H_8. I determined that the mole fractions obtained by 0-D simulation were acceptable to discuss the effects of multicomponent thermophysical properties on the thermal flow.

Subsequently, I simulated supercritical octane flows in a heated circular pipe with the reaction model and thermophysical properties model using in-house code. The conventional $k-\omega$ SST and $k-\omega$ SST+M_τ models were used as the RANS turbulence models. In particular, the $k-\omega$ SST+M_τ model considered the production of turbulent kinetic energy by density change, whereas all the component models considered the endothermic energy by octane pyrolysis. Because of the effects of low-density components in the 4- and 12-component models, the density near the heated wall was much lower than that of the fed octane.

At wall temperatures below 923.15 K, the numerical simulations reproduced the outlet temperature in all component models. However, in high wall temperature conditions, all the component models with conventional RANS underestimated the outlet temperature at which rapid pyrolysis occurred. In terms of turbulent kinetic energy production by density change, the turbulent thermal diffusivity increased near the heated wall. Nevertheless, the outlet temperature and conversion rate of the 4- and 12-component models with $k-\omega$ SST+M_τ were consistent with the experimental data, whereas the density of the mixture was much lower than that of the fed octane because of thermal expansion and the decomposed components near the heated wall. Simulated results suggest that accurate prediction of the density change and the corresponding production of turbulent kinetic energy are key issues for reproducing the thermal fluid flows of supercritical hydrocarbons with pyrolysis. In the present numerical simulation, uniform wall temperature conditions were employed to reproduce the experimental conditions and pyrolysis occurs near the heated wall. When pyrolysis occurs in the main flow region, the production of turbulent kinetic energy by the density fluctuation may have less impact on the conversion rate. Even though the pyrolysis reaction occurs near the heated wall, the turbulent kinetic energy by density fluctuation has little effect on the conversion rate in the case below 873.15 K. The turbulence model effect should be properly studied under different heating conditions.

References

1. S. Tomioka, T. Hiraiwa, T. Saito, K. Kato, M. Kodera, K. Tani, “System analysis of a hydrocarbon-fueled RBCC engine applied to a TSTO launch vehicle,” Transaction of Japan Society for Aeronautical and Space Sciences, 12(29), (2014), 91–99.
2. M. Pizzarelli, F. Nasuti, R. Votta, F. Battista, “Validation of conjugate heat transfer model for rocket cooling with supercritical methane,” Journal Propulsion Power, 32(3), (2016), 726–733.
3. T.A. Ward, J.S. Ervin, R.C. Striebich, S. Zabarnick, “Simulations of flowing mildly-cracked normal alkanes incorporating proportional product distributions,” Journal Propulsion Power, 20(3), (2004), 394–402.
4. B. Ruan, S. Huang, H. Meng, X Gao, “Transient responses of turbulent heat transfer of cryogenic methane at supercritical pressures,” International Journal of Heat and Mass Transfer, 109, (2017), 326–335.
5. Y. Feng, J. Qin, S. Zhang, W. Bao, Y. Cao, H. Huang, “Modeling and analysis of heat and mass transfers of supercritical hydrocarbon fuel with pyrolysis in mini-channel,” International Journal of Heat and Mass Transfer, 91, (2015), 520–531.
6. Y. Feng, Y. Jiang, X. Li, S. Zhang, J. Qin, Y. Cao, H. Huang, “Numerical study on the influences of heat and mass transfers on the pyrolysis of hydrocarbon fuel in mini-channel,” Applied Thermal Engineering, 119, (2017), 650–658.
7. Y. Feng, S. Liu, J. Qin, Y. Cao, Y. Jiang, S. Zhang, “Numerical study on the influence of turbulence on the pyrolysis of hydrocarbon fuel in mini-channel,” International Journal of Heat and Mass Transfer, 119, (2018), 768–776.
8. Y. Feng, J. Qin, S. Liu, S. Zhang, Xin Li and Y. Cao, H. Huang, “A simplification of pyrolytic reaction model of hydrocarbon fuel and its application in simulation of heated channel flow,” International Journal of Thermal Sciences, 130, (2018), 10–18.
9. R.P. Jiang, G.Z. Liu, X.W. Zhang, “Thermal cracking of hydrocarbon aviation fuels in regenerative cooling microchannels,” Energy Fuels, 27(5), (2013), 2563–2577.
10. K. Xu, H. Meng, “Modeling and simulation of supercritical-pressure turbulent heat transfer of aviation kerosene with detailed pyrolytic chemical reactions,” Energy Fuels, 29, (2015), 4137−4149.
11. Y.H. Zhu, B. Liu, P.X. Jiang, “Experimental and numerical investigations on *n*-decane thermal cracking at supercritical pressures in a vertical tube,” Energy Fuels, 28(1), (2014), 466–474.
12. K. Xu, B. Ruan, H. Meng, “Validation and analyses of RANS CFD models for turbulent heat transfer of hydrocarbon fuels at supercritical pressures,” International Journal of Thermal Sciences, 124, (2018), 212–226.
13. K. Xu, H. Meng, “Numerical study of fluid flows and heat transfer of aviation kerosene with consideration of fuel pyrolysis and surface coking at supercritical pressures,” International Journal of Heat and Mass Transfer, 95, (2016), 806–814.
14. Z. Tao, X. Hu, J. Zhu, Z. Cheng, “Numerical study of flow and heat transfer of n-decane with pyrolysis and pyrolytic coking under supercritical pressures,” Energy Fuels, 31, (2017), 8698−8707.

15. K. Xu, X. Sun, H. Meng, “Conjugate heat transfer, endothermic fuel pyrolysis and surface coking of aviation kerosene in ribbed tube at supercritical pressure,” International Journal of Thermal Sciences, 132, (2018), 209–218.
16. T. Jing, G. He, W. Li, D. Zhang, F. Qin, R. Li, “Flow and thermal analyses of supercritical hydrocarbon fuel in curved regenerative cooling channel around cavity in rocket based combined cycle engine,” Applied Thermal Engineering, 145, (2018), 423–434.
17. S. Liu, Y. Feng, Y. Chu, K. Gong, Y. Cao, “Numerical study of catalytic steam reforming of aviation kerosene at supercritical pressures,” Fuel, 212, (2018), 375-386.
18. S. Liu, Y. Feng, Y. Cao, K. Gong, W. Zhou, W. Bao, “Numerical simulation of supercritical catalytic steam reforming of aviation kerosene coupling with coking and heat transfer in mini-channel,” International Journal of Thermal Sciences, 137, (2019), 199–214.
19. S. Kawai, Y. Oikawa, “RANS modelling of density fluctuations for turbulent boundary layers at supercritical pressure,” NAGARE, 37, (2018), 105–110 (in Japanese).
20. S. Kawai, Y. Oikawa, “Turbulence modeling for turbulent boundary layers at supercritical pressure: A model for turbulent mass flux,” Flow, Turbulence and Combustion, 104, (2020), 625–641.
21. E.W. Lemmon, I.H. Bell, M.L. Huber, M.O. McLinden, “NIST standard reference database 23: Reference fluid thermodynamic and transport properties-REFPROP,” Version 10.0, National Institute of Standards and Technology, (2018).
22. S. Yamamoto, “Preconditioning method for condensate fluid and solid coupling problems in general curvilinear coordinates,” Journal of Computational Physics, 207(1), (2005), 240–260.
23. J.M. Weiss, W.A. Smith, “Preconditioning applied to variable and constant density flows,” AIAA Journal, 33(11), (1995), 2050–2056.
24. F.R. Menter, “Two-equation eddy-viscosity turbulence models for engineering applications,” AIAA Journal, 32(8), (1994), 598–1605.
25. A. Miyoshi, “Knowledge-basing utilities for complex reaction systems (KUCRS) software library,” http://akrmys.com/KUCRS/.
26. D.G. Goodwin, H.K. Moffat, R.L. Speth, “Cantera: An object-oriented software toolkit for chemical kinetics, thermodynamics and transport processes,” http://www.cantera.org.
27. K. Kurihara, T. Miyaura, Y. Daimon, S. Tomioka, “Study on chemical heat sink of *n*-dodecane under supercritical condition,” Proceedings of 32nd ISTS & NSAT, (2019), 2019-i-13.
28. D. Kunzru, Ph.D. Thesis, University of Pittsburgh, Pittsburgh, PA, (1972).
29. R. M. Abgrall, “How to prevent pressure oscillations in multicomponent flow calculations: A quasi conservative approach,” Journal of Computational Physics, 125, (1996), 150–160.

Chapter 5

Numerical investigations on flow instability of hydrocarbons at supercritical pressure

5.1 Introduction

Flow instability is a crucial issue in the design and operation of industrial systems such as steam generators, boiling water reactors, and high-power-density boilers. The work on flow instability was started by Ledinegg [1], who demonstrated that the pressure drop in a heated channel is expressed as a cubic curve with respect to the flow rate. This relationship is well-known as the multi-valued hydrodynamic characteristic curve. The negative slope region in the hydrodynamic characteristic curve has been recognized as a cause of flow excursion, which is one of the static instabilities. In addition, the flow excursion studied by Ledinegg is often called the Ledinegg instability. After Ledinegg's research [1] on flow instability, a great deal of experimental and numerical data [2-4] has been accumulated to the present. While much of previous studies focus on the two-phase flow instabilities under subcritical pressure, the flow instabilities under supercritical pressure have recently attracted the attention of researchers as the industrial use of supercritical fluids has expanded. In particular, the flow instabilities of supercritical hydrocarbon in the regenerative cooling system have been a barrier to the development of an engine of hypersonic aerospace vehicle such as a Rocket-Based Combined Cycle engine [5]. Flow instabilities can disturb heat transfer and induce mechanical vibration, and in extreme situations, possibly cause even mechanical breakdown.

Several researchers have studied the flow instability of water, CO_2, and refrigerant at supercritical pressure. Ambrosini [6] numerically analyzed the Ledinegg instability, a typical static instability, and density wave oscillation (DWO), a type of dynamic instability, for several different fluids, including H_2O, CO_2, R23, and ammonia. Ambrosini [6] confirmed that two dimensionless parameters sub-pseudo-critical number (N_{SPC}) and true trans-pseudo-critical number (N_{TPC}) are effective in representing the dynamic behavior of different fluids. In addition, Ambrosini [7] demonstrated the analogies between the dynamic behavior in a heated channel at subcritical and supercritical pressur. Sharabi et al. [8] carried out the three-dimensional simulation based on the Computational-Fluid-Dynamics (CFD) to investigate whether flow instability can be predicted by CFD models and whether the results qualitatively match with the results obtained by their one-dimensional models. Zhang et al. [9] conducted the two-dimensional axisymmetric flow simulations to

investigate the flow instability and heat transfer of water at supercritical pressures in a vertical tube. They also summarized the recent study on the flow instabilities under supercritical pressure conditions. Garg and Dutta [10] analyzed the Ledinegg instability, DWOs, and PWOs. They also investigated these interactions and the influence of the presence or absence of a surge tank. They used a similar methodology with Refs [11-13] to incorporate a steady-state pressure drop into the transient calculation. In the context of experimental study, Xiong et al. [14] experimentally studied the flow instability of water in parallel channels at supercritical pressure. Swapnalee et al. [15] experimentally demonstrated the presence of Ledinegg instability for supercritical water in a natural circulation loop, whereas any static instability for supercritical CO_2 has not been observed. Liu et al. [16] also conducted the experiment for supercritical CO_2 natural circulation, but eventually found no flow instabilities.

The flow instability of the hydrocarbon at supercritical pressure is one of the key issues in terms of the development of a regenerative cooling system. Hitch and Karpuk [17] were experimentally investigated and reported the flow instabilities of methylcyclohexane and JP-7 near the pseudocritical temperature and demonstrated that no substantial improvements by flow instabilities in heat transfer coefficients were realized with respect to normally forced convection. Wang et al. [18] experimentally investigated the thermo-acoustic instability of RP-3 in mini-tubes under a supercritical pressure condition and employed two dimensionless parameters of the true trans-pseudocritical number (N_{SPC}) and the sub-pseudocritical number (N_{TPC}) [7] to evaluate stability boundaries. Zhou et al. [19] experimentally studied the pressure-drop type instability of *n*-dodecane in a system with a horizontal circular tube and accumulator, and the mechanism of instability that occurs in pseudocritical temperature region and in pyrolysis temperature region was investigated using a zero-dimensional homogeneous model. Yang et al. [20-22] demonstrated the multi-valued hydrodynamic characteristics curve, which is a necessary condition of static instability, for hydrocarbon flows at supercritical pressure. Guo et al. [23] experimentally investigated the flow of endothermic hydrocarbon fuel in circular mini channels at supercritical pressures and clarified that the multi-valued hydrodynamic characteristics curve is expressed as a quintic function of flow rate because of the effects of the boiling (or pseudo-boiling) and the pyrolysis reaction. Jin et al. [24] conducted one-dimensional flow simulations of hydrocarbon using the proportional product distribution pyrolysis model [25], which did not demonstrate the fifth-order multi-valued characteristic curve.

Although numerous works on the flow instabilities have been conducted, the study of flow instabilities on endothermic hydrocarbon fuel (EHF) is still rare. The fifth-order hydrodynamic characteristic curve shown by Guo et al. [23] means that five stable equilibrium points can exist for a constant driving pressure drop $\Delta p_d = p_{\mathrm{in}} - p_{\mathrm{out}}$ in a heated circular channel and implies that flow instabilities may be more complicated. They explained that the large amount of non-condensable gas products produced by the pyrolysis reaction increases the pressure drop (which is why the fifth-order hydrodynamic characteristic curve was formed). For your information, the generation of non-condensable gases under pyrolysis conditions of kerosene fuel was also reported by Yang [26] et al. Although Guo et al. [23] researched the effect of heat flux, pressure, and diameter of the tube on the hydrodynamic characteristic curve as well, the effects of increasing order of the hydrodynamic characteristic curve on the behavior of flow instabilities have not been elucidated.

Another crucial issue is to elucidate the mechanism of multi-valued hydrodynamic characteristic curves at supercritical conditions. The hydrodynamic characteristic curve is related to several flow instability mechanisms: static instabilities such as Ledinegg instability and dynamic instabilities such as DWO and PWO [2]. Although Yang et al. [20-22] reported the multi-valued hydrodynamic characteristics curve at supercritical pressure, the mechanisms involved in the formation of the negative slope region of the multi-valued hydrodynamic characteristic curve is not clear enough.

To clarify the flow instability phenomenon, it is necessary to understand the rapid flow fluctuation in systems including pumps and heated tubes, as well as the mass flux-pressure drop characteristics in a heated tube. Since the mass flux-pressure drop characteristics in a heated tube are closely related to the initiation and maintenance mechanisms of the flow fluctuation, ideally, a numerical simulation that can handle these two issues at once is required. However, such a simulation is currently difficult in terms of computational cost. Regarding the former issue, flow instability is a large-scale problem both in time and space because the periodicity of flow fluctuations can be several tens of seconds or longer for long periods and because the entire system should be considered due to its principle. Therefore, detailed simulations considering multiple dimensions are not realistic due to the large computational cost. In addition, since the flow instability should be considered in the early design stage, an analysis method with a small computational cost is desirable when considering the future development process. That is why a one-dimensional numerical simulation method was employed to investigate the flow instability. Next, regarding the latter issue, there are many unresolved aspects in the mass flux-pressure drop characteristics under supercritical pressure conditions, and numerical simulations based on empirical lows or mathematical models should be avoided as much as possible. In addition, the analysis focuses on the mass-flux and pressure-drop characteristics at the steady state in a single heated tube, and the computational cost is relatively small, thus a detailed numerical method can be used. In the present study, the three-dimensional LES method is employed to investigate the mass-flux and pressure-drop characteristics in a heated tube.

First, I developed a robust numerical method to simulate flow instabilities in the EHF. The DFM in preconditioning system, which is shown in Chapter 2, was introduced to the one-dimensional simulation method to avoid spurious oscillations and realize robust simulations of flow instabilities. The present method was first used to obtain the hydrodynamic characteristic curve (steady-state pressure drop versus mass flow rate in the heated tube) of water and mass flow rate transient data, and these results were compared with available previous numerical data [6] to demonstrate that the method is as capable as the previous numerical method. Besides, the simulated results of cyclohexane flow in a horizontal circular tube were compared with experimental data [20] to demonstrate the capability of qualitatively predicting the outlet pressure and outlet temperature. Eventually, the present method was applied to transcritical *n*-dodecane flows with the pyrolysis reaction in a heated circular tube. As discussed in previous research by Guo et al. [23], the fluid flow of EHF in a heated tube may be more complicated because the hydrodynamic characteristic curve of EHF has an order of five, and five cross points (equilibrium points) would be expected for a constant pressure drop. In the present study, a new phase separation model (PSM) was developed to consider the effect of non-condensable gas products generated by pyrolysis reaction and to reproduce the fifth-order hydrodynamic characteristic curve of EHF. First, the steady-state simulations were conducted to obtain the hydrodynamic

characteristic curve for *n*-dodecane flows in a horizontal heated circular tube. The effects of DFM and PSM on the hydrodynamic characteristic curves were investigated. The influences of heat flux and pressure conditions on the hydrodynamic characteristic curves were also discussed. Then, the transient simulations of *n*-dodecane flows in a heated circular tube were performed to numerically investigate the dynamic behavior. The effects of phase separation, heat flux, and pressure conditions on flow instability were evaluated. Special attention was paid to the mechanism of flow instability under pyrolysis conditions, where knowledge is lacking.

Next, I investigated the mechanisms behind the formation of the multi-valued hydrodynamic characteristic curves using the large eddy simulation (LES) code. To validate the numerical method of LES, the turbulent channel flows were conducted. The average velocity and root mean square (RMS) velocity in the parallel channel were compared with available DNS data. Besides, the simulated adiabatic friction factors in a horizontal circular tube were compared with theoretical value and previous correlation to evidence enough capability of predicting the pressure field. Eventually, the LES were conducted for *n*-dodecane flows in a horizontal heated circular tube at supercritical pressure. Hydrodynamic characteristic curves were obtained under different three supercritical pressure conditions. To clarify the generation mechanisms of pressure-drop behind the formation of the hydrodynamic characteristic curves, the present LES analyzed the flow properties, such as the thermodynamic properties and local Nusselt number, and turbulence statistics in the heated circular tube.

Nomenclature

A	cross-sectional area (m^2)
c	speed of sound (m/s)
C_p	isobaric specific heat (J/kg/K)
D	diameter (m)
E	total internal energy per unit volume (J/m^3)
G	mass flux ($kg/m^2/s$) or mass flow rate (g/s)
H	total enthalpy (J/kg)
h	enthalpy per unit mass (J/kg)
h_p	partial derivative of enthalpy with respect to pressure
h_T	partial derivative of enthalpy with respect to temperature
h_{Y_n}	partial derivative of enthalpy with respect to mass fraction of nth component
L	tube length (m)
p	pressure (Pa)
q	heat flux (kW/m^2)
R	gas constant
T	temperature (K)
t	time (s)
U_i	contravariant velocities ($i = 1, 2, 3$)
u_i	velocities ($i = 1, 2, 3$)
x_i	Cartesian coordinates ($i = 1, 2, 3$)
Δp	pressure drop in a heated tube (Pa)
	Greek symbol
β	isobaric thermal expansion coefficient (K^{-1})
θ	preconditioning parameter
κ	thermal conductivity (W/m/K)
μ	molecular viscosity (Pa s)
ξ_i	general curvilinear coordinates ($i = 1, 2, 3$)
ρ	density (kg/m^3)
ρ_p	partial derivative of density with respect to pressure
ρ_T	partial derivative of density with respect to temperature
τ_{ij}	viscous stress tensors ($i, j = 1, 2, 3$)
	Subscripts
c	critical point
g	gas phase
in	inlet
l	liquid phase
out	outlet
pc	pseudocritical
w	wall

5.2 Numerical methods of one-dimensional simulations

5.2.1 Fundamental equations

The fundamental equations are the preconditioned compressible Navier–Stokes equations of conserved forms for the mass, momentum, and total energy. To solve the compressible unsteady flows at low-Mach numbers accurately and effectively, a preconditioning method with a dual time-stepping technique [27] were adopted for the system of equations. The system of equations is written in the vector form as follows:

$$\frac{\partial \boldsymbol{Q}}{\partial t}+\boldsymbol{\Gamma}\frac{\partial \widehat{\boldsymbol{Q}}}{\partial \tau}+\frac{\partial \boldsymbol{F}}{\partial x}+\boldsymbol{F_v}+\boldsymbol{S}=0, \tag{5.1}$$

where

$$\boldsymbol{Q}=\begin{bmatrix}\rho\\ \rho u\\ E\\ \rho Y_0\end{bmatrix},\widehat{\boldsymbol{Q}}=\begin{bmatrix}p\\ u\\ T\\ Y_0\end{bmatrix},\boldsymbol{F}=\begin{bmatrix}\rho u\\ \rho uu+p\\ (E+p)u\\ \rho Y_0 u\end{bmatrix},\boldsymbol{F_v}=\begin{bmatrix}0\\ -\dfrac{f_{l0}}{D_{\mathrm{h}}}\phi_{l0}^2\dfrac{\rho u^2}{2}\\ q\dfrac{\Pi_{\mathrm{h}}}{A}\\ 0\end{bmatrix},\boldsymbol{S}=\begin{bmatrix}0\\ 0\\ 0\\ s_{Y_0}\end{bmatrix}.$$

$$\boldsymbol{\Gamma}=\begin{bmatrix}\theta & 0 & \rho_T & \rho_{Y_0}\\ \theta u & \rho & \rho_T u & \rho_{Y_0}u\\ \theta H-(1-\rho h_p) & \rho u & \rho_T H+\rho h_T & \rho_{Y_0}H+\rho h_{Y_0}\\ \theta Y_0 & 0 & \rho_T Y_0 & \rho+\rho_{Y_0}Y_0\end{bmatrix}.$$

$\boldsymbol{Q}$, $\widehat{\boldsymbol{Q}}$, $\boldsymbol{F}_i$, $\boldsymbol{F}_v$, and $\boldsymbol{S}$ are the vectors of the conservative variables, unknown variables, inviscid flux, viscous flux, and source term respectively. $\boldsymbol{\Gamma}$ is the preconditioning matrix derived from the Jacobian matrix for $\widehat{\boldsymbol{Q}}$. The pseudo-time term in Eq. (5.1) converges to zero as $\tau\to\infty$, and the system of equations becomes the conservative form. When performing the steady-state simulation, the physical-time term in Eq. (1) was omitted. The diffusion flux of streamwise direction was neglected in the present study because the flows solved in the present study were forced convection, and the streamwise diffusion is weak compared to the streamwise convection [28]. s_{Y_0} is the decomposition rate of *n*-dodecane pyrolysis reaction that was evaluated using a zero-dimensional pyrolysis reaction modeling method shown in detail in Chapter 3. The pyrolysis reaction model was a one-step global reaction model and considers 16 decomposed components (H_2, CH_4, C_2H_4, C_2H_6, C_3H_6, C_3H_8, 1-C_4H_8, *n*-C_4H_{10}, 1-C_5H_{10}, *n*-C_5H_{12}, *n*-C_6H_{14}, *n*-C_7H_{16}, *n*-C_8H_{18}, *n*-C_9H_{20}, *n*-$C_{10}H_{22}$, and *n*-$C_{11}H_{24}$). The production rate was modeled as a function of temperature based on preliminary detailed zero-dimensional reaction simulations. f_{l0} is the friction factor in smooth tubes and is expressed by the Filonenko correlation as follows:

$$f_{l0} = \begin{cases} \dfrac{64}{Re}, & \text{when } Re < Re_{cr}. \\ [1.58 \times \log_e(Re) - 3.28]^{-2}, & \text{when } Re_{cr} < Re \end{cases} \tag{5.2}$$

ϕ_{l0}^2 is the appropriate two-phase multiplier. In the present study, ϕ_{l0}^2 was used for modeling the two-phase flow induced by pyrolysis reaction which produces non-condensable gas products [23, 26]. The detail is shown in the subsection of 5.2.4. The preconditioning parameter θ is defined as follows:

$$\theta = \frac{1}{U_r^2} - \frac{\rho_T(1 - \rho h_p)}{\rho h_T}, \tag{5.3}$$

where U_r is the switching parameter as

$$U_r = \min[c, \max(u, 3u_\infty)]. \tag{5.4}$$

The local velocity is defined as $u = \sqrt{u_i u_i}$, and u_∞ is a reference velocity which defined by the inlet or the maximum velocity.

5.2.2 Numerical methods

The numerical flux was evaluated using the preconditioned flux-vector splitting scheme [29] of the approximate Riemann solver. The unknown variables were interpolated using the MUSCL scheme [30]. The second-order explicit Runge–Kutta scheme with dual-time stepping technique was employed for time integration of pseudo time. The physical time-derivative in Eq. (5.1) was evaluated by using a second-order backward difference scheme. The DFM in the preconditioning method, which is shown in detail in Chapter 2, was employed to prevent the spurious oscillations and stably simulate the transcritical flow.

5.2.3 Thermodynamic and transport properties model for mixture

The thermodynamic and transport properties were calculated by using the same technique in Chapter 2. However, the partial derivatives of the density and enthalpy with respect to the mass fraction were modified because of the change in the fundamental equations as follows:

$$\rho_{Y_0} = \rho^2 \left(\sum_{i=1}^{n} \frac{\alpha_i}{\rho_i} - \frac{1}{\rho_0} \right), \tag{5.5a}$$

$$h_{Y_0} = h_0 - \sum_{i=1}^{n} \alpha_i h_i. \tag{5.5b}$$

α_i is production ratio of pyrolysis products shown in Table 5.1.

Due to the complexity of the calculation procedure for thermophysical properties, a look-up table method was used to reduce computational time. In this method, thermodynamic and transport properties in the pressure and temperature parameter space were calculated using REFPROP at constant intervals. In the present study, the data points of look-up tables in the pressure and temperature parameter space were set with a constant interval of $\Delta p = 0.005$ MPa and $\Delta T = 1.0$. The thermophysical properties were interpolated with linear interpolation. The pre-prepared lookup tables were used to calculate thermophysical properties in flow simulations. Figure 5.1 shows the density, isobaric-specific heat, viscosity, and thermal conductivity for *n*-dodecane with respect to temperature at three different pressure conditions. These thermophysical properties strongly depend on the pressure and drastically change near the pseudocritical temperature where the isobaric-specific heat reaches the maximum value. The plots tabulated by the look-up table method were consistent with the NIST data at 3.0 MPa.

Table 5.1. Critical properties and production ratios of *n*-dodecane and decomposed components

Components	Chemical formula	p_c (MPa)	T_c (K)	Production ratio
Hydrogen	H_2	1.30	33.15	0.0176
Methane	CH_4	4.60	190.6	0.1223
Ethylene	C_2H_4	5.04	282.4	0.1942
Ethane	C_2H_6	4.87	305.3	0.1379
Propylene	C_3H_6	4.56	364.2	0.1204
Propane	C_3H_8	4.25	369.9	0.0647
1-butene	C_4H_8	4.01	419.3	0.0391
N-butane	C_4H_{10}	3.80	425.1	0.0154
1-pentene	C_5H_{10}	3.60	465.7	0.0440
N-pentane	C_5H_{12}	3.37	469.7	0.0174
N-hexane	C_6H_{14}	3.04	507.8	0.0667
N-heptane	C_7H_{16}	2.74	540.2	0.0463
N-octane	C_8H_{18}	2.48	568.7	0.0416
N-nonane	C_9H_{20}	2.28	594.6	0.0374
N-decane	$C_{10}H_{22}$	2.10	617.7	0.0255
N-undecane	$C_{11}H_{24}$	1.99	638.8	0.0095
N-dodecane	$C_{12}H_{26}$	1.82	658.1	-

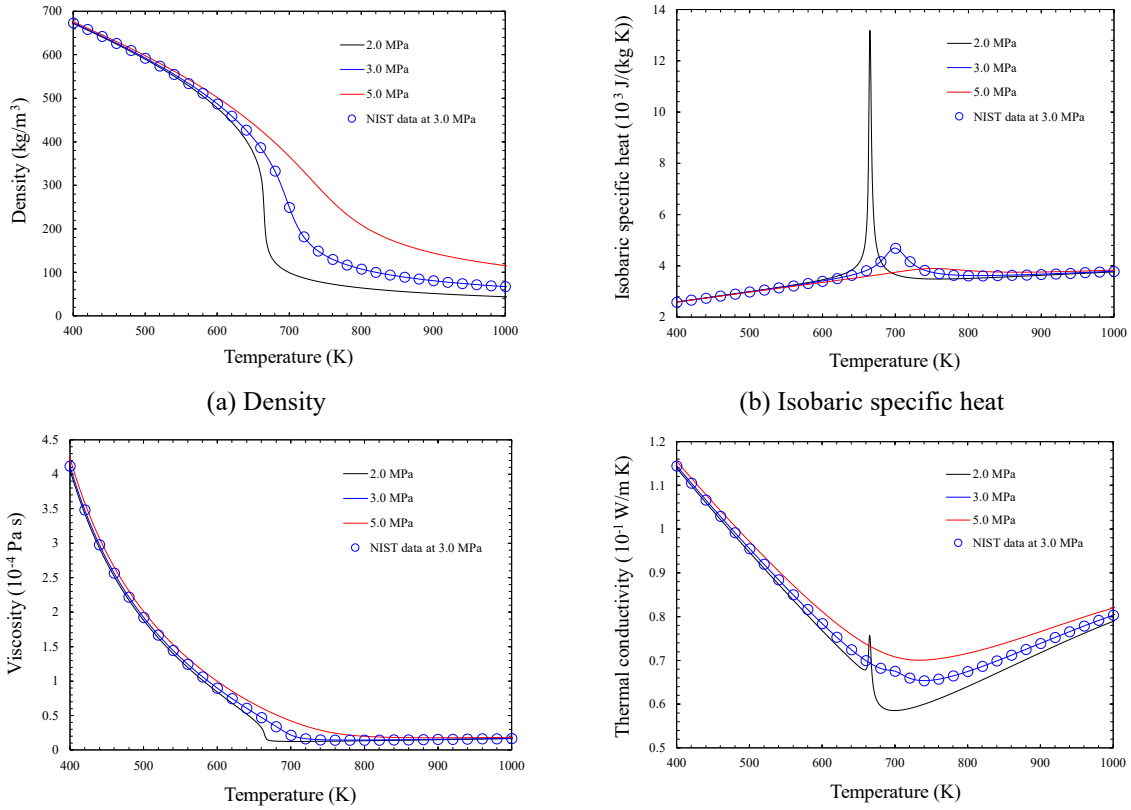

(a) Density (b) Isobaric specific heat

(c) Viscosity (d) Thermal conductivity

Figure 5.1. Thermophysical and transport properties for *n*-dodecane at different pressure conditions. Circles, NIST data; lines, look-up table method.

5.2.4 Phase-separation model by using two-phase correction of friction factor

As discussed by Guo et al. [23], the non-condensable gaseous products from pyrolysis may affect the pressure drop in a heated pipe. To consider the effect of non-condensable gaseous products from pyrolysis, the two-phase correction of friction factor was extended to the pyrolysis condition. Chisholm [34] proposed the friction factor of two-phase flow. The ratio of two-phase friction drop Δp_{TP} and single phase friction drop Δp_{l0} is expressed as follows:

$$\phi_{l0}^2 = \frac{\Delta p_{TP}}{\Delta p_{l0}} = 1 + \frac{c_1}{X} + \frac{1}{X^2}, \tag{5.6}$$

where

$$c_1 = \left[a + (c_2 - a)\left(1 - \frac{\rho_g}{\rho_l}\right)^{0.5}\right]\left(\sqrt{\frac{\rho_l}{\rho_g}} + \sqrt{\frac{\rho_g}{\rho_l}}\right), \tag{5.7a}$$

$$X = \left(\frac{1-x}{x}\right)^{(2-n)/2}\left(\frac{\rho_g}{\rho_l}\right)^{0.5}\left(\frac{\mu_l}{\mu_g}\right)^{n/2}. \tag{5.7b}$$

Here, the value of a was set to 0.75 assuming a smooth tube in the present study ($a = 1$ for rough tube). c_2 is a constant or a function of mass flux G shown in Table 5.2, and values for the smooth cases ware used in the present study. The value of n was set to 0.2 assuming a smooth tube ($n = 0$ for rough tube). The subscripts g and l represent the gas phase and liquid phase, respectively. x is so-called dryness fraction.

Table 5.2. Value of c_2 in Eq. (5.7a) for smooth and rough tubes

	Smooth tube		Rough tube	
G $[\mathrm{kg/m^2/s}]$	$G > 204$	$G < 204$	$G > 153$	$G < 153$
c_2	1	$\frac{204}{G}$	1	$\frac{153}{G}$

Dryness fraction x should be the sum of mole fraction for non-condensable gas components. Therefore, the phase equilibrium of the mixture formed as a result of the pyrolysis reaction need to be considered. In the present study, the vaper-liquid equilibrium (VLE) analysis conducted to identify the phase separation conditions of hydrocarbon mixture. The calculations were performed using the routines for VLE analysis defined in REFPROP. The present VLE analysis calculated the temperature, the liquid phase composition, and the thermophysical properties at phase equilibrium conditions by giving the pressure and the gas phase composition as an input. The problem here was how to decide the input composition. Diffusion changes the composition of the mixture in a flow field. Therefore, the composition patterns of the 17-component mixture, which is shown in Table 5.1, to be considered are very numerous. Although the composition pattern can be greatly reduced by ignoring diffusion, the validation of the calculation is difficult because of the lack of vapor-liquid equilibrium data for the present 17-component mixture. The detailed model for a 17-component mixture has little benefit. In the present study, assuming that all decomposed components are surrogated by ethane, which is the main (more than 10%) decomposed component, a binary mixture of *n*-dodecane–ethane was considered. Ethylene, the most abundant component (19.42% of the decomposed components), was not selected as a representative component because the binary mixing coefficient for *n*-dodecane and ethylene was not defined in the REFPROP.

Before performing the phase separation analysis of *n*-dodecane–ethane mixtures, the validation of the VLE analysis method was performed. Figure 5.2 compares the calculated results for the pressure-density diagram of an *n*-dodecane–ethane mixture with the experimental data [36]. The circles are the experimental data, and the lines are the calculated results. In the temperature range from 0 °C to 100 °C and at pressures up to 62 atm, five bubble point isotherms were calculated. The calculated results agreed well with the experimental data for all temperature conditions. The results demonstrated the capability of the present VLE analysis method to correctly predict phase equilibrium for *n*-dodecane–ethane mixture.

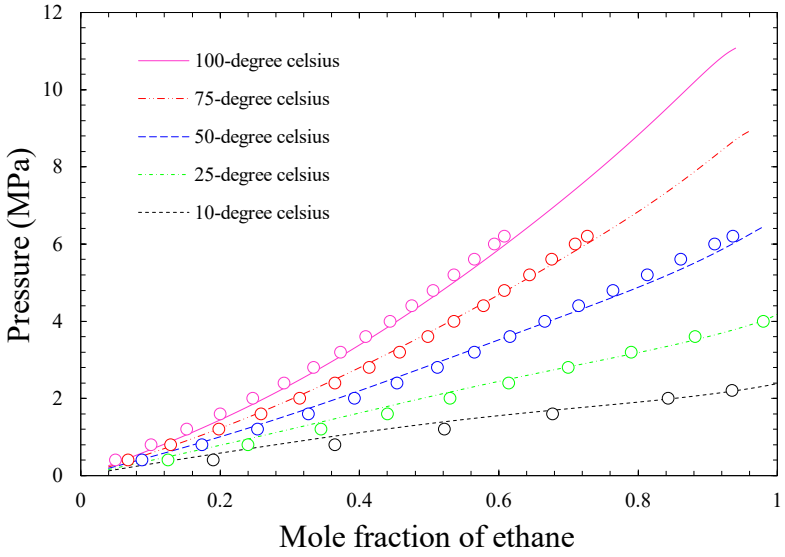

Figure 5.2. Equilibrium pressure at each mole fraction of ethane in the liquid phase. Circles, experimental data; lines, calculated results.

Figure 5.3 presents VLE compositions for a binary system consisting of *n*-dodecane–ethane at different pressures. The critical mixing temperature decreased with increasing pressure as more ethane dissolves into the liquid phase. Interestingly, the critical pressure of a mixture could be greater than the critical pressure of the pure substances that compose the mixture. For example, whereas the critical pressure of *n*-dodecane–ethane is 1.817 MPa and 4.872 MPa, that of mixture could reach 10 MPa or higher as shown in Fig. 5.3.

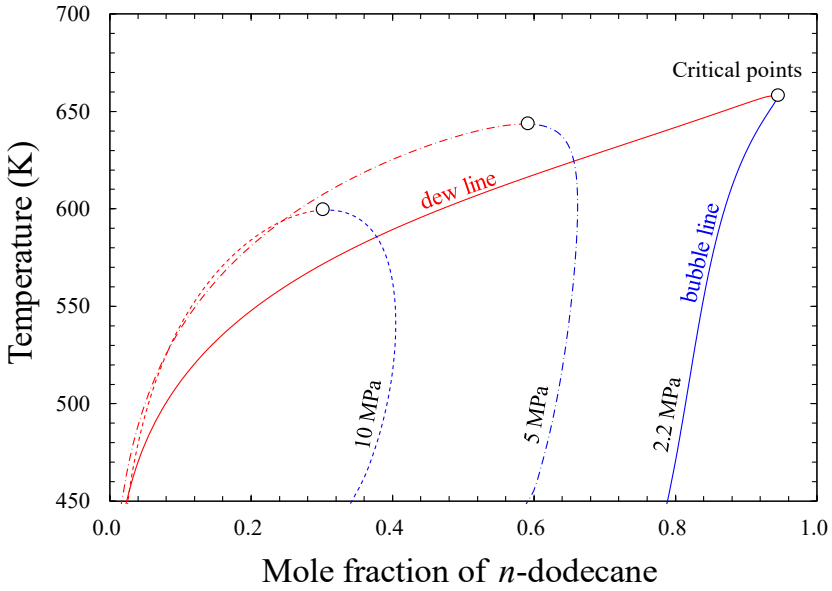

Figure 5.3. Phase diagrams with respect to temperature and *n*-dodecane mole fraction at different pressures. Red, bubble lines; Blue, dew lines; solid lines, 2.2 MPa; dashed-dotted lines, 5 MPa; dashed line, 10 MPa.

Even over the critical pressure of all pure materials, dew lines and bubble lines existed in a fluid mixture, suggesting that a two-phase state may be unavoidable. For reference, Figure 5.4 shows the VLE analysis results of a binary mixture of *n*-dodecane and the other main components of methane, ethylene, and propane, as well as the 17-component mixture shown in Table 5.1. Although the bubble lines in Fig. 5.4 indicate clear differences depending on the mixture, i.e., the difference in dissolvability into the liquid side, the difference between the dew lines and the critical temperatures is relatively small. Interestingly, Fig. 5.4 shows similar phase separation regions of the binary mixtures and the complex 17-component mixture. Note that although the composition of the 17-component mixture is given uniquely here, the composition patterns in the actual flow field are numerous because of diffusion.

Estimation of representative interface conditions in a flow field requires the consideration of a mixing process in addition to the VLE analysis. Assuming the adiabatic mixing [37] or isochoric mixing [38] as previous studies, the representative interface state expressed by pressure, temperature, and composition can be defined. However, in terms of hydrocarbon mixing at supercritical pressure, the measured data is still rare, the validation of the assumptions for mixing conditions is difficult. Therefore, the equilibrium composition at the average equilibrium temperature was defined as the representative interface state in the present study. Figure 5.5 shows the equilibrium composition of liquid and vapor side at the averaged equilibrium temperature of 529 K and the pressure of 2.2 MPa. *N*-dodecane was the main component of the liquid phase, accounting for about 83%, while ethane accounted for about 82% of the vapor phase. The density and viscosity of the liquid phase were 518 kg/m^3 and 1.13×10^{-4} Pa s, respectively. Those of the vapor phase were 26.4 kg/m^3 and 1.50×10^{-5} Pa s, respectively. As a result of the VLE analysis, a representative interface state of the *n*-dodecane–ethane mixture at 2.2 MPa condition was defined.

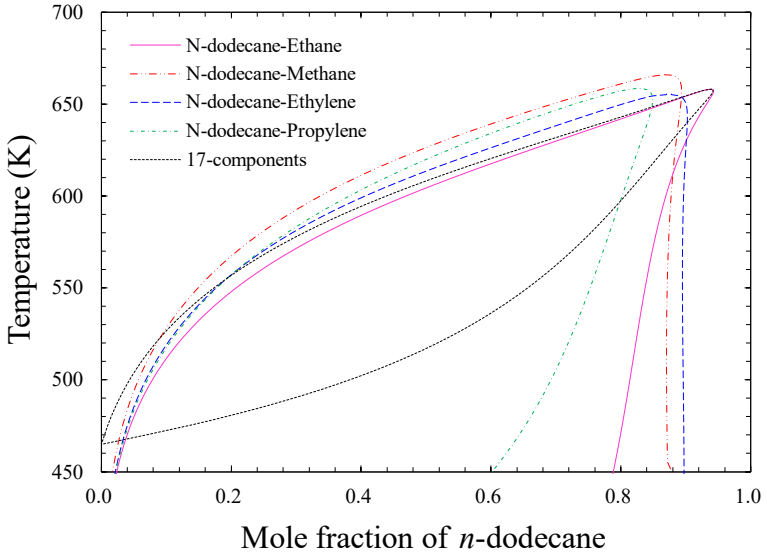

Figure 5.4. Phase diagrams with respect to temperature and *n*-dodecane mole fraction for different mixtures, which include *n*-dodecane, at $p = 2.2$ MPa.

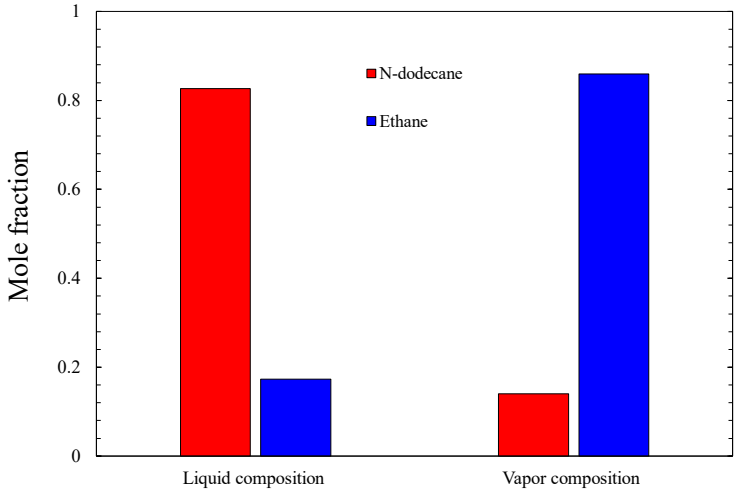

Figure 5.5. Composition of both phase at the averaged equilibrium temperature of $T = 529$ K at $p = 2.2$ MPa. Liquid side density and viscosity are 518 kg/m^3 and 1.13×10^{-4} Pa s; vapor side density and viscosity are 26.4 kg/m^3 and 1.50×10^{-5} Pa s.

Next, the phase separation process in the flow field was discussed. The critical temperature of the *n*-dodecane–ethane mixture was 658 K as shown in Fig. 5.3, which is below the initiation tempareture of the pyrolysis reaction. Therefore, I may assume the phase separation process in a heated tube as follows: First, the pyrolysis reaction occurs in the high-temperature region near the heated wall, and decomposed components are generated. Next, the decomposed components are transported to the low-temperature mainstream region by radial mass transport. Finally, phase separation occurs when the temperature of the mixture decreases below the critical temperature of the mixture and the composition is between the dew line and the bubble line. When the mainstream temperature is heated sufficiently to exceed the critical temperature, the phase-separated gas components condense. And the mixture is to be single-phase and homogeneous flow again. Figure 5.6 shows the series of phase-separation processes in a heated tube.

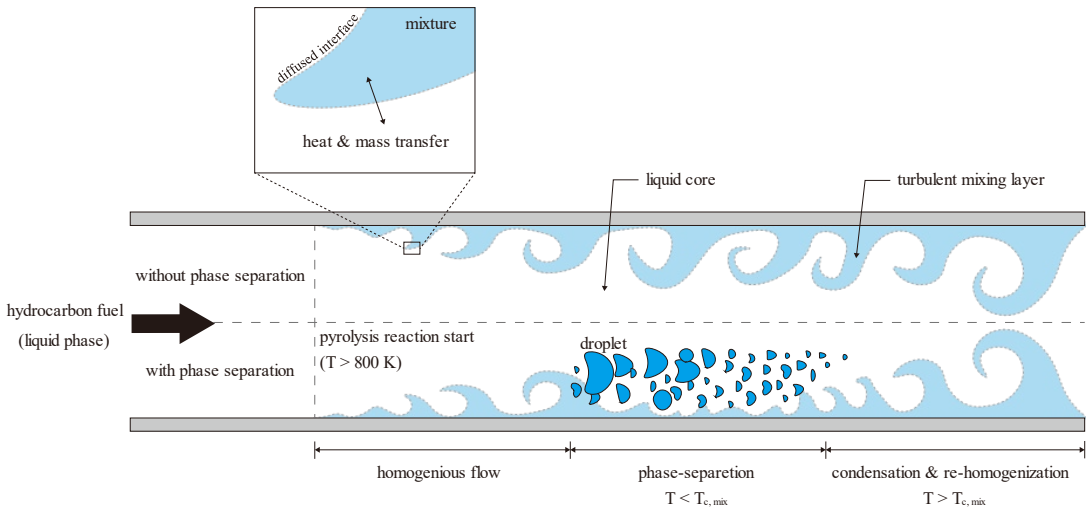

Figure 5.6. Expected phase separation process of hydrocarbon mixture in a heated circular tube.

An estimation of the mainstream temperature, which is the lowest temperature in the cross-section, is necessary to judge the possibility of phase separation in a one-dimensional simulation. In the present study, the mainstream temperature was defined as follows:

$$T_m = 2T_b - T_w, \tag{5.8}$$

where

$$T_w = T_b + \frac{q_w d}{2kNu}, \tag{5.9a}$$

$$Nu = 0.041 Re^{1.117} Pr^{1/3} f_{l0}. \tag{5.9b}$$

Eq. (5.8) was derived by defining the bulk temperature T_b as the arithmetic average of the wall temperature T_w and mainstream temperature T_m. Here, the bulk temperature T_b was obtained as a solution of the fundamental equation. Eq. (5.9b) is the correlation of the Nusselt number proposed by Meyer et al. [39]. If the mainstream temperature is lower than the critical temperature of the mixture and the composition is between the dew line and the bubble line, judge that phase separation occurs and consider the two-phase correction of friction factor expressed as Eq. (5.6). Note that the dryness fraction x and thermophysical properties required in Eq. (5.7a) and (5.7b) were given based on the result in Fig. 5.5.

5.3 Numerical results of one-dimensional simulations

5.3.1 Comparison of present 1-D simulations with existing data

To validate the capability of analyzing the hydrodynamic characteristic curves and the flow instabilities for the present method, two case studies were conducted in this section. At first, the supercritical water flows in a horizontal heated circular tube [6] were simulated to obtain the hydrodynamic characteristic curves and transient mass flow rate data. Results obtained at three different inlet temperatures were compared with those obtained by Ambrosini. Then, the supercritical cyclohexane flows in a horizontal heated circular tube were performed, and the pressure-drop and outlet temperature were compared with existing experimental data reported by Yang et al. [20].

Figure 5.7 shows a schematic diagram of a horizontal heated circular tube targeted in the present simulations. Table 5.3 shows the geometrical parameters and computational conditions of the steady-state simulations for water flows in a horizontal heated channel conducted by Ambrosini [6]. The outlet pressure was set to 25 MPa, which is above the critical pressure of 22.064 MPa. The computational grid number was

48 following Ambrosini's study [6], and the grid spacing was set to uniform. The CFL number of the pseudo time was set to 0.9. For steady-state calculations, the physical-time term in Eq. (5.1) was omitted, and the dual-time stepping method was not applied (as well in the following sections).

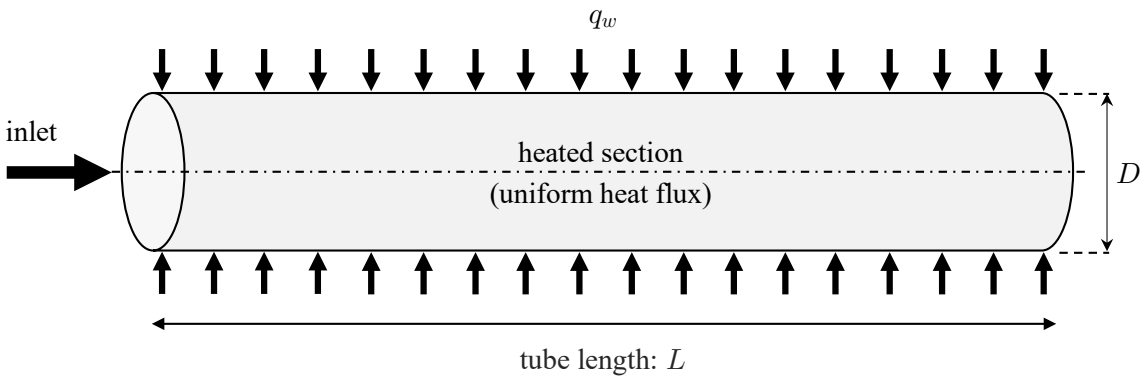

Figure 5.7. Schematic diagram of the horizontal heated circular tube targeted in the present simulations.

Table 5.3. Geometrical parameters and computational conditions of static analysis conducted by Ambrosini [6]

Fluid	Water
Heated section length [m]	4.2672
Diameter [mm]	8.36
Heat flux [kW/m^2]	25
Outlet pressure [MPa]	25

The procedures of steady-state and transient simulations in this section were as follows: Firstly, steady-state simulations were run at all pre-specified inlet mass flow rates to obtain the pressure drop $\Delta p\ (= p_{\mathrm{in}} - p_{\mathrm{out}})$ to be applied in the subsequent transient analysis. Then, transient simulations were run using certain pairs of the mass flow rate and pressure drop obtained from the steady-state simulation as initial conditions. Gradually increasing the heat flux while maintaining the pressure drop constant, i.e., fixed the inlet and outlet pressure. Iterative calculations were continued until the residue (L2 norm) decreased by 3 orders of magnitude.

Figure 5.8 shows the hydrodynamic characteristic curves obtained from steady-state simulations at different inlet temperatures. A reference friction coefficient of 0.017 was adopted in this case following Ambrosini's study [6]. The results obtained by the present method were in good agreement with Ambrosini's results for all inlet temperature conditions except the high mass flow rate conditions. Focusing on the results for the inlet temperature condition of 373 K, the negative slope region, which has known as a cause of Ledinegg instability, was consistent in both the present and Ambrosini's simulations.

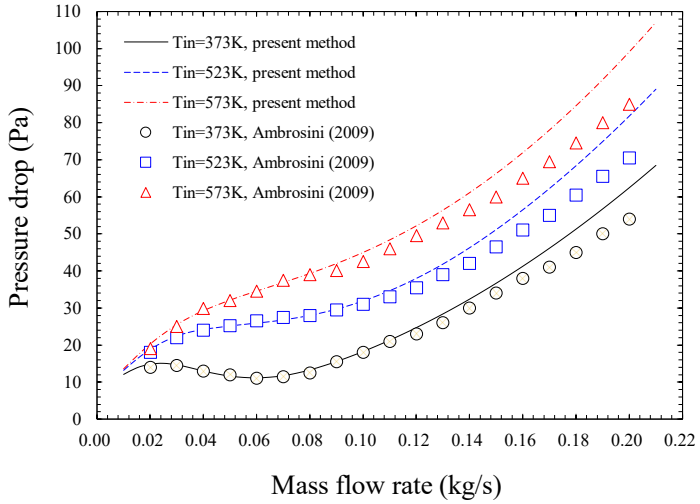

Figure 5.8. Hydrodynamic characteristic curves of water at different inlet temperatures in heated horizontal channel.

Figures 5.9 show the $\mathrm{N_{TPC}}$ fluctuations of supercritical water predicted by present transient simulations under two different $\mathrm{N_{SPC}}$ conditions. Here, the dimensionless parameters $\mathrm{N_{TPC}}$ and $\mathrm{N_{SPC}}$ proposed by Ambrosini [7] are written as follows:

$$\mathrm{N_{TPC}} = \frac{q\Pi_{\mathrm{h}} L}{\rho_{\mathrm{in}} u_{\mathrm{in}} A} \frac{\beta_{\mathrm{pc}}}{C_{p,\ \mathrm{pc}}}, \tag{5.10a}$$

$$\mathrm{N_{SPC}} = \frac{\beta_{\mathrm{pc}}}{C_{p,\ \mathrm{pc}}} (h_{\mathrm{pc}} - h_{\mathrm{in}}). \tag{5.10b}$$

Also, two plots obtained with the fixed friction factor of 0.017 and the friction factor f_{l0} were plotted in Fig. 5.9. As Ambrosini [6] showed in the previous study, differences in the friction factor did not affect qualitative behavior and had a small quantitative effect. At $\mathrm{N_{SPC}} = 1.5$ (Fig. 5.9(a)), typical DWOs were observed. Here, DWOs are the following phenomena. Considered a heated tube with constant heat flux under a constant driving pressure condition, when a fluctuation in the inlet velocity occurs, it takes some time for the fluctuation to propagate to the outlet. The enthalpy, density, velocity, and pressure drop fluctuate with a time delay relative to the inlet velocity fluctuation. These fluctuations then feedback to the inlet velocity in relation to the constant driving pressure. Since disturbances of flows can be the initial fluctuation, the self-excited oscillation occurs even if no external force is applied, and limit cycles with constant amplitude and period are generated [2]. At $\mathrm{N_{SPC}} = 2.5$ (Fig. 5.9(b)), the dynamic behavior is an excursive type Ledinegg instability, oscillating with a much longer period than at $\mathrm{N_{SPC}} = 1.5$. This change in behavior according to $\mathrm{N_{SPC}}$ value was very similarly seen in the Ambrosini simulation [6]. Furthermore, the $\mathrm{N_{TPC}}$ values in which the instability occurs were in good agreement between the present simulation and the previous Ambrosini simulation [6]. Results of transient simulations demonstrate the equivalent ability of the previous method [6] to analyze the flow instabilities at supercritical pressure.

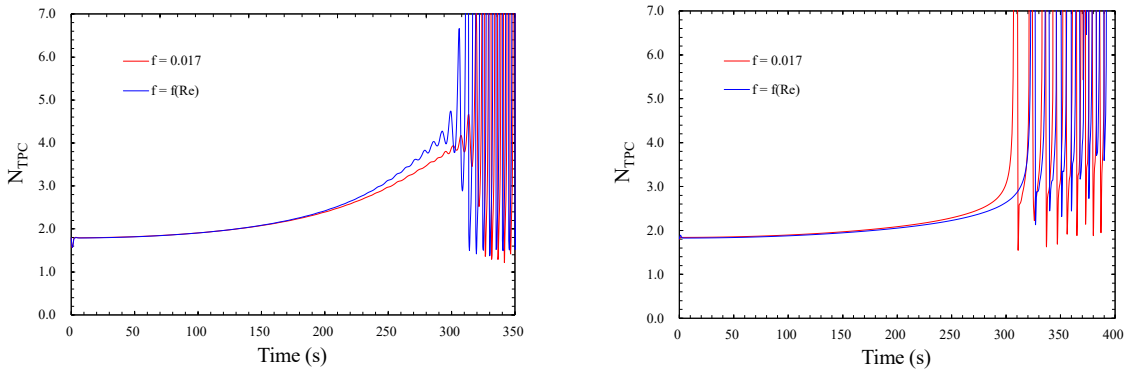

(a) $\mathrm{N_{SPC}} = 1.5$ (b) $\mathrm{N_{SPC}} = 2.5$

Figure 5.9. Flow instabilities of water predicted at 25 MPa under two different $\mathrm{N_{SPC}}$ conditions.

Table 5.4 shows the experimental conditions for cyclohexane flows in a horizontal heated channel conducted by Yang et al. [20]. The pressure was set to 4.5 MPa, which is above the critical pressure of 4.08 MPa. The physical time step was set to 2.0×10^{-3}. The CFL number of the pseudo time was set to 0.9, however the value of $\delta\tau/\delta t$ was limited to less than unity for stability.

Table 5.4. Conditions of the experiment conducted by Yang et al. [20].

Fluid	Cyclohexane
Heated section length [m]	0.38, 0.61
Diameter [m]	0.002
Heat flux [kW/m^2]	265
Outlet pressure [MPa]	4.5
Inlet temperature [K]	323.15

A grid convergence study was conducted before the numerical studies to ensure the consistency of the numerical method to be used. The three sets of grids, 101, 201, and 401 were used for the grid convergence study. Calculating the pressure drop at $q = 465\ \mathrm{kW/m^2}$ for each grid system, the maximum relative errors at the onset point of flow instability (OFI) point were within 1% among three grids. Therefore, the grid system with 101 grids was employed. Note that the grid spacing was uniform.

Figures 5.10 show the pressure drop and outlet temperature with respect to the mass flow rare obtained from steady-state simulations at different channel length. Although the heat flux value in the present simulation of $q = 465\ \mathrm{kW/m^2}$ is different from the experiment value of $q = 265\ \mathrm{kW/m^2}$, the simulated results were in qualitative agreement with the experimental data. The present method was able to reproduce the negative slope region of hydrodynamic characteristic curves, which is the cause of Ledinegg instability, and the OFI point, which is a local minimum point. One of the problems faced by 1D simulations of supercritical flows is the less valid friction factor options for supercritical fluids, which make the prediction of pressure drop difficult. Currently, several friction factor correlations for supercritical fluids have been

proposed [40-43]: however, the number of studies for the friction factor at supercritical pressure is few, and the applicable range is limited. Therefore, it seems that the conventional friction factor correlations such as Churchill-Chu, Filonenko, and Colebrook-White (implicit) correlations were often used in the previous study [10, 44]. Quantitative prediction of supercritical flow by one-dimensional simulation is still a challenge. The present study used our numerical methods to qualitatively discuss flow instabilities at supercritical pressures.

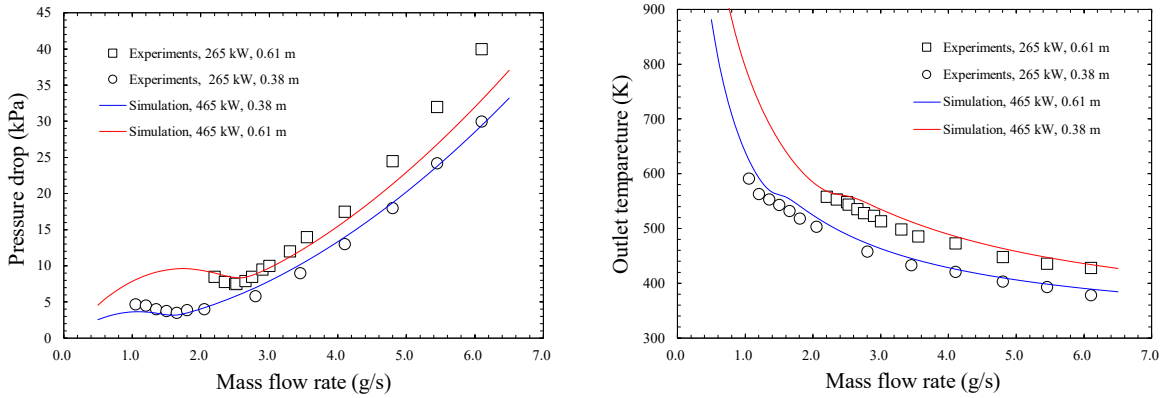

(a) Pressuredrop with mass flow rate (b) Outlet temperature with mass flow rate

Figure 5.10. Comparison of simulated results and experimental data.

5.3.2 Steady-state simulation for *n*-dodecane flows at supercritical pressure

The computational target of this section is the same in Fig. 5.7. Table 5.5 shows the computational conditions of the present simulation. The inlet temperature was set to 300 K, and the *n*-dodecane was liquid state at the inlet. The four different outlet pressure conditions and three different heat flux conditions were considered. Note that all pressure conditions were above the critical pressure of 1.817 MPa. The CFL number of the pseudo time was set to 0.1, and the value of $\delta\tau/\delta t$ was limited to less than unity for stability. Iterative calculations were continued until the residue (L2 norm) decreased by 3 orders of magnitude.

Table 5.5. Computational conditions of the present simulation

Fluid	*N*-dodecane
Heated tube length [m]	0.80
Diameter [m]	0.001
Heat flux [kW/m^2]	500, 1000, 1500
Outlet pressure [MPa]	2.2, 3.0, 3.6, 5.0, 10.0
Inlet temperature [K]	300

A grid convergence study was conducted before the numerical studies to ensure the consistency of the numerical method to be used. I used the three sets of grids, 51, 101, and 201 for the grid convergence study. Calculating the pressure drop at $q = 1500\ \mathrm{kW/m^2}$ and $p = 2.2\ \mathrm{MPa}$ for each grid system, the maximum

relative errors at the OFI point was within 1% among three grids. Therefore, the grid system with 51 grids was employed in the present study. Note that the grid spacing was uniform.

Figure 5.11 shows the difference in the hydrodynamic characteristic curves of *n*-dodecane with and without DFM at $q = 1000\ \mathrm{kW/m^2}$ and three different pressure conditions of 2.2, 3.0, 5.0 MPa. Here, to clearly discuss the effect of DFM to avoid the spurious oscillations in the transcritical region, the pyrolysis reaction model was not applied. Hydrodynamic characteristic curves at 2.2 MPa and 3.0 MPa had the negative slope region. The negative slope became more pronounced as the pressure approaches critical pressure of 1.817 MPa. This trend was also reported in the experimental study of cyclohexane flows in a horizontal heated circular tube by Yang et al [20]. The difference in results with and without DFM began to appear when the outlet fluid temperature exceeds a pseudo-critical temperature T_{pc}. The mass flow rate where the outlet fluid temperatures reach T_{pc} are shown in Fig. 5.11. Thermophysical properties drastically change near the pseudo-critical temperature region as shown in Fig. 5.1. And, as discussed in Chapter 2, the thermophysical properties change in the transcritical region induces spurious oscillations of pressure. The spurious oscillation may cause the pressure difference in the hydrodynamic characteristic curve. The effects of pressure spurious oscillations became more pronounced as the critical pressure is approached because of the drastic changes in thermophysical properties. Under more severe thermodynamic conditions, the solution may not converge due to spurious oscillations, and in the worst case, the calculation may diverge and stop. The all results after here were obtained by using the DFM.

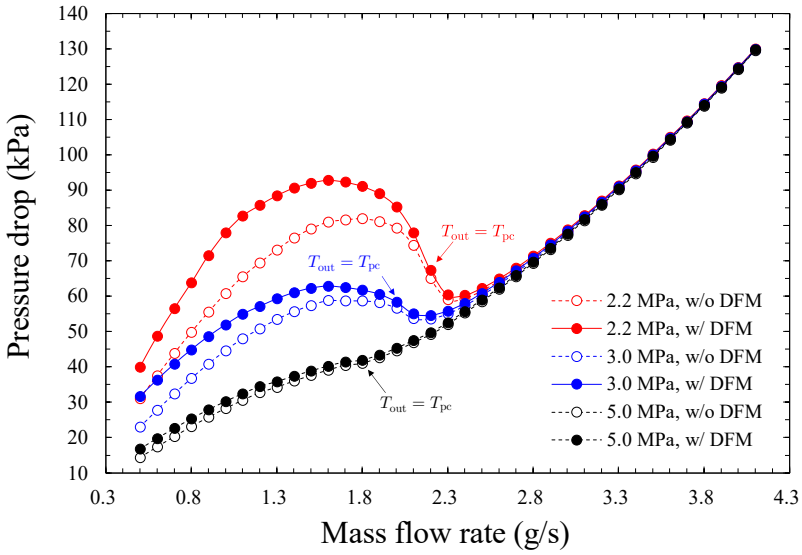

Figure 5.11. Hydrodynamic characteristic curves of *n*-dodecane with and without DFM at $q = 1000\,\mathrm{kW/m^2}$ and three different outlet pressure conditions.

Figure 5.12 shows the hydrodynamic characteristics curve of *n*-dodecane with and without the PSM at three different heat flux conditions for the pressure of 2.2 MPa $(p/p_c = 1.2)$ in a horizontal heated circular tube. Whereas the hydrodynamic characteristic curves calculated without the PSM were typical cubic curves in a heated tube, those calculated with the PSM have a second negative slope region and were fifth order with respect to the mass flux. The two minimum points indicated by A and B in Fig. 5.12 were related to the

occurrence of pseudo-boiling and pyrolysis reactions, respectively. The existence of a fifth-order characteristic curve for endothermic hydrocarbon fuels was reported in an experimental study of kerosene fuel at $p = 3.0$ MPa $(p/p_c = 1.2)$ by Guo et al. [23]. These results indicates that the phase separation by pyrolysis reaction cause the pressure drop in the heated tube, despite the difference in fed-fuel. It is also

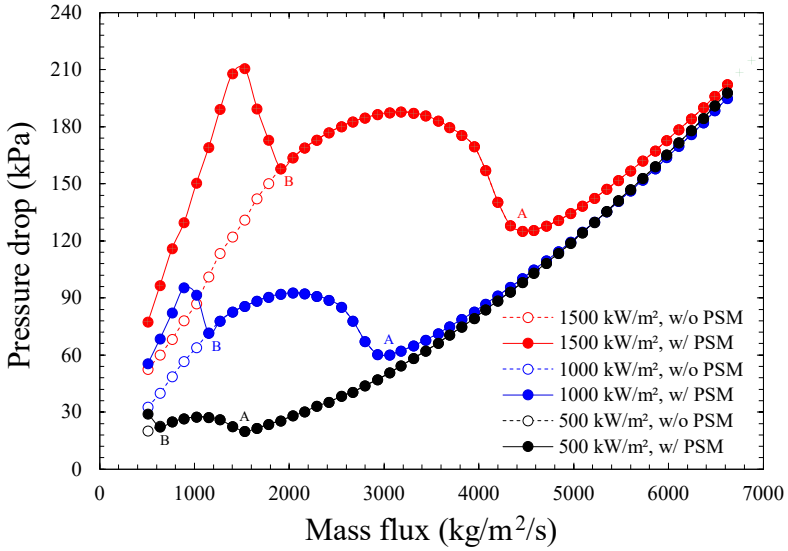

Figure 5.12. Hydrodynamic characteristic curves of *n*-dodecane with and without PSM at $p = 2.2$ MPa $(p/p_c = 1.2)$ and three different heat flux conditions.

noteworthy that the present simple PSM was able to qualitatively reproduce the trend of the experimental data. Also, Fig. 5.12 demonstrates the non-negligible effect of two-phase flow in the low mass flux region (left side from points B). The outlet temperatures at the minimum points B were 959 K ($q = 1500$ kW/m^2), 969 K ($q = 1000$ kW/m^2), and 946 K ($q = 500$ kW/m^2). which exceeded the initiation temperature of the pyrolysis reaction of about 800 K. Under these conditions, the outlet decomposition rate exceeded several percent, indicating that the second minimum point B corresponds to the region where the effect of pyrolysis reaction intensify. At the mass flux conditions lower than the minimum points B, the fluid temperatures are higher than 800 K, and the reaction rate of the pyrolysis reaction and the conversion rate increase further. The pyrolysis reaction generates the decomposed components and expects to induce the phase separation by the mechanism as discussed in Section 5.2.4. The results show that the pressure drop increases on the low mass flux side for all heat flux conditions when considering the PSM. This is the effect of the two-phase correlation of the friction factor expressed in Eq. (5.6). As the heat flux increases, the high-temperature state above 800 K, in the condition that the pyrolysis reaction initiates, is maintained even at the high mass flux side. Therefore, the minimum point B, which is related to the pyrolysis reaction, shifted toward the high mass flux side with increasing heat flux. Although the fifth-order characteristic curve for endothermic hydrocarbon fuel was demonstrated in this section, it is not clear how changes in the order of the hydrodynamic characteristic curve affect the flow instability.

Figure 5.13 shows the hydrodynamic characteristics curve of *n*-dodecane with and without the PSM at $q = 1500$ kW/m^2 and three different outlet pressure conditions. In contrast to the results in Fig. 5.12 at

$q = 1500\ \mathrm{kW/m^2}$ and $p = 2.2$ MPa $(p/p_c = 1.2)$, the minimum point A related to the pseudo-boiling was almost disappeared at $p = 3.6$ MPa $(p/p_c = 2.0)$. The minimum points A at $p = 5.0$ and 10.0 MPa disappeared completely. This means that the increase in pressure condition moderated the thermophysical property changes at the transcritical state, resulting in the pressure drop decreased. Namely, the increase in

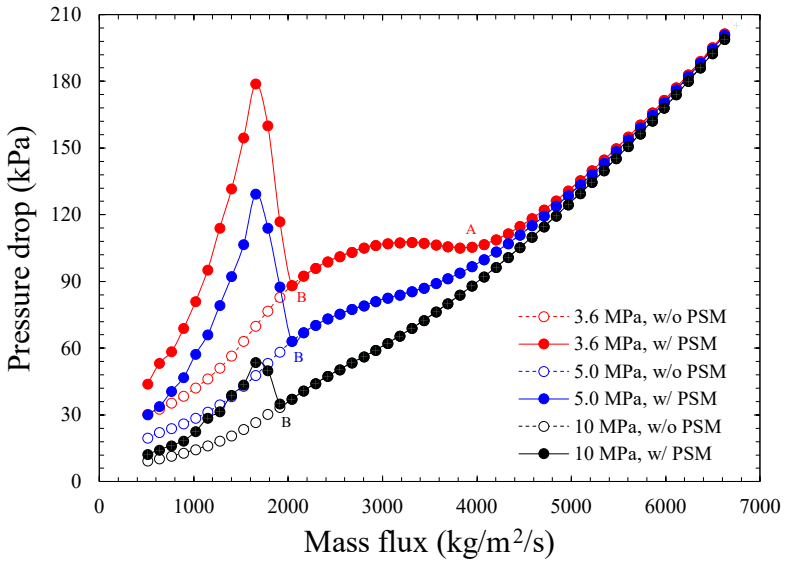

Figure 5.13. Hydrodynamic characteristic curves of *n*-dodecane with and without PSM at $q = 1500\ \mathrm{kW/m^2}$ and three different outlet pressure conditions.

pressure may stabilize the flow in the heated tube. However, the pyrolysis reaction under high-temperature conditions was inevitable, and the non-condensable decomposition gas component caused the flow to become a two-phase flow. As a result, a clear negative gradient region existed in the hydrodynamic characteristic curve even under the high-pressure condition of 10 MPa. Guo et al. [23] also experimentally investigated the pressure effect on the hydrodynamic characteristic curve of kerosene fuel and reported the existence of the negative gradient region at high-pressure conditions because of the pyrolysis reaction. . At the same time, Fig. 5.13 shows the pressure dependence of this stubbornly existing negative slope region, the higher the pressure, the narrower the negative slope region. This tendency is related to the pressure dependence of the phase separation phenomenon shown in Fig. 5.3. The phase separation region in the temperature and the mole fraction space becomes narrow with increasing pressure. That is why the increase in pressure drop due to phase separation decreases under high-pressure conditions, narrowing the negative slope region shown in Fig. 5.13. Under supercritical pressure conditions of water, the hydrodynamic properties are monotonically increasing curves at sufficiently high-pressure conditions. On the other hand, for endothermic hydrocarbon fuels under supercritical pressure conditions, the multivalued characteristic curves were maintained due to pyrolysis reaction even under high pressure conditions to the extent that the effect of quasi-boiling disappears. The results suggest that flow instability may exist up to higher pressure conditions than previously thought possible.

5.3.3 Transient simulation for *n*-dodecane flows at supercritical pressure

Unless otherwise noted, the computational target and conditions are the same in Table 5.5. In accordance with the simulation method for flow instability by Ambrosini [6], the driving pressure is fixed here, i.e., specified the inlet and outlet pressure. The Neumann boundary condition with a gradient of 0 was applied for the inlet velocity. The physical time step was set to 10^{-4} s. The CFL number of the pseudo time was set to 0.1, however the value of $\delta\tau/\delta t$ was limited to less than unity for stability. Iterative calculations were continued until the residue (L2 norm) decreased by 3 orders of magnitude.

First, the possibility of flow instability on the *n*-dodecane flows in a horizontal heated circular tube was investigated at $q = 1500\ \mathrm{kW/m^2}$ and $p = 2.2\ \mathrm{MPa}$. The driving pressures were fixed to 189 kPa, 170 kPa, and 125 kPa. Figure 5.14 shows the initial mass flow rate expressed by the points E1-1, E1-2, and E1-3. These were crossing points between the hydrodynamic characteristic curves with the PSM and the driving pressure drop lines. The crossing points are called the equilibrium points as well. In the case of $\Delta p_d = 189\ \mathrm{MPa}$, three different equilibrium points exist for the hydrodynamic characteristic curves with the PSM, and one equilibrium point existed for the hydrodynamic characteristic curves without the PSM. In the case of $\Delta p_d = 170\ \mathrm{MPa}$, the situation was more complicated, and different five equilibrium points existed for the hydrodynamic characteristic curves with the PSM, and three different equilibrium points existed for the hydrodynamic characteristic curves without the PSM. In the case of $\Delta p_d = 125\ \mathrm{MPa}$, there were two equilibrium points regardless of the PSM, however, the location of the left equilibrium point was different depending on the presence or absence of the model.

Figures 5.15 show the temporal evolution of the mass flux in the case with and without PSM at three different driving pressure drop conditions. Figs. 5.15(a) and 5.15(b) demonstrate large mass flux variation from the initial state. The temporal variation without PSM at $\Delta p_d = 189\ \mathrm{MPa}$ simply indicated a convergence process to the equilibrium point because the initial mass flux was not an equilibrium point.

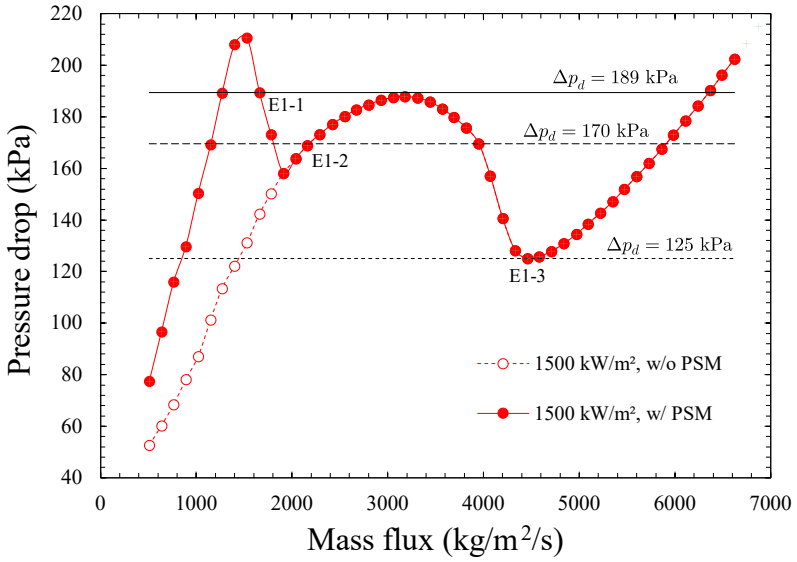

Figure 5.14. Superimposition of the driving pressure lines onto the hydrodynamic characteristic curves at $q = 1500\ \mathrm{kW/m^2}$ and $p = 2.2\ \mathrm{MPa}$ in Fig. 5.12. E1-1, E1-2, and E1-3 indicate the initial state or initial equilibrium points.

On the other hand, since the initial state in other cases were equilibrium points, the results could be understood as a flow excursion, which is the so-called Ledinegg instability. The excursions in Fig. 5.15(b) have been relatively well studied related to pseudo-boiling [6, 10, 15]. In addition to this, the present method also predicted the presence of excursion under pyrolysis condition, as shown in Fig. 5.15(b). The flows eventually converged to the rightmost equilibrium points in the cases of $\Delta p_d = 189$ MPa (Fig. 15(a)) and $\Delta p_d = 170$ MPa (Fig. 5.15(b)). Fig. 5.15(c) demonstrates the different dynamic behavior from other cases. First, the result without the PSM (the dashed and blue line) in Fig. 5.15(c) is discussed. In this case, the driving pressure drop $\Delta p_d = 125$ MPa passed through the point E1-3 in Fig. 5.14. As can be seen in Fig. 5.15(c), the mass flux first stabilizes at the point E1-3, yet the flow does not converge finally, and the flow excursion toward the low mass flux side occurs around $t = 0.56$ s. The flow then oscillated with a specific period and amplitude while temporarily wandering near the point E1-3 ($G = 4400$ kg/m^2/s) and another equilibrium point ($G = 1400$ kg/m^2/s) or overshooting at the point E1-3. The wandering and overshooting around the point E1-3 mean that the equilibrium point is very close to the point E1-3, or nonexistent: because the transient pressure drop in the heated tube is not necessarily equal to the hydrodynamic characteristic curve, which is a convergent solution. Note that even once overshooting, the mass flux decreases gradually

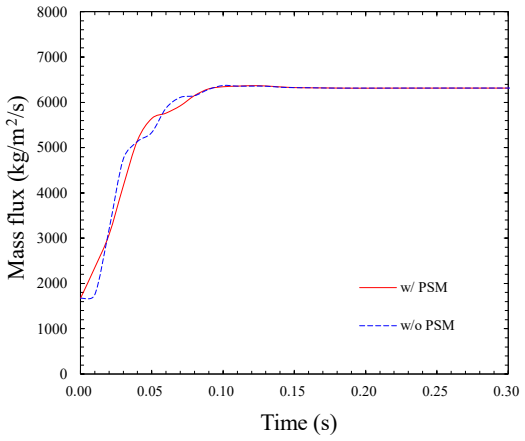

(a) $\Delta p_d = 189$ kPa

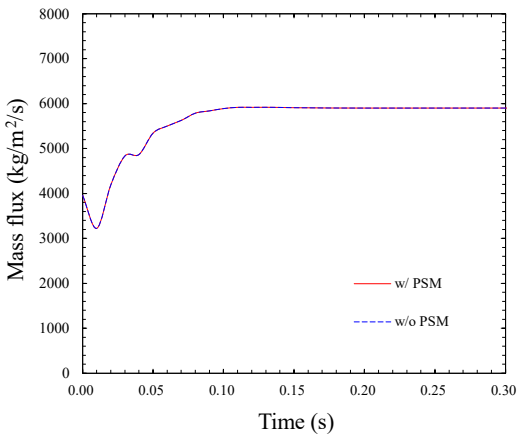

(b) $\Delta p_d = 170$ kPa

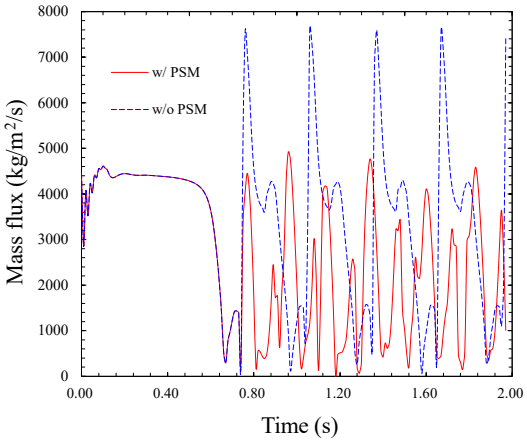

(c) $\Delta p_d = 125$ kPa

Figure 5.15. Temporal evolution of the mass flux at $q = 1500$ kW/m^2 and $p = 2.2$ MPa.

and does not diverge because there is a relationship of $\Delta p_d < \Delta p$. An equilibrium point certainly exists in the positive slope region on the low mass flux side (around $G = 1400\ \mathrm{kg/m^2/s}$). However, this region corresponded to the so-called DWOs region as remarked by Ambrosini [7] based on the analogy between boiling flow and pseudo boiling flow and was unstable. Therefore, the flow wanders around $G = 1400\ \mathrm{kg/m^2/s}$ and then shifts finally toward the higher mass flux side. A series of dynamic behavior was caused by the dynamic feedback of the system previously explained in Section 5.3.1 and Fig. 5.9(a). As a result, the system could not stabilize because of the DWOs, flow excursions, and the interaction of these. Incidentally, the interaction of different flow instabilities was studied in the previous study [10]. Next, the result with the PSM in Fig. 5.15(c) was discussed. The flow instabilities in this case were more complex. What is distinctive compared to the result without PSM is that the flow cannot overshoot to the high muss flux side beyond the point E1-3 and seems to be trapped on the relatively low mass flux side. This is related to the increase in pressure drop in the heated tube due to phase separation as discussed in Section 5.3.2. When the pressure drop increases due to phase separation, the relationship $\Delta p_d < \Delta p$ is intensified at low mass flux region as shown in Fig. 5.12 or Fig. 5.14. This increases the influence of the negative pressure term in the momentum equation and reduces the mass flux. As a result, the flow cannot reach the high mass flux side beyond the point E1-3 and looks as trapped at the low flow side. This decrease in mass flux can increases the rate of enthalpy rise, inducing an unexpected increase in tube temperature. It may also trigger intense pyrolysis reactions under high-temperature conditions, which leads to coking or overheating.

Next, the possibilities of flow instability on the *n*-dodecane flows in a horizontal heated circular tube were investigated at $q = 1500\ \mathrm{kW/m^2}$ and three different outlet pressure conditions. The driving pressures were fixed to 88.2 kPa, 63.1 kPa, and 35.1 kPa. The initial mass flux of flows were given by the points E2-1, E2-2, and E2-3 in Figure 5.16.

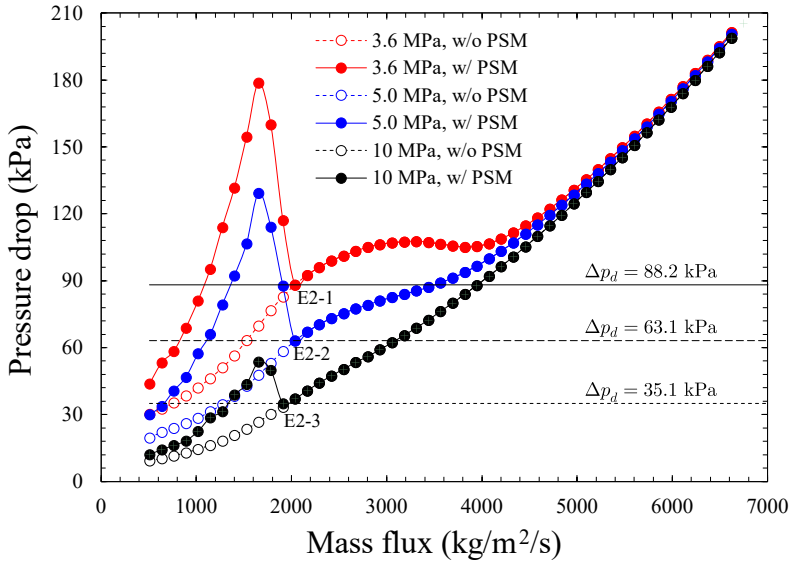

Figure 5.16. Superimposition of the driving pressure lines onto the hydrodynamic characteristic curves at $q = 1500\ \mathrm{kW/m^2}$ and three different outlet pressure conditions in Fig. 5.13. E2-1, E2-2, and E2-3 indicate the initial equilibrium points.

Figures 5.17 show the temporal mass flux for three different outlet pressure conditions. The DWOs always occurred at $p_{\text{out}} = 3.6$ MPa and 5.0 MPa. The oscillations were complex in the cases with PSM because of two equilibrium points. In addition, the frequency in the cases with PSM were increased. Figs. 5.17 clearly indicate that the rapid decrease process of the mass flux from the peak value to the minimum value is the main cause of the frequency increase.

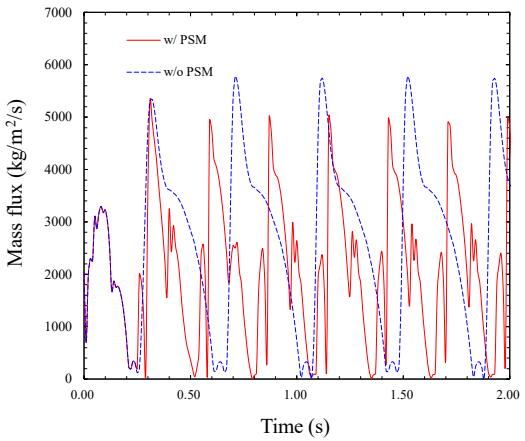

(a) $p_{\text{out}} = 3.6$ MPa and $\Delta p_d = 88.2$ kPa

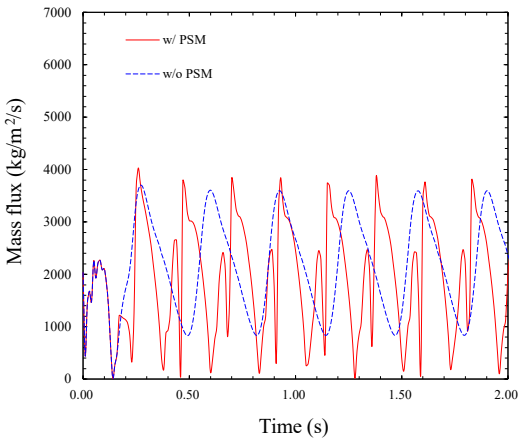

(b) $p_{\text{out}} = 5.0$ MPa and $\Delta p_d = 63.1$ kPa

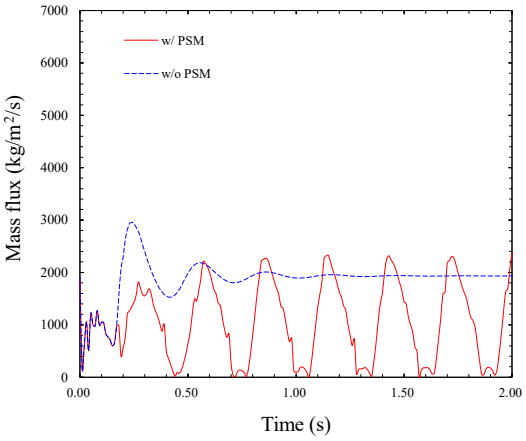

(c) $p_{\text{out}} = 10$ MPa and $\Delta p_d = 35.1$ kPa

Figure 5.17. Temporal evolution of the mass flux at $q = 1500$ kW/m^2 and three different outlet pressure conditions.

The rapid decrease in mass flux resulted from an increase in pressure drop, i.e., enhancement of the $\Delta p_d > \Delta p$ relationship. At $p = 10$ MPa, The DWOs occurred only in the case with PSM and didn't occur in that without PSM. The reason why DWOs do not disappear even at $p = 10$ MPa when using the phase separation model is because of the strong feedback effects between pressure drop, density, and mass flux caused by the large gradient, i.e., large pressure-drop, in the positive slope region. These DWOs in the pyrolysis region would ideally be expected to be existence unless sufficiently high pressure, i.e., critical pressure of the mixture, is reached to make phase separation impossible. However, the phase separation does not occur when all flow field are heated sufficiently above the critical temperature of the mixture, even the

pressure below the critical pressure of the mixture. The amplitude of DWO gradually decreased with increasing outlet pressure conditions. This indicates a weakening of the dynamic feedback. The pressure drop decreased with increasing outlet pressure conditions because of the moderation of thermophysical properties change and phase separation phenomena. As a result, the positive gradient slope on the low mass flux side decreased, weakening the dynamic feedback.

5.4 Numerical methods of large eddy simulations

5.4.1 Fundamental equations

The fundamental equations consist of the conservation equations of mass, momentum, total energy. The set of equations is expressed in the system of equations in the three-dimensional general curvilinear coordinates. To solve the compressible unsteady flows at low-Mach numbers accurately and effectively, a preconditioning method and a dual time-stepping technique [27] are adopted for the system of equations. The preconditioning technique has been used in the context of LES for low-Mach number flows [45-47]. The system of equations is written in the vector form as follow:

$$\frac{\partial \boldsymbol{Q}}{\partial t}+\boldsymbol{\Gamma}\frac{\partial \widehat{\boldsymbol{Q}}}{\partial \tau}+\frac{\partial \boldsymbol{F}_i}{\partial \xi_i}+\frac{\partial \boldsymbol{F}_{vi}}{\partial \xi_i}=0 \quad (i=1,2,3), \tag{5.11}$$

where

$$\boldsymbol{Q}=J\begin{bmatrix}\rho\\ \rho u_1\\ \rho u_2\\ \rho u_3\\ E\end{bmatrix},\widehat{\boldsymbol{Q}}=J\begin{bmatrix}p\\ u_1\\ u_2\\ u_3\\ T\end{bmatrix},\boldsymbol{F}_i=J\begin{bmatrix}\rho U_i\\ \rho u_1 U_i+\dfrac{\partial \xi_i}{\partial x_1}p\\ \rho u_2 U_i+\dfrac{\partial \xi_i}{\partial x_2}p\\ \rho u_3 U_i+\dfrac{\partial \xi_i}{\partial x_3}p\\ (E+p)U_i\end{bmatrix},\boldsymbol{F}_{vi}=J\frac{\partial \xi_i}{\partial x_j}\begin{bmatrix}0\\ \tau_{j1}\\ \tau_{j2}\\ \tau_{j3}\\ \tau_{jk}u_k+\kappa\dfrac{\partial T}{\partial x_j}\end{bmatrix},$$

$$\boldsymbol{\Gamma}=\begin{bmatrix}\theta & 0 & 0 & 0 & \rho_T\\ \theta u_1 & \rho & 0 & 0 & \rho_T u_1\\ \theta u_2 & 0 & \rho & 0 & \rho_T u_2\\ \theta u_3 & 0 & 0 & \rho & \rho_T u_3\\ \theta H-(1-\rho h_p) & \rho u_1 & \rho u_2 & \rho u_3 & \rho_T H+\rho h_T\end{bmatrix}.$$

$\boldsymbol{Q}$, $\widehat{\boldsymbol{Q}}$, $\boldsymbol{F}_i$, and $\boldsymbol{F}_{vi}$ are the vectors of the conservative variables, primitive variables, inviscid flux, and viscous flux, respectively. $\boldsymbol{\Gamma}$ is the preconditioning matrix derived from the Jacobian matrix for $\widehat{\boldsymbol{Q}}$. As $\tau \to \infty$, the pseudo-time term in Eq. (5.11) converges to zero and the equation becomes the conservative system. $H=(E+p)/\rho=h+u_i^2/2$. The preconditioning parameter θ is defined by Eq. (5.3).

5.4.2 Numerical methods

The present LES used the dual-time stepping scheme [27] and preconditioning LU-SGS scheme [29] for the time integration of pseudo time and a second-order three-point backward difference scheme for the time integration of physical time. The fifth-order alternative weighted essentially non-oscillatory scheme (AWENO) [48] was applied for higher-order accuracy. According to the AWENO [48] approach, the fifth-order numerical flux is expressed as follow:

$$\tilde{\boldsymbol{F}}_{j\pm1/2} = \tilde{\boldsymbol{F}}^{\mathrm{FV}}_{j\pm1/2} - \frac{\Delta x^2}{24}\frac{\partial^2 \boldsymbol{F}}{\partial x^2}\bigg|_{j\pm1/2} + \frac{7\Delta x^4}{5760}\frac{\partial^4 \boldsymbol{F}}{\partial x^4}\bigg|_{j\pm1/2}. \tag{5.12}$$

Here, $\tilde{\boldsymbol{F}}^{\mathrm{FV}}_{j+1/2}$ is the finite-volume numerical flux and was evaluated using the preconditioned flux-vector splitting scheme [29] in the present study. The second and third terms on the right-hand side were evaluated by the central differences scheme with 4th-and 2nd-order accuracy, respectively. The advantage of the AWENO scheme is able to employ standard finite-volume numerical fluxes, i.e., can use variable interpolation, despite finite difference formulation. Thus, the DFM in the preconditioning method using the primitive variable interpolation shown in Chapter 2 can be easily implemented in a high-order finite difference formulation. The present numerical method of LES employed the DFM in the preconditioning method to avoid the spurious oscillations in the transcritcal flow. The viscous flux was evaluated by a tridiagonal sixth-order compact difference scheme [49].

5.4.3 Thermodynamic and transport properties model for *n*-dodecane

Thermodynamic properties of *n*-dodecane were calculated using the Helmholtz free-energy EoS proposed by Lemmon and Huber [50], and the transport property for *n*-dodecane were given by using the correlations proposed by Huber et al. [51]. These EoS and correlation are defined in the REFPROP [31]. As well as Section 5.2.3, the look-up table method was used to reduce the calculation cost of thermophysical properties. The data points of look-up tables in the pressure and temperature parameter space were set with a constant interval of $\Delta p = 0.005$ MPa and $\Delta T = 0.75$ K. The thermophysical properties were interpolated with linear interpolation. The prepared lookup tables were used to calculate thermophysical properties in flow simulations.

Figure 5.18 shows the density, isobaric-specific heat, viscosity, and thermal diffusivity for *n*-dodecane with respect to temperature at three different pressure conditions. As also discussed in Fig. 5.1, thermophysical properties depend on the pressure and drastically change near the pseudocritical temperature. The density and viscosity monotonically reduce with increasing the fluid temperature. The isobaric-specific heat has a peak around the pseudocritical temperature at $p = 2.0$ MPa and 2.5 MPa. The thermal diffusivity has a minimum value around the pseudocritical temperature at $p = 2.0$ MPa and 2.5 MPa. The peak and minimum values of the isobaric-specific heat and the thermal diffusivity are no longer present at $p = 6.0$ MPa.

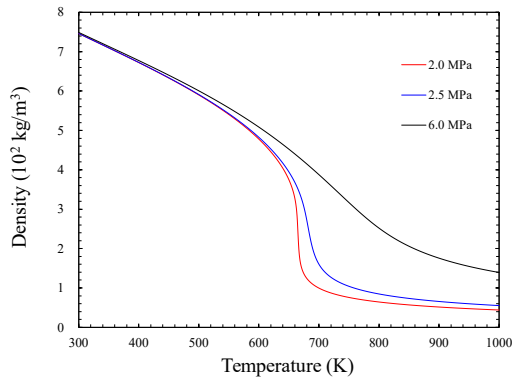

(a) density

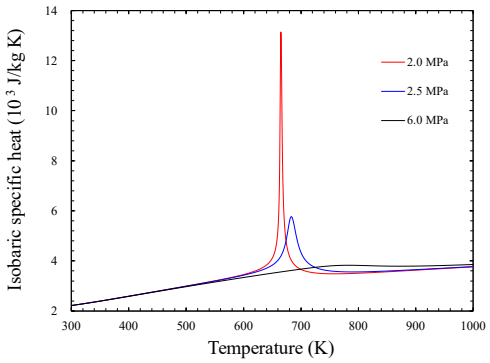

(b) isobaric-specific heat

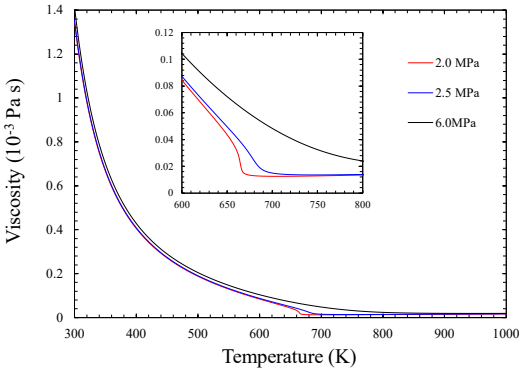

(c) viscosity

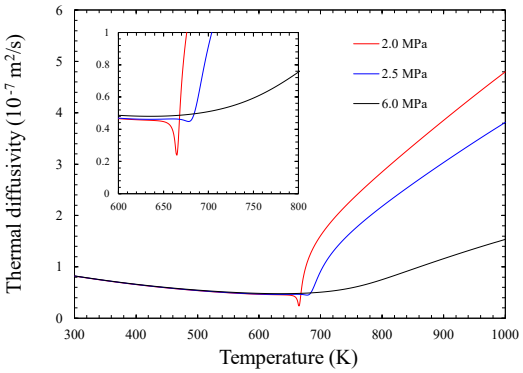

(d) Thermal diffusivity

Figure 5.18. Thermophysical and transport properties for *n*-dodecane at different pressure conditions. Circles, NIST data; lines, look-up table method.

5.5 Numerical results of large eddy simulations

5.5.1 Turbulent channel flow

To validate the numerical method of LES, turbulent channel flows of *n*-dodecane between two infinity flat plates were conducted using different four computational grid systems. The simulated results were compared with the available DNS data [53].

Figure 5.19 shows the schematic of the present LES with the instantaneous Mach number distributions. The x, y, and z directions correspond to streamwise, wall-normal, and spanwise directions. The computational domain size was the same in the reference DNS [53]. The different four grid systems used in this section are shown in the Table 5.5. The friction Reynolds number was set to $Re_\tau = u_\tau \delta/\nu \cong 180$ in accordance with the DNS [53]. Here, $u_\tau = \sqrt{\tau_w/\rho}$ is the friction velocity, and δ is the channel half length. The pressure and temperature at the wall boundaries were calculated by the fourth order polynomial extrapolation to keep the gradients of zero. Periodic boundary conditions were applied for the stream-wise and span-wise directions. Nonslip and adiabatic boundary conditions were imposed to the top and bottom walls. The maximum Mach number in the present case was 0.05 as shown in Fig. 5.19. Also, Fig. 5.19 demonstrates the fully developed turbulent channel flow and the typical narrow low-speed (blue-colored

region) and high-speed (red-colored region) streak structures near the wall. Here, the calculated Re_τ of fine, medium-fine, medium, and coarse grid systems were 179.1, 179.2, 179.6, and 179.5, respectively.

Figures 5.20 show the mean streamwise velocity profiles and root mean square (RMS) values of velocity fluctuations profiles in the wall unit for the different four grid systems. Here, $u^+ = u/u_\tau$ and $y^+ = yu_\tau\mu_w/\rho_w$. Figs. 5.20 demonstrates the clear grid convergence. The fine grid system well reproduced the gradient in logarithmic region and the peak position of each RMS values, resulting in good agreement with the incompressible DNS. Since the present *n*-dodecane channel flows were conducted at $M = 0.05$ and under unheated conditions, the thermophysical properties could be regarded as almost constant. Therefore, the turbulent statics in the present LES were consistent with the incompressible DNS. These results showed the capability of the present numerical method for LES.

Table 5.5. Grid resolution study for unheated turbulent channel flows at $Re_\tau \cong 180$

Grid	N_x	N_y	N_z	Δx^+	Δy^+	Δz^+
Fine	251	173	212	3.4	0.19-5.2	2.0
Medium-fine	221	152	186	3.8	0.19-6.1	2.3
Medium	161	111	136	4.9	0.20-8.7	2.9
Coarse	101	70	85	7.2	0.20-15.0	4.3

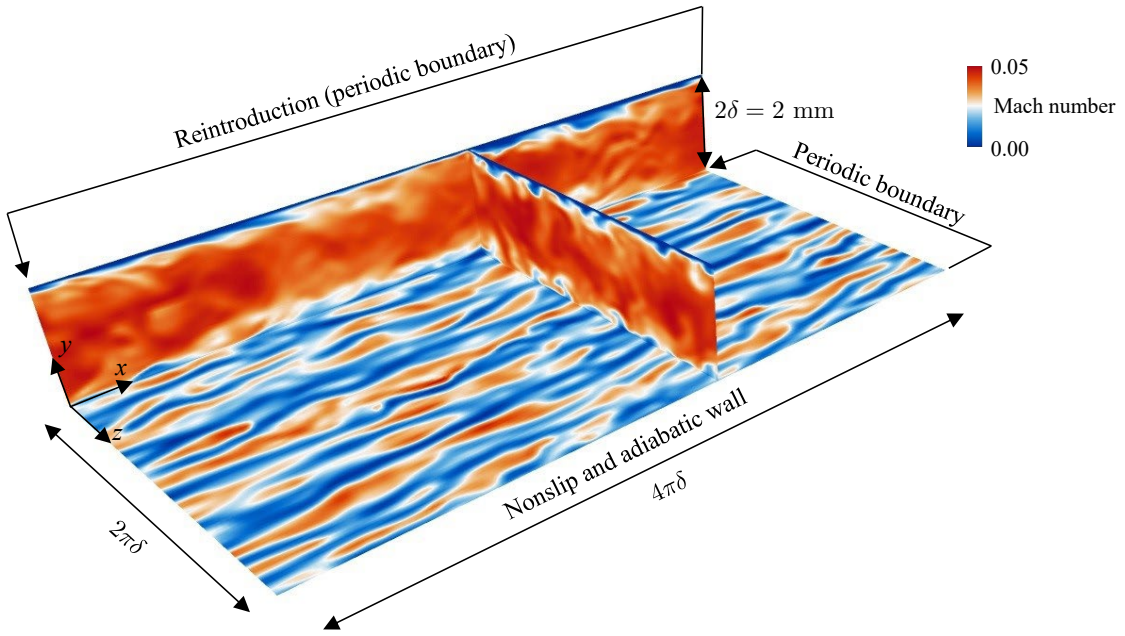

Figure 5.19. Schematic of the present large eddy simulation for turbulent channel flows with Mach number contours at each cross and wall-parallel planes.

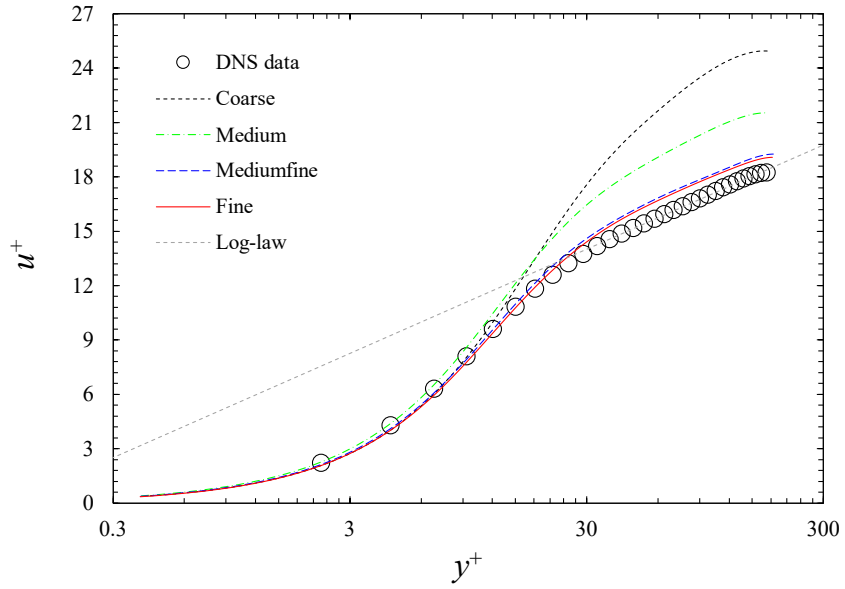

(a) Mean streamwise velocity

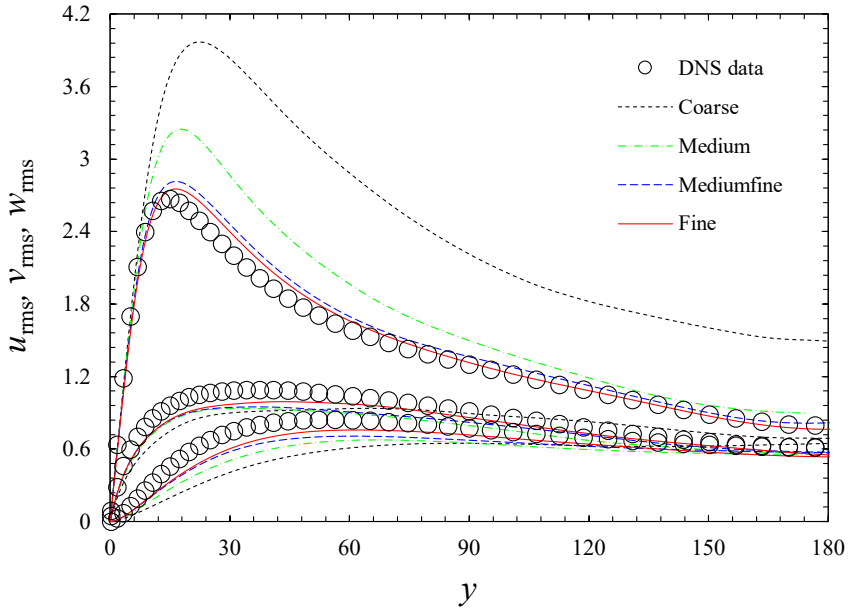

(b) RMS values of velocity fluctuations

Figure 5.20. Mean streamwise velocity and root mean square values of velocity fluctuations profiles in the wall unit for the different four grid systems.

5.5.2 LES of *n*-dodecane flows in a horizontal unheated circular tube

Figure 5.21 shows the schematic of the present LES for horizontal circular tube flows. The r, θ, and z directions correspond to radial, circumferential, and axial directions. A radial, circumferential, and axial velocities were expressed as u_r, u_θ, and u_z, respectively. The computational domain consisted of inflow generator and test section. The length of inflow generator and test section were $L/D = 20$ and $L/D = 250$. Here, the tube diameter was $D = 1$ mm. The additional buffer region was placed at the outlet of the test

section to remove the outlet boundary reflections. The periodic boundary condition was applied to the streamwise direction in the inflow generator to generate a fully developed turbulent velocity profile for the inlet boundary of test section. The inlet temperature and outlet pressure were specified. The outlet pressure was set to 2.0 MPa in all cases. The wall heat flux was $q_{\mathrm{w}} = 0$, i.e., an adiabatic wall condition, in this section. The present simulations considered the inlet Reynolds number conditions $220 \leq Re \leq 44500$. Here, $Re = \rho_{\mathrm{in}} u_{\mathrm{in}} D / \mu_{\mathrm{in}}$. Nonslip and adiabatic boundary conditions were imposed to the *r*-minimum wall. Table 5.6 shows the different three grid systems used in the present LES. Here, the dimensional wall spacings were set to $\Delta r_{\mathrm{w}} = 0.001\ \mathrm{mm}$ in all grid systems. The nondimensional physical time step was set to 4.0×10^{-2}. The CFL number of the pseudo time was set to 4.0, however the value of $\delta\tau / \delta t$ was limited to less than unity for stability. Iterative calculations were continued until the residue (L2 norm) decreased by 2 orders of magnitude.

Figure 5.22 shows the adiabatic friction factors with respect to the Reynolds number for the different three grid systems. The solid and dashed lines indicate the friction factor of laminar flow $f = 64/Re$ and the Filonenko correlation, respectively. In the laminar region, all grids agreed with the theoretical values, and grid convergence was good. In the turbulent region, although the coarse grid underestimated the Filonenko correlation at high Reynolds number conditions $Re > 10000$, the medium and fine grids were in good agreement with the Filonenko correlation and clearly showed the grid convergence. The results demonstrated enough capability of the present LES to reproduce the pressure drop in a horizontal circular tube. In the following section, the medium grid was used to conduct the LES for *n*-dodecane flows.

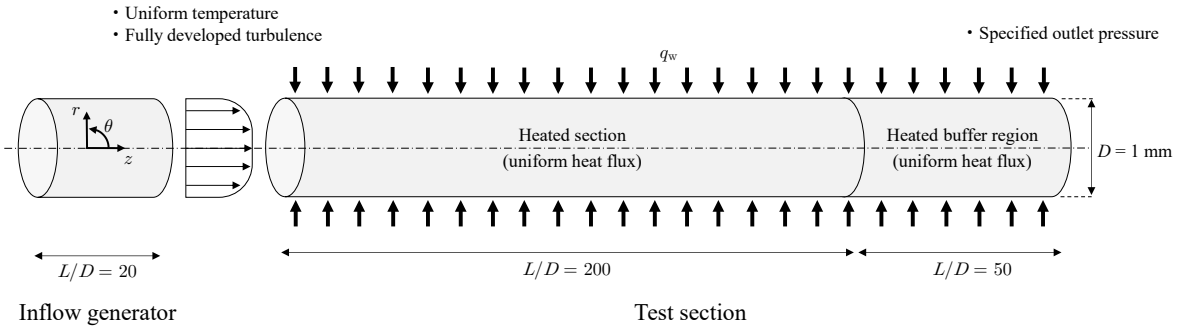

Figure 5.21. Schematic of the present large eddy simulation for horizontal circular tube flows.

Table 5.6. Computational grid for horizontal circular tube flows under unheated condition

Grid	Inflow generator			Test section		
	N_r	N_θ	N_z	N_r	N_θ	N_z
Fine	61	61	151	61	61	1561
Medium	41	41	101	41	41	1041
Coarse	21	21	51	21	21	521

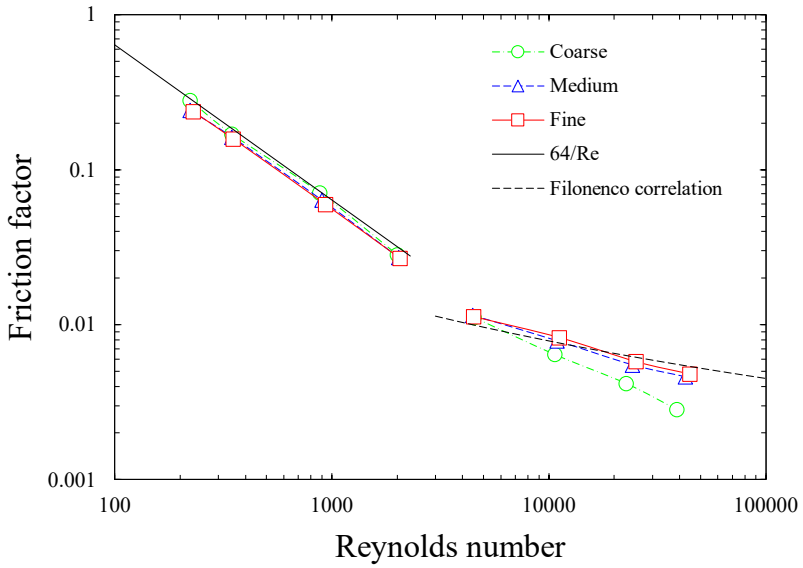

Figure 5.22. Adiabatic friction factors with respect to the Reynolds number for the different three grid systems.

5.5.3 LES of *n*-dodecane flows in a horizontal heated circular tube

The computational target was the same in Fig. 5.21. Table 5.7 shows the computational conditions of the present LES for *n*-dodecane flows. The inlet temperature was set to 500 K, where *n*-dodecane is in the liquid state. The heat flux of 600 kW/m^2 was applied to the wall boundary conditions. The different three outlet pressure conditions of 2.0, 2.5, and 6.0 MPa, which are above the critical pressure of 1.82 MPa, were considered in the present LES. The LES conducted on several mass flow rate conditions between 0.5 and 4.0 g/s. The inlet Reynolds numbers in these pressure and mass flow rate conditions were $3102 \leq Re \leq 27055$.

Figure 5.23 shows the hydrodynamic characteristic curves with respect to the mass flow rate for different three pressure conditions. The hydrodynamic characteristic curve at $p = 2.0$ MPa has a clear negative slope from 1.25 g/s to 2.0 g/s. On the one hand, the negative slope at $p = 2.5$ MPa exists only in the narrow region from 1.25 g/s to 1.50 g/s, and it no longer exists at 6.0 MPa. The negative slope region in the hydrodynamic characteristic curve has been well-known as a cause of flow excursion, which is one of the static instabilities. Fig 5.23 demonstrates the possibility of flow instability at $p = 2.0$ MPa and 2.5 MPa. The points A in Fig. 5.23 indicate minimum points of hydrodynamic characteristic curves. In the case of $p = 2$ MPa, the outlet bulk temperature at the minimum points was $T_{\mathrm{out}} = 652$ K $(T_{\mathrm{out}}/T_{\mathrm{pc}} = 0.98)$, and the streamwise averaged wall temperature was $T_{\mathrm{w}} = 749$ K $(T_{\mathrm{w}}/T_{\mathrm{pc}} = 1.13)$. Yang et al. [20] also experimentally demonstrated the relationship of $T_{\mathrm{out}} < T_{\mathrm{pc}} < T_{\mathrm{w}}$ at the minimum point. In addition, Fig. 5.23 exhibits the dependence of pressure drop on outlet pressure conditions, and the pressure drop significantly increased with approaching the critical pressure. The trend was also reported by Yang et al. [20]. In the following, the transcritical hydrocarbon flows at $p = 2$ MPa and 6 MPa will be compared under the mass flow rate condition of $G = 1.75$ g/s to clarify the generation mechanisms of pressure drop behind the formation of the multi-valued hydrodynamic characteristic curves in a heated circular tube.

Table 5.7. Computational conditions of the present LES

Fluid	Inlet temperature (K)	Heat flux (kW/m^2)	Outlet pressure (MPa)	Mass flow rate (g/s)
N-dodecane	500	600	2.0, 2.5, 6.0	0.5-4.0

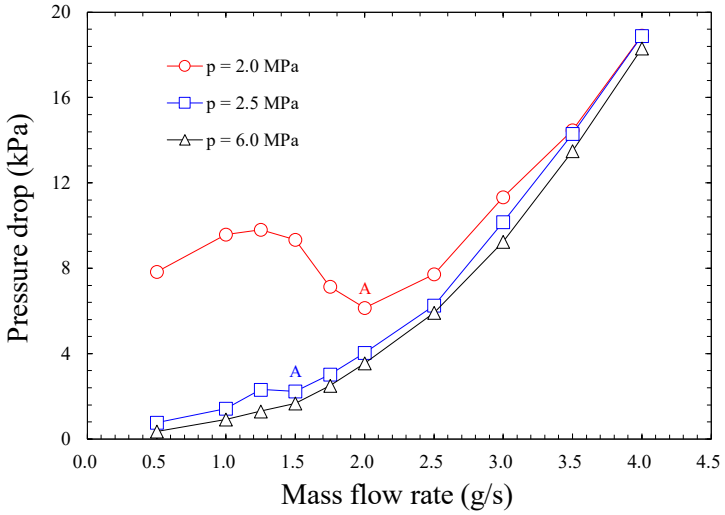

Figure 5.23. Hydrodynamic characteristic curves for different three outlet pressure conditions.

Figure 5.24 shows profiles of mean temperature, density, viscosity, and thermal diffusivity in the radial direction for different two pressure conditions. The fluid temperature rises toward the outlet by heating from the wall surface at $r/D = 0.5$. The wall temperatures at $z/D = 100$ and 200 exceed the pseudocritical temperature in all outlet pressure conditions. Focusing on the temperature profile at $z/D = 200$, the thermal boundary layer at $p = 2$ MPa is thicker than that at $p = 6$ MPa which is related to the transcritical turbulent transportation as will be discussed later. When crossing the pseudocritical temperature, the density and viscosity decrease, and the thermal diffusivity drastically increases. The change in thermophysical properties at $p = 2$ MPa is significant because of the strong real-gas effects as shown in Fig. 5.18. The minimum density at $p = 2$ MPa and 6 MPa are $\overline{\rho}/\rho_0 = 0.12$ and 0.40, respectively. The minimum viscosity at $p = 2$ MPa and 6 MPa are $\overline{\mu}/\mu_0 = 0.07$ and 0.12, and the pressure dependence of viscosity in the supercritical state is small compared to that of density. The thermal diffusivity at $p = 2$ MPa and 6 MPa achieve $\overline{\alpha}/\alpha_0 = 4.58$ and 1.69 at the heated wall. Therefore, the thermal diffusion related to the heat conduction is enhanced near the heated wall at $p = 2$ MPa.

Figure 5.25 shows profiles of Reynolds- and Favre-averaged streamwise velocity in the radial direction for different two pressure conditions. The streamwise velocity is nondimensionalized by the mainstream velocity at the inlet. The flow acceleration in the streamwise direction was clearly observed at $p = 2$ MPa, and the streamwise velocity in the mainstream increases by 1.6 times from inlet to outlet. On the one hand, the streamwise velocity at $p = 6$ MPa accelerates only near the heated wall. There is little acceleration in the mainstream.

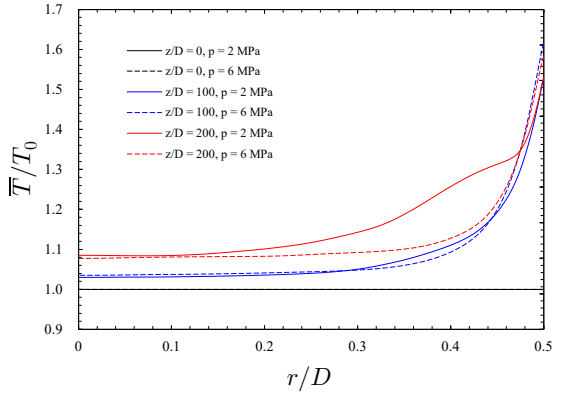

(a) temperature

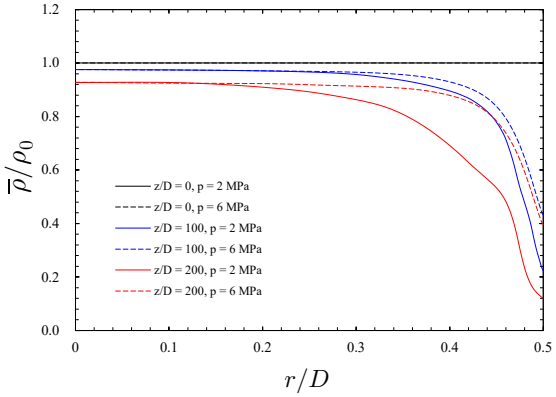

(b) density

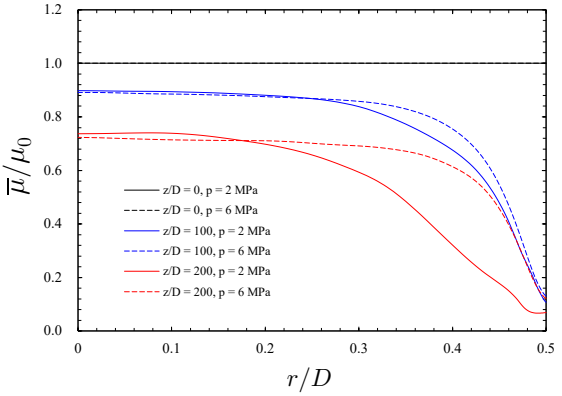

(c) viscosity

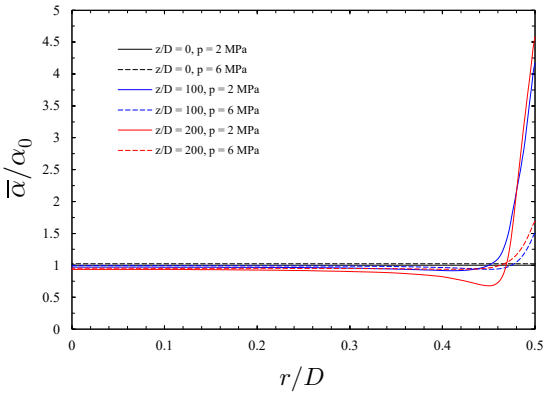

(d) Thermal diffusivity

Figure 5.24. Profiles of mean temperature, density, viscosity, and Prandtl number in the radial direction for different two outlet pressure conditions at $G = 1.75$ g/s..

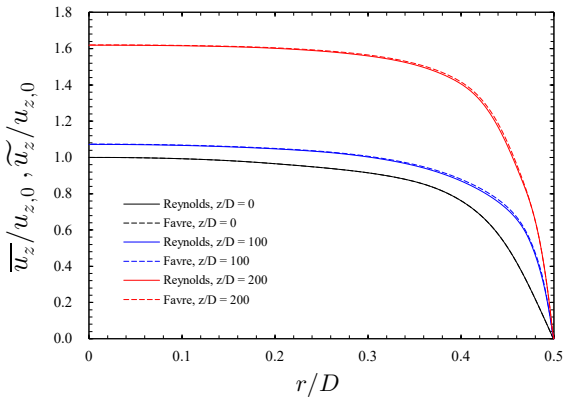

(a) $p = 2$ MPa

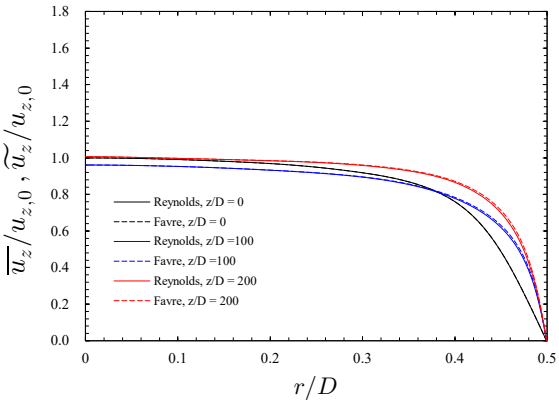

(b) $p = 6$ MPa

Figure 5.25. Profiles of Reynolds- and Favre-averaged streamwise velocity in the radial direction for different two outlet pressure conditions at $G = 1.75$ g/s.

Figure 5.26 shows profiles of Reynolds- and Favre-averaged radial velocity in the radial direction for different two pressure conditions. Focusing on the difference in the streamwise direction, the radial velocity decreased toward the outlet and finally become negative in wide region. Note that the negative radial velocity

is the flow from the wall toward the mainstream. The formation of negative radial velocity was pronounced at $p = 2$ MPa and especially near the heated wall. The mechanisms of the formation of negative radial velocity will be discussed later.

Figure 5.27 shows profiles of spatial-averaged mean viscous shear stress in the radial direction for different two outlet pressure conditions. The absolute value of the viscous shear stress reduces toward the outlet and the heated wall because the viscosity decreases as shown in Fig. 5.24. The wall shear stress at $p = 2$ MPa is slightly smaller than that at $p = 6$ MPa.

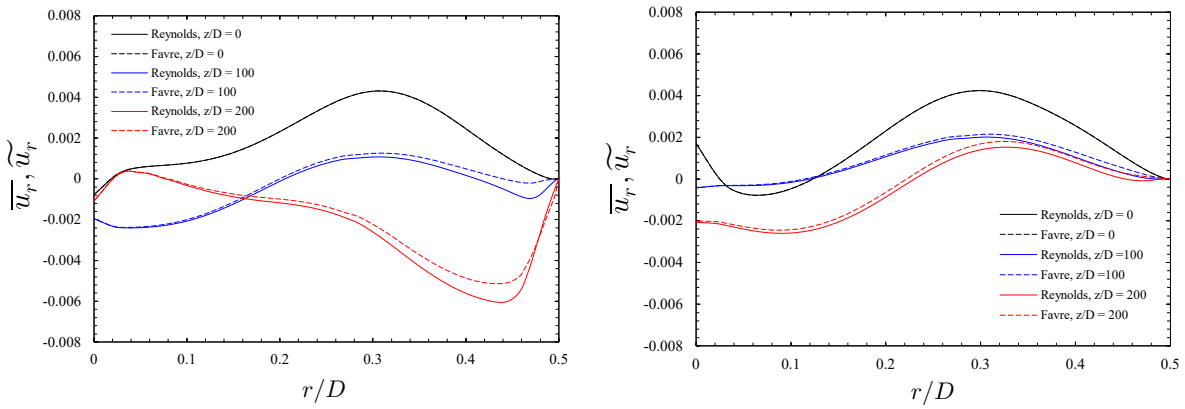

(a) $p = 2$ MPa (b) $p = 6$ MPa

Figure 5.26. Profiles of Reynolds- and Favre-averaged radial velocity in the radial direction for different two outlet pressure conditions at $G = 1.75$ g/s.

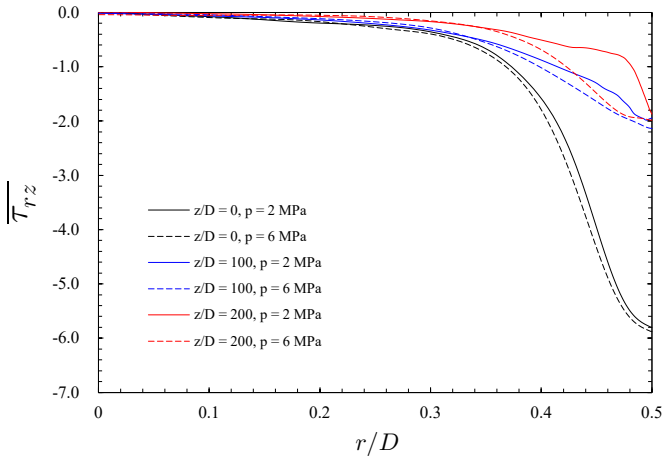

Figure 5.27. Profiles of spatial-averaged mean viscous shear stress in the radial direction for different two outlet pressure conditions at $G = 1.75$ g/s..

Figure 5.28 shows profiles of density variances in the radial direction for different two outlet pressure conditions. The maximum density variances show near the heated wall. The fluid density changes drastically across the pseudo-critical temperature near the heated wall as shown in Fig. 5.24. The large density fluctuation is caused by the drastic density change in a narrow temperature range, which is unique behavior of transcritical flow. The density gradient in temperature space is steeper approaching to the critical pressure as shown in Fig. 5.18, which leads to larger density fluctuations in the transcritical flow as shown in Fig.

5.28. is around unity. For example, the maximum density variance at $p = 2$ MPa is greater than unity, while that at $p = 6$ MPa is 0.3.

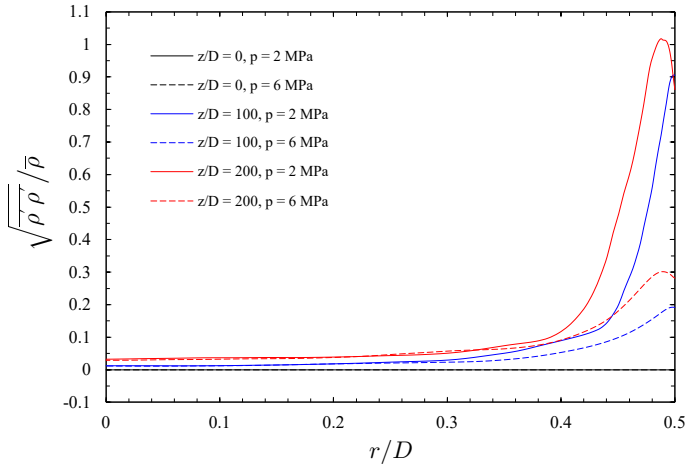

Figure 5.28. Profiles of density variances in the radial direction for different two outlet pressure conditions at $G = 1.75$ g/s..

Figure 5.29 shows profiles of Favre-averaged streamwise and wall-normal velocity fluctuations in the radial direction for different two outlet pressure conditions. The velocity fluctuation profiles in the radial direction have $\overline{u_z''} < 0$ and $\overline{u_r''} < 0$. Therefore, the ejection motion ($\overline{u_z''} < 0$ and $\overline{u_r''} < 0$) was dominant in

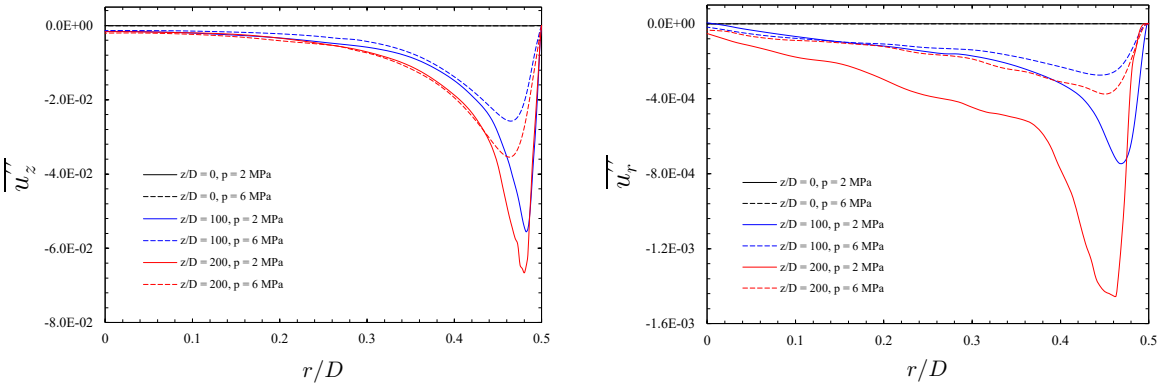

(a) streamwise velocity (b) wall-normal velocity

Figure 5.29. Profiles of Favre-averaged streamwise and wall-normal velocity fluctuations in the radial direction for different two outlet pressure conditions at $G = 1.75$ g/s.

the transcritical flows in the heated circular tube. The previous DNS [54] demonstrated the enhancement of the ejection motion in a transcritical turbulent boundary layer. The ejection motion is enhanced toward the outlet at both pressure conditions, and with more intense ejection at $p = 2$ MPa. These results can be explained by the following definitions for Favre-averaged velocity fluctuations.

$$\overline{u_i''} = \overline{u_i - \widetilde{u_i}} = \overline{u_i - \frac{\overline{(\overline{\rho} + \rho')(\overline{u_i} + u_i')}}{\overline{\rho}}} = -\frac{\overline{\rho' u_i'}}{\overline{\rho}}. \tag{5.13}$$

Eq. (5.13) shows that the Favre-averaged velocity fluctuations are enhanced by the density fluctuation. In the present case, the density fluctuation increases near the pseudo-critical temperature as shown in Figure 5.28, and hence the Favre-averaged velocity fluctuations related to the ejection motion ($\overline{u_z''} < 0$ and $\overline{u_r''} < 0$) are enhanced. The enhancement of ejection motion associated with density fluctuations provides a certain explanation for the development of negative radial velocity in the streamwise direction shown in Fig. 5.26. The reasons of $\overline{u_z''} < 0$ and $\overline{u_r''} < 0$, i.e., $-\overline{\rho' u_z'} < 0$ and $-\overline{\rho' u_r'} < 0$, will be discussed later with results of flow visualization.

In the following, the mechanism of the increase in pressure-drop approaching the critical pressure shown in Fig. 5.23 will be further discussed. The pressure drop can be decomposed into the following three contributions: acceleration pressure-drop Δp_a, frictional pressure-drop Δp_f and gravitational pressure drop Δp_g. Since the present LES had $Ri \leq 5 \times 10^{-3}$, the gravitational pressure drop can be neglected. Therefore, the total pressure drop Δp is expressed as follow:

$$\Delta p = \Delta p_a + \Delta p_f + \Delta p_g \approx \Delta p_a + \Delta p_f \tag{5.14}$$

Further, in the present study, the acceleration pressure-drop and the frictional pressure drop are evaluated by the following relations:

$$\Delta p_a = (\rho_b u_b^2)_{\mathrm{out}} - (\rho_b u_b^2)_{\mathrm{in}}, \tag{5.15a}$$

$$\Delta p_f = \frac{4L\overline{\tau_w}}{D}. \tag{5.15b}$$

Where L is tube length, τ_w is wall shear stress, and D is the tube diameter. Figure 5.30 shows the comparison of the pressure drop evaluated by Eq. (5.14) and the total pressure drop $\Delta p = p_{\mathrm{in}} - p_{\mathrm{out}}$ for different two outlet pressure conditions. The errors for the total pressure drop at $p = 2$ MPa and at 6 MPa were 7.6% and 1.9%, respectively. Fig. 5.30 shows the strong pressure dependence of acceleration pressure-drop. Although the frictional pressure drop was slightly lower at $p = 2$ MPa, the difference due to the pressure condition is relatively small. Note that the decrease in the frictional pressure drop approaching the critical pressure was also reported in the existing study [55]. Eventually, it was clarified the increase in acceleration pressure drop at $p = 2$ MPa caused the formation of a negative slope region in the hydrodynamic characteristic curve. From Eq. (5.15a), the increase in the acceleration pressure-drop at $p = 2$ MPa was caused by the decrease in bulk density. There are two factors that cause of the decrease in bulk density at $p = 2$ MPa. The first factor is that the density in the supercritical state at $p = 2$ MPa is lower than that at $p = 6$ MPa as shown in Fig. 5.18(b). Therefore, the fluid density in the heated tube at $p = 2$ MPa significantly decreases because of thermal expansion. The second factor is that the low-density region has expanded to the mainstream region due to the heat transfer enhancement and the expansion of the temperature boundary layer at $p = 2$ MPa as shown in Figure 5.28(a). In the following, I focus on the mechanisms of heat transfer enhancement directly related to the increase in the acceleration pressure drop at $p = 2$ MPa. To clarify the heat transfer enhancement in the transcritical flow, the local Nusselt number at $z/D = 200$ is evaluated for both outlet pressure conditions of $p = 2$ MPa and 6 MPa.

Fukagata et al. [56] proposed the Fukagata, Iwamoto and Kasagi (FIK) identity which can express the individual contribution for the frictional pressure-drop. The FIK identity has been extended to the Nusselt number. From now on, the FIK identity has been applied to several type flows such as fully developed channel and pipe flows [57], compressible turbulent channel flows [58], developing turbulent boundary layer [59], heated developing turbulent boundary layer [60], strong heated air flows [61], supercritical fluid flows [55, 62-64]. An expression for the FIK identity for the Nusselt number is obtained by double integrating the Favre-averaged energy equation. The FIK identity for the Nusselt number derived by Zhao et al. [64] as follows:

$$
\begin{aligned}
Nu_{FIK} = & \underbrace{\frac{8}{k_b(T_w - T_b)} \int_0^1 r\overline{\alpha} \frac{\partial \overline{h}}{\partial r} rdr}_{N1} \underbrace{- \frac{8Re_{b0}Pr_0}{k_b(T_w - T_b)} \int_0^1 r\overline{\rho h'' u_r''} rdr}_{N2} \\
& \underbrace{- \frac{4Re_{b0}Pr_0}{k_b(T_w - T_b)} \int_0^1 (1 - r^2) \left\langle \frac{1}{r} \frac{\partial r \overline{\rho} \widetilde{h} \widetilde{u_r}}{\partial r} \right\rangle rdr}_{N3} \\
& \underbrace{- \frac{4Re_{b0}Pr_0}{k_b(T_w - T_b)} \int_0^1 (1 - r^2) \left\langle \frac{\partial \overline{\rho} \widetilde{h} \widetilde{u_z}}{\partial z} \right\rangle rdr}_{N4} \\
& \underbrace{- \frac{4Re_{b0}Pr_0}{k_b(T_w - T_b)} \int_0^1 (1 - r^2) \left\langle \frac{\partial \overline{\rho h'' u_z''}}{\partial z} \right\rangle rdr}_{N5} \\
& \underbrace{+ \frac{4}{k_b(T_w - T_b)} \int_0^1 (1 - r^2) \left\langle \frac{1}{r} \frac{\partial}{\partial r} \left(\overline{r\alpha' \frac{\partial h'}{\partial r}} \right) \right\rangle rdr}_{N6} \\
& \underbrace{+ \frac{4}{k_b(T_w - T_b)} \int_0^1 (1 - r^2) \left\langle \frac{\partial}{\partial z} \left(\overline{\alpha} \overline{\frac{\partial h}{\partial z}} \right) \right\rangle rdr}_{N7} \\
& \underbrace{+ \frac{4}{k_b(T_w - T_b)} \int_0^1 (1 - r^2) \left\langle \frac{\partial}{\partial z} \left(\overline{\alpha' \frac{\partial h'}{\partial z}} \right) \right\rangle rdr}_{N8}
\end{aligned}
\tag{5.16}
$$

where the first term $N1$ in the right-hand side is the laminar contribution, the second term $N2$ is the turbulent contribution, and the other terms $N3 - N8$ are inhomogeneous contribution.

Figure 5.31 shows the local Nusselt numbers calculated by Eq. (5.16) at $z/D = 200$ for different two outlet pressure conditions. The $N6$, $N7$, and $N8$ terms are not shown here because they are negligibly small in the present case. The total Nusselt numbers of $p = 2$ MPa and 6 MPa calculated by Eq. (5.16) were $Nu_{FIK} = 68$ and 38, respectively. The Nusselt numbers of $p = 2$ MPa and 6 MPa calculated by the original definition of $Nu = q_w D / k_b(T_w - T_b)$ were $Nu = 40$ and 28, respectively. Although the FIK identity slightly overestimate the Nusselt numbers calculated by the original definition, the trend for pressure conditions were reproduced. Focusing on the $N1$ term, that at $p = 2$ MPa was larger because the thermal diffusivity greatly increases as shown in Fig. 5.24(d). Differences depending on pressure conditions in the

$N2$ and $N5$ terms were relatively small and were less than 1%. The differences depending on pressure conditions were abviously seen in $N3$ and $N4$. In the present case, the strong ejection motion induces negative radial velocities as shown in Fig 5.26(a), thus $\partial\widetilde{u_r}/\partial r$, which is the component of $N3$, is negative in most regions. As a result, the $N3$ term had a major and positive contribution at $p = 2$ MPa. On the one hand, $N4$ term had a large negative contribution. Note that the negative contribution of $N4$ is intensified at $p = 2$ MPa whereas the positive contribution of $N3$ increases. As already discussed, the radial transport of the low-density fluid near the heated wall to the mainstream by vigorous ejection motion leads to a decrease in bulk density and a significant flow acceleration. The flow acceleration increases the $\partial\widetilde{u_z}/\partial z$, which is the components of $N4$, resulting in the negative contribution of $N4$ being intensified. The series of heat transfer enhancement/deterioration mechanisms related to $N3$ and $N4$ were not found at $p =$ 6 MPa, and the dominant in the heat transfer at $p = 6$ MPa was the turbulent contribution term of $N2$.

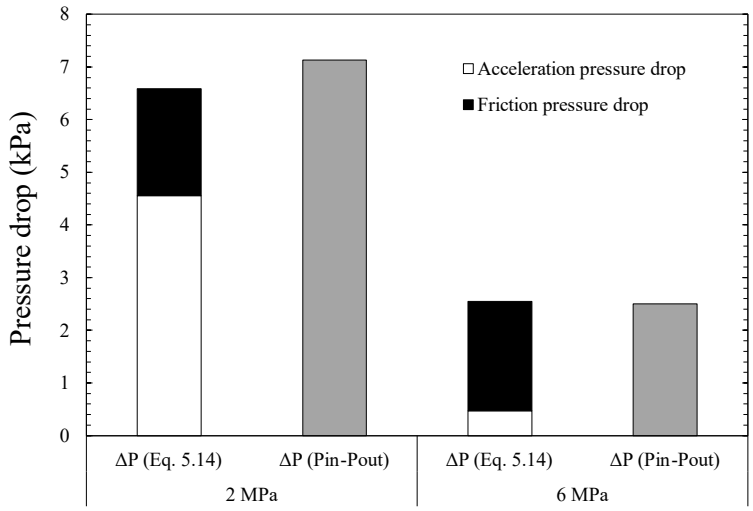

Figure 5.30. Comparison of the pressure drop evaluated by Eq. (5.14) and the total pressure drop $\Delta p = p_{\mathrm{in}} - p_{\mathrm{out}}$ for different two outlet pressure conditions at $G = 1.75$ g/s.

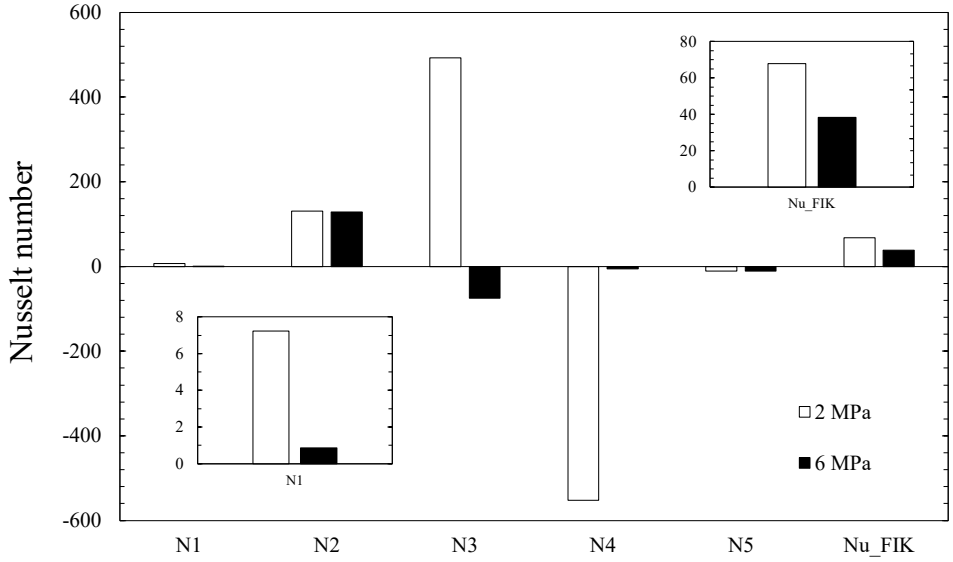

Figure 5.31. Local Nusselt numbers calculated by the FIK identity at $z/D = 200$ for different two outlet pressure conditions at $G = 1.75$ g/s.

To investigate the flow phenomenon in the negative slope region, Figure 5.32 visualizes instantaneous snapshots for the temperature, isobaric-specific heat, and streamwise velocity in the cross section at $z/D = 180$ under the computational conditions of $G = 1.75$ g/s and $p = 2.0$ MPa. The black and white contour lines indicate the c_p filaments of 5000 and 10000 J/kg/K, respectively. Instantaneous cross-stream velocity vectors are superimposed on the Fig. 5.32(c). Whereas the fluid temperature in the mainstream region was around $T = 570$ K, which is in the liquid state of *n*-dodecane, it raised to $T = 840$ K by constant heat flux from the heated wall. The temperature varied in the cross-section through the pseudocritical temperature of $T_{\mathrm{pc}} = 665$ K at $p = 2.0$ MPa. Therefore, the flow field was in the transcritical condition. The isobaric-

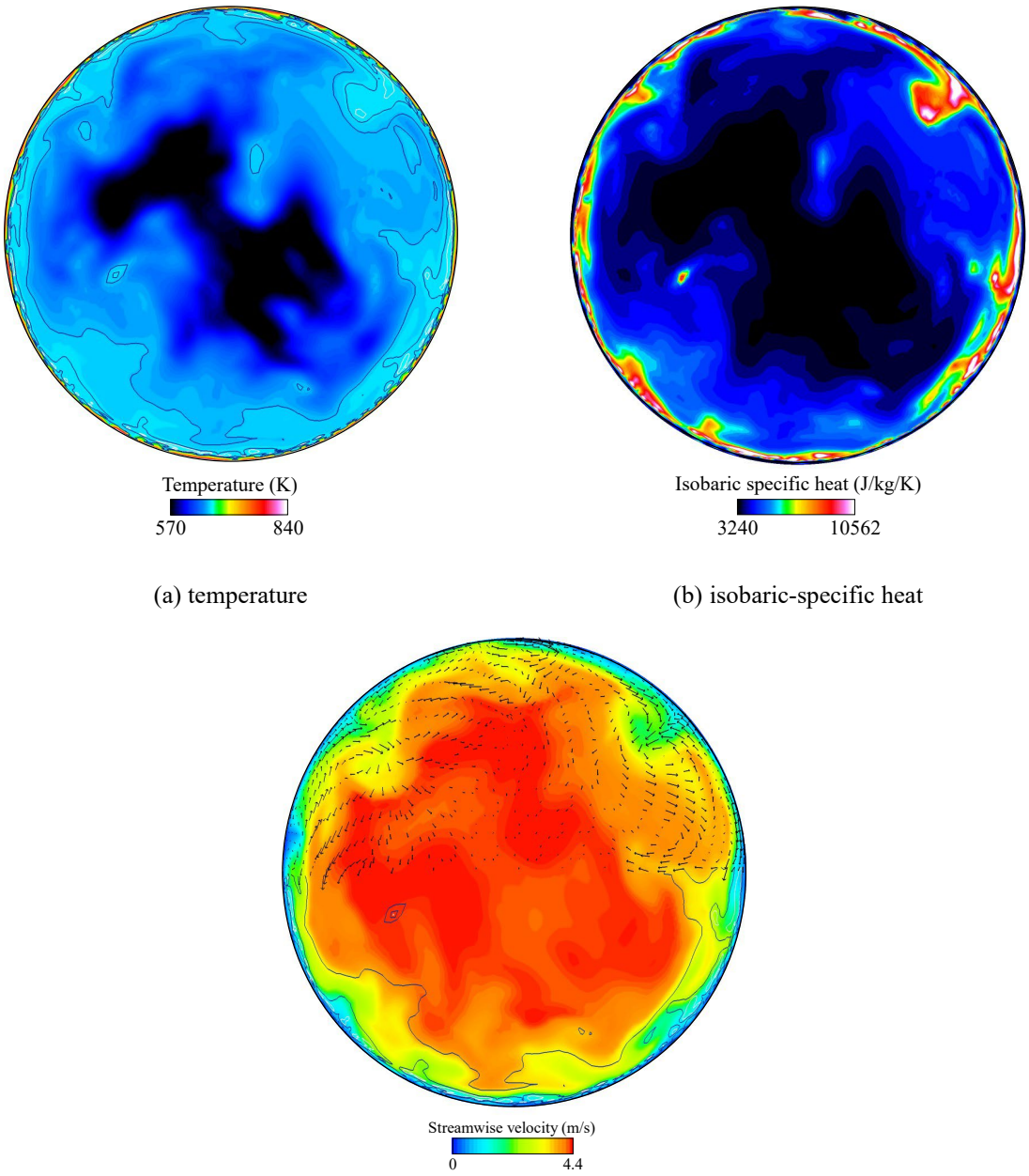

(a) temperature

(b) isobaric-specific heat

(c) streamwise velocity

Figure 5.32. Instantaneous snapshots in the cross section at $z/D = 180$ with superimposed black ($c_p = 5000$) and white ($c_p = 10000$) contour lines at $G = 1.75$ g/s and $p = 2.0$ MPa.

specific heat shows the peak at the pseudo-critical temperature as shown in Fig. 5.18. Most of the peak regions of the isobaric-specific heat were near the heated wall, while some peak regions extended in the mainstream direction. Fig. 5.32(c) shows the streamwise velocity with cross-stream velocity vectors superimposed. Secondary flows orthogonal to the streamwise velocity existed near the wall. The high-temperature region accompanied by low-speed streamwise velocity was transported by outward flow near the heated wall.

Figure 5.33 shows instantaneous snapshots of the wall-parallel plane for the temperature, density fluctuation, Favre-averaged streamwise velocity fluctuation, and Favre-averaged wall-normal velocity fluctuation at $r/D = 0.45$ under the computational conditions of $G = 1.75$ g/s and $p = 2.0$ MPa. The black contour lines in Fig. 5.33(a) indicate the high isobaric-specific heat region of $c_p > 4000$. Figs. 5.33(c, d) shows the high-speed ($u_z'' > 0$) and low-speed ($u_z'' < 0$) streaks near the heated wall. These streaks formed the streamwise-elongated structure, which typically exists in wall turbulence. The high-speed streaks corresponded to outward flows ($u_r'' > 0$) and transported the low-temperature ($T < T_{\mathrm{pc}}$) liquid-like fluid toward the heated wall (note the area framed in white in Fig. 5.33(a)). The turbulent structure had the properties of $u_z'' > 0$, $u_r'' > 0$, and $\rho' > 0$, and corresponds to the Q4 sweep event. On the one hand, the low-speed streaks corresponded to inward flows ($u_r'' < 0$) and transported the high-temperature ($T > T_{\mathrm{pc}}$) gas-like fluid toward the heated wall. The turbulent structure had the properties of $u_z'' < 0$, $u_r'' < 0$, and $\rho' < 0$, which corresponds to the Q4 sweep event.

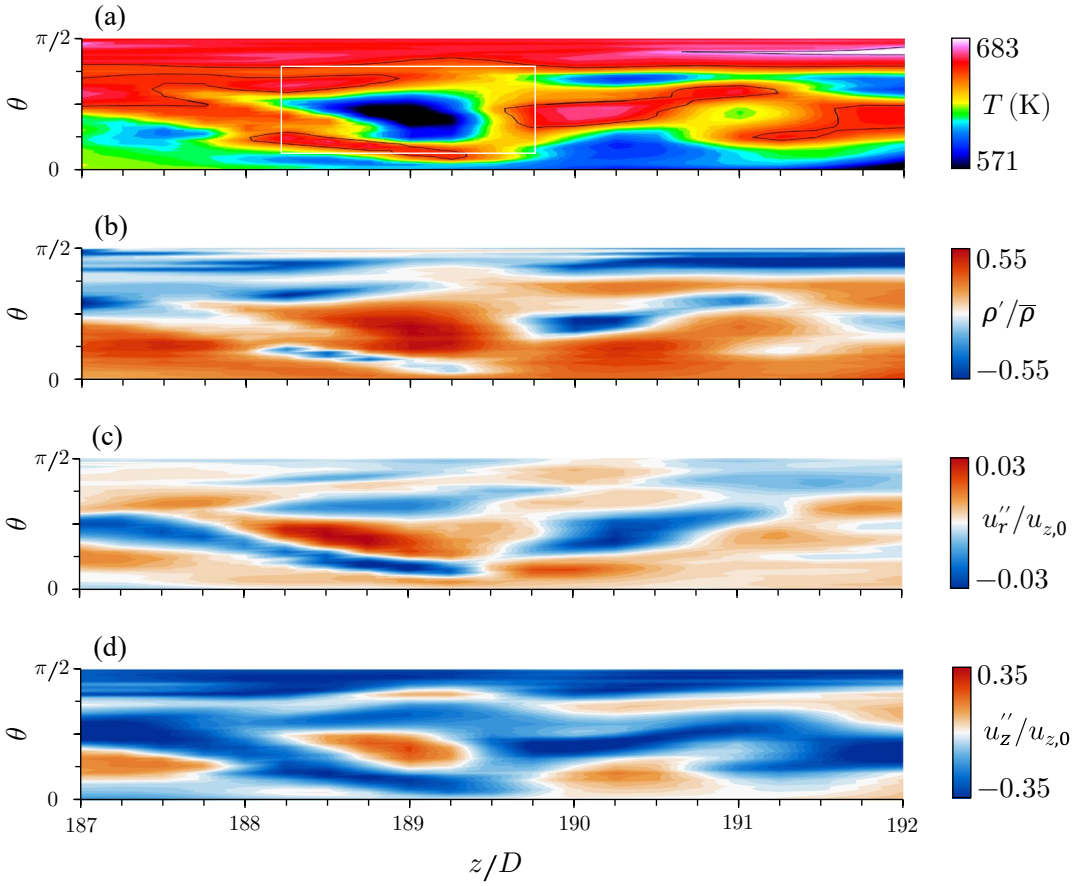

Figure 5.33. Instantaneous snapshots of the wall-parallel plane at $r/D = 0.45$ under the computational conditions of $G = 1.75$ g/s and $p = 2.0$ MPa.

Figure 5.34 shows instantaneous snapshots of velocity fluctuations and turbulent mass fluxes in the cross section at $z/D = 195$ under the computational conditions of $G = 1.75$ g/s and $p = 2.0$ MPa. Fig. 5.34 demonstrates that high-speed and low-speed streaks correspond to outward and inward flows, respectively. Figs. 5.34 (c, d) shows streamwise and radial turbulent mass fluxes. Here, there is a relationship between the turbulent mass flux and instantaneous Favre-averaged velocity fluctuation as follow:

$$u_i'' = u_i - \widetilde{u_i} = u_i' - \frac{\overline{\rho' u_i'}}{\overline{\rho}}. \tag{5.17}$$

Eq. (5.17) indicates that Favre-averaged velocity fluctuations are enhanced or reduced by the turbulent mass fluxes $\rho' u_i'$ related to the density fluctuation. In the present case, positive turbulent mass fluxes corresponded to both high-speed and low-speed streaks in most of the flow fields. Therefore, the turbulent mass fluxes reduced the Q4 sweep event ($u_z'' > 0$ and $u_r'' > 0$) and enhanced the Q2 ejection event ($u_z'' < 0$ and $u_r'' < 0$). The enhancement and reduction in Favre-averaged velocity fluctuations by the effect of density fluctuation were also demonstrated in the DNS of heated transcritical flat-plate turbulent boundary layers [54] and in DNS of heated transcritical spatial-developing pipe flows [55]. The present study newly

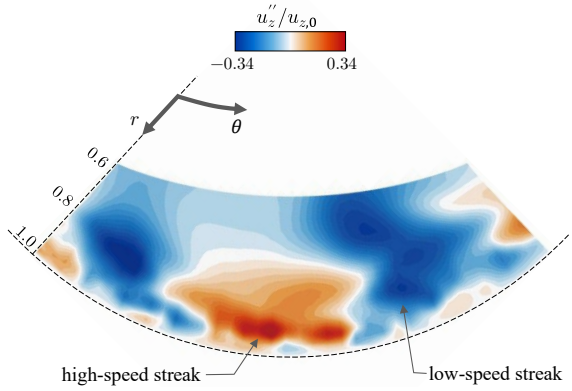

(a) streamwise velocity fluctuation

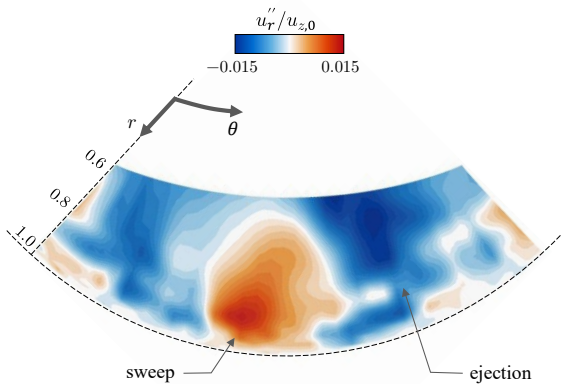

(b) radial velocity fluctuation

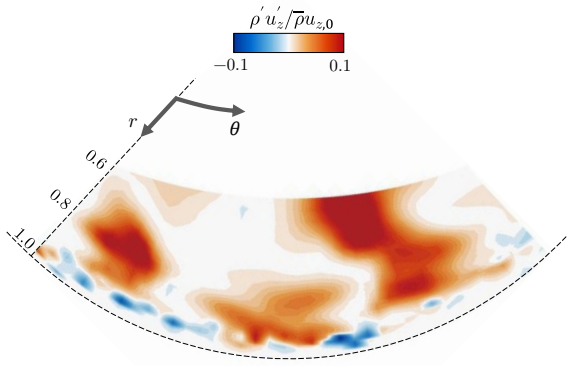

(c) streamwise turbulent mass flux

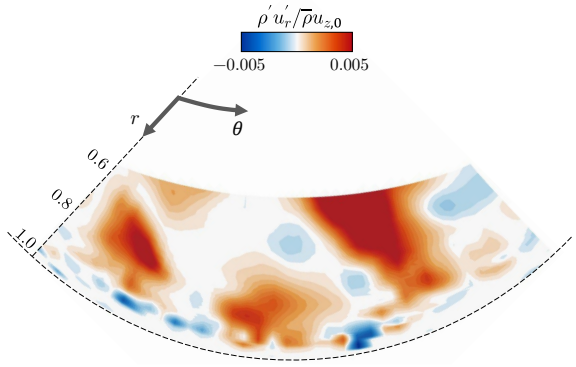

(d) radial turbulent mass flux

Figure 5.34. Instantaneous snapshots of Favre-averaged velocity fluctuations and turbulent mass fluxes in the cross section at $z/D = 195$ under the computational conditions of $G = 1.75$ g/s and $p = 2.0$ MPa.

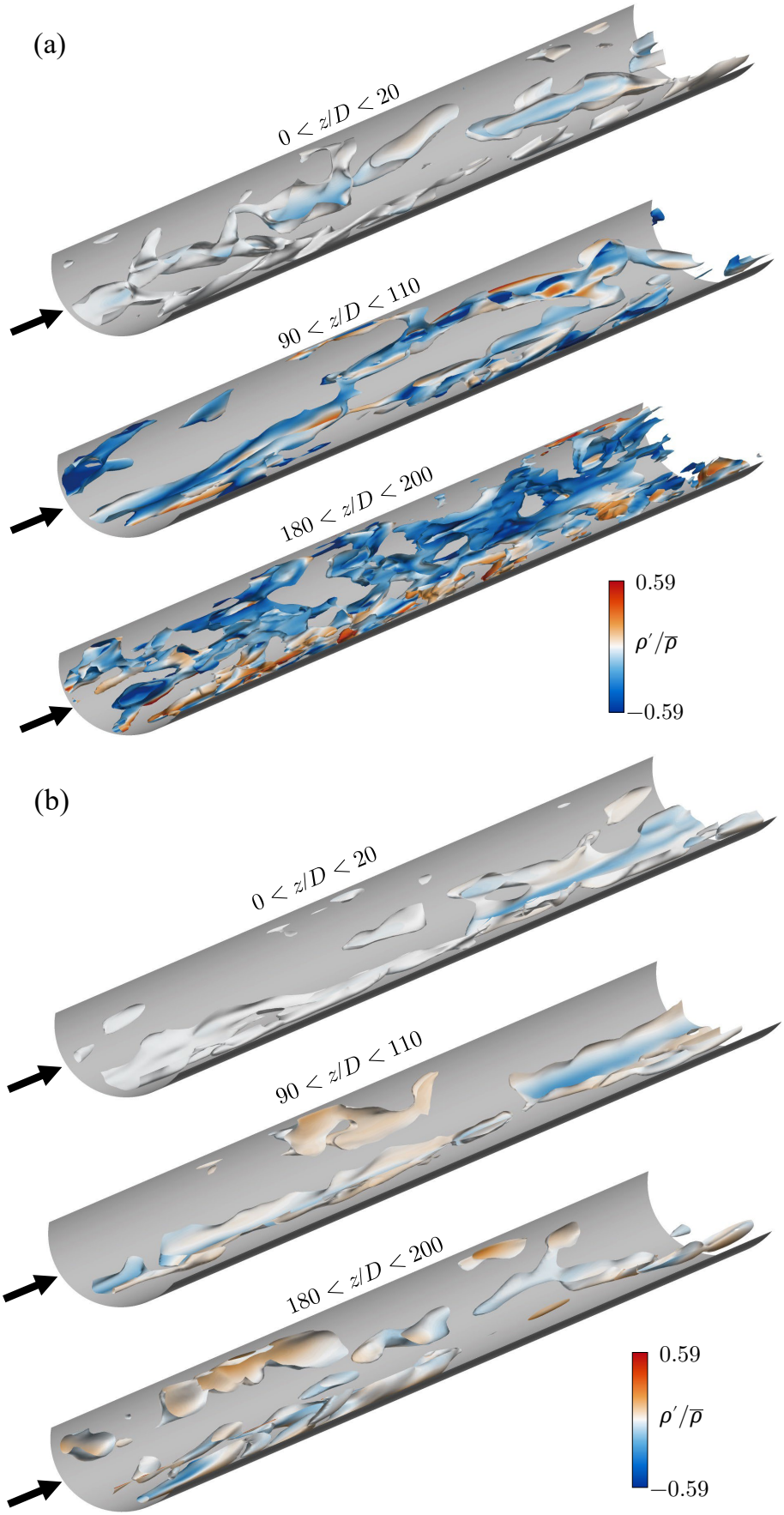

Figure 5.35. Instantaneous snapshots of iso-surfaces of ejection ($u_r'' = -0.01$) motions colored by density fluctuations at (a) $p = 2$ MPa and (b) $p = 6$ MPa under the mass flow rate condition of $G = 1.75$ g/s.

showed that the density fluctuation effect common in transcritical flows exhibited in the negative slope region of the hydrodynamic characteristic curves.

Figure 5.35 shows instantaneous snapshots of iso-surfaces of near-wall low-speed streaks at $p = 2\ \mathrm{MPa}$ and $p = 6\ \mathrm{MPa}$ under the mass flow rate condition of $G = 1.75\ \mathrm{g/s}$. Three-dimensional turbulent structures, which are colored by the density fluctuation, at different three streamwise positions were visualized to investigate the spatial-developing flow. Arrows in Fig. 5.35 indicate inflows. At the inlet region ($0 < z/D < 20$), the density fluctuations were less for both pressure conditions $p = 2\ \mathrm{MPa}$ and $p = 6\ \mathrm{MPa}$ because the fluid was not heated sufficiently to cause a large density change. The fluid was gradually heated toward the outlet, and the fluid density was drastically changed when crossing the pseudo-critical temperature, resulting in density fluctuation appeared. Fig. 5.35 shows that the density fluctuation at $p = 2\ \mathrm{MPa}$ is intensified compared with that at $p = 6\ \mathrm{MPa}$. As shown in Fig. 5.18, the fluid density significantly changes approaching the critical pressure. In addition, the density change in the transcritical condition becomes abrupt, i.e., slight changes in temperature lead to large changes in density. As a result, large density fluctuations are induced under pressure conditions near the critical point. Inward flows accompanied by negative density fluctuations were clearly observed at $p = 2\ \mathrm{MPa}$. From Eq. (5.17), the ejection ($u_z'' < 0$ and $u_r'' < 0$) was intensified by negative density fluctuations associated with the pseudo-boiling. That is why the ejection at $p = 2\ \mathrm{MPa}$ was gradually intensified toward the downstream. At $p = 6\ \mathrm{MPa}$, there was little density fluctuation and no obvious development of the ejection in the streamwise direction compared with the case of $p = 2\ \mathrm{MPa}$. The density fluctuation is highly dependent on pressure, and the effect significantly appeared in the outlet region ($180 < z/D < 200$) as a difference in discharge behavior.

5.6 Conclusions

The mechanism of flow instability and the hydrodynamic characteristic curve, which is related to the dynamic behavior of flow instability, were investigated in this chapter.

First, new robust numerical methods were developed to investigate flow instabilities in the EHF under the transcritical and pyrolysis conditions. The fluid flow of EHF in a heated tube may be more complicated because the hydrodynamic characteristic curve of EHF has an order of five, i.e., five equilibrium points of mass flow rate would be expected for a constant pressure drop. In the present study, the phase separation model (PSM) was developed for the hydrocarbon mixture to consider the effect of non-condensable gas products generated by pyrolysis reaction and to reproduce the fifth-order hydrodynamic characteristic curve of EHF. Note that the present study is the first attempt to introduce the PSM of multi-component supercritical fluids into the one-dimensional numerical simulation. Then, the DFM in preconditioning system, which is shown in Chapter 2, was introduced to the present numerical method to avoid spurious oscillations and realize robust simulations of flow instabilities. The numerical methods were validated by referring to available numerical and experimental data on pressure drop and mass flow rate in a heated circular tube. Besides, the simulated results of cyclohexane flow in a horizontal circular tube were compared with existing experimental data to demonstrate the capability of qualitatively predicting the pressure and temperature. Eventually, the present method was applied to transcritical *n*-dodecane flows with the pyrolysis reaction in a horizontal heated circular tube. First, the steady-state simulations were conducted to obtain the hydrodynamic characteristic curve for *n*-dodecane flows. The effects of DFM and PSM on the hydrodynamic characteristic curves were investigated. Results with DFM and without DFM indicated that the spurious oscillation may cause the pressure difference in the hydrodynamic characteristic curve. Results with PSM demonstrated that the pressure drop increases at low mass flux conditions for all heat flux conditions because of the phase separation effect. As a result, hydrodynamic characteristic curves with the PSM have a second negative slope region and were fifth order with respect to the mass flux. In addition, a clear negative gradient region of the hydrodynamic characteristic curves was observed when using PSM even under the high-pressure condition of $p = 10\ \mathrm{MPa}$. Then, the transient simulations of *n*-dodecane flows in a heated circular tube were performed to numerically investigate the dynamic behavior. The flow instability behavior was changed because of the phase separation. The flow could not reach the high mass flux side over the equilibrium point and was trapped at the low mass flux side. This decrease in mass flux can increases the rate of enthalpy rise, inducing an unexpected increase in tube temperature. It may also trigger intense pyrolysis reactions under high-temperature conditions, which leads to coking or overheating. When using the PSM, DWOs do not disappear even at $p = 10\ \mathrm{MPa}$ because of the strong feedback effects between pressure drop, density, and mass flux.

Next, I investigated the mechanisms behind the formation of the multi-valued hydrodynamic characteristic curves using the large eddy simulation (LES) code. To validate the numerical method of LES, the turbulent channel flows were conducted. The average velocity and root mean square (RMS) velocity in the parallel channel were compared with available DNS data. Besides, the simulated adiabatic friction factors in a horizontal circular tube were compared with theoretical value and previous correlation to evidence

enough capability of predicting the pressure field. Eventually, the LES were conducted for *n*-dodecane flows in a horizontal heated circular tube at supercritical pressure. Hydrodynamic characteristic curves were obtained under different three supercritical pressure conditions. The hydrodynamic characteristic curve at $p = 2.0\ \mathrm{MPa}$ and $2.5\ \mathrm{MPa}$ have negative slope regions. The pressure-drop significantly increased with approaching to the pseudocritical pressure. The enhancement of ejection motion associated with large density fluctuations at $p = 2.0\ \mathrm{MPa}$ induced the negative radial velocity. The radial transport of the low-density fluid near the heated wall to the mainstream by vigorous ejection motion led to a decrease in bulk density and a significant flow acceleration. Eventually, it was clarified that the increase in acceleration pressure drop at $p = 2.0\ \mathrm{MPa}$ caused the formation of a negative slope region in the hydrodynamic characteristic curve of the heated circular tube. In addition, the mechanisms of heat transfer enhancement/deterioration related to the intense ejection motion and the flow acceleration were elucidated by using the FIK identity for the Nusselt number. The present LES analyzed transcritical flows in the heated circular tube by visualizing flow properties, such as temperature and density profiles, and turbulence statistics. As a result of the visualization, the enhancement and reduction mechanism of Favre-averaged velocity fluctuations by the effect of density fluctuation were demonstrated in the transcritical flows. Besides, the visualized conditions corresponded with the negative slope region of the hydrodynamic characteristic curve. More detailed analyses of transient flows in a heated circular tube are expected in the next step to clarify the formation mechanism of hydrodynamic characteristic curves.

References

1. M. Ledinegg, “Instability flow during natural forced circulation,” Die Waerme, 61, (1938), 891–898.
2. S. Kakac, B. Bon, “A Review of two-phase flow dynamic instabilities in tube boiling systems,” International Journal of Heat and Mass Transfer, 51, (2008), 399–433.
3. L.C. Ruspini, C.P. Marcel, A. Clausse, “Two-phase flow instabilities: A review,” International Journal of Heat and Mass Transfer, 71, (2014), 521–548.
4. J.A. Boure, A.E. Bergles, L.S. Tong, “Review of two-phase flow instability,” Nuclear Engineering and Design, 25, (1973), 165–192.
5. S. Tomioka, T. Hiraiwa, T. Saito, K. Kato, M. Kodera, K. Tani, “System analysis of a hydrocarbon-fueled RBCC engine applied to a TSTO launch vehicle,” Transactions of the Japan Society for Aeronautical and Space Sciences, Aerospace Technology Japan, 12 (29) (2014) 91–99.
6. W. Ambrosini, “Discussion on the stability of heated channels with different fluids at supercritical pressures,” Nuclear Engineering and Design, 239, (2009), 2952–2963.
7. W. Ambrosini, “On the analogies in the dynamic behaviour of heated channels with boiling and supercritical fluids,” Nuclear Engineering and Design, 237, (2007), 1164–1174.
8. M. Sharabi, W. Ambrosini, S. He, “Prediction of unstable behaviour in a heated channel with water at supercritical pressure by CFD models,” Annals of Nuclear Energy, 35, (2008), 767–782.
9. Z. Zhang, C. Zhao, X. Yang, P. Jiang, J. Tu, S. Jiang, “Numerical study of the heat transfer and flow stability of water at supercritical pressures in a vertical tube,” Nuclear Engineering and Design, 325, (2017), 1–11.
10. V. Garg, G. Dutta, “Numerical study of external inertia and compressible volume on nuclear coupled density wave oscillations in a supercritical pressure channel,” Nuclear Engineering and Design, 363, (2020), 110607.
11. H.T. Liu, H. Kocak, S. Kakac, “Dynamical analysis of pressure-drop type oscillations with a planar model,” International Journal of Multiphase Flow, 21, (1995), 851–859.
12. P.R. Mawasha, R.J. Gross, “Periodic oscillations in a horizonatl single boiling channel with thermal wall capacity,” International Journal of Heat and Fluid Flow, 22, (2001), 643–649.
13. M.E. Rahman, S. Singh, “Flow excursions and pressure drop oscillations in boiling two-phase channel,” International Journal of Heat and Mass Transfer, 138, (2019), 647–658.
14. T. Xiong, X. Yan, Z. Xiao, Y. Li, Y. Huang, J. Yu, “Experimental study on flow instability in parallel channels with supercritical water,” Annals of Nuclear Energy, 48, (2012), 60–67.
15. B.T. Swapnalee, P.K. Vijayan, M. Sharma, D.S. Pilkhwal, “Steady state flow and static instability of supercritical natural circulation loops,” Nuclear Engineering and Design, 245, (2012), 99–112.
16. G. Liu, Y. Huanga, J. Wang, F. Lv, L.K.H. Leung, “Experiments on the basic behavior of supercritical CO2naturalcirculation,” Nuclear Engineering and Design, 300, (2016), 376–383.
17. B. Hitch, M. Karpuk, Experimental investigation of heat transfer and flow instabilities in supercritical fuels, AIAA 3043 (1997).
18. H. Wang, J. Zhou, Y. Pan, N. Wang, “Experimental investigation on the onset of thermo-acoustic instability of supercritical hydrocarbon fuel flowing in a small-scale channel,” Acta Astronautica, 117,

(2015), 296–304.
19. W. Zhou, B. Yu, J. Qin, D. Yu, “Mechanism and influencing factors analysis of flowing instability of supercritical endothermic hydrocarbon fuel within a small-scale channel,” Applied Thermal Engineering, 71, (2014), 34–42.
20. Z. Yang, Y. Shan, B. Zhang, Y. Liu, “Hydrodynamic characteristics of cyclohexane in a horizontal mini-tube at trans- and supercritical pressures,” Applied Thermal Engineering, 129, (2018), 62–69.
21. Z. Yang and Y. Shan, “Experimental study on the onset of flow instability in small horizontal tubes at supercritical pressures,” Applied Thermal Engineering, 135, (2018), 504–511.
22. Z. Yang, T. Li, X. Zhao, T. Gao, B. Zhang, “Hydrodynamic and heat transfer characteristics of binary hydrocarbons at trans- and supercritical pressures,” Experimental Thermal and Fluid Science, 116, (2020), 110128.
23. Y. Guo, Q. Bi, Z. Liu, Z. Yang, L. Jiang, “Experimental investigation on thermal-hydraulic characteristics of endothermic hydrocarbon fuel in 1 mm and 2 mm diameter minichannels,” Applied Thermal Engineering, 122, (2017), 420–428.
24. Y. Jin, K. Wu, Y. Lu, X. Fan, “A one-dimensional transient calculation method for flow instability of supercritical hydrocarbon in cooling channels,” AIAA Propulsion and Energy Forum, (2021).
25. T.A. Ward, J.S. Ervin, R.C. Striebich, S. Zabarnick, “Simulations of flowing mildlycracked normal alkanes incorporating proportional product distributions,” Journal of Propulsion and Power, 20 (3), (2004), 394–402.
26. Z. Yang, Q. Bi, Z. Liu, Y. Guo, J. Yan, “Heat transfer to supercritical pressure hydrocarbons flowing in a horizontal short tube,” Experimental Thermal and Fluid Science, 61, (2015), 144–152.
27. J.M. Weiss, W.A. Smith, “Preconditioning applied to variable and constant density flows,” AIAA Journal, 33, (1995), 2050–2056.
28. Y. Feng, S. Liu, J. Qin, Y. Cao, Y. Jiang, S. Zhang, “Numerical study on the influence of turbulence on the pyrolysis of hydrocarbon fuel in mini-channel,” International Journal of Heat and Mass Transfer, 119, (2018), 768–776.
29. S. Yamamoto, “Preconditioning method for condensate fluid and solid coupling problems in general curvilinear coordinates,” Journal of Computational Physics, 207, (2005), 240–260.
30. B.V. Leer, “Towards the ultimate conservative difference scheme. V. A second-order sequel to Godunov’s method,” Journal of Computational Physics, 32, (1979), 101–136.
31. E.W. Lemmon, I.H. Bell, M.L. Huber, M.O. McLinden, NIST Standard Reference Database 23: Reference Fluid Thermodynamic and Transport Properties-REFPROP, Version 10.0, National Institute of Standards and Technology, 2018.
32. C.R. Wilke, “A viscosity equation for gas mixtures,” Journal of Chemical Physics, 18, (1950), 517–519.
33. F. Herning, L. Zipperer, “Beitrag zur berechnung der zähigkeit technischer gasgemische aus den zähigkeitswerten der einzelbestandteile,” Gas-Wasser-fach, 79, (1936).
34. D. Chisholm, “A theoretical basis for the Lockhart–Martinelli correlation for two-phase flow,” International Journal of Heat and Mass Transfer, 10, (1967), 1767–1778.
35. J.V. Ribeiro, A.A. Susu, and J.P. Kohn, “Heterogeneous-phase equilibrium in ethylene–*n*-dodecane system,” Journal of Chemical and Engineering Data, 17, (1972), 279–280.

36. K.H. Lee, J.P. Kohn, “Heterogeneous phase equilibrium in the ethane–*n*-dodecane system,” Journal of Chemical and Engineering Data, 14, (1969), 292–295.
37. Rainer N. Dahms and Joseph C. Oefelein, “On the transition between two-phase and single-phase interface dynamics in multicomponent fluids at supercritical pressures,” Physics of Fluids, 25, (2013), 092103.
38. P.C. Ma, H. Wu, D.T. Banuti, M. Ihme, “On the numerical behavior of diffuse-interface methods for transcritical real-fluids simulations,” International Journal of Multiphase Flow, 113, (2019), 231–249.
39. J.P. Meyer, M. Everts, N. Coetzee, K. Grote, M. Steyn, “Heat transfer coefficients of laminar, transitional, quasi-turbulent and turbulent flow in circular tubes,” International Communications in Heat and Mass Transfer, 105, (2019), pp. 84–106.
40. X. Fang, Y. Xu, X. Su, R. Shi, “Pressure drop and friction factor correlations of supercritical flow,” Nuclear Engineering and Design, 242, (2012), 323– 330.
41. K. Zhu, G. Xu, Z. Tao, H. Deng, Z. Ran, C. Zhang, “Flow frictional resistance characteristics of kerosene RP-3 in horizontal circular tube at supercritical pressure,” Experimental Thermal and Fluid Science, 44, (2013), 245–252.
42. H. Wang, Q. Bi, G. Wub, Z. Yang, “Experimental investigation on pressure drop of supercritical water in an annular channel,” The Journal of Supercritical Fluids, 131, (2018), 47–57.
43. Y. Liu, G. Xu, Y. Fu, J. Wen, G. Gong, L. Lyu, “Frictional resistance of supercritical pressure RP-3 flowing in a vertically downward tube at constant heat fluxes,” Chinese Journal of Aeronautics, 35, (2022), 117–128.
44. G. Dutta, C. Zhang, J. Jiang, “Analysis of flow induced density wave oscillations in the CANDU supercritical water reactor,” Nuclear Engineering and Design, 286, (2015), 150–162.
45. N. Alkishriwi, M. Meinke, W. Schroder, “A large-eddy simulation method for low Mach number flows using preconditioning and multigrid,” Computers & Fluids, 35, (2006), 1126–1136.
46. P. Renze, W. Schroder, M. Meinke, “Large-eddy simulation of film cooling flows at density gradients,” International Journal of Heat and Fluid Flow, 29, (2008), 18–34.
47. S. Yang, X. Wang, V. Yang, W. Sun, H. Huo, “Comparison of flamelet/progress-variable and finite-rate chemistry LES models in a preconditioning scheme,” 55th AIAA Aerospace Sciences Meeting (AIAA 2017-0605).
48. Y. Jiang, C.-W. Shu, and M. Zhang, “An Alternative Formulation of Finite Difference Weighted ENO Schemes with Lax--Wendroff Time Discretization for Conservation Laws,” SIAM Journal on Scientific Computing, 35, (2013), A1137–A1160.
49. S.K. Lele “Compact finite difference schemes with spectral-like resolution,” Journal of Computational Physics, 103, (1992),16–42.
50. E.W. Lemmon and M.L. Huber, "Thermodynamic properties of *n*-dodecane," Energy & Fuels, 18(4), (2004), 960–967.
51. M.L. Huber, A. Laesecke, R.A. Perkins, “Transport properties of *n*-dodecane,” Energy & Fuels, 18, (2004), 968–975.

52. J.C. Rainwater, D.G. Friend, “Second viscosity and thermal-conductivity virial coefficients of gases: Extension to low reduced temperature,” Physical Review A, 36, (1987), 4062–4066.
53. J. Kim, P. Moin, R. Moser, “Turbulent statistics in fully developed channel flow at low Reynolds number,” Journal of Fluid Mechanics, 177, (1987), 133–166.
54. S. Kawai, “Heated transcritical and unheated non-transcritical turbulent boundary layers at supercritical pressures,” Journal of Fluid Mechanics, 865, (2019), 563-601.
55. J. Liu, P. Zhao, M. Lei, S. Yang, H. Nemati, “Numerical investigation of spatial-developing turbulent heat transfer in forced convections at different supercritical pressures,” International Journal of Heat and Mass Transfer, 159, (2020), 120128.
56. K. Fukagata, K. Iwamoto, N. Kasagi, “Contribution of Reynolds stress distribution to the skin friction in wall-bounded flows,” Physics of Fluids, 14, (2002), L73–L76.
57. K. Fukagata, N. Kasagi, “Drag reduction in turbulent pipe flow with feedback control applied partially to wall,” International Journal of Heat and Fluid Flow, 24, (2003), 480–490.
58. T. Gomez, V. Flutet, P. Sagaut, “Contribution of Reynolds stress distribution to the skin friction in compressible turbulent channel flows,” Physical Review E, 79, (2009), 035301.
59. Y. Kametani, K. Fukagata, “Direct numerical simulation of spatially developing turbulent boundary layers with uniform blowing or suction,” Journal of Fluid Mechanics, 681, (2011), 154–172.
60. J. Lee, S.Y. Jung, H.J. Sung, T.A. Zaki, “Effect of wall heating on turbulent boundary layers with temperature-dependent viscosity,” Journal of Fluid Mechanics, 726, (2013), 196–225.
61. P. Zhao, J. Liu, Z. Ge, Y. Li, N. Zhao, Y. Wan, “Direct numerical simulation of strongly heated air flows in a vertical pipe using a thermophysical property table,” International Journal of Heat and Mass Transfer, 124, (2018), 1181–1197.
62. H. Nemati, A. Patel, B.J. Boersma, R. Pecnik, “The effect of thermal boundary conditions on forced convection heat transfer to fluids at supercritical pressure,” Journal of Fluid Mechanics, 800, (2016), 531–556.
63. S. Pandey, X. Chu, E. Laurien, B. Weigand, “Buoyancy induced turbulence modulation in pipe flow at supercritical pressure under cooling conditions,” Physics of Fluids, 30, (2018), 065105.
64. P. Zhao, T. Wan, Y. Jin, Z. Chen, Y. Li, and C. Peng, “Direct numerical simulation analysis of heat transfer deterioration of supercritical fluids in a vertical tube at a high ratio of heat flux to mass flowrate,” Physics of Fluids, 33, (2021), 055114.

Chapter 6

Conclusions

6.1 Conclusions

The main objective of this work was to develop a robust numerical method for supercritical multicomponent flows and to clarify the multiphysics flows of supercritical hydrocarbons that govern the characteristics of regenerative cooling systems. The conclusions regarding each part are detailed as follows.

In Chapter 2, the robust numerical method for simulating the multicomponent supercritical flows is established to accurately simulate the hydrocarbon flows in the regenerative cooling system. The spurious oscillations associated with the multicomponent and transcritical flows in preconditioning systems were investigated in detail. First, in a one-dimensional Euler system, I derived the temporal variation of the unknown variables in the case of a single fluid interface for different temperatures, and also at the material interface for a uniform fluid temperature. The temporal variation in the preconditioned system indicated that the spatial variations of the mass fraction and temperature caused spurious oscillations. Based on the analytical results, the double-flux model was extended to the preconditioning method to eliminate the spurious pressure oscillations. Furthermore, the conservation errors due to the use of a quasi-conservative form were quantitatively evaluated. The proposed numerical methods were applied to a series of test cases to examine the performance of the double-flux model and to demonstrate its suitability in simulations for multicomponent supercritical flows.

In Chapter 3, the modeling method for the pyrolysis reaction of hydrocarbons was established. Using Cantera software and the JetSurf model, a series of zero-dimensional pyrolysis reaction calculations of *n*-dodecane were conducted. The pyrolysis reaction of *n*-dodecane was incorporated into the flow simulation as a one-step reaction, and the reaction rate constant was expressed by using the Alenius equation. Supercritical *n*-dodecane flows in a horizontal heated circular pipe with pyrolysis were investigated using the pyrolysis reaction model. The numerical results were compared with the experimental data about the outlet temperature and the conversion rate to validate the present pyrolysis reaction model. In addition, the results of the *n*-dodecane flow were compared to those of the *n*-octane flow and the differences between both flows are discussed. The difference in thermophysical properties affects the temperature distribution and residence time in the heated pipe, resulting in differences in the conversion rate.

In Chapter 4, the effects of pyrolysis reaction on supercritical *n*-octane flows in a horizontal heated circular tube were elucidated. To clarify the effect of density change related to the pyrolysis reaction, the k–ω SST+Mτ turbulence model was introduced to the numerical method based on the preconditioning method. The pyrolysis reaction model developed in Chapter 3 was incorporated into the numerical method. The

thermophysical properties of the pure fluid were calculated by using the polynomial equations defined in the Reference Fluid Thermodynamic and Transport Properties Database, and the mixture properties were modeled on the basis of the mass fraction. Supercritical *n*-octane flows in a horizontal heated circular pipe with pyrolysis were conducted, and numerical results were compared with the experimental data about the outlet temperature and the conversion rate to validate the present numerical methods. The capabilities and limitations of simple thermophysical property models for the mixture were evaluated through a comparison of results obtained using three mixture property models. The effect of density fluctuations on turbulent thermal diffusivity was discussed by employing the k–ω SST+M_τ turbulence model. Simulated results suggested that the consideration of the density fluctuations effect and the corresponding production of turbulent kinetic energy are key issues for reproducing the thermal fluid flows of supercritical hydrocarbons with pyrolysis.

In Chapter 5, the mechanism of flow instability and the hydrodynamic characteristic curve, which is deeply related to the dynamic behavior of flow instability, were investigated. First, new numerical methods that can simulate the flow instabilities under the transcritical and pyrolysis conditions were developed to clarify the mechanism of flow instability. The numerical methods were validated by referring to available numerical and experimental data on pressure drop and mass flow rate in a heated circular tube. First, steady-state simulations were conducted to obtain the hydrodynamic characteristic curve for *n*-dodecane flows. The effects of DFM and PSM on the hydrodynamic characteristic curves were investigated. Then, transient simulations were conducted for the flow instability of *n*-dodecane flows in a horizontal heated circular tube. The effects of pyrolysis reactions and pressure on the flow instability were evaluated for *n*-dodecane flows in a horizontal heated circular tube. Next, the hydrodynamic characteristic curves of a horizontal heated circular tube at supercritical pressure are investigated by using the LES code. The numerical methods were validated by referring to available direct numerical simulation data of the turbulent channel flows and also the friction factor correlation of the adiabatic circular tube. After the validation, the simulations for *n*-dodecane flows in a horizontal heated circular tube are conducted, and the pressure drop with respect to the mass flow rate, i.e., the hydrodynamic characteristic curves, were obtained under different three supercritical pressure conditions. Eventually, it was clarified that the increase in acceleration pressure drop caused the formation of a negative slope region in the hydrodynamic characteristic curve of the heated circular tube.

6.2 Future studies

The present work covers several aspects of numerical methods for supercritical hydrocarbon flows and their application. However, some minor questions still remain. In the following, some recommendations for improving our knowledge about supercritical hydrocarbon flows are stated.

- Definition of stable/unstable conditions for hydrocarbon flows in a heated tube:
  In Chapter 5, the mechanisms of flow instabilities for hydrocarbon flows were investigated at supercritical pressure. In addition to the present investigation, the definition of stable/unstable conditions for flow instabilities is also crucial for the application. According to existing studies,

flow instability occurs when the heat flux gradually increases and exceeds a certain threshold. Once flow instability occurs, it is believed that the instability will continue unless the heat flux is reduced. However, JAXA experiments reported that the flow instabilities disappear when the heat flux is increased. More detailed investigation on stable/unstable conditions of flow instability is needed to provide insights for the reliable regenerative cooling system.

- Understanding of phase separation phenomena in multicomponent hydrocarbon flows:
  In Chapter 5, I showed that phase separation in hydrocarbon mixtures can occur at significantly high pressures beyond the critical pressure of the pure substance in the mixture. The effects of phase separation on flow characteristics such as heat transfer and friction have never been discussed at all in the context of regenerative cooling systems. Modeling phase separation phenomena in multidimensional CFD can be useful to understand the complex phenomenon in regenerative cooling systems. Also, it might be interesting to investigate differences or similarities between phase separation and boiling, which is the same interfacial phenomenon, in heat transfer and friction characteristics. For multi-component hydrocarbon flows in a heated tube relevant to regenerative cooling systems, the significance of phase separation needs to be investigated.

- Catalytic pyrolysis reactions in transcritical hydrocarbon flows:
  It is known that the use of catalysts can dramatically decrease the initiation temperature of pyrolysis reactions and thereby reduce carbon deposition, which can cause heat transfer deterioration in regenerative cooling systems. As an example, using a platinum catalyst, the initiation temperature of the pyrolysis reaction can be lowered by several hundred Kelvin. In this case, the pyrolysis reaction occurs near the pseudocritical temperature of the parent fuel. Thermophysical properties change drastically in the transcritical condition that crosses the pseudocritical temperature. Although the interference between the drastic change in thermophysical properties and the pyrolysis reaction is expected, the impact of the interference has not been clarified.

Acknowledgements

The present study and this thesis would have been impossible without the guidance and support of Prof. Satoru Yamamoto. His expertise and understanding in the field of computational fluid dynamics have helped me to shape my current understanding of this field. He gave me not only strategies on how to conduct research and attitudes on how to be a good researcher, but also ideas to guide my life. I am proud to have studied under him.

I am deeply grateful to my adviser, Prof. Takashi Furusawa for his support and encouragement of my study and dissertation. His deep insights and understanding of supercritical fluid flow have helped me in carrying out my research. I am happy to have taken my first steps as a researcher under his guidance.

I sincerely thank Prof. Yuji Hattori, Prof. Jun Ishimoto, and Prof. Sadatake Tomioka for serving on my committee and as thesis referee. Their suggestions and comments help to improve the quality of the thesis.

I really appreciate Dr. Hironori Miyazawa and Dr. Shota Moriguchi for sharing with me their knowledge of computational fluid dynamics and software. I was fortunate to have senior colleagues close to me who were role models as researchers.

I am really indebted to my co-researcher that I worked with: Dr. Takuo Onodera and Dr. Tatsushi Isono who are researchers at Japan Aerospace Exploration Agency. Their guidance and advice made this thesis better.

I am thankful to supercritical fluid simulator group members at Yamamoto and Furusawa laboratory who have guided and worked with me: Mr. Kenji Kagaya, Mr. Noriyuki Taki, Mr. Ryotaro Sato, and Mr. Kensho Haba. Then, I am also thankful to members at Tomioka laboratory with whom I collaborated: Mr. Takuto Miyaura, Mr. Ko Kurihara, Mr. Yosuke Kono, and Mr. Motoki Hattori.

This study was done with the NEC SX-Aurora TSUBASA supercomputing system (AOBA-A and -C) at Cyberscience Center, Tohoku University. Especially the AOBA-C cloud service, which started this October, must have saved not only me but many other students. I would like to thank all people related to the system.

Financial support by JST SPRING, Grant Number JPMJSP2114 is gratefully acknowledged.

I would like to thank all the lab members for both my research and my life. I could really enjoy my life in this laboratory.

Then, I have to say thank my friends: Mr. Kazutoshi Hayashi and Mr. Keisuke Kanayama who are Ph.D. students at Tohoku University, and Mr. Noritaka Sako who is a Ph.D. student at Kyoto University, and Yuya Shimizu who is a Ph.D. student at Université Paris-Saclay. I was very lucky to have friends with whom I could share the joys and pains of research.

Furthermore, let me take this occasion to say thank my beloved parents for their endless love and support for their child. I owe them everything.

Finally, I would like to thank my beloved wife. She had been always by my side. Thank you always.

January 10, 2023

Shuto Yatsuyanagi

発表論文リスト

学術論文 (Journal)

1. Shuto Yatsuyanagi, Takashi Furusawa, Hironori Miyazawa, Satoru Yamamoto, Takuo Onodera, Sadatake Tomioka, “Numerical Study of Supercritical Octane Flow with Multicomponent Effects by Pyrplysis,” International Journal of Thermal Sciences, 171, (2022), 107103.

(第 4 章)

2. ShutoYatsuyanagi, Takashi Furusawa, Satoru Yamamoto, “Double-flux model for supercritical multicomponent flows at low Mach numbers with preconditioning method,” Journal of Computational Physics, 458, (2022), 111091.

(第 2 章)

学術論文 (Proceedings)

1. Shuto Yatsuyanagi, Takashi Furusawa, Satoru Yamamoto, Takuo Onodera, Sadatake Tomioka, “Numerical Investigation of Supercritical *N*-Dodecane Flows in a Heated Circular Pipe with Thermal Cracking,” Proceedings of The ASME Fluids Engineering Division Summer Meeting 2021, FEDSM2021-65261, (2021).

(第 3 章)

国際会議等発表論文 (アブストラクト査読)

1. Shuto Yatsuyanagi, Takashi Furusawa, Satoru Yamamoto, Sadatake Tomioka, “Numerical Investigation of Supercritical Hydrocarbon Flows with Pyrolysis,” Proceedings of the 17th International Conference on Flow Dynamics, Sendai, October, (2020).

(第 4 章)

2. Shuto Yatsuyanagi, Takashi Furusawa, Satoru Yamamoto, Sadatake Tomioka, Takuo Onodera, “Numerical Study on Supercritical N-Dodecane Flows with Endothermic Pyrolysis Reaction,” Proceedings of The 18th International Conference on Flow Dynamics, Sendai, October, (2021).

(第 3 章)

参考論文

学術論文 (Proceedings)

1. Takashi Furusawa, Kenta Matsui, Shuto Yatsuyanagi, Satoru Yamamoto, Akira Yoko, Tadafumi Adschiri, “Turbulent Flow Simulation of Supercritical Hydrothermal Synthesis in T-Shaped Channel,” Proceedings of The ASME Fluids Engineering Division Summer Meeting 2021, FEDSM2021-66023, (2021).

国際会議等発表論文 (アブストラクト査読)

1. Kenta Matsui, Shuto Yatsuyanagi, Takashi Furusawa, Akira Yoko, Satoru Yamamoto, Tadafumi Adschiri, “Numerical Simulation of Turbulent Mixing Flow in Supercritical Hydrothermal Synthesis Reactors,” Proceedings of The 18th International Conference on Flow Dynamics, Sendai, October, (2021).

国内会議発表

1. 八柳秀門，古澤卓，山本悟，“熱分解反応を伴う遷臨界炭化水素流れの数値解析”，第 34 回数値流体力学シンポジウム，オンライン開催，(2020).

2. 八柳秀門，古澤卓，山本悟，小野寺卓郎，富岡定毅,“水平加熱矩形管内部における遷臨界炭化水素流動の LES”，第 35 回数値流体力学シンポジウム，オンライン開催，(2021).